

Soft multimodal neural interfaces for unravelling sensory neurological circuits

Thèse N° 9046

Présentée le 1^{er} mars 2019

à la Faculté des sciences et techniques de l'ingénieur
Chaire Fondation Bertarelli de technologie neuroprosthétique
Programme doctoral en biotechnologie et génie biologique

pour l'obtention du grade de Docteur ès Sciences

par

Frédéric Pierre Gérald MICHOU

Acceptée sur proposition du jury

Prof. A. Ijspeert, président du jury
Prof. S. Lacour, directrice de thèse
Prof. I. Decosterd, rapporteuse
Prof. O. Paul, rapporteur
Prof. H. Shea, rapporteur

2019

Every act of perception, is to some degree an act of creation,
Every act of memory is to some degree an act of imagination.

— Oliver Sachs

Acknowledgements

This thesis marks the conclusion of four years of doctorate work. This endeavour would certainly not have been possible without the contribution, support and encouragement of many people.

First and foremost, I would like to express my gratitude to Prof. Stéphanie Lacour who offered me the opportunity to pursue my Ph.D. in her laboratory. I deeply acknowledge her trust, invaluable support and scientific advice. I am indebted to the freedom I was granted, which allowed me to independently explore new ideas. Throughout these years, Stéphanie has transmitted her genuine enthusiasm and optimism, flourishing a truly stimulating environment. I would also like to thank Prof. Clifford Woolf for his guidance and scientific enlightenment. Since the beginning of our collaboration, Clifford has been an inspiring mentor who has granted me personal attention and many fruitful discussions. I would also like to thank Prof. Grégoire Courtine who introduced me to his scientific journey years before I started my Ph.D. The devotion and energy Grégoire has for his research has been inspirational.

I am also grateful to Prof. Isabelle Decosterd, Prof. Oliver Paul and Prof. Herbert Shea for taking the time to critically review my work, and to Prof. Auke Ijspeert for accepting to preside on the examination jury.

I most sincerely thank Ivan Minev, Liam Browne and Ignacio Delgado Martinez, with whom I had the chance to work during numerous projects preceding or during the doctorate. Their formative experience laid down the bedrock of my scientific education. I acknowledge their insights, high-quality standards and the pleasant atmosphere they brought every day to the lab.

Next, I would like to thank my colleagues at the Laboratory for Soft Bioelectronic Interfaces for all the precious help I received during these years. Many of them contributed to the success of my projects and deserve significant credit. I am grateful to Amélie for her early work on optoelectronic implants and for the time she spent debugging my initial "bright" ideas. Special thanks go to Giuseppe, Xiaoyang, Nicolas, Arthur and Florian, with whom I shared exciting times developing soft neural interfaces. My gratitude also goes to Katia and Ivan, who were so proficient in their work. I must also thank Liz and Noaf, who kindly reviewed several parts of

Acknowledgements

this thesis. I would like to thank all the other members of the lab who made these years very enjoyable, including Hadrien, Aaron, Jennifer, Laurent, Sandra, Michael and Florent.

An essential part of my research would not have been possible without the numerous collaborators involved. First, I sincerely thank all the members of the Clifford Woolf lab who always welcomed me as a member of their team. My gratitude goes especially to Rachel, Sebastien, Corey, Ben, David, Miyuki, Ivan and Alban, who actively took part in the translation of my work into real neurobiological tools. I am also very grateful for all the exchange I had with the members of the Courtine lab, including Claudia, Jérôme, Léonie, Polina, Arnaud and Quentin. Their outstanding work is reflected in all the projects we carried out together. I wish them the best of luck in the implementation of their innovative therapies in humans. I must also thank Philipp and Noé from the Qiuting lab at ETH for their crucial contributions to the peripheral and spinal optoelectronic projects. I enjoyed our continual communication and our common desire to make the most of our technologies.

I am seriously indebted to all the staff of the EPFL Center for MicroNanoTechnologies and to Mickaël, Anthony and Valérian from the Geneva Wyss Center. I started my Ph.D. with no experience in microengineering and would certainly not have been able to develop my own processes without their constant assistance and firm patience. I would also like to thank Laura and Aurélien from the histology core, who helped me during the final months of the doctorate.

Of course, I must acknowledge the hard work and dedication of all the students I had the chance to supervised: Loïc, Tamara, Manon, François and Morten.

A special thank you goes to the Micera lab for providing a table tennis "platform" and to all my interim adversaries for intruding my thesis work.

On a more personal note, I feel extremely lucky to be surrounded by many friends who actively supported this endeavor. These "indirect" contributors excelled in making my days joyful and I shared countless exciting memories with them. They are scattered around the globe, from San Francisco to Hong-Kong, Paris ("les Kims") to Boston, Zurich to Geneva, and will certainly recognize themselves reading these lines.

Finally, I will forever treasure the unconditional support of my family who always encouraged me through the years.

To all of you, sincerely, Merci!

Geneva, November 2018

F. M.

Abstract

Diseases or injuries affecting the nervous system can dramatically disrupt the quality of life. Despite extensive efforts towards treating dysfunctional nervous systems, the pharmacological and electrical approaches generally involved lack the temporal and spatial resolutions needed to selectively modulate neural activity. The somatosensory system intertwines numerous neural populations with distinct functionalities, whose specific neuromodulation would be beneficial for the alleviation of chronic pain and the restoration of locomotion after spinal cord injury. This thesis aims to develop a new generation of electrical and optical neural interfaces to selectively parse the somatosensory system.

At the peripheral nerve level, we proposed an optical cuff and a wireless optoelectronic system to deliver epineural optogenetic stimulations in freely-behaving mice. The former consists of a soft elastomeric cuff wrapped around the sciatic nerve and integrated into a thin optic fiber. We demonstrated consistent orderly recruitment of motor units with optical stimulations in *Thy1::ChR2* mice. This optocuff represents a simple, yet efficient, solution to probe the peripheral nervous system using optogenetics. However, untethered experimentation offers more versatility for fine neuromodulation applications. Within this framework, we developed a system comprising an ultra-miniaturized wireless stimulator and a soft circumneural μ -LED array to deliver optogenetic stimulations to the sciatic nerve. This optoelectronic implant conformed to the nerve's morphology and complied with its dynamic motion. We demonstrated the system's efficacy via optogenetic activation of nociceptors in *TRPV1::ChR2* mice. Both the optocuff and the wireless optoelectronic system exhibited seamless bio-integration after chronic implantation, thus highlighting the benefits of soft neurotechnologies for interfacing with peripheral nerves.

At the spinal level, we introduced a transversal electrode array for multipolar epidural stimulation of the spinal cord. The silicone materials used for its fabrication conferred this implant with mechanical properties matching the dura mater, allowing for remarkable biocompatibility following long-term implantation. Based on the spinal cord anatomy, this implant displayed a wide distribution of neural electrodes at a single spinal level, which enabled selective stimulation of posterior spinal roots. This novel paradigm was implemented to a spatio-temporal stimulation protocol and demonstrated potential in restoring locomotion after spinal cord injury. Finally, we reported a soft μ -LED array to deliver optogenetic stimulations in deep spinal structures. Insertion of this thin ($< 100 \mu\text{m}$) optoelectronic implant in the mouse epidu-

Acknowledgements

ral space did not provoke tissue damages while maintaining its functionality with normal dynamic motion. As a proof-of-principle, we showed concomitant electromyographic activity with epidural optical stimulations in *Thy1::ChR2* mice. This premise offers a large range of opportunities to probe the spinal circuits involved in sensory processing and locomotion.

In conclusion, these selective neural interfaces are proposed as innovative tools to unravel peripheral and spinal neural circuits. This venue will support the development of relevant clinical treatments for tackling dysfunctional neural systems. Eventually, these implant concepts pave the way for the translation of fine neuromodulation therapies in humans.

Keywords: neural interfaces, optoelectronics, soft electronics, flexible electronics, optogenetics, somatosensory system, micro-cracked gold, bio-integration, chronic pain, spinal cord injury

Résumé

Les pathologies affectant le système nerveux peuvent avoir un impact dramatique sur la qualité de vie. De multiples efforts ont été entrepris pour traiter des systèmes nerveux dysfonctionnels. Les approches pharmacologiques et électriques généralement utilisées n'ont pas les résolutions temporelle et spatiale nécessaires pour moduler l'activité neuronale de manière sélective. De nombreuses populations neuronales aux fonctionnalités distinctes sont enchevêtrées à travers le système somatosensoriel. Une modulation spécifique de l'activité de certains de ces groupes neuronaux pourrait permettre le soulagement de douleurs chroniques et le rétablissement de la locomotion après lésion de la moelle épinière. Cette thèse a pour but le développement d'une nouvelle génération d'interfaces neuronales offrant des capacités de modulation électriques et optiques pour analyser précisément le système somatosensoriel.

Au niveau des nerfs périphériques, nous proposons une ceinture optique (ou cuff) ainsi qu'un système opto-électronique sans-fil pour délivrer des stimulations optogénétiques épineurales chez la souris. Ce premier consiste en une membrane souple élastomérique s'enroulant autour du nerf sciatique et intégrant une fine fibre optique. Nous démontrons le recrutement cohérent d'unités motrices avec des stimulations optiques dans des souris *Thy1 : ChR2*. Cette ceinture optique représente une solution simple mais efficace de sonder le système nerveux périphérique par optogénétique. Cependant, une expérimentation sans-fil offre davantage de versatilité pour des applications nécessitant des neuromodulations plus subtiles. Nous avons donc développé un système comprenant un stimulateur sans fil ultra-miniaturisé et un champs souple de μ -LEDs se plaçant autour du nerf pour permettre des stimulations de type optogénétiques. Cet implant opto-électronique se conforme à la morphologie et aux mouvements répétés du nerf. Nous démontrons l'efficacité de ce système via l'activation optogénétique de nocicepteurs dans des souris *TRPV1 : ChR2*. Le cuff optique et le système opto-électronique présentent tous les deux une intégration biologique transparente, soulignant les avantages d'une neurotechnologie souple pour se connecter aux nerfs périphériques.

Au niveau spinal, nous présentons un champ d'électrodes transversal à la moelle épinière et permettant sa stimulation de manière multipolaire. Les élastomères utilisés dans sa fabrication confèrent à cet implant des propriétés mécaniques proches de la dure-mère, favorisant ainsi une biocompatibilité remarquable pour des implantations de longue durée. La répartition d'électrodes sur un axe médio-latéral est inspirée de l'anatomie de la moelle épinière, et permet de recruter sélectivement les racines nerveuses postérieures. Ce nouveau paradigme

Acknowledgements

est implémenté dans un protocole de stimulation spatio-temporelle et démontre un potentiel pour le rétablissement de la locomotion après lésion de la moelle épinière. Pour terminer, nous présentons un champ souple de μ -LEDs pour la stimulation optogénétique de structures profondes dans la moelle épinière. L'introduction de cet implant fin ($< 100 \mu\text{m}$) dans l'espace épidural de la souris ne provoque pas de dégât sur la moelle alors que l'implant maintient sa fonctionnalité avec les comportements dynamiques imposés. Nous démontrons la faisabilité de délivrer des stimulations optogénétiques épidurales par l'activité électromyographique concomitante à ces stimulations. Ces résultats préliminaires offrent de nombreuses opportunités pour sonder les circuits impliqués dans le traitement d'informations sensorielles et dans la locomotion.

En conclusion, nous proposons ces interfaces neuronales sélectives comme des outils innovants permettant de dénouer le fonctionnement des circuits neuronaux périphériques et spinaux. Ces dispositifs expérimentaux aideront au développement de traitements cliniques plus adaptés aux systèmes nerveux dysfonctionnels. Finalement, ces concepts d'interfaces neuronales constituent un premier pas vers des thérapies de modulation plus sélectives appliquées à l'homme.

Mots-clés : interface neuronale, opto-électronique, électronique souple, électronique flexible, optogénétique, système somatosensoriel, or micro-fissuré, intégration biologique, douleur chronique, lésion de la moelle épinière

Contents

Acknowledgements	v
Abstract (English/Français)	vii
List of figures	xiv
List of tables	xvi
1 Introduction	1
1.1 The somatosensory system	2
1.1.1 Anatomy and sensory processing	3
1.1.2 Heterogeneity of the primary sensory neurons	3
1.2 Clinical relevance for neuromodulation therapies	5
1.2.1 The chronic pain burden	5
1.2.2 Spinal cord injuries	7
1.3 Modalities for neural activity modulation	7
1.3.1 Electrical stimulation	8
1.3.2 Optical stimulation	9
1.4 Interfacing soft neural tissues	11
1.5 Outline of the thesis	13
2 Optical cuff for optogenetics in the peripheral nervous system	15
2.1 Background and state of the art	16
2.1.1 Light delivery strategies for optogenetics in the PNS	16
2.1.2 Optical stimulation using optic fibers	18
2.1.3 Mechanical and optical nerve properties	19
2.2 The optocuff, an optical interface with the PNS	21
2.2.1 Optocuff fabrication	21
2.2.2 Optocuff bio-integration	22
2.3 Epineural optogenetic stimulation	23
2.3.1 ChR2 expression in Thy1 ⁺ neurons	23
2.3.2 Orderly recruitment of motor units	23
2.3.3 Optocuff stimulation in awake, freely-behaving mice	24
2.4 Discussion	26
	xi

2.5	Conclusion	28
2.6	Contribution	28
3	A wireless optoelectronic system for optogenetic control of the peripheral nervous system	29
3.1	Optoelectronic wireless systems in optogenetics	30
3.1.1	μ -LED: an implantable light source	30
3.1.2	Wireless system technologies	32
3.1.3	An ultra-miniaturized wireless head-stage	33
3.2	A soft μ -LED-based peripheral interface	35
3.2.1	μ -LED array microfabrication	35
3.2.2	Integration of μ -LEDs on a flexible substrate	36
3.2.3	Characterisation of the μ -LED array	37
3.2.4	μ -LED array bio-integration	42
3.3	Remote optogenetic stimulation of peripheral pain pathways	44
3.3.1	Targeted expression of ChR2 in TRPV1 ⁺ neurons	45
3.3.2	Single-pulse optogenetic activation of nociceptors	46
3.3.3	Conditioned place aversion	47
3.3.4	Study of the neuroimmune interaction	49
3.4	Discussion	51
3.5	Conclusion	52
3.6	Contribution	53
4	A transversal spinal electrode array for rehabilitation of locomotion after spinal cord injury	55
4.1	Epidural electrical stimulations to restore locomotion after SCI	56
4.1.1	Specific recruitment of sensory proprioceptive neurons	56
4.1.2	Spinal implant neurotechnologies	57
4.2	A soft transversal epidural spinal implant, the belt array	58
4.2.1	Micro-cracked gold film topography	59
4.2.2	Soft neurotechnology for transversal spinal array	62
4.2.3	Belt array functionality	64
4.2.4	Belt array biocompatibility	67
4.3	Selective, multipolar stimulation of the spinal cord	68
4.3.1	Spatially-selective electrode distribution	68
4.3.2	Acute multipolar stimulation of the spinal cord	69
4.3.3	Multipolar stimulation combined with spatiotemporal neuromodulation	71
4.4	Discussion	73
4.5	Conclusion	75
4.6	Contribution	76

5	A soft optoelectronic implant for optogenetics in deep spinal structures	77
5.1	Background and state of the art	78
5.1.1	Fiber-based interfaces with the spinal cord	78
5.1.2	Optoelectronics interfacing with the spinal cord	79
5.2	A soft spinal optoelectronic implant	80
5.2.1	Spinal μ -LED array microfabrication	80
5.2.2	Spinal μ -LED array functionality	82
5.2.3	Optical and thermal modelling	85
5.2.4	Bio-integration of the spinal μ -LED array	87
5.3	Epidural optogenetic stimulation in the spinal cord	90
5.4	Discussion	94
5.5	Conclusion	95
5.6	Contribution	96
6	Discussion and perspectives	97
6.1	Selective neuromodulation	97
6.2	Towards softer and more robust neurotechnologies	98
6.3	The advent of optogenetics and novel modalities for parsing the nervous system	100
6.4	Translation to the clinic	101
A	Appendix	103
A.1	Optical cuff for optogenetics in the peripheral nervous system	103
A.1.1	Optocuff implantation	103
A.1.2	Thy1::ChR2 mouse breeding	104
A.1.3	Mechanical sensitivity assessment	104
A.1.4	Thermal sensitivity assessment	104
A.1.5	Dynamic weight bearing	104
A.1.6	Motor sciatic nerve assessment	104
A.1.7	DRG neuron culture and electrophysiology	105
A.1.8	Histology and immunohistochemistry	105
A.1.9	EMG electrode implantation and data acquisition	106
A.1.10	Optogenetic control <i>in vivo</i> and high-speed behavioural imaging	106
A.1.11	Stretchable optic fiber fabrication	106
A.2	A wireless optoelectronic system for optogenetic control of the peripheral nervous system	108
A.2.1	Meander-track geometry	108
A.2.2	μ -LED implant surgery	108
A.2.3	Histology and immunochemistry	109
A.2.4	Behavioural experiments	110
A.2.5	ChR2 expression in TRPV1 ⁺ neurons	111
A.2.6	Single pulse optogenetic stimulation <i>in vivo</i>	111
A.2.7	Conditioned place aversion	111
A.2.8	Flow cytometry	112

Contents

A.3	A transversal spinal electrode array	113
A.3.1	Dorsal root trajectories	113
A.3.2	Scanning electron microscopy and micro-cracked gold morphology . . .	113
A.3.3	Surface topography measurement and analysis	114
A.3.4	Electrochemical characterization of belt electrodes under elongation . .	115
A.3.5	Surgical procedures	115
A.3.6	Microcomputed tomography	116
A.3.7	Histology of the spinal cord	116
A.3.8	Acute EES of the spinal cord	117
A.3.9	Spinal cord injury model	117
A.3.10	Rehabilitation after spinal cord injury	118
A.3.11	Belt array substrate and superstrate material properties	120
A.4	A soft optoelectronic implant for optogenetics in deep spinal structures	121
A.4.1	Comparison between the peripheral and spinal optoelectronic implants	121
A.4.2	Model of the light propagation in the spinal cord	121
A.4.3	Thermal model	122
A.4.4	Spinal μ -LED array implantation	122
A.4.5	Microcomputed tomography	123
A.4.6	Histology and immunochemistry	123
A.4.7	EMG electrode implantation and data acquisition	123
	Bibliography	148
	Glossary	149
	Curriculum Vitae	151

List of Figures

1.1	Organisation of the somatosensory system	2
1.2	Classification of the primary sensory neurons	4
1.3	Implantable medical devices for the treatment of neuropathic pain	6
1.4	Optogenetics concept in neuroscience	9
1.5	Mechanical mismatch between biological tissues and implantable electronics .	11
2.1	Light delivery strategies to the PNS	17
2.2	Optic fiber working principle and its application in optogenetics	18
2.3	Mouse sciatic nerve mechanical and optical properties	19
2.4	Optical coupling to the mouse PNS with the optocuff	21
2.5	Histology and behavioural experiments following optocuff implantation	22
2.6	Expression of ChR2 in the PNS of <i>Thy1::ChR2</i> mice	24
2.7	Optical stimulation of the sciatic nerve in anaesthetized <i>Thy1::ChR2</i> mice . . .	25
2.8	Optogenetic control of peripheral neurons in awake behaving mice	26
2.9	Stretchable optic fibers	27
3.1	Wireless optoelectronic systems in neuroscience	31
3.2	A miniaturized wireless optogenetics stimulation head-stage	34
3.3	Optoelectronic system for wireless optogenetic modulation in the mouse PNS .	35
3.4	Peripheral μ -LED implant microfabrication	36
3.5	μ -LED integration on a flexible substrate	37
3.6	μ -LED array for epineural optogenetic stimulation in the PNS	38
3.7	A stretchable μ -LED array for the mouse PNS	39
3.8	μ -LED encapsulation enables long-term, safe experimentation	40
3.9	Phosphor-based light conversion enables broad optogenetic experiments . . .	42
3.10	Histology following μ -LED array implantation	43
3.11	Mouse behaviour following the μ -LED array implantation	44
3.12	Expression of ChR2 in <i>TRPV1::ChR2</i> mice	45
3.13	Channelrhodopsin-specific μ -LED implant	46
3.14	Remote, single-pulse, epineural activation of TRPV1 ⁺ neurons results in fast protective behaviour	47
3.15	Place aversion following remote, optogenetic stimulation of peripheral TRPV1 ⁺ neurons	48

List of Figures

3.16 Recruitment of activated immune cells driven by nociceptor activity	50
4.1 Neurotechnologies for electrical stimulation of the spinal cord in animal models	57
4.2 A transversal spinal electrode array	59
4.3 Intrinsically stretchable micro-cracked gold thin film	59
4.4 Atomic force microscopy of the micro-cracked gold film	60
4.5 Analysis of the micro-cracked gold film topography under uni-axial strain . . .	61
4.6 Transversal spinal electrode array microfabrication	63
4.7 Platinum-PDMS mesocomposite for electrode coating	64
4.8 Electrode properties <i>in vitro</i> and under tensile strain	65
4.9 Insertion of the spinal transversal array	66
4.10 Histology of the spinal cord following long-term belt implantation	67
4.11 Transversal, monopolar stimulation of the spinal cord	68
4.12 Monopolar versus multipolar stimulation of the spinal cord	70
4.13 Multipolar neuromodulation for locomotion rehabilitation after spinal cord injury	72
4.14 Softer neurotechnology for future spinal implants	74
5.1 Neural interfaces for optogenetics in the spinal cord	79
5.2 Spinal μ -LED array microfabrication	81
5.3 μ -LED array for epidural optogenetic modulation in the spinal cord	83
5.4 Phosphor-based light conversion in the spinal μ -LED array	84
5.5 Light propagation in spinal tissues	86
5.6 Heat generation with μ -LED activation	87
5.7 Implantation of the spinal μ -LED array in the mouse epidural space	88
5.8 Histology of the spinal cord following long-term belt implantation	89
5.9 Behaviour analyses following implantation of the spinal μ -LED array and hindlimb EMG electrodes	90
5.10 Expression of ChR2 in the spinal cord of <i>Thy1::ChR2</i> mice	91
5.11 Orderly recruitment of motor units with epidural optical stimulations in <i>Thy1::ChR2</i> mice	92
5.12 Wavelength and modality specific recruitment of motor units	93
A.1 Stretchable interconnects using a serpentine design	108
A.2 μ -LED array implantation procedure on the mouse sciatic nerve	109
A.3 Rat spinal cord anatomy	113
A.4 Morphology of the micro-cracked gold thin film	113
A.5 Topography of PDMS	114
A.6 Spinal cord injury model	117
A.7 Real-time control platform	119

List of Tables

3.1	Emission spectra of the peripheral μ -LED array	41
A.1	Mechanical properties of the belt silicone elastomers	120
A.2	Optoelectronic implant dimensions	121
A.3	Absorption and scattering coefficients depending on the light wavelength . . .	122
A.4	Parameters of the heat transfer equation	122

1 Introduction

Abstract Diseases or injuries affecting the nervous system can lead to highly debilitating cognitive and sensorimotor deficits. For example, lesions to the somatosensory system can trigger severe neuropathic pain, and damages to the spinal cord can provoke complete paralysis. These neural disorders affect millions of people worldwide and have major health, social and economic consequences. Despite global efforts towards improving requisite medical treatments, a question still remains: Why are we not more capable of tackling dysfunctional nervous systems? To answer partially, the nervous system is a complex dynamical network composed of billions of neurons with myriad functionalities that we lack the capability to probe accurately. Within this context, implantable neuroprostheses are engineered systems designed to study or repair the injured nervous system. Neuroprosthetics is interfacing with the nervous system with man-made devices to restore lost functions. Cochlear implants and deep-brain stimulation systems are examples of neuroprosthetic applications to alleviate symptoms of hearing loss and Parkinson's disease. Neuroprosthetics relies essentially on the interface selectivity to write precisely into the nervous system. However, the physics underlying the commonly-used electrical modality limits selectivity. The advent of optogenetics, a cell-type specific neuromodulation strategy using light, offers an alternative approach to parse the nervous system with unmatched selectivity. Although optogenetic translation to humans has not yet been demonstrated, future therapeutical treatments will benefit from the outcomes of its application in experimental animal models. In this chapter, I first introduce the high heterogeneity of the somatosensory system and the clinical relevance for delivering neuromodulation therapies within this system. Next, I describe the electrical and optical neuromodulation modalities proposed to unravel the somatosensory system. Finally, I review the challenges for interfacing soft neural tissues with implantable electronics.

1.1 The somatosensory system

The ability to sense internal and external stimuli dwells in the somatosensory system. Its basic components are receptors localized in the peripheral organs (e.g. skin, smooth and striated muscles) and their associated primary afferent neurons that convey the somatosensory information to the central nervous system (CNS). Interoception (i.e. the sense of the body internal state) relies on sensory informations arising from afferents in the autonomic nervous system and proprioceptive fibers innervating the musculoskeletal system (Figure 1.1.a). Exteroception (i.e. the sense of the surrounding environment) arises from cutaneous afferents in the epidermis (Figure 1.1.b). Furthermore, detection of innocuous (i.e. non-harmful) and noxious (i.e. harmful) stimuli engaged distinct, specialized afferent pathways [1]. Nociception is the process of sensing intense stimuli and is essential for survival. In this section, I review the anatomy and the general mechanisms for sensory processing in the peripheral nervous system (PNS) and the spinal cord. Then, I emphasize the diversity of the neurons involved in somatosensory processing.

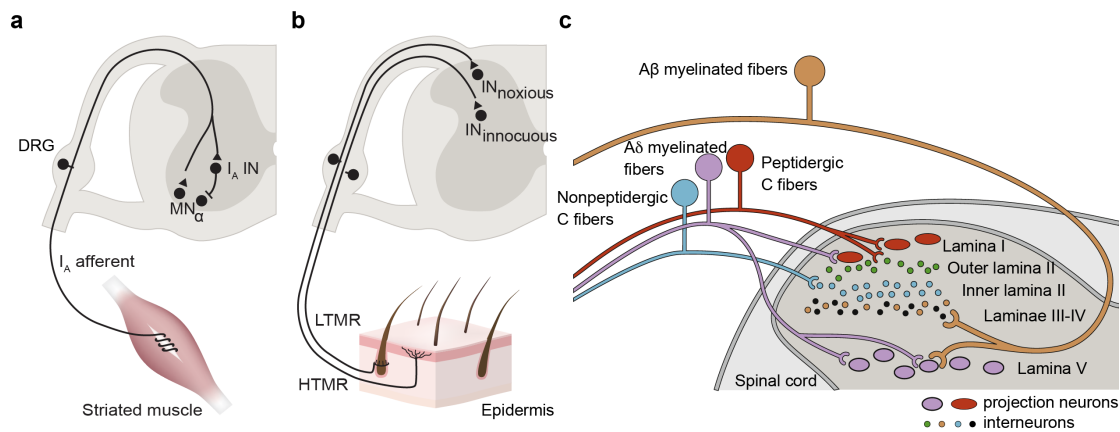


Figure 1.1 – Organisation of the somatosensory system

a, Proprioception relies on primary afferents sensing elongation within striated muscle. In the case of muscle stretching, a type I_A afferent monitors at the muscle spindle rapid changes in muscle length and conveys this information in the ventral horn of the spinal cord to activate an agonist alpha motoneuron (MN_α). In parallel, inhibitory interneurons (INs) suppress activity of antagonist MN_α s. **b**, Exteroception arises from primary afferents innervating the hairy and glabrous skin within the epidermis. These sensory neurons are activated by external stimuli (e.g. mechanical, thermal, chemical) and transmit these informations to the dorsal horn of the spinal cord. Depending on the intensity of a mechanical stimulus, a low-threshold mechanoreceptor (LTMR) or a high-threshold mechanoreceptor (HTMR) activate distinct INs in the spinal cord. Illustrations adapted from [2]. **c**, Primary afferent fibers project to different layers in the dorsal horn of the spinal cord. Tactile and proprioceptive information is carried in large, myelinated sensory $A\beta$ fibers that target interneurons in lamina II and projection neurons in lamina V. Inputs from thin, unmyelinated C fibers (nociception) are concentrated in laminae I and II. Its peptidergic subset projects in laminae I and outer II, whereas non-peptidergic fibers target interneurons in the inner part of lamina II. Thinly-myelinated $A\delta$ fibers synapse with projections neurons both in laminae I and V. Adapted from [3].

1.1.1 Anatomy and sensory processing

The first critical step for sensory processing is the conversion from a stimulus into an electrical signal in the primary sensory neurons, a process called sensory transduction [4]. This transduction arises from changes in cell membrane ionic permeability of receptors in response to a stimulus, generating a depolarizing current to trigger an action potential. Peripheral receptors are diverse and generally stimulus-specific. In the case of proprioception (i.e. information on the body position), muscle spindles in the striated muscles detect dynamic and static changes in muscle length (Figure 1.1.a), and trigger action potentials in the I_A afferents according to the muscle elongation. The proprioceptive information is transmitted to spinal circuits and modulate the activity in the agonist and antagonist alpha motoneurons via intermediate inhibitory interneurons. The process of proprioception is essential for proper phasing of movements during locomotion [5] and requires afferents with high conduction velocity.

Similarly, cutaneous afferents have specialized receptors located in the epidermis to sense multimodal variations in the external environment (Figure 1.1.b). For example, Merkel's discs and Meissner's corpuscles are mechanoreceptors sensing light touch applied to the skin. Innocuous stimuli are transmitted by low-threshold mechanoreceptor (LTMR) afferents. These afferents are regrouped in a subset of large, thickly-myelinated (i.e. fast-conducting) $A\beta$ fibers. Conversely, noxious stimuli are detected by the free nerve endings of specialized, high-threshold afferents, called nociceptors. These afferents are generally polymodal as they include neurons with both mechanical and thermal sensitivities [6]. Furthermore, these afferents are commonly categorized depending on their conduction velocity. $A\delta$ fibers are thinly-myelinated afferents and C fibers are unmyelinated (i.e. slow conducting) afferents. Peptidergic C fibers contain nociceptors that release peptides, including substance P and calcitonin-gene related peptide (CGRP). Primary afferents project to specific laminae in the dorsal horn of the spinal cord (Figure 1.1.c), highlighting a complex degree of anatomical and functional segregation [2]. Finally, subsequent neural activity in the spinal cord is transmitted to several regions in the brain (mostly the thalamus and the brainstem), where tactile sensation and pain are perceived.

1.1.2 Heterogeneity of the primary sensory neurons

The somatosensory system contains a variety of fibers that transmit proprioceptive, tactile and nociceptive informations arising from the periphery to the CNS. The primary sensory neurons are highly specialized in order to detect a range of internal and external modalities (e.g. mechanical, thermal, chemical). Yet, primary sensory neurons have a similar structure. Their cell bodies are located in the dorsal root ganglia (DRG) or in the trigeminal ganglia (for facial innervation) and their axons divide into a peripheral branch innervating the target tissue and a central branch that synapse with second-order neurons in the spinal cord or in the brainstem. These are also essentially excitatory neurons that use glutamate as a primary neurotransmitter. Although primary sensory neurons share some similitude, functional specialization and

Chapter 1. Introduction

somatosensory information coding require a diversity of neurons. Extensive efforts towards the classification of these neurons using molecular-based strategy [7] and, more recently with single-cell RNA transcriptome analyses [8, 9], have emphasized a high heterogeneity across primary sensory neurons (Figure 1.2).

Nociception is initiated by the activation of dedicated primary sensory neurons in response to noxious stimuli. Nociceptors have distinct peripheral targets, ion channels and receptor repertoires [11]. For example, nociceptors expressing the tachykinin precursor 1 (TAC1) gene release substance P and are therefore peptidergic. Conversely, nociceptors that bind isolectin B4 (IB4) are generally nonpeptidergic. The differential expression of ion channels confer nociceptors with sensitivity to heat, cold and chemical irritants [12]. For instance, the transient receptor vanilloid type 1 (TRPV1) is a ligand-gated ion channel activated by painful heat ($> 42^{\circ}\text{C}$) or by capsaicin (the pungent ingredient in chili pepper) and is mainly expressed in peptidergic C fibers [13]. Selective ablation of peptidergic (e.g. TRPV1-expressing) or nonpeptidergic (e.g. Mas-related G protein-coupled receptor subtype D-expressing; MrgprD) nociceptors produce distinct changes in heat and mechanical nociception respectively [3]. Genetic manipulations, including selective marking and ablation, constitute an intense field of research to tease out the precise functionality of nociceptor subsets [14, 15].

In addition to the primary neurons, spinal interneurons involved in somatosensory processing display an important structural organisation and anatomical/functional heterogeneity [2, 10]. Briefly, these interneurons can be excitatory, which generally express vesicular glutamate transporter 2 (vGluT2) and use glutamate as a primary neurotransmitter hereof. They can also be inhibitory and use GABA for neurotransmitter, while some of them coexpress glycine [3].

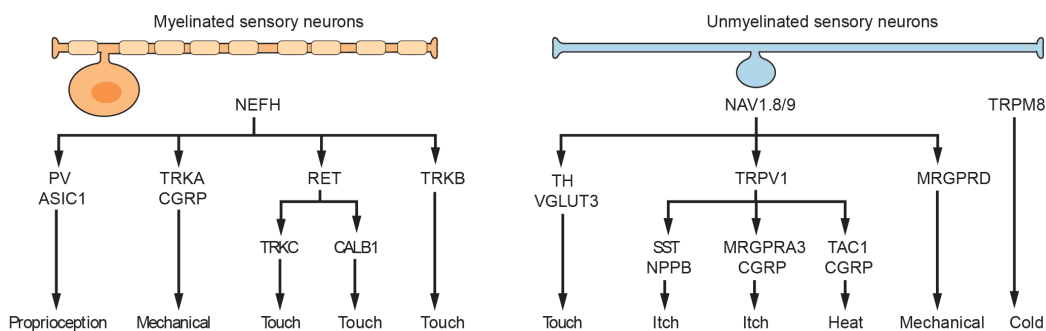


Figure 1.2 – Classification of the primary sensory neurons

The primary sensory neuron structure includes a peripheral terminal to transduce stimuli in action potentials that are conveyed in the axon to the neuron central terminal in the spinal cord. The diversity of primary sensory neurons is presented here. The tree representations display the different categories of myelinated and unmyelinated neurons and their respective functional roles. These hierarchies were extracted from transcriptional, immunohistological and behavioural analyses. Myelinated sensory neurons express neurofilament heavy chain (NEFH) whereas unmyelinated neurons predominantly express the sodium channels Nav1.8 and Nav1.9. Adapted from [10].

1.2 Clinical relevance for neuromodulation therapies

Detection of internal and external events by the somatosensory system plays an essential role in tactile sensation, nociception, and to a lesser extent, in locomotion. Therefore, injuries, diseases, genetic mutations or ageing affecting the somatosensory system can severely impede the quality of life. For instance, ongoing pain is commonly a protective mechanism facilitating healing processes, resulting in hypersensitivity to innocuous stimuli (i.e. allodynia) and in heightened experience of pain with noxious stimuli (i.e. hyperalgesia). However, pain can become maladaptive with the dysfunction of the somatosensory system, caused by damages to the nervous system (i.e. neuropathic pain) for example. In this case, severe pain is spontaneously experienced and responses to stimuli are pathologically amplified [16]. Medical conditions requiring activity modulation therapy in the somatosensory system are numerous. These treatments can target the somatosensory components to alleviate symptoms, such as chronic pain (i.e. pain experienced for > 6 months). Other neuromodulation therapies take advantage of the functional organisation of the somatosensory system to restore lost functions, such as epidural electrical stimulation following spinal cord injury (SCI).

1.2.1 The chronic pain burden

Pain is the most common reason for seeking medical attention [17]. Chronic pain affects deeply the life of the persons experiencing it, having consequences on health (e.g. depression), social life and economy. The prevalence of chronic pain is staggering. In the US, more than 30% of the population is experiencing chronic pain [18]. In Europe, the prevalence differs from one country to the other and is in average 20% [19]. Chronic pain is more frequent among older adults and women. Furthermore, chronic neuropathic pain prevalence is estimated between 6.9 and 10% [20]. The direct (i.e. healthcare) and indirect (i.e. work productivity) costs associated with persistent pain ranges from \$560 to \$635 billion per year in the US [21]. Chronic pain is symptomatic of a variety of diseases and injuries. A non-exhaustive list includes arthritis, cancer, migraine, low back pain, neck pain, post-surgery complications and heart diseases. Pharmacological treatments are generally inadequate to relieve chronic pain. The use of opioid analgesics is associated with the worst drug crisis in the US history [22]. Although these drugs can provoke adverse side-effects and dependence, they became the most commonly prescribed class of medications in the country [23]. It has been estimated that legal and illegal (e.g. heroin, fentanyl) opioids caused more than 350'000 deaths by overdose between 1999 and 2016 [24]. Over this period, the number of deaths attributable to opioids increased by nearly 300% [25].

The prevalence and the debilitating effects of chronic pain steered the development of alternative treatment strategies. In the case of severe neuropathic pain, these treatments include the implantation of invasive medical devices that deliver neuromodulation therapies in the somatosensory system (Figure 1.3).

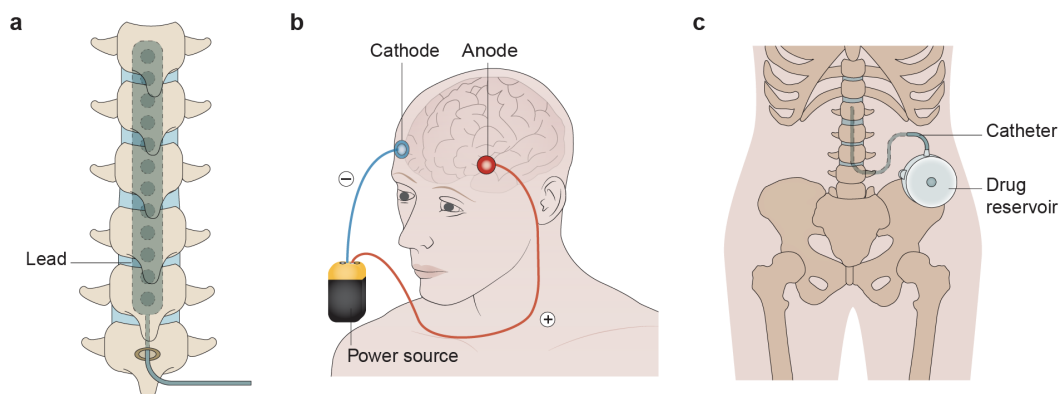


Figure 1.3 – Implantable medical devices for the treatment of neuropathic pain

a, Electrical stimulations are carried with a lead inserted in the epidural space of the spinal cord. This neuromodulation therapy induces paraesthesia in the painful region. **b**, Deep-brain electrode arrays are implanted in various brain regions involved in pain processing (e.g. thalamus, hypothalamus, nucleus accumbens) to deliver high frequency stimulations. **c**, Intrathecal drug delivery systems comprise a drug reservoir, a pump and a catheter, to provide analgesia in patients suffering from severe chronic pain. Adapted from [32].

Epidural electrical stimulation (EES) of the spinal cord for pain alleviation has been introduced based on the gate control theory (GCT) proposed by Melzack and Wall in 1965 [26]. Briefly, this theory suggests that the perception of pain involves a gated mechanism in the spinal cord, receiving concomitant inputs from small nerve fibers (i.e. pain-associated) and large myelinated fibers (i.e. sensory-associated). Activation in the large sensory fibers (i.e. $A\beta$ fibers) drives activation in an inhibitory interneuron, that in turn inhibits a pain-associated projection neuron. In this configuration, the gate, symbolized by the interneuron activity, is closed and pain is consequently silenced. Application of the GCT involves the implantation of a spinal cord stimulation system (Figure 1.3.a). Due to the low chronaxy of large myelinated fibers, EES specifically targets activation in the $A\beta$ fibers, resulting generally in paraesthesia in the painful area. Electrical stimulation may also be carried in the DRG to alleviate chronic pain in very localized areas [27]. The number of spinal cord stimulation systems implanted annually worldwide has been estimated to 14'000 [28]. Despite its clinical application, the spinal circuitry underlying the GCT remains an active field of research [29]. Neuromodulation therapies may also target deep brain structures (Figure 1.3.b). High-frequency stimulations are delivered in areas involved with the processing of pain, such as the sensory thalamus, the nucleus accumbens or the anterior cingulate cortex [30]. However, the use of deep brain stimulation (DBS) to treat chronic pain remains controversial and is not approved by the American Food and Drug Administration (FDA). Eventually, severe chronic pain can be treated with intrathecal drug delivery (Figure 1.3.c). This pharmacological neuromodulation therapy involves the implantation of a refillable drug reservoir and a catheter to infuse drugs (e.g. morphine) locally in the spinal cord [31]. Compared with a systemic delivery, the intrathecal approach can reduce the drug dosage and the side-effects associated with it.

1.2.2 Spinal cord injuries

Damages to the spinal cord lead to devastating medical conditions, including complete paralysis. Spinal cord injuries occur with an estimated incidence of 250'000 to 500'000 cases every year, worldwide [33]. The prevalence for traumatic SCI in the US is 906 per million and its etiology includes mostly car accidents, falls and forms of violence [34]. Due to the disruption of the ascending and descending spinal tracts, approximately 50% of SCI victims present complete sensorimotor impairments below the level of injury, and only 5% of them regain the ability to walk. In addition, nearly 40% of SCI result in severe neuropathic pain [35]. Moreover, a range of disabilities, including respiratory complications, bladder dysfunction and depression may arise following SCI. The medical care complexity and the debilitating effects associated with SCI generate a total cost of \$9.7 billion annually in the US [36]. Although recent improvements in the healthcare have greatly reduced the mortality in SCI patients [37], the restoration of sensorimotor functions remains an intense field of research.

Current rehabilitation strategies mainly focus on compensating the functional disabilities in order to restore some degrees of freedom in the SCI patients [38]. These therapies may also prevent the progression of the weakening state, including muscle atrophy and bone degradation, by the means of intensive trainings and functional electrical stimulations [39]. Alternatively, neuromodulation applied to the "dormant" spinal circuits located below the injury is emerging as an approach for the restoration of motor functions. EES of the spinal cord after SCI resulted in impressive rehabilitation of voluntary motor functions, both in experimental animal models of SCI [40] and in humans [41, 42]. The effect of EES on motor functions was initially unexpected, as it appeared for the first time during pain alleviation treatments [43]. Computational models have demonstrated that EES of lumbar segments recruits proprioceptive afferents in the $A\beta$ fibers, engaging motor spinal circuits normally involved with locomotion [44, 45]. Optimisation of the EES spatial and temporal components to recruit the somatosensory system more selectively may improve the functional motor outcomes of these neuromodulation therapies. These mechanisms will be described in Chapter 4.

1.3 Modalities for neural activity modulation

The modulation of neural activity, or neuromodulation, is a shared component of neuroscience and therapies targeting dysfunctional nervous systems. Electrical and pharmacological approaches are well-established neuromodulation modalities and are commonly used in the laboratory and the clinic. However, deeper understanding of neural networks and the refinement of neurorehabilitation necessitated the development of additional modalities with finer spatial and temporal resolutions. Over the past 20 years, exciting alternative modalities have emerged, including transmagnetic, optical, thermal and mechanical [46]. Within the scope of my work, I introduce here the mechanisms of electrical and optical stimulations.

1.3.1 Electrical stimulation

The natural activity of neurons is intrinsically electrical, resulting from both passive and active cellular mechanisms. Neuron cell membrane is composed of a lipid bilayer, acting as a capacitor, and transmembrane ion channels, allowing ion flux across its membrane. The difference between the extra- and intracellular potentials, or transmembrane potential, is kept constant (~ -65 mV) in the neuron resting state. If a neuron receives inputs at the synapse, or if the extracellular potential is driven negative, voltage-gated ion channels produce an inward ionic current, depolarizing the neuron membrane. This depolarization induces an action potential, the neuron primary electrical signal, that is transmitted along the axon via the sequential activation of the voltage-gated ion channels (mainly Na^+ and K^+ channels). Biophysics models, notably the Hodgkin-Huxley model, describe the generation and the propagation of action potentials [4].

Neuromodulation by electrical means has been introduced thousands of years ago, through the use of electric rays for headache treatments [47]. Fortunately, this venue has been considerably improved, albeit the mechanisms of electrical stimulation remain the same. Electrical stimulations generate a cathodic electrical field through the injection of charges at the electrode site, changing the extracellular membrane potential (i.e. depolarization region), thus artificially generating action potentials in the neighbouring neurons. Due to the anisotropic nature of the neural tissues (e.g. neuron morphology, orientation, conductance), electrical stimulations create a complex electrical field distribution [48]. Furthermore, neuron excitability is not constant across neuronal populations. For instance, myelinated axons have a lower membrane capacitance and a higher resistance compared to unmyelinated axons. Consequently, the dynamics for electrical recruitment of these neurons is different. The chronaxy (i.e. minimum pulse duration to reach threshold of activation if the stimulation current is twice the rheobase; rheobase is the minimal current at infinite pulse duration to elicit an action potential) of myelinated fibers is lower compared with unmyelinated fibers [49]. This implies that short pulse duration (e.g. $100\text{-}300\ \mu\text{s}$) preferentially elicit activation in myelinated fibers. This phenomenon enables EES of the spinal cord to target myelinated $\text{A}\beta$ fibers.

Finally, the spatial selectivity of electrical stimulation depends on several parameters, such as the distance to the electrode or the electrode geometry [50]. Penetrating probes have smaller electrode areas and reduced distance to the targeted tissue. In this configuration, a lower current is necessary to elicit activation, reducing the current spread and improving the electrical stimulation selectivity. In comparison, surface electrodes display larger electrode areas and a longer distance to the targeted region. This configuration requires higher current thresholds and by default, hinders the electrical stimulation selectivity [51]. However, surface electrodes are less invasive and are arguably prone for longer interfacing with the neural tissues. In addition, the stimulation protocol may also improve the spatial selectivity. Multipolar stimulation, or the addition of an anodic electrical field (i.e. hyperpolarizing region), enables fine tuning of the activation area, promoting higher spatial selectivity. This stimulation strategy has been used in DBS [52] and peripheral nerve experiments [53, 54].

1.3.2 Optical stimulation

Although the previous modality achieves a level of structural and spatial selectivity, electrical stimulation is not a cell-type specific approach and limits thorough parsing of the nervous system. In 1999, Francis Crick stressed the need to control one type of cells in the brain without altering other cell types and proposed light as an ideal signal [55]. This perspective echoed for several years until optogenetics was invented. Optogenetics is the combination of optics and genetics to deliver instructions to specific cells using light [56]. This technology relies on the expression of opsins (i.e. light-sensitive proteins) in genetically-selected neural populations, and the subsequent delivery of light to those tissues. This new paradigm enables both *in vitro* and *in vivo*, cell-type specific, millisecond-scale control of neural activity [57, 58].

The first component of optogenetics is the opsin. These transmembrane light-sensitive proteins are found in microorganisms (e.g. alga) that use electromagnetic radiation (i.e. light) to regulate their homeostasis [60]. Microbial opsins undergo a conformational change in response to light at a specific wavelength. The main types of opsins in optogenetics are

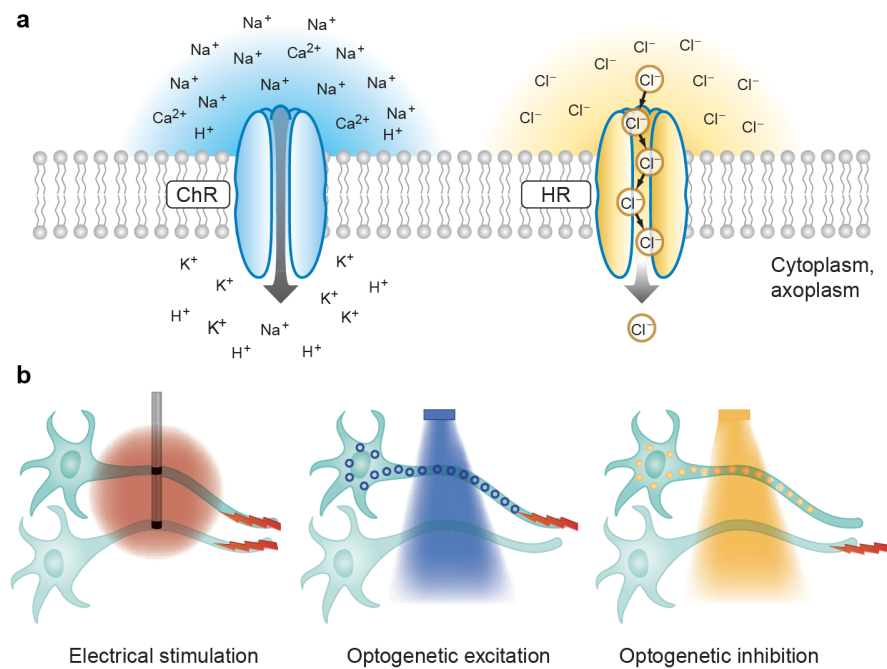


Figure 1.4 – Optogenetics concept in neuroscience

a, Light-sensitive proteins localized in the neuronal membrane modulate neuron's activity in response to light. Channelrhodopsins (ChR) are cation channels that depolarize neurons upon blue illumination. Halorhodopsins (HR) are chloride pumps that hyperpolarize neurons upon yellow light illumination. Adapted from [59]. **b**, Principles of electrical and optogenetic neuromodulations. Electrical stimulation activates neurons within a volume of activation and is therefore not cell-type specific. Targeted optogenetic stimulation and inhibition of neurons expressing blue light-activated ChR and yellow light-activated HR respectively. The optogenetic neuromodulation is cell-type specific. Adapted from [56].

channelrhodopsin (a cation channel), archaerhodopsin (a proton pump) and halorhodopsin (a chloride pump). For instance, channelrhodopsin-2 (ChR2) is a blue-light-activated opsin and a non-specific cation channel commonly used for neural excitation (Figure 1.4.a). Illumination at 470 nm of neurons expressing ChR2 on their membrane induce cation (mostly Na^+ and Ca^{2+}) influx inside the neurons, depolarizing the membrane and consequently generating an action potential. Conversely, neurons expressing halorhodopsins are hyperpolarized upon 590 nm illumination with chloride anions entering the cell, preventing the generation of action potentials. The opsin toolbox in optogenetics has been considerably extended with opsins displaying different light sensitivities (i.e. wavelength, irradiance), conductance and kinetics, facilitating neuromodulation of deeper neural structures [61, 62].

The second component of optogenetics is the specific expression of opsins in genetically-targeted neural populations. Common gene delivery techniques used in neurobiology can achieve this goal [63]. Using a viral vector (e.g. lentivirus, adeno-associated virus (AAV)), the gene coding for the opsin is packaged under a specific promoter in the virus genome. The virus genetic payload is then predominately expressed in neurons displaying this specific promoter, enabling cell-type specific expression of the opsin. Although neurons are transfected locally to the virus injection site, specific viruses (e.g. AAV1, AAV6) enable anterograde or retrograde transport of the opsin gene [64]. This route allows to decouple the site of injection from the area of optical stimulation. Further cell-type specificity can be obtained using a Cre-recombinase technique and a Cre-dependent virus [65]. The virus recombination enables expression of the opsin only in neurons expressing Cre. Finally, the generation of transgenic animals with both the opsin and the Cre transgenes enables cell-type specific expression of the opsin over the whole nervous system.

The third component of optogenetics is the light delivery. To achieve efficient activation, the optical stimulation must be tailored to the absorption spectrum of the opsin. Then, the opsin sensitivity requires stimulation above a threshold of radiant flux (i.e. optical power). Translated to the neuron cell surface, the opsin activation is dependent of the stimulation irradiance (\sim light intensity). For example, ChR2 is activated for an irradiance above 1 mW/mm^2 at 470nm [66]. However, as the absorption and scattering properties of neural tissue attenuate exponentially light propagation, optical stimulations have typically an initial irradiance 100-fold higher than required at the target cell. Furthermore, the light propagation in the tissue is wavelength-specific, longer-wavelength light being less absorbed and scattered, more suitable for neuromodulation in deep tissue volumes hereof [67]. Finally, optogenetics steered the development of an array of optical neural interfaces for *in vivo* neuromodulation [68]. These interfaces consist of implanted thin optic fibers or optoelectronic devices, and will be described in Chapter 2 and Chapter 3. Light delivery in tissues expressing opsins in genetically-selected neural populations grants optogenetics with exquisite temporal and spatial resolutions, enabling meticulous parsing of the nervous system (Figure 1.4.b).

1.4 Interfacing soft neural tissues

A neural interface establishes a communication link, in the form of electrons or photons, between a technical device and the nervous system [69]. When implantable, a neural interface should mimic the morphology and the mechanical properties of the targeted tissue to reduce the foreign body reaction resulting from its insertion [70]. Furthermore, the nervous system is composed of soft tissues, with elastic moduli ranging from 100 Pa to 100 kPa for the brain and the spinal cord [71]. Protective membranes, such as the dura mater for the spinal cord and the epineurium for the peripheral nerves, preserve the integrity of these delicate tissues and accommodate their physiologic motions. Conversely, traditional neurotechnologies employ stiff materials with Young's moduli in the GPa range. These rigid and static implants can limit long-term functional interfacing, as breakdown may occur with the imposed mechanical load or the triggered immune reactions [72]. This mechanical mismatch between neural interfaces and the nervous system is highlighted in Figure 1.5.

From a mechanical point of view, interfacing soft neural tissues raises a handful of challenges. Within the nervous system, tissues are arranged in complex shapes, generally displaying bending radii in the millimeter range. For instance, the spinal cord has a tubular structure with a characteristic bending radius of 10 mm [76]. Development of neural interfaces in rodent animal models has to tackle significantly smaller dimensions. The mouse sciatic nerve exhibits a maximum diameter < 1 mm [77]. For proper interfacing, surface implants need to conform adequately to the morphology of these structures. This compliance can be obtained with

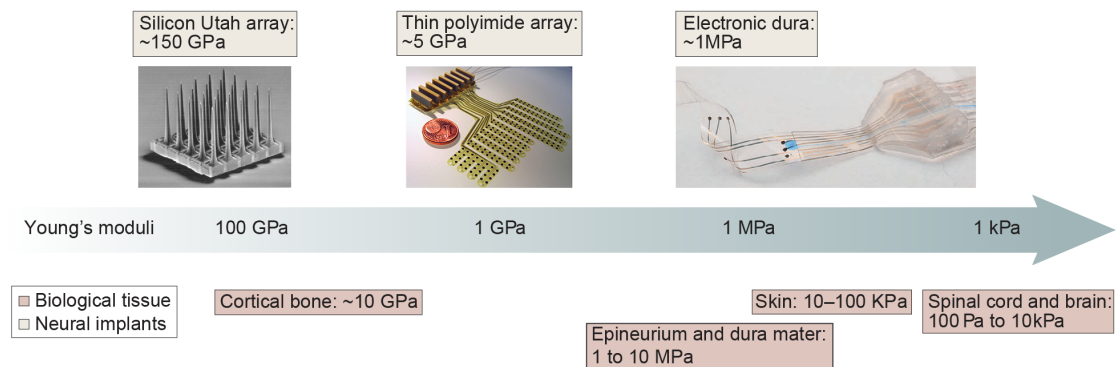


Figure 1.5 – Mechanical mismatch between biological tissues and implantable electronics

Comparison of biological tissues and man-made neural interfaces Young's moduli. Soft neural tissues are wrapped in the epineurium (nerve) or the dura mater (spinal cord, brain). These protective elastic membranes deform to accommodate with the normal physiologic motion of neural tissues. Conversely, neural interfaces are generally made of stiff materials, such as silicon (e.g. Utah array [73]) and plastics (e.g. polyimide ECoG electrode array [74]). Recently developed neural interfaces made of soft silicones (e.g. electronic dura [75]) match the dura mater mechanical characteristics. Adapted from [70].

ultrathin materials, decreasing its flexural stiffness (D), as ruled by the following formula:

$$D = \frac{Eh^3}{12(1 - \nu^2)} \quad (1.1)$$

with E , h , ν the material Young's modulus, thickness and Poisson's ratio respectively. Micrometer-thick flexible polymers such as polyimide (PI) or parylene ($E = 3\text{-}5$ GPa) can bend to the desired extent. However, the complex morphology of neural structures displays *de facto* a non-zero gaussian curvature and cannot be perfectly matched with a plain layer of PI. Patterning of the PI through standard microengineering processes into an intricate mesh structure can improve conformability [78]. The use of soft and stretchable elastomeric substrates, like polydimethylsiloxane (PDMS; $E \sim 1$ MPa), provides an alternative approach for surface implants to accommodate the shape of neural structures.

Furthermore, the dynamic nature of the neural tissues hinders interfacing with stiff and static implants. Normal postural movements can induce strains larger than 15% in the spinal cord [79] and 11% in the peripheral nerves [80]. To allow similar ranges of deformation, stretchability must be engineered into the neural interfaces. Patterning of the implant interconnects to a meander geometry enables elongation by out-of-plane deflection of the track structure [81]. Although this approach can accommodate large uniaxial strains, complex elongations require more fastidious patterning (e.g. horse-shoe design) [82]. Another approach consists in the deposition of metal thin films onto a pre-stretched elastomeric substrate [72]. Due to the buckling of the film at 0 strain, the structure can elongate to predefined directions. Finally, thin metal films displaying a micro-cracked morphology on an elastomeric substrate enables multi-axial strains to tens of percent [83, 84]. These intrinsically stretchable films demonstrate their *in vivo* application by interfacing with highly-dynamic spinal tissues [75].

Finally, the technological routes utilized for interfacing with soft neural tissues are not depending only on these aforementioned mechanical aspects. Increasing the density of tracks allows higher resolution interfacing, but logically reduces the track dimensions. Soft lithography processes tend to be more manual compared with photolithography. Stencil masks used in soft lithography are generally not suitable for small ($< 100 \mu\text{m}$) feature sizes. In addition, stretchable metallization techniques can display size-dependent rupture strains. For instance, reducing the width of micro-cracked gold films below $50 \mu\text{m}$ hampers significantly their potential of elongation [85]. Conversely, photolithography processes are more convenient for high density arrays and allow feature sizes below $1 \mu\text{m}$. From an electrical point of view, the metallization should be adapted to the application needs. Although electrophysiological recordings can usually accommodate resistive interconnects, this is not the case for applications requiring mA currents (e.g. optoelectronics). The interconnect resistance is ruled by the following formula:

$$R = R_{\square} \frac{L}{W} \quad (1.2)$$

With L , W the interconnect length and width respectively, and R_{\square} the sheet resistance of the

conductive film. The calculation of the sheet resistance is dependant of the material resistivity and the thickness of the film. As the micro-cracked gold films are thin (< 60 nm) and physically fractured, their sheet resistances are relatively high (i.e. 10 to 100 Ω/\square).

1.5 Outline of the thesis

The heterogeneity exposed by the somatosensory system hinders further comprehension of the neural mechanisms involved in sensory and pain perception. Due to the large range of severe disabilities arising from its dysfunctionality, the lack of adequate treatments represents a burden for society. More selective neuromodulation within the somatosensory system would allow to unravel its constituents and their associated functions. However, neural interfacing with implantable electronics is challenging due to the soft and dynamic nature of these tissues. In this thesis, I describe the development of soft multimodal neural interfaces aiming at establishing precise and long-term control over neural populations of the somatosensory system. First, I report on an optical cuff for epineural light delivery in the mouse peripheral nervous system (**Chapter 2**). Although this concept represents a straightforward approach for optogenetics outside of the brain, tethered conditions hamper fine behavioural studies. This statement drove the development of a wireless optoelectronic system to deliver optical stimulations to the mouse sciatic nerve (**Chapter 3**). This system enabled the neuromodulation of pain-associated neural circuits and was used to investigate neuroimmune interactions. Next, I present a soft epidural transversal implant for multipolar electrical stimulations of the spinal cord (**Chapter 4**). Its unique electrode distribution allowed for functionally-selective stimulations in the context of spinal cord injury. Finally, I report on a soft optoelectronic implant for optogenetics in deep structures of the mouse spinal cord (**Chapter 5**). This implant demonstrated seamless bio-integration and has the potential to unravel peripheral and spinal neural circuits.

2 Optical cuff for optogenetics in the peripheral nervous system

Abstract Nerves in the peripheral nervous system (PNS) contain axons with specific motor, somatosensory and autonomic functions. Optogenetic stimulation offers an efficient approach to selectively activate axons within the nerve and to precisely unravel these neurons. However, achieving reliable epineural light delivery to small, delicate and dynamic peripheral nerves is challenging. To extend the use of optogenetics within the PNS, I propose an optical peripheral nerve interface, called optocuff. In this chapter, I review the challenges associated with interfacing optically the mouse sciatic nerve that drove the development of the optocuff. Behavioural experiments and histology demonstrate that this soft optical cuff neither damages the nerve nor hinders the mouse normal behavior. Using this optical interface, I show orderly recruitment of motor units with epineural optogenetic stimulation of genetically targeted Thy1^+ axons, both in anaesthetized and in awake, freely behaving animals. I conclude in discussing the advantages and the limitations for using this simple, yet powerful, optogenetic implant.

This chapter is adapted from the following publication:

- [86] MICHOU D Frédéric, SOTTAS Loïc, BROWNE Liam E., ASBOTH Léonie, LATREMOLIERE Alban, SAKUMA Miyuki, COURTINE Grégoire, WOOLF Clifford J., LACOUR Stéphanie P, Optical cuff for optogenetic control of the peripheral nervous system, *Journal of Neural Engineering*, 2018, vol. 15, n° 1, p. 15002.

2.1 Background and state of the art

2.1.1 Light delivery strategies for optogenetics in the PNS

The use of optogenetics in the PNS has to date been relatively modest compared to optogenetic control in the brain [87], because of several physiological and technological challenges. Peripheral nerves are complex, heterogeneous tissues embedded in muscle and connective tissue, which strongly scatter and absorb visible light. Under normal physiological conditions, peripheral nerves are stretched as joints move and muscles elongate, making consistent light delivery complex. Researchers have been using two strategies to conduct optogenetic interrogation in the PNS.

Transdermal illumination

Transdermal optical stimulation is a non-invasive approach to optogenetically stimulate primary afferent neurons (Figure 2.1.a). Excitation [13, 88, 89] and inhibition [90, 91] of mouse peripheral sensory neurons have been demonstrated using such an experimental design. However, axon activation efficacy strongly depends on the optical properties of the intermediate tissues e.g. skin and subcutaneous tissue [87, 92]. Subsequently, optical stimulation is limited to nerve terminals in the skin whose superficial epidermal layers are innervated by nociceptors. Significant scattering and absorption of the biological tissues within the working optogenetic spectrum limit the effective depth of stimulation.

Although transdermal illumination is restricted to the modulation of sensory neurons, this method is also not suitable for reproducible pulsed (i.e. frequency) stimulation in physiological *in vivo* conditions. Normal animal behaviour includes motion, preventing external, controlled and repeatable light delivery to the targeted tissues. To overcome these drawbacks, direct optical stimulation of nerves using an implant is a promising alternative for PNS optogenetics.

Optical and optoelectronic implants in the PNS

The rapid expansion of optogenetics in the CNS has triggered development of a variety of optoprobes in the form of waveguide, miniaturized optical fibers and optoelectronic μ LED-based arrays [93–96].

In a pioneer study, Llewellyn *et al.* demonstrated that optical stimulation of motor units in a nerve of a transgenic mouse expressing the light-activated cation channel ChR2 in Thy1⁺ neurons better approximated physiological recruitment of motor fibers than electrical stimulation [100]. For the first time, this study presented an optoelectronic implant for optical modulation of the sciatic nerve. However, the stiffness of the hybrid implant hosting 16 millimeter-sized light emitting diodes (LEDs) on a glass cuff limited its application to acute, anaesthetized conditions only.

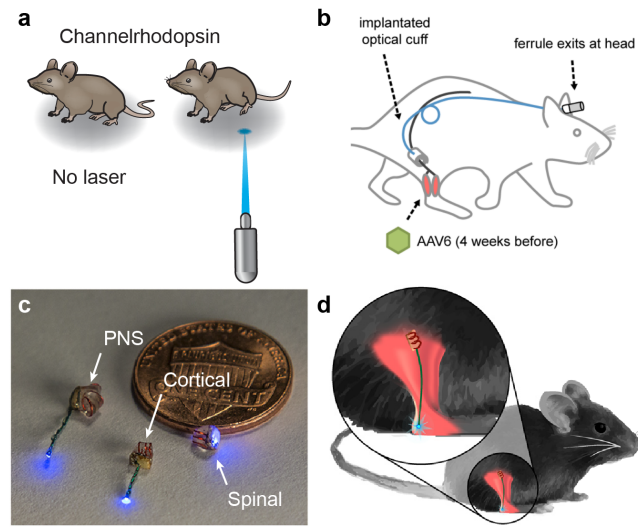


Figure 2.1 – Light delivery strategies to the PNS

a, Transdermal illumination for optogenetic stimulation of primary afferent neurons. Adapted from [97]. **b**, An optical nerve cuff delivers epineurial optogenetic stimulation to the rat sciatic nerve. Adapted from [98]. **c, d**, A miniaturized wireless optoelectronic system for untethered optogenetic control throughout the nervous system (brain, spinal cord and peripheral nerve endings). Adapted from [99].

A solution enabling *in vivo* optogenetic stimulation directly to the peripheral nerves was proposed by Towne *et al.* [98]. In this study, an optical fiber-based nerve cuff for epineurial light delivery on the rat sciatic nerve was presented. Intramuscular injection of adeno-associated virus serotype 6 (AAV6) had enabled retrograde ChR2 expression across non-genetically-targeted axons (Figure 2.1.b). Optogenetic stimulation via the optical nerve cuff provided sufficient irradiance to the nerve axons, thus enabling non-specific muscle activation both in anesthetized and in freely-behaving rats. Eventually, this optical nerve cuff concept for long-term, efficient light-delivery to genetically-selected subsets of peripheral neurons allows more extensive peripheral optogenetics.

Other groups have proposed miniaturized and wireless optoelectronic systems for optogenetics in the PNS [99, 101]. These systems presented the advantages of being fully implantable for long-term experiments in mice. Additionally, their versatile technologies allowed to optically target different tissues in the nervous system (e.g. brain, spinal cord), widening their potential application spectrum. However, in the case of PNS applications, these optoelectronic systems provided poor to none interfacing with the peripheral nerves and their light delivery remained subcutaneous and non-directional to the nerve (Figure 2.1.c,d). Using this approach, their effective optogenetic stimulation was restricted to a small subset of nerve terminals or nerve fibers, similarly as transdermal illumination.

Finally, controlled and long-term light delivery to peripheral nerves requires advances in neurotechnology to both enable long lasting and efficient opsin expression in specific subsets

of axons in peripheral nerves and the production of implantable interfaces bio-integrated with the flexible nerves and capable of sufficient light power delivery over extended periods of time without producing nerve damage.

2.1.2 Optical stimulation using optic fibers

Implantable optic fibers are commonly used for optogenetic experiments [102, 103]. These thin constructs work as a waveguide, transmitting light with minimal internal losses (i.e. attenuation, usually in dB/km). Because of lower attenuation, optic fibers are preferred over traditional metal wires for long-distance telecommunication.

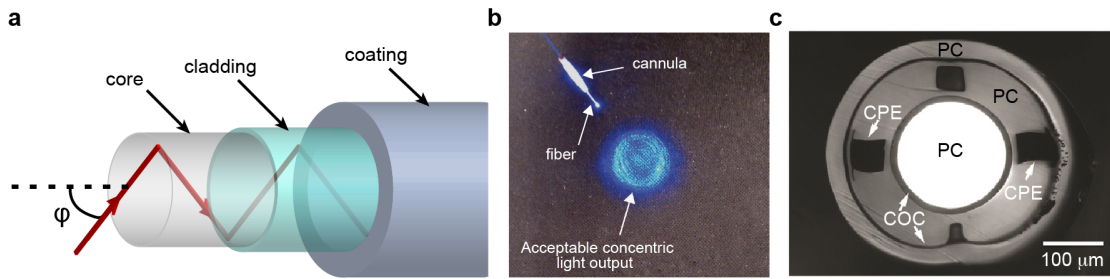


Figure 2.2 – Optic fiber working principle and its application in optogenetics

a, An optic fiber is generally composed of a core, a cladding and a coating. An incident light ray (showed in red) reflects internally within the optic fiber, minimizing losses. The maximum angle of incidence φ for a refracted incident ray defined the critical angle and the fiber acceptance cone. **b**, A typical implantable optic fiber for optogenetics in cortical tissues. The fiber cannula is usually head-mounted. Adapted from [104]. **c**, Multimodal optic fiber cross-section enables simultaneous and colocalized optical stimulation, drug delivery and neural recording. Adapted from [105].

Photons travelling down an optic fiber bounce at the edge of the fiber core (Figure 2.2.a). This phenomenon, called total internal reflection, is explained by the refractive index difference of the fiber core and cladding. An optic fiber is also defined by its Numerical Aperture (NA), that defined the incident light ray maximum angle φ to be reflected in the fiber core. Consequently, an optic fiber with a larger NA will have a wider illumination cone. The relation from the material refractive indexes to the fiber NA is derived from Snell's law:

$$NA = \sin(\varphi) = \sqrt{n_{core}^2 - n_{cladding}^2} \text{ in air} \quad (2.1)$$

With n being the material refractive index. The optic fiber core and cladding are usually made of silica (of different refractive indexes). As these are brittle materials, the optic fiber structure is secured with a coating layer. The coating layer does generally not play a role in light transmission.

In optogenetic experiments, optic fibers are coupled to an external light-source (e.g. laser, LED) and are implanted in the region of interest to deliver effective optical stimulation. The widespread use of optic fibers for optogenetic cortical experiments is explained by a combi-

nation of factors, including its optical performances (high irradiance, low heat generation) and its availability (inexpensive, on-the-shelf component). However, the optic fiber stiffness relative to the neural tissues can prevent chronic, seamless insertion. Additionally, coupling to an optic fiber is challenging and prevents the use of an implantable light source [106, 107], hence optic fiber experiments remain generally tethered.

The rapid expansion of optogenetics in neuroscience has triggered the development of a variety of optic fiber-based neural interfaces. Integration of electrodes to the optic fiber enables neural activity recording with concomitant optogenetic modulation [108–110]. Multimodal optic fiber may also integrate a micro-fluidic channel to allow local drug or viral delivery [105, 111]. These optic fiber-based interfaces have been designed exclusively to be implanted in the brain, with few exceptions for the spinal cord and the PNS [98, 112, 113]. Although made of silica, optic fibers can be fairly thin (e.g. 100 μm in diameter) and flexible (bending radii in the mm range).

2.1.3 Mechanical and optical nerve properties

An implantable optic fiber is an appealing approach to deliver efficient optical stimulations to the peripheral nerves. In order to validate this hypothesis, we have conducted experiments to characterize the mouse sciatic nerve elongation and optical transmittance properties. The results are presented in Figure 2.3.

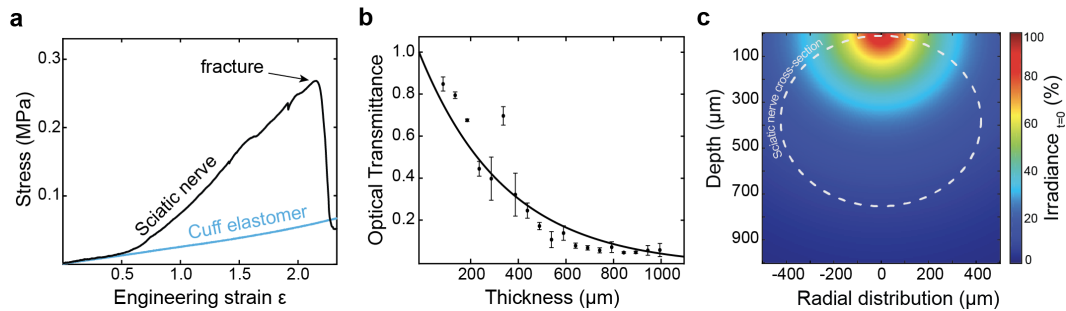


Figure 2.3 – Mouse sciatic nerve mechanical and optical properties

a, Tensile strain-stress curves recorded from a fresh sciatic nerve immersed in physiological conditions and from the elastomeric cuff. **b**, Relative optical power transmission at 473 nm through fresh dissected sciatic nerve tissue ($n = 4$ per thickness, in cross-section, mean \pm s.d.). **c**, Relative radial light propagation through sciatic nerve tissues for a non-directional light source.

Tensile strain

Method: The sciatic nerve was explanted from an adult mouse (C57BL/6, 3-month old) and placed in saline solution. Immediately after the explantation, the sciatic nerve (8 mm long, 0.8 mm in diameter) had its ends fixed to two glass cover slips using a cyanoacrylate adhesive. Delicately, the sciatic nerve and the cover slips were inserted into the clamps of a tensile testing equipment (Model 42, MTS Criterion). This machine is equipped with a circulating

bath that allowed the nerve to be kept in warm (37 °C) saline during the experiment. Extension at a strain rate of 0.1 %. s^{-1} was continuously applied until the sciatic nerve sample failed. Following the nerve tensile test, we clamped a thin elastomeric membrane in the tensile testing equipment and repeated the extension procedure. This membrane will be used as a soft cuff for interfacing the mouse sciatic nerve.

Results: The stress-strain curves of the mouse sciatic nerve and the elastomeric membrane are presented in Figure 2.3.a. The sciatic nerve sample showed a quasi-linear relation until 50% strain, describing the soft tissue elastic regime. Under physiological conditions, we can expect the nerves to be stretched with the body motion. At strains above 50%, the sciatic nerve presented a non-linear stiffening, with partial tear appearing for strains larger than 150%. This behavior is characteristic of the elongation of collagen constructs and is found across mammalian species [77]. In comparison, the elastomer stress-strain curve remained linear for large elongation, displaying a similar stiffness to the mouse sciatic nerve until 50% strain.

Optical transmittance

Method: Sciatic nerves of five naïve adult mice were explanted after CO₂ asphyxiation, immersed in PBS then embedded in 2.5% agarose gel. Cross-sectional slices (100–1000 μm thick) were obtained with a vibratome apparatus (VTS1200, Leica) and mounted on microscopic glass slides (Superfrost, Thermo Scientific). Saline was added to prevent slices from drying. Tissue transmittance was immediately measured with an optical system composed of a photodiode (S170C, Thorlabs), a power meter console (PM100D, Thorlabs) and a 473 nm DPSS laser (100 mW, LaserGlow) coupled to a multimode SMA optic fiber (105 μm core diameter, 1 m length, Thorlabs). The sensor was shaded with a mask matching nerve cross-section dimensions and a constant intensity (15 mW. mm^{-2}) illuminated the slices. The light radial distribution in sciatic nerve tissue was finally modelled using the modified 1D Beer–Lambert law:

$$\frac{dI(z)}{dz} = -\mu_{eff}I(z) \quad (2.2)$$

This equation was solved by:

$$I(z) = I_0 e^{-\mu_{eff} * z} \quad (2.3)$$

where I_0 is the optic fiber output irradiance, μ_{eff} the effective attenuation coefficient and z the slice thickness [114]. We define the tissue optical transmittance the ratio $\frac{I(z)}{I_0}$, that follows an exponential decay with z .

Results: We measured light transmission *ex vivo* $I(z)$ through slices of freshly dissected sciatic nerves, Figure 2.3.b. From these measurements, we were able to extract the sciatic nerve optical transmittance. Light is rapidly absorbed with an effective attenuation coefficient μ_{eff} of 3.503 mm^{-1} at 473 nm. This attenuation coefficient was measured as in the same range of different brain tissues [114]. For visualisation, we represented the changes in irradiance for an

isotropic light source placed above sciatic nerve (Figure 2.3.c). The nerve optical transmittance validates a high irradiance light delivery approach for deep efficient optogenetic stimulation.

2.2 The optocuff, an optical interface with the PNS

Inspired by the report from Towne *et al.* on an optical fiber-based nerve cuff for optical stimulation in freely-behaving rats [98], we have constructed a soft optocuff as an optical neural implant for chronic peripheral optogenetic stimulation in freely-behaving mice. The optocuff system is presented in Figure 2.4.

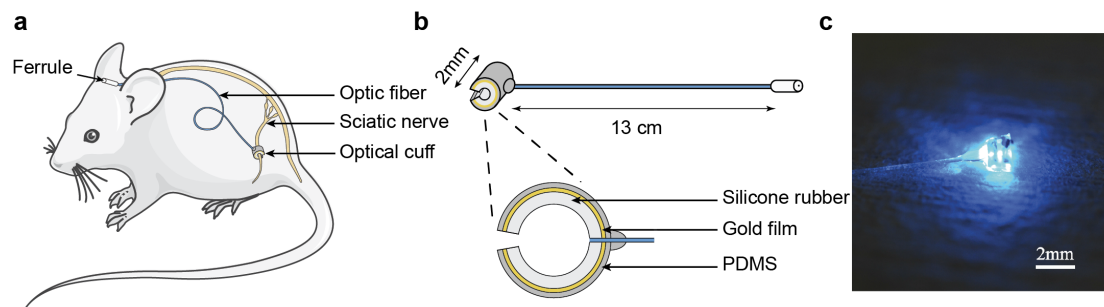


Figure 2.4 – Optical coupling to the mouse PNS with the optocuff

a, Optical stimulation carried out epineurally in mice implanted with an optocuff. **b**, Optical cuff illustration. A thin flexible optic fiber terminates on a silicone rubber-based cuff to deliver an optical stimulation on the mouse sciatic nerve. A gold thin film enables light to reflect internally. **c**, Picture of the optocuff.

2.2.1 Optocuff fabrication

The cuff cylinder was built upon a polystyrene rod template (0.88 mm diameter, Evergreen). A soft 150 μm thick platinum-catalyzed silicone (Ecoflex 00-50, Smooth-On) was vertically spin-coated and cured (2h at 80 $^{\circ}\text{C}$). A gold film was sputtered (80 nm, DP650, Alliance Concept) on the silicone to act as a light reflective coating. Finally, a micrometric film of PDMS (Sylgard 184, Dow Corning) was used for encapsulation by spray deposition of a PDMS–Heptane mixture. Solvent dilution of PDMS reduced its viscosity. A 12 cm optic fiber (FG105UCA, 105 μm core diameter, Thorlabs) was processed similarly to previous papers [115]. Briefly, the acrylate coating tip-end of the fiber was dissolved in acetone and terminated with a 1.25 mm ceramic ferrule (CFLC128, Thorlabs). The fiber was polished using a dedicated kit (Thorlabs) and its light transmission controlled with a power sensor. The distal end of the fiber was perpendicularly coupled to the cuff template and polymer sealed (Kwik-Sil, World Precision Instruments). Finally, the rod was removed, the cuff trimmed (2 mm in length, 0.8 mm inner diameter) and a sharp incision was applied transversally to the cuff. The compressive stress built during elastomer curing caused the cuff to spontaneously fold spirally.

2.2.2 Optocuff bio-integration

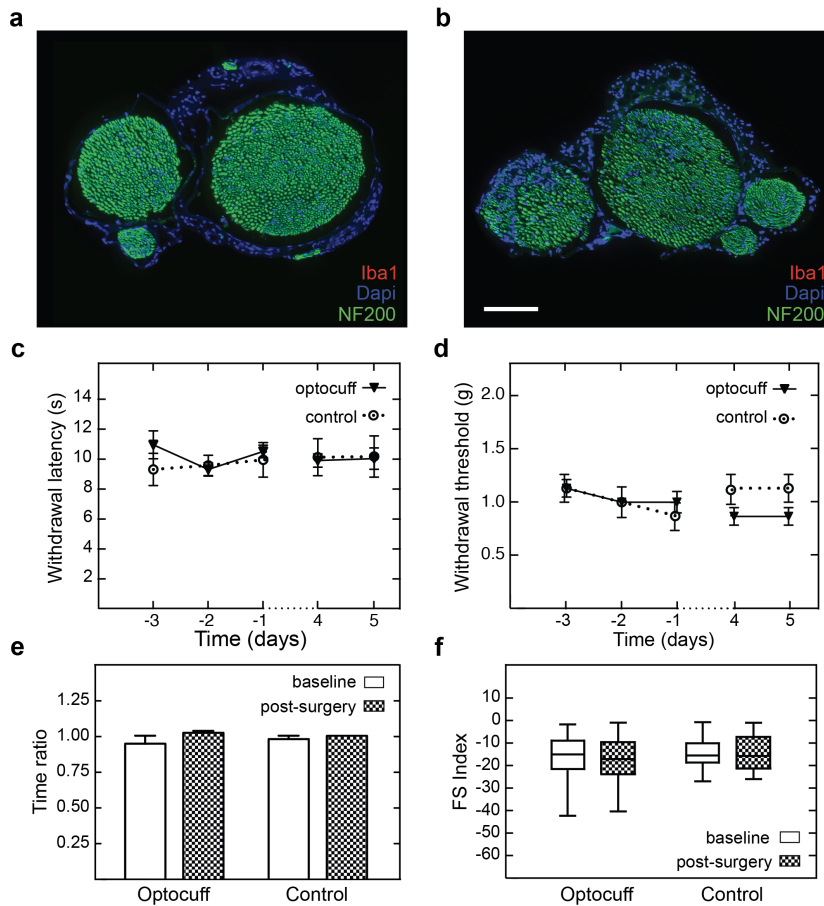


Figure 2.5 – Histology and behavioural experiments following optocuff implantation

Sciatic nerve cross-sectional images 20 days following cuff implantation (**a**) or sham surgery (**b**) revealing the nerve structure (Dapi), myelination (NF200) and inflammation (Iba1). Thermal (**c**) and mechanical (**d**) sensitivity assessed with Hargreaves and von Frey's methods respectively, in cuff implanted ($n = 6$) and control groups ($n = 3$). Surgery was performed on day 0. **e**, Dynamic weight bearing analysis of the duration of time spent on the ipsilateral versus the contralateral hindpaw, before surgery and 5 days post-surgery (mean \pm s.d.). **f**, Box plot representation of the functional sciatic index calculated gait analysis on treadmill (20 cm/s).

After implantation of the optocuff on the mouse left sciatic nerve (surgical procedure described in Appendix A.1.1), we investigated if this neural interface affected the sciatic nerve over time. One end of the optic fiber was permanently anchored to its head-mounted ferrule. Histological cross-sections of the nerve at the cuff site did not show any sign of demyelination or signs of inflammation after 20 days of implantation as shown in Figure 2.5 (methods described in Appendix A.1.8).

Coherent with the histological results, sensory and motor behavioural assessments did not reveal any change at various times after implantation (Figure 2.5.c-f). Thermal and mechanical

pain-related assays as well as weight bearing and gait were conducted prior and after surgery and did not reveal any significant change ($p > 0.05$, ANOVA with Dunnett's method). The behavioural experiment methods are described in Appendix A.1.

2.3 Epineural optogenetic stimulation

We presented a soft optical cuff interfacing with the mouse sciatic nerve. The optocuff did not damage the nerve thus was suitable for long-term experiments. In this section, the optocuff is evaluated for epineural optogenetic stimulation of $Thy1^+$ axons *in vivo*.

2.3.1 ChR2 expression in $Thy1^+$ neurons

Methods similar to those used in the brain can be used to express opsins in peripheral neurons; however several groups have reported on the difficulties in doing so with sufficient stability and efficacy and without interfering with the regular function of the peripheral neurons [116]. The light-activated ion channel ChR2 was expressed in a broad class of sensory and motor neurons using a Cre recombinase transgenic approach; Cre-dependent ChR2-tdTomato mice were crossed with $Thy1$ -Cre driver mice (breeding detailed in Appendix A.1.2). The resultant $Thy1::ChR2$ mice were heterozygous for both transgenes and ChR2 was found in dorsal root ganglion (DRG) neurons and in sciatic nerve axons (Figure 2.6.a-b). Of the $ChR2^+$ DRG neurons, 41% were myelinated (NF200), 4% were CGRP⁺ and 5% IB4⁺. Electrophysiological studies using whole-cell current clamp recordings from $ChR2$ -tdTomato⁺ DRG neurons showed action potentials were elicited by light (Figure 2.6.c). The large range of membrane capacitances ([11–51] pF; mean 28 ± 4 pF) and thresholds ([-56 to -35 mV]; mean -44 ± 2 mV) indicate a broad neuron population was targeted, as expected for the $Thy1$ promoter [117]. Functional expression of ChR2 at the mid-axon enables an epineural light-delivery strategy with the optocuff.

2.3.2 Orderly recruitment of motor units

To measure electromyographic (EMG) responses of anaesthetized $Thy1::ChR2$ mice to peripheral optical stimulation of motor axons (methods described in Appendix A.1.9), the sciatic nerve of the mouse was exposed and implanted with the optocuff (Figure 2.7.a). Then, thin EMG electrodes were inserted into the ipsilateral tibialis anterior (TA), an ankle flexor muscle innervated by the peroneal branch of the sciatic nerve. EMG recordings were synchronized with optical stimulation generated by an external 473 nm laser. Short pulses of light consistently triggered unilateral TA contractions, resulting in light-activated twitches. We characterized the muscle recruitment with the peak-to-peak value of EMG signal in the early phase of the response. We found the muscle fibers were recruited in an orderly fashion with the power of epineural irradiance of the optical stimulation (Figure 2.7.b-c). These results suggest more motor units were recruited with higher irradiance stimulation, consequently inducing larger

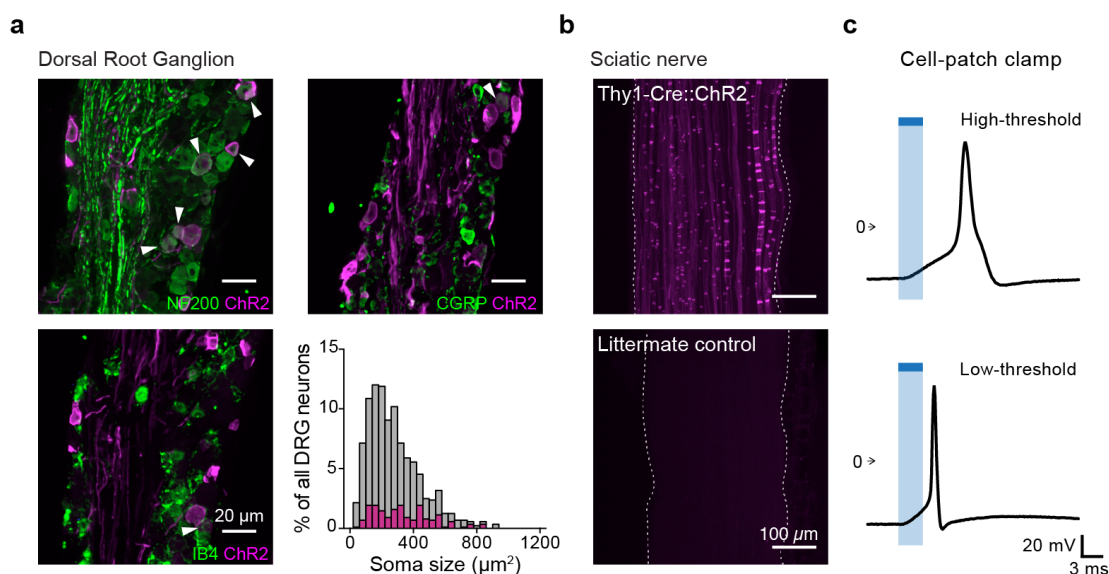


Figure 2.6 – Expression of ChR2 in the PNS of *Thy1::ChR2* mice

a, Expression of ChR2-tdTomato in DRG soma was found in a broad class of neurons, myelinated (NF200, top left), CGRP (top right) and IB4 (bottom left). White arrows indicate overlapping fluorescence emitting neurons. Scale bar, 20 μm . ChR2 was expressed in a wide range of cell sizes as estimated using NeuN as a marker for all neurons (bottom right). **b**, Expression of ChR2-tdTomato in sciatic nerve fibers validates the epineural light delivery. Scale bar 100 μm . Fluorescence was not observed in any of the littermate controls. **c**, Whole-cell current clamp recordings of action potentials elicited by light in cultured *Thy1::ChR2* DRG neurons (17 neurons, 3 mice). These cells displayed a wide range of membrane capacitances and thresholds. Neurons from littermate controls did not show any effect of light ($n = 6$ neurons). Light (473 nm for 3 ms) applied at $6 \text{ mW}\cdot\text{mm}^{-2}$.

muscle responses. Latency for the EMG onset (mean 6.1 ± 0.3 ms, 60 trials, 10ms pulse width) was stable relative to the optical stimulation intensity and peak-to-peak amplitude (mean 6.1 ± 0.25 mV), implying direct activation of large and fast motor axons. The TA EMG amplitude directly correlated with optical pulse width (Figure 2.7.d), indicating an increased activation of motor neurons with longer pulses. These results demonstrated peripheral optogenetic modulation in anesthetized mice with the optocuff.

2.3.3 Optocuff stimulation in awake, freely-behaving mice

Finally, we tested whether the optocuff could reliably deliver epineural optical stimulation in awake, freely-behaving mice (detailed methods in Appendix A.1.10). We applied epineurally short (2–100 ms) light pulses at 473 nm with the optocuff while continuously monitoring the behavior of *Thy1::ChR2* mice at 1 kHz with a camera (Basler Ace acA2040-180km). Optogenetic stimulation of the *Thy1*⁺ axons resulted in short latency hindlimb muscle contraction (Figure 2.8.a-b). We observed global limb extension and paw opening with short (≥ 5 ms) blue illumination. Probability of behavioural response to optical stimulation was higher with longer

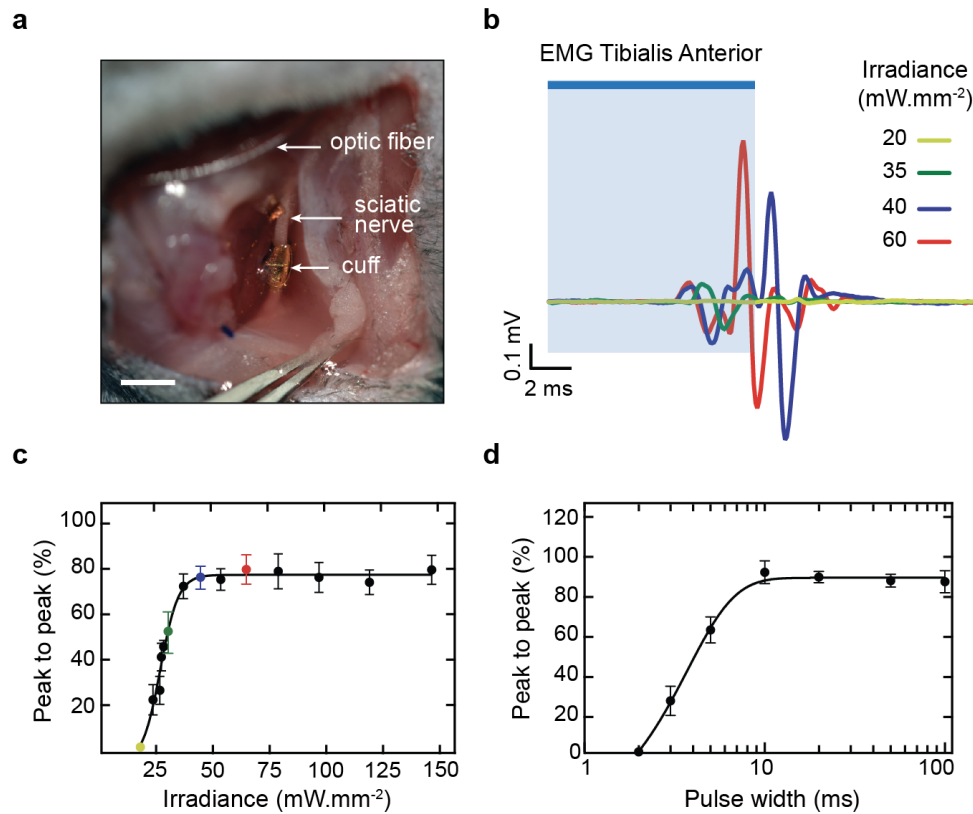


Figure 2.7 – Optical stimulation of the sciatic nerve in anaesthetized *Thy1::ChR2* mice

a, Optocuff implantation on the sciatic nerve. Scale bar, 2 mm. **b-d**, Optogenetic stimulation of peripheral axons in anaesthetized *Thy1::ChR2* mice. Light-activated Tibialis Anterior (TA) EMG at various stimulation irradiances. The threshold for muscle contraction was 25 mW.mm⁻². The blue bar indicates the stimulation duration (10ms). EMG amplitude is directly correlated with stimulation irradiance (**c**) and pulse width (**d**), ($n = 3$ *Thy1::ChR2* mice, 5 trials per condition, mean \pm s.d.; irradiance set at 60 mW.mm⁻²).

pulses (Figure 2.8.c) and reached 100% for pulses longer than 20 ms. We found the delay for the change in behavior elicited by epineural stimulation was stable through different effective pulse duration (mean 17.9 ± 0.58 ms, Figure 2.8.d). Using conduction velocity analysis, we concluded these changes in behavior were elicited by direct activation of motor neurons [118]. Furthermore, absence of response to optical stimulation carried with the optocuff in control littermate mice implies that light-responses were not caused by heat or visual artifact.

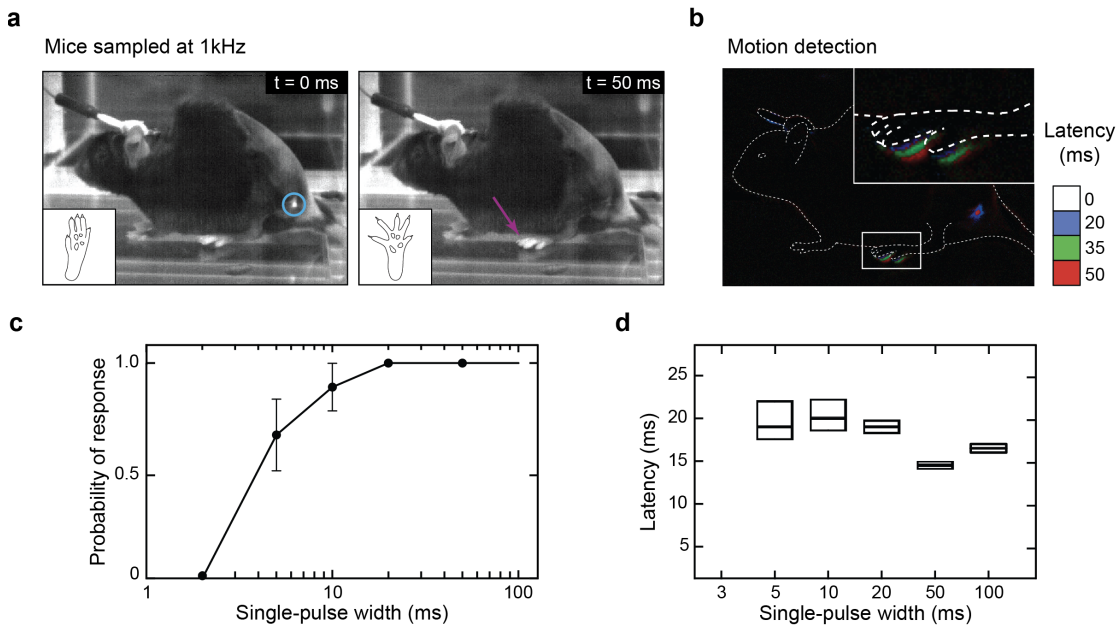


Figure 2.8 – Optogenetic control of peripheral neurons in awake behaving mice

a, Behaviour recorded at 1 kHz elicited by a single pulse of light (50 ms, $40 \text{ mW} \cdot \text{mm}^{-2}$) applied to the sciatic nerve using the optocuff. Onset of the optical stimulation can be seen transdermally. Epineural optical stimulation of *Thy1* axons in the sciatic nerve results in hindlimb muscle contraction and paw opening. **b**, Motion detection reveals the kinetics of this behaviour. The latency to the response was 17 ms. This analysis was conducted by comparing the difference in pixel intensity between frames. **c**, Probability of behavioural response to an epineural optogenetic stimulus depends on the pulse width ($n = 3$ mice, 5 trials per condition, mean \pm s.e.m.). **d**, Response latency upon epineural activation of *Thy1* neurons demonstrates more stability with longer pulses. The mean latency did not depend on pulse duration ($n = 3$ *Thy1::ChR2* mice, 5 trials per condition). Littermate control cuff implanted mice did not show any response to light stimuli.

2.4 Discussion

We have developed an implantable optical interface that enables optogenetic modulation of the PNS in freely-behaving small animals such as mice. The soft elastomeric cuff can be wrapped around the sciatic nerve inducing minimal foreign body reaction as demonstrated by histology and behavioural experiments. Using transgenic *Thy1::ChR2* mice, direct and robust muscle activation was obtained by optical stimulation of axons in the sciatic nerve, both in anaesthetized and awake animals. The muscular response can be finely tuned with the optical stimulation parameters i.e. pulse width and spectral irradiance.

Stable light delivery to neurons or axons *in vivo* is challenging, particularly for applications in the peripheral nerves [87]. The relative motion of these soft biological tissues prevent long-term and reliable interface with stiff implants. Although studies have bypassed this problem by stimulating nerve-endings via transdermal illumination [13, 88–90] or using implanted wireless LEDs [99, 101], interfacing the whole nerve directly offers a broad range of opportu-

nities. Epineural stimulation allows to access the entirety of fibers within the nerve whereas transdermal illumination target only a fiber subset. We find that reducing the mechanical mismatch between the nerve and implant and optimizing the surgical procedure were key for successful long-term optical coupling with the mouse PNS. The system relies on thin, compliant, subcutaneously tethered fibers that enable a higher intensity and thermally safer light stimulation compared to optoelectronic systems. Additionally, the commercially available external light-sources allow for a large range of solutions for future optogenetic experiments.

Optic fibers are commonly used for a wide variety of applications, including telecommunications, illumination, imaging and sensing. For example, an optic fiber can be used as a strain sensor by measuring the strain-induced interference to light transmission through the fiber. Using this phenomenon, several groups have reported on highly stretchable optic fibers for strain sensing [119–121]. These mechanically-soft optic fibers have a great potential for long-term optical coupling with biological tissues. Within the optocuff concept, they may also provide a solution to process the fiber and the nerve cuff simultaneously, allowing for more robustness. In that regard, I crafted soft stretchable optic fibers, as shown in Figure 2.9. Exploiting the total internal reflection phenomenon, the fiber core was made with an optical clear gel ($n_{core} = 1.52$ at 589 nm) surrounded with a PDMS cladding ($n_{core} = 1.41$), resulting in a high aperture fiber ($NA = 0.57$). The optic fiber fabrication is detailed in Appendix A.1.11. These fibers transmitted light under large strains with acceptable optical losses for optogenetic applications. Although the problematic coupling to a light source hindered further work on these fibers, soft stretchable fibers may be a good candidate for probing the nervous system.

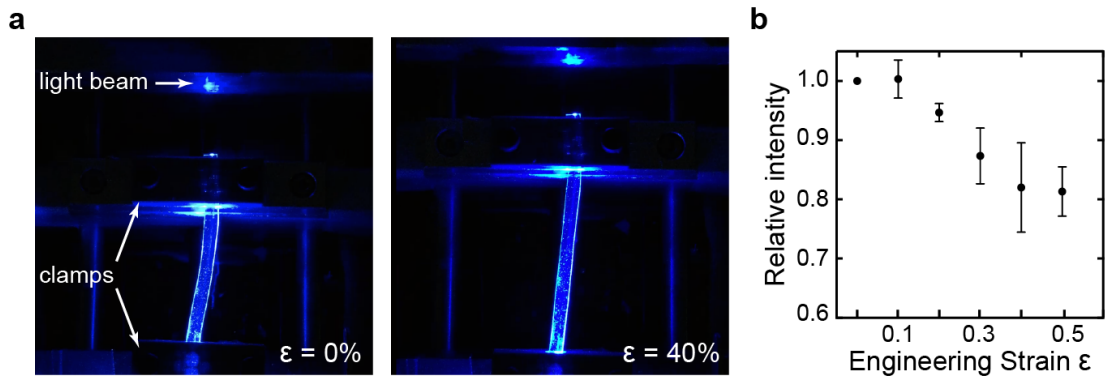


Figure 2.9 – Stretchable optic fibers

a, A soft optic fiber (core $100\ \mu\text{m}$ in diameter) is clamped on an uni-axial stretching machine and connected to a 473 nm laser. The fiber is stretched to $\epsilon = 40\%$. The output optical power is measured with a photodetector. **b**, The output optical power decreases for larger strains ϵ (mean \pm s.d.).

Opsin expression in the mouse PNS was achieved using the transgenesis route. Although recent studies have exploited optogenetics in rats or primates [122–125], mice are still the predominant species used in the neurobiology field. This animal model presents obvious advantages for genetic manipulations, resulting in a large number of Cre lines and Cre-dependent viral vectors available. We show that ChR2 opsin expression in PNS neurons was robust enough

for optical modulation *in vitro* and *in vivo*. The optocuff system can be used for a wide variety of optogenetic experimental approaches, including activation as shown here and neural inhibition with opsins such as halorhodopsin (NpHr) or archaerhodopsin (Arch). Multi-spectra modulation using multimodal optic fibers will further broaden opportunities for the soft optocuff system [61, 126, 127].

Finally, long-term selective modulation of the PNS by light delivery offers new experimental opportunities. Optical stimulation of peripheral axons has great implications for muscle control and nerve regeneration [128, 129], for the study of sensory biology [13] and for autonomic output [130]. Similarly, optogenetic inhibition *in vivo* will enable to tease out the functional role of specific neurons involved in complex disease mechanisms, such as tactile allodynia following nerve injury [91].

2.5 Conclusion

In summary, we introduced the concept of soft optical cuff for epineural light delivery in the mouse PNS. Soft optocuffs are a simple and efficient tool to probe the PNS with optogenetics. We have demonstrated consistent optical recruitment of motor units both in anesthetized and in freely-behaving mice using the optocuff. Its manufacturing does not require extensive microfabrication processes, making this neural interface widely available. Further miniaturization would allow for an even broader use of the implant, especially to study smaller nerves, such as autonomic and visceral nerves [131, 132]. However, the optocuff relies on thin and fragile optic fibers hindering more chronic experiments. Additionally, the optocuff requires coupling to an external, bulky light source. Untethered experimental conditions and seamless optical stimulations using a wireless system would improve *in vivo* optogenetic experimentation. Finally, the optocuff system supports optogenetics as a versatile tool to unravel the PNS function, an essential step to study potential therapies for many diseases, such as chronic pain.

2.6 Contribution

Data presented in this chapter are the result of a team effort :

- I developed the optocuff neural interface and designed the experimental plan for its validation *in vivo*. I have also performed the optocuff surgical implantation and led the behavioural experiments.
- Loïc Sottas ran the behavioural experiments and participated with the data analysis.
- Liam Browne bred the transgenic animals and performed the electrophysiology *in vitro*.
- Léonie Asboth participated with the acute EMG recordings.
- Alban Latrémolière and Miyuki Sakuma from the Clifford Woolf team provided precious help with the experimental plan and the surgical procedure.

3 A wireless optoelectronic system for optogenetic control of the peripheral nervous system

Abstract In the previous chapter, I introduced the concept of epineural light delivery using an optical cuff on the sciatic nerve. The optocuff relied on subcutaneous optic fibers coupled to an external light source. Although this approach enabled optogenetic modulation of the PNS, the experimental outcomes were hindered by the tethered conditions, preventing seamless neural modulations and impeding naturalistic behaviour. In this chapter, I present a wireless optoelectronic system for optogenetic control in the PNS. This system comprises an ultra-miniaturized head-stage powering a soft and compliant circumneural μ -LED array, delivering effective optical stimulations to the mouse sciatic nerve. The μ -LED array implantation did not impede the animal behaviour and the histology revealed the optoelectronic implant was not harmful to the nerve. To determine the utility of the system in the study of PNS pathways, we tested whether it could modulate pain-related behaviors in mice expressing ChR2 in genetically-targeted TRPV1⁺ neurons. We demonstrate single-shot optogenetic activation of sensory afferents, resulting in a rapid protective behaviour. The system enabled epineural pulsed stimulations, inducing real-time place aversion in these mice. Then, we investigated the recruitment of the immune system via optogenetic nociceptor activation. Finally, this wireless optoelectronic system supports deciphering peripheral neural pathways using optogenetics.

Some of the information presented in this chapter appears in the following manuscripts:

- [133] SCHÖNLE Philipp, MICHOUÉ Frédéric, BRUN Noé, GUÉX Amélie, LACOUR Stéphanie P., WANG Qing, HUANG Qiuting, A Wireless System with Stimulation and Recording Capabilities for Interfacing Peripheral Nerves in Rodents, *in proceedings EMBC meeting*, 2016, pp 4439-4442, IEEE.
- [134] MICHOUÉ Frédéric, SCHÖNLE Philipp, SEEHUS Corey, BRUN Noé, MOON Rachel, DOYLE Benjamin, GALAN Katia, BROWNE Liam E., HUANG Qiuting, WOOLF Clifford J., LACOUR Stéphanie P., A wireless optoelectronic system for optogenetic control of the peripheral nervous system, *in preparation*, 2018.

3.1 Optoelectronic wireless systems in optogenetics

Optical neural stimulation is emerging as an exciting and more advantageous alternative to traditional electrical stimulation. In the last decade, optogenetics has been used extensively to modulate neural activity in the central nervous system, often relying on the implantation of optic fibers coupled to an external light source. More recently, Park *et al.* have reported on multifunctional fibers, combining light and drug delivery with electrophysiology recording [135]. Unfortunately, this innovative technology requires multiple, external connections, physically tethering the animal to bulky equipments in a way that impede movement and can lead to entanglement [136]. Optogenetic tethered systems alter behavioural studies and animal motion, reducing the quality of experimental outcomes and the development of optogenetics *in vivo*. To significantly relieve these constraints, optoelectronic systems combining an implantable light source with a wireless module were developed. I review the existing strategies for wireless optoelectronics and then present an ultra-miniaturized wireless head-stage developed in this context to drive a μ -LED array.

3.1.1 μ -LED: an implantable light source

The progress of optoelectronic systems is intricately linked to the development of light-emitting diodes (LEDs) and LED-based neural interfaces. Recent advances in miniaturization and efficiency enabled μ -LEDs to be implanted in the vicinity of neural tissues for optogenetic interrogation. Briefly, a LED is a p-n junction diode (semiconductor) that emits light when a current is applied, a phenomenon called electroluminescence. In the case of a blue LED, the N and P-regions are usually made of Gallium Nitride (GaN) and the quantum well layer (i.e. active region) is made of Indium Gallium Nitride (InGaN) [137, 138]. The quantum well material determines the LED emission spectrum and the recent use of InGaN promoted the development of high-brightness blue LEDs. Structure optimization made μ -LEDs with high efficiency possible (optical power in the range of one to tens of mW). However, LEDs pose several challenges for their use in optogenetic experiments. First, the quantum well is an isotropic emitting volume, meaning light is equally emitted in all directions. As the beam of light is not coherent, coupling of the LED to a light waveguide is not ideal (usually $< 10\%$ efficiency [139]). Although several groups have reported on optrode fabrication with LED-coupled waveguides, deep-tissue light penetration was limited by their modest irradiance [140]. Straight implantation of the μ -LED in the target neural tissue improves the optical stimulation efficiency, but is limited by potentially harmful heat generation during LED activation [141].

Implantable optogenetic interfaces incorporate μ -LEDs onto their substrates to deliver fine optical stimulations to the nervous system. These LED-based neural interfaces can be divided in two categories: penetrating or surface implants. The former is exclusively used for light-delivery in the brain. The probes may include sensors [142] (Figure 3.1.a), neural recording electrodes [143, 144] or a drug delivery system [145] (Figure 3.1.e). These probes may also display an array of μ -LEDs enabling more spatial optical selectivity [146, 147]. Such

3.1. Optoelectronic wireless systems in optogenetics

penetrating probes generally have a footprint similar to an implanted optic fiber, with the same order-of-magnitude mechanical mismatch implant to the neural tissues. Therefore, these probes trigger moderate to severe immune reactions with chronic implantation, limiting their stimulation effectiveness with time [148]. An alternative approach for light delivery in neural tissue resides in the use of surface implants. The μ -LEDs are integrated on a flexible substrate that complies with the biological tissue. The optical stimulation is delivered at the tissue boundaries, requiring higher irradiance than penetrating probe to reach deep tissue volumes. Similarly to penetrating probes, surface-mounted LED implants may integrate neural recording electrodes [149] or wireless capabilities [101] (Figure 3.1.c).

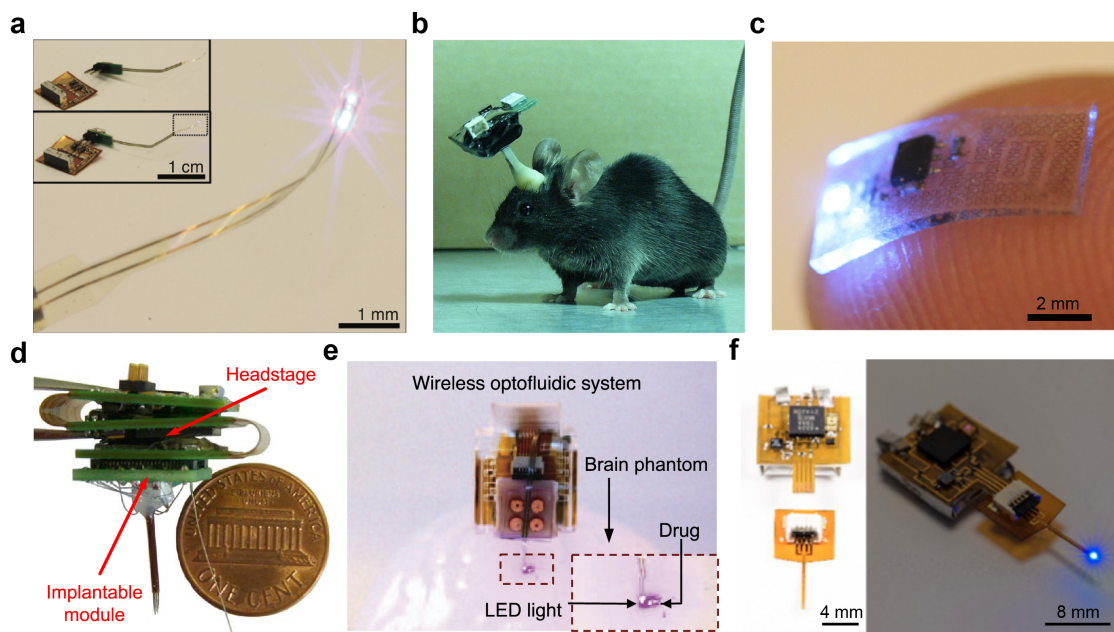


Figure 3.1 – Wireless optoelectronic systems in neuroscience

a, An injectable, cellular scale optoelectronic probe with multifunctional operation. The system is wirelessly powered via RF scavenging. Connectorized device showed on top left insets. Adapted from [142]. **b**, A deep-brain optogenetic stimulation wireless system. Adapted from [150]. **c**, A fully implantable soft optoelectronic system for wireless optogenetics. The systems comprises a RF harvesting unit to power a μ -LED. Adapted from [101]. **d**, A wireless head-stage for deep-brain optogenetic stimulation and electrophysiological recording. The battery-powered system features an implantable optic fiber coupled to a LED and 8 microelectrodes. Adapted from [151]. **e**, An optofluidic wireless system for concomitant optical stimulation and local drug delivery. The battery-powered infrared module enables wireless operations. The picture showcases the system implanted into an agarose gel brain mockup. Adapted from [145]. **f**, An injectable fluorescence photometry system that enables calcium indicator excitation and neural activity recording. The battery-powered transponder (top left) allows for wireless recording of GCaMP6 fluorescence. Adapted from [152].

3.1.2 Wireless system technologies

The development of μ -LEDs and implantable LED-based devices converged with the advent of wireless optoelectronic systems. The low-power consumption and reliability of μ -LED allowed for untethered control, removing the tangling wires from the experimental set-up. These wireless optoelectronic systems can be divided in two categories: battery-powered or battery-less systems.

Battery-powered systems generally comprise an implantable LED-device and a detachable head-stage. The latter is composed of a microcontroller to drive the implant, a connectivity chip for wireless control and a rechargeable battery. Prior to the experiment, the head-stage is connected to the μ -LED implant, and the whole system is controlled via an external unit (e.g. computer, tablet). This configuration allows to parametrize wirelessly the stimulation patterns such as pulse frequency and duration. Several examples of battery-powered systems have been reported. They can enable independent control over an array of μ -LEDs [150] (Figure 3.1.b) or simultaneous electrophysiological recording [151] (Figure 3.1.d). More advanced systems may also enable local drug delivery [145] (Figure 3.1.e) or neural activity recording via calcium imaging [152] (Figure 3.1.f). Battery-powered systems offer a consistent and straightforward method to wirelessly deliver light to the neural tissues. However, some of these systems can be cumbersome (i.e. size, weight) for small rodents and hamper their natural behaviour [150, 153]. Further system miniaturization would prevent interferences with the animal behaviour.

Battery-less systems offer an alternative to the previously described systems. They rely on wireless power transfer that can be achieved with either inductive coupling or Radio-Frequency (RF) scavenging. The first approach requires a power receiving coil and a resonant cavity chamber to supply energy to the system components via electromagnetic induction. RF scavenging powers electrical components with the transduction of microwave energy from a transmitter antenna to a receiver. Battery-free systems may employ a head-stage [154, 155] similarly as battery-powered systems. Further optimization enables these systems to be completely implanted [99, 142] (Figure 3.1.a) and to maintain functionality under mechanical deformation [101, 156] (Figure 3.1.c). These battery-less systems are promising for the development of untethered optogenetic experiments in freely-behaving conditions. However, wireless powering suffers from several negative features. First, due to power transmission efficiency, the LED implant output irradiance is limited to a few $\text{mW}\cdot\text{mm}^{-2}$. This outcome may not be sufficient for certain optogenetic applications, including surface stimulation. Moreover, the receiving coil/antenna relative position in space influences coupling efficiency, leading to stimulation inconsistency. In addition, wireless power transmission induces biological tissue heating due to the electromagnetic energy absorption [139]. Finally, fully implantable wireless systems have larger dimensions (due to electronic component integration) that could inhibit their versatility in peripheral or spinal applications [101, 132].

3.1.3 An ultra-miniaturized wireless head-stage

Through our collaboration with Huang's group at ETH, we designed an ultra-miniaturised wireless head stage for driving a μ -LED array implanted on the sciatic nerve with emphasis on minimal obtrusiveness to the animal, usage comfort for the experimenter and reusability. The device (Figure 3.2.a) measures only 0.5 cm³ including its 12 mAh battery (w/o connector) and weighs 0.9 g. Encapsulation in silicone typically adds another 0.4 g. A fully charged battery lasts for ca. 4 hours of experiments; for recharging, the head stage is plugged on a USB charging station (Figure 3.2.e) which further features buttons to turn the device on and off. The head-stage itself has no switch and its only mechanical component is a single 6-pin connector (A79109-001, Omnetics), which is used for both connection to implants and to the charging station. This design reduces size and eases packaging. We developed a proprietary Android application to wirelessly configure and control our head-stages. The Android application further allows updating the head-stage firmware wirelessly, which may e.g. be required when a new experiment demands different pulse-train configuration ranges. The ranges currently available are given in Figure 3.2.g.

The cornerstone of the head stage electronics is a commercial Bluetooth Low Energy (BLE) system-on-chip (SoC) (Nordic Semiconductor, nRF52832), as illustrated in the device block diagram (Figure 3.2.c). It is responsible for wireless connectivity and controlling of the remaining circuitry, i.e., DC/DC (Murata LXDC2HN series) and linear voltage regulators (ST Microelectronics LD39130S series) as well as a custom photoplethysmography (PPG) integrated circuit (IC) [157] - used here to drive the μ -LED array. The circuit is switched on by pulling the enable signal of the DC/DC converter to ca. 2 V, establishing the 1.8 V supply of the SoC, which then immediately sets the corresponding GPIO pin to keep the signal high. The SoC goes in BLE advertising mode and waits for an Android device to connect. Upon connection, device characterisation information is exchanged. The user can configure the pulse train according to Figure 3.2.g and initiates a stimulation. The PPG IC requires further 1.2 V and 3.3 V supply voltages, which are enabled only during stimulation to reduce stand-by power. To shut the device off, the enable signal of the DC/DC converter is grounded, disabling the 1.8 V supply and thus the enable signal by the SoC. An overall leakage current of 500 nA was measured, corresponding to a battery self-discharge duration of 1000 days.

The Transimpedance Medical Amplifier for Oximetry (TMA-O) [157] features a LED driver controlled by a configurable finite state machine (FSM) - enabling fine-grained pulse-train setting. Figure 3.2.f depicts the driving circuit: the LED current is defined by the voltage drop on R_{sense} , which is regulated to a value set by the digital-to-analogue converter (DAC). With some extra transistors in the amplifier, a pulse signal closes the regulation loop only during the LED-on time. This allows power stage multiplexing while maintaining the amplifier operating points and ensures steep rising and falling edges of the current pulses. Due to the low headroom between Li-Ion battery voltage (3.5-4.2 V) and blue LED forwards voltage (3.1 V) the set current might not be reached if the battery is exhausted or the series wiring resistance R_s in the implant is too high. We included a comparator to check for each pulse if the set

Chapter 3. A wireless optoelectronic system for optogenetic control of the peripheral nervous system

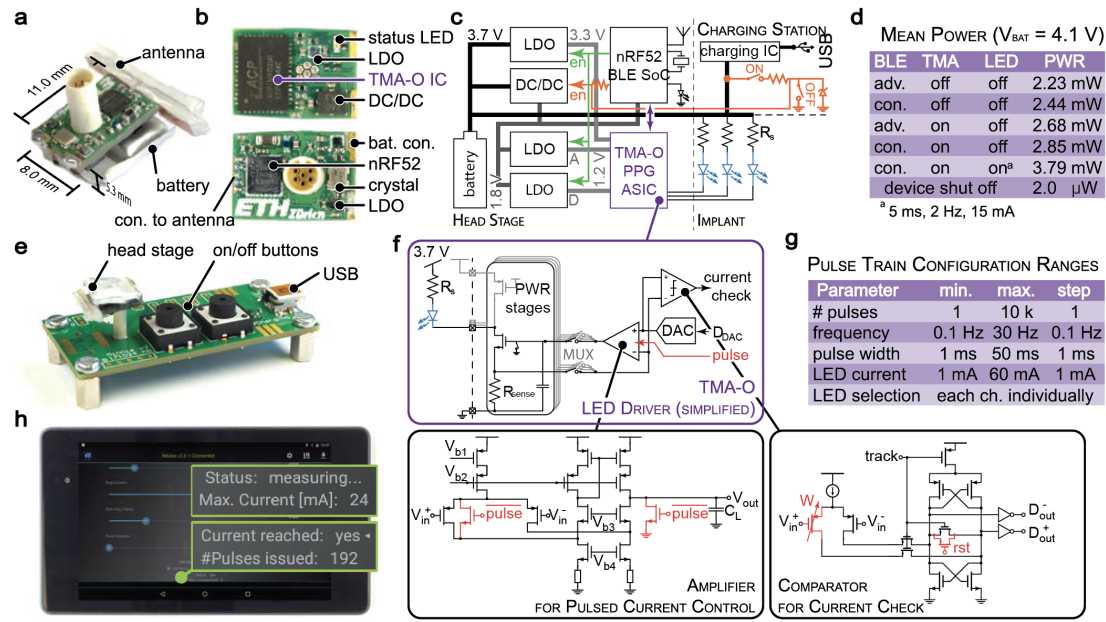


Figure 3.2 – A miniaturized wireless optogenetics stimulation head-stage

a, The completely assembled device measures 0.5 cm³ and weighs only 0.90 g. **b**, Detailed views of both sides of the assembled head stage PCB. **c**, Block diagram of the head stage with external circuitry, i.e., LED implant and battery charging station. The latter is further used to enable and disable the device which itself is too tiny to carry buttons or switches. The head stage is based on a commercial BLE SoC (nRF52832) and the LED driver circuits of our custom PPG ASIC (TMA-O). **d**, Overall head stage power consumption characterization for different operation modes of the BLE SoC (advertising, connected) and TMA-O (on, off, stimulation). **e**, Charging station. **f**, Circuit schematics of the LED driver. Circuitry is included to survey the effective LED current and thus the condition of the LED implant: a decay of its electrical characteristics over time could be observed. **g**, Configuration ranges for pulse-train parameters. **h**, The head stage is controlled by a proprietary Android app. Feedback on the LED current is displayed live during a stimulation experiment (insets). If required, the head stage firmware can be updated wirelessly via the app.

current is actually reached and provide a live feedback to the user via the Android application (Figure 3.2.h). As illustrated in the inset of Figure 3.2.f, the width of the comparator positive input transistor can be adjusted to provide a slight decision bias to overcome random process variation induced offsets. We further added a low-resistance reset switch to the classic latched comparator design to suppress any memory on previous decisions while maintaining the gain during the track phase [158].

The current check functionality can give precise feedback on the implant condition in the field and enables us to detect faulty ones or even to observe slowly degenerating ones. The head stage therefore also includes an operation mode in which the maximum achievable current can automatically be determined: Short (20-100 μ s) pulses with stepwise increasing current are emitted at a low pace (2 Hz) such that no optogenetic stimulation is evoked. As soon as we detect that the set current is not reached, we abort the procedure and display the result on the Android application (inset Figure 3.2.h).

3.2 A soft μ -LED-based peripheral interface

As discussed in the previous chapter (2.1.1), the use of optoelectronic implants in the PNS has been relatively modest compared to the brain. To deliver wireless optogenetic stimulations in the PNS, we developed a soft μ -LED array for implantation adjacent to the mouse sciatic nerve. The implant compliance enables the circumneural disposition of 4 μ -LEDs around the nerve for homogeneous and effective light delivery. In addition, the implant stretches to accommodate with the nerve relative motion. This optoelectronic implant was designed to be controlled via the ultra-miniaturized wireless head-stage. A head-mounted connector (Omnetics) provides mechanical and electrical coupling between the μ -LED device and the wireless head-stage. This system is presented in Figure 3.3.

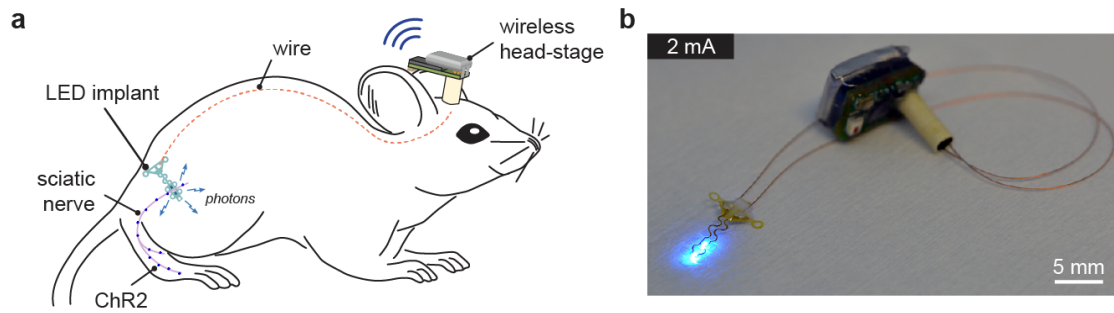


Figure 3.3 – Optoelectronic system for wireless optogenetic modulation in the mouse PNS

a, Epineural optogenetic stimulation of peripheral axons in the mouse PNS is carried out by a LED array implanted around the sciatic nerve and controlled via a wireless, battery-powered head-stage. **b**, Picture of the optoelectronic system during the μ -LED array activation.

3.2.1 μ -LED array microfabrication

The implant fabrication was initiated with the electrical circuit microfabrication, followed by the μ -LED integration. The microfabrication process flow is illustrated in Figure 3.4. A sacrificial layer of Ti/Al (20/200 nm) was deposited on a 4-inch silicon wafer by e-beam evaporation (EVA760, Alliance Concept). Then, a 3 μ m-thick layer of polyimide (PI2611, HD Microsystems GmbH) was spin-coated on the wafer and cured (2 hours at 300°C in a N₂ oven for hard bake). A layer of Ti/Au (20/300 nm) was sputtered on the polyimide substrate after O₂ plasma surface activation (AC450, Alliance Concept). The conductive film was patterned to the array interconnects by photolithography (Figure 3.4.c), Au wet etching and Ti Reactive Ion Etching (RIE) (201RL, Corial). Next, a second 3 μ m-thick layer of polyimide was spin-coated and cured to encapsulate the tracks. A 2nd photolithography and RIE of the 6 μ m-thick polyimide patterned the implant and defined the connection pads for future LED integration (Figure 3.4.f). To allow the adhesion of a PDMS layer, SiO₂ (25 nm) was sputtered on the gold and polyimide structures after plasma surface activation [159, 160]. Then, a 35 μ m-thick layer of PDMS (Sylgard 184, Dow Corning) was spin-coated with previous O₂ surface activation of the SiO₂. Following PDMS curing (2 hours at 80°C), a layer of Al (600 nm) was deposited to serve

Chapter 3. A wireless optoelectronic system for optogenetic control of the peripheral nervous system

as an etch mask. Finally, a 3rd photolithography and RIE patterned the PDMS to the implant external shape and revealed the μ -LED integration sites [161] (Figure 3.4.i). After optical and electrical inspections, the μ -LED array fabrication pursued with the LED integration.

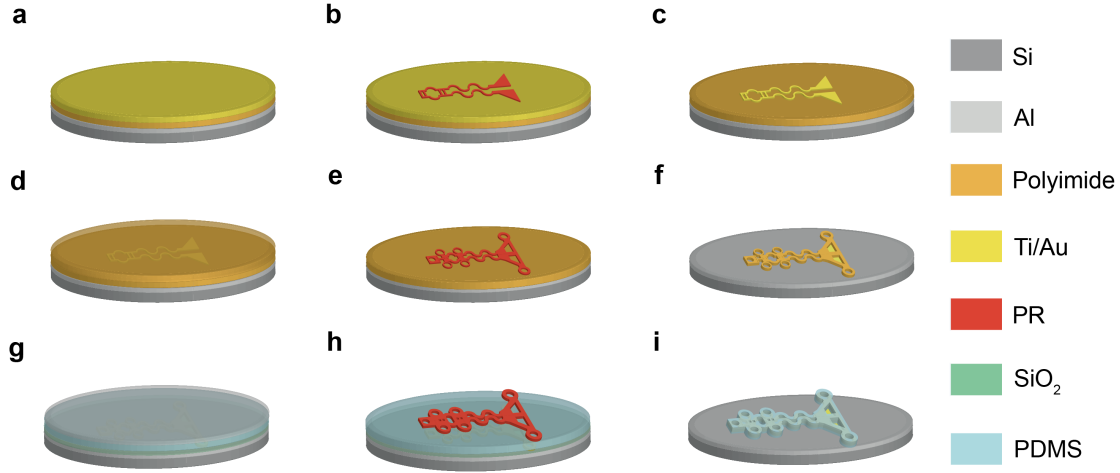


Figure 3.4 – Peripheral μ -LED implant microfabrication

a - c, Ti/Au photolithography and etching (wet & RIE) reveals the implant interconnects. **d**, Circuit encapsulation via polyimide superstrate spin-coating and curing. **e, f**, Polyimide etching through photolithography and reactive ion etching. **g**, PDMS is spin-coated after O₂ plasma activation of SiO₂. **h, i**, PDMS is patterned through photolithography and reactive ion etching to the implant shape.

3.2.2 Integration of μ -LEDs on a flexible substrate

Following microfabrication, the μ -LED bare dies were integrated to the electrical circuit. The integration process is presented in Figure 3.5. First, small (240 x 320 x 140 μm^3) μ -LEDs (DA2432, Cree Inc.) were detached from their carrier and aligned on a glass slide with their connection pads facing down. In parallel, Sn/Bi/Ag solder paste (SMDLTLP10T5, Chipquik) bumps ($\varnothing \sim 50 \mu\text{m}$) were spread to the circuit connection pads (Figure 3.5.f). Then, the μ -LEDs were deposited onto the solder paste using a state-of-the-art pick-and-place equipment (JFP Microtechnic). The solder paste reflow (melting point at 138°C) ensures the die mechanical and electrical connections. After the μ -LED integration, a 14% by weight ratio solution of polyisobutylene (PIB, Oppanol, BASF) in cyclohexane (Sigma-Aldrich) was drop-casted using a semi-dispensing tool (KDG 1000, Abatech) on the μ -LED surface (Figure 3.5.c). After solvent evaporation (3 minutes at 60°C), the PIB was allowed to flow homogeneously around the μ -LED (overnight at RT). PIB is a transparent polymer that has a unique property of low permeation rate, preventing the electrical circuit from moisture penetration [162]. Next, the μ -LEDs were encapsulated with a drop of PDMS (Sylgard 184, Dow Corning) after O₂ plasma surface activation (Figure 3.5.g). The array interconnects were soldered to copper wires (CZ 1103, Cooner wires) and the connector was sealed with silicone (734, Dow Corning). Finally, the μ -LED array was released from the wafer (Figure 3.5.d) by anodic dissolution of the Al layer (2 V bias in saturated NaCl solution [163]).

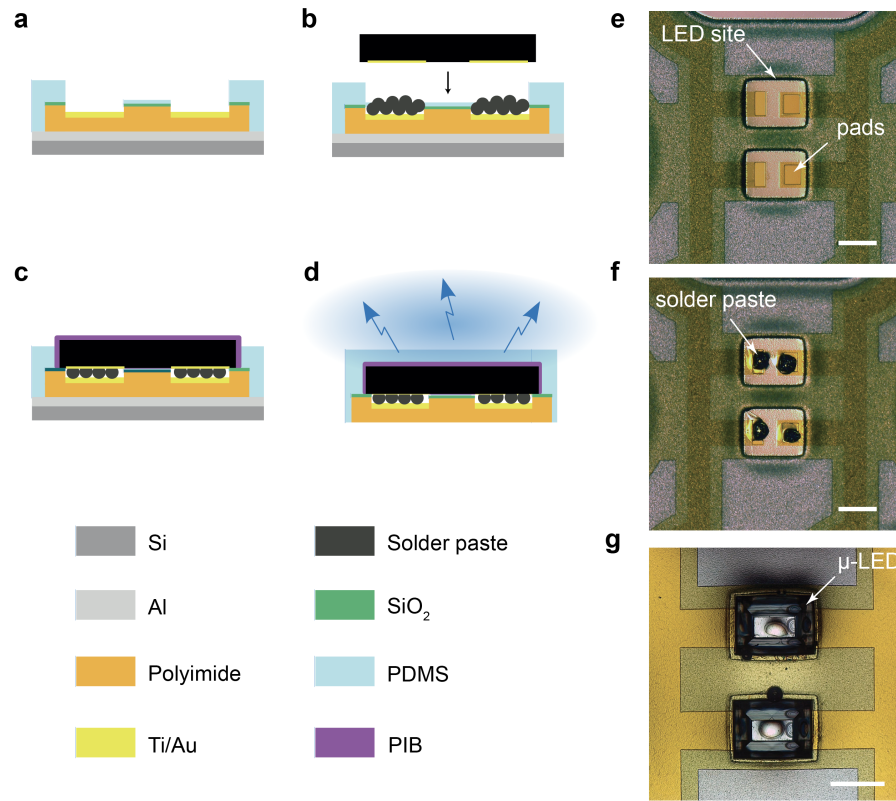


Figure 3.5 – μ -LED integration on a flexible substrate

a, PDMS etching reveals the sites for μ -LED integration. **b**, Solder paste is carefully spread to the connection pads on the array interconnects (5-10 particles). The μ -LED bare die is flipped and accurately deposited onto the LED site with a pick-and-place equipment. **c**, A drop of 15% wt PIB in cyclohexane is dispensed at the surface of the LED. **d**, The μ -LED is finally encapsulated with a thin layer of PDMS after O_2 plasma activation. The device is then detached from the wafer via anodic release. **e - f**, Optical images illustrating the μ -LED integration process flow. Scale bars, 200 μ m.

3.2.3 Characterisation of the μ -LED array

General and opto-electrical characteristics

The implantable μ -LED array is presented in Figure 3.6. The array integrated 4 μ -LEDs distributed on 2 separate panels. The array was designed to be implanted transversally, with the mouse sciatic nerve laid between the 2 LED panels. The substrate flexibility allowed for the disposition of the μ -LEDs circumneural to the nerve, enabling homogeneous epineural light delivery. The optical emitting area was separated from the connector via wavy interconnects that elongate to accommodate the nerve natural motion. The stretchability dwelled in these meanders, whereas plain polyimide substrate serves as a strain relief island to the μ -LEDs. The polyimide substrate also strengthened the anchoring sites and the connector that maintained the implant in a secured position. Interfacing with the nerve was softened by the addition of a PDMS coating (Figure 3.6.b). This silicone layer served as a soft mechanical buffer, removing

Chapter 3. A wireless optoelectronic system for optogenetic control of the peripheral nervous system

polyimide sharp edges. Eventually, the μ -LED PDMS encapsulation has a strong adhesion to the PDMS coating. Furthermore, silicone PDMS is a suitable material for optoelectronic applications [164], due to its high transparency in the UV-visible spectra and its dielectric properties.

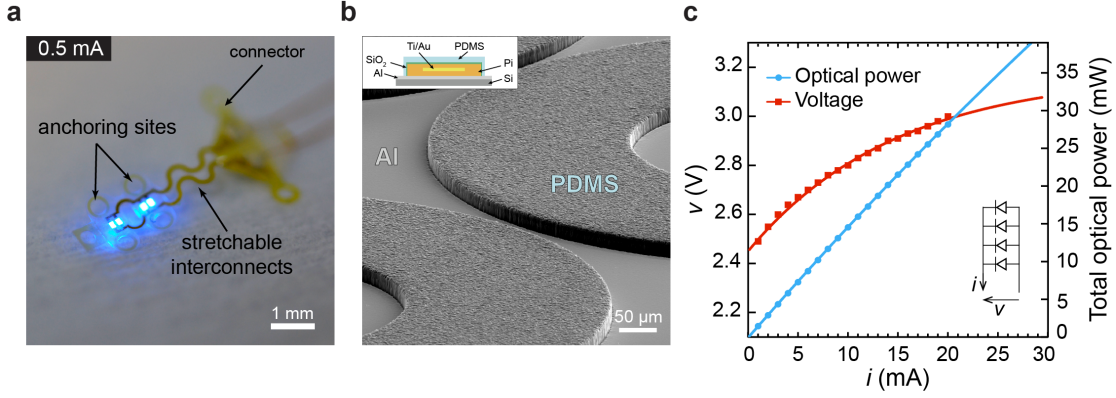


Figure 3.6 – μ -LED array for epineural optogenetic stimulation in the PNS

a, Picture of the optoelectronic implant. The device is composed of 4 μ -LEDs integrated on a flexible and stretchable circuit, complying to the mouse freely-behaving motion. The implant is designed to be circumneural to the mouse sciatic nerve. Anchoring sites secure the implant around the nerve. **b**, Scanning electron microscope image of the interconnects (tilted view, 60°). Silicone PDMS is patterned to the implant design. Top left inset shows a schematic cross-section of the interconnect. **c**, Implant optoelectronic characterisation, I-V-P. The voltage across the 4 μ -LEDs and the total optical power were measured for incrementing current.

We measured the opto-electrical properties of the μ -LED device while sweeping gradually the current applied to the 4 parallel μ -LEDs (Figure 3.6.c). The total optical power at 470 nm was measured with a large photodiode (S170C, Thorlabs) and a power meter console (PM100D, Thorlabs). As expected with LEDs, the array optical output has a linear relation with current i . The μ -LED array produced a high optical power for high constant current ($P(20 \text{ mA}) = 28.8 \text{ mW}$), enabling effective epineural optogenetic stimulation. Coherent with diodes, the voltage across the μ -LED array evolved logarithmically when the current increased. As we intended to integrate this μ -LED array to the battery-powered miniaturized system (i.e. limited compliance), we aimed at reducing the circuit resistance. Applying Kirchhoff's current law, we can estimate the array series wiring resistance R_s from Figure 3.6.c:

$$R_s = \frac{v - V_f}{4I_{LED}} = \frac{v - V_f}{I_f} \quad (3.1)$$

Given a minimum forward voltage $V_f = 2.8 \text{ V}$ at $I_f = 20 \text{ mA}$ (from LED supplier datasheet), we estimate $R_s \sim 10 \Omega$.

Mechanical properties

Under normal physiologic conditions, the sciatic nerve moves and stretches to comply with the hindlimb movements. In order to deliver light consistently, we engineered stretchability into the μ -LED array. The tracks that connect the μ -LEDs to the implant connector have a horse-shoe-like design. To reduce stress concentrations under tensile strain, these interconnects stretch and deflect out-of-plane, resulting in a relative elongation [165]. The geometry of these meanders determines the maximum elongation (cf. Appendix A.2.1).

To evaluate the μ -LED array functionality under tensile strains, a device was placed in a custom-built linear stretcher (Figure 3.7.a). An uniaxial stretch cycle to 40% strain was applied (strain rate of $1\%.\text{s}^{-1}$) while measuring the voltage for a continuous $i = 5$ mA (Keithley 2400 source meter). The results are presented in Figure 3.7.b. During the stretch cycle, the μ -LED array remained functional while the elongation minimally impacted the voltage. The device compliance to strains up to 40% facilitated the surgical procedure, e.g. the surgeon has to pull on the implant to place the light-emitting areas around the nerve.

In addition, the μ -LED implant needs to comply with the nerve motion over repetitive cycles. We measured intra-operatively a maximum strain applied to the implant $\sim 20\%$ when the hindlimb is fully extended. To evaluate the device robustness and reliability, we clamped the μ -LED array to a second custom-built linear stretcher and 100k stretch cycles to 20% strain were applied (1 cycle per second). The voltage was measured continuously, with $i = 5$ mA applied. The results are presented in Figure 3.7.c. The voltage remained relatively stable up to 100k cycles, demonstrating a relative functionality for *in vivo* applications.

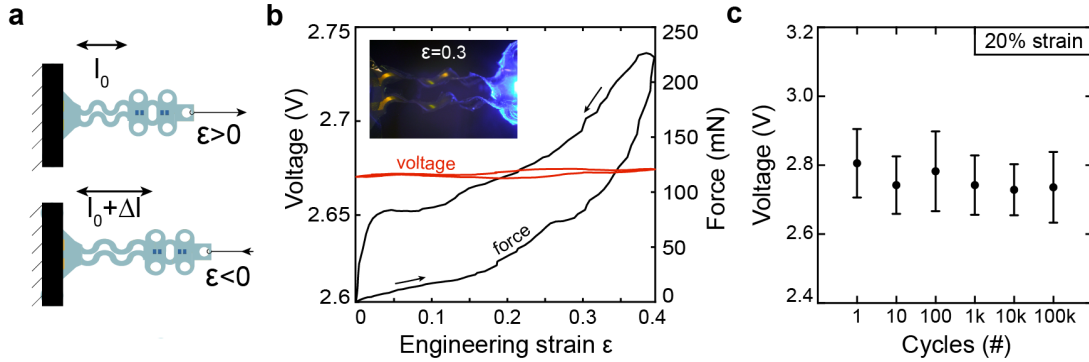


Figure 3.7 – A stretchable μ -LED array for the mouse PNS

a, Illustration of the experimental design to mechanically characterize the μ -LED array. The array connector is clamped on an uniaxial stretching machine. On the opposite side, a thread applies a controlled displacement to the array. The following stretching experiments were conducted with $i = 5$ mA applied continuously. **b**, The voltage and the force applied to the implant during an uniaxial stretch cycle to 40% strain. The voltage remains stable during the elongation. Top left inset displays a picture of the array interconnects stretched to 30% strain. **c**, Changes in voltage for a uniaxial fatigue cycling to 20% strain ($n = 5$ arrays, mean \pm s.d.).

Chapter 3. A wireless optoelectronic system for optogenetic control of the peripheral nervous system

Encapsulation safety

Following implantation, neural implants must not harm the body and remain functional over a certain life-time [166]. The implant encapsulation should protect the implant electronics from moisture and ions. In the case of the μ -LED array, the active electronics was encapsulated with PIB and PDMS. The former is known for its extremely low gas permeability and it is used commonly as a sealant in various applications [167, 168]. The water-vapor permeability of PIB is several folds lower compared to PDMS ($P = 110 \text{ cm}^3 \cdot \text{cm}^{-2} \cdot \text{s}^{-1} \cdot \text{cm-Hg}^{-1}$ for butyl rubber [169], against $P = 40000$ for PDMS [170]).

In order to evaluate the μ -LED implant functionality over time, we conducted accelerated ageing tests. The μ -LED devices were immersed in saline and placed at 67°C . We measured regularly the voltage of the μ -LED arrays for a current applied ($i = 5 \text{ mA}$). Measurements were made at RT and the results are presented on Figure 3.8.b. We found that the μ -LED arrays encapsulated with only PDMS were no longer functional after 6-7 ageing days. In comparison, devices encapsulated with PIB and PDMS remained stable and functional for a longer time. These devices started failing after 130 ageing days (not shown). Further accelerated ageing experiments would enable to extrapolate the device functionality at 37°C based on the Arrhenius equation:

$$Age_{37} = Age_{67} Y^{\left(\frac{\Delta T}{10}\right)} \quad (3.2)$$

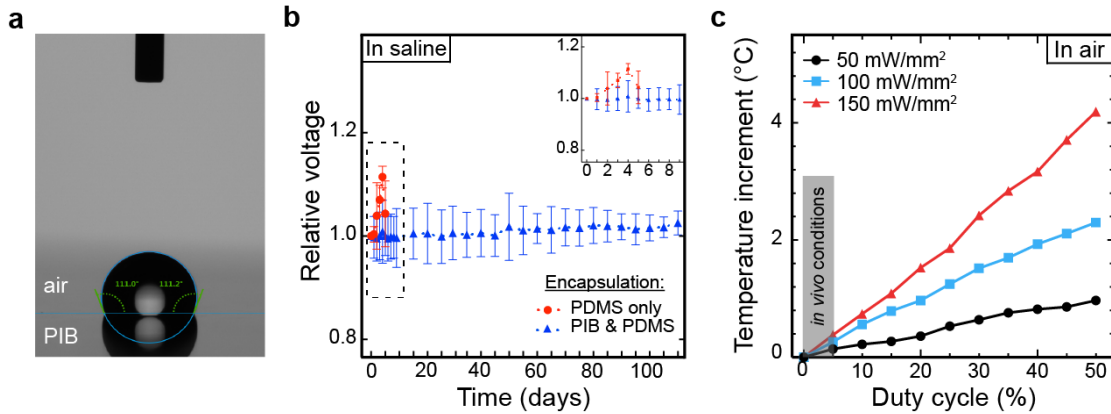


Figure 3.8 – μ -LED encapsulation enables long-term, safe experimentation

a, contact angle measurement on a PIB surface with deionized water. Measurement was made with the Wilhelmy balance method and sessile drop at room temperature. The surface was measured to be highly hydrophobic ($\alpha = 111.1^\circ$). **b**, Accelerated ageing of μ -LED arrays in saline solution at 67°C depending on the encapsulation materials used. The combination of PIB and PDMS for encapsulation reveals the arrays are suitable for long-term experiments. There was no implant with a PDMS encapsulation only functioning after day 7 ($n = 3$ per group, mean \pm s.d.). **c**, Changes in temperature at the surface of an operating array depending on the optical irradiance and the μ -LED duty cycle. Temperature was measured in air with an infrared camera. The grey rectangle shows the stimulation parameter range for the future *in vivo* experiments.

The encapsulation also needs to protect biological tissues from the heating generated by the μ -LED activation. Temperature changes at the surface of the μ -LED array were measured using an infrared camera (A325sc, FLIR). These measurements were made for various duty cycles ($DC = \frac{\text{pulse width}}{\text{period duration}}$) and irradiances (150 mW.mm⁻² corresponds to 46 mW total optical power). The results are presented in Figure 3.8.c. Consistent with LED activation, we measured higher temperature for larger DC and bigger irradiances. A 1°C temperature increment in neural tissues has been reported to generate changes in neuronal activity [171]. Our experimental needs required a low DC and are therefore not hindered by the heat generated.

Light emission spectra

The expansion of optogenetics drove the development of opsins with absorption spectra shifted from the blue (for a detailed list, see [64]). To broaden the use of the μ -LED array, we tailored its light emission spectrum by introducing a phosphor-polymer matrix in the μ -LED encapsulation (Figure 3.9.a). This matrix was a blend of phosphor particles and silicone. The composite was prepared by mixing phosphors (PhosphorTech) with PDMS (Sylgard 184, Dow Corning) at 50% weight ratio. The two components were stirred thoroughly until the mixture became a paste. Drops of the phosphor-PDMS mixture were precisely dispensed (KDG 1000, Abatech) at the surface of the μ -LED. After curing (overnight at 60°C), the μ -LED array was finally encapsulated with PDMS. The phosphor-PDMS drop-casting usually increased the thickness by 30-40 μ m. We measured the emission spectra of the μ -LED arrays with a spectrometer (CCS200/M, Thorlabs). The normalized spectral flux emitted is represented in Figure 3.9.c and quantified in Table 3.1. The blue and green μ -LEDs had narrow emission spectra with peak wavelengths respectively around 470 and 535 nm. The down-conversion of blue light with the phosphor-based encapsulation produced larger emission spectra around their peak wavelengths. The light conversion was almost total with only a fraction of light emitted at 470 nm, except for the yellow-emitting phosphor (570 nm). The full widths at half maximum (FWHM) were then larger for the yellow-emitting and far-red-emitting phosphors. Conversely, the down-conversion with orange and red-emitting phosphors resulted in smaller FWHM. The color conversion can also be observed in the CIE color space diagram (Figure 3.9.d). In comparison, the color conversion from blue to orange or red was more efficient.

Table 3.1 – Emission spectra of the peripheral μ -LED array

Type	Peak wavelength (nm)	FWHM (nm)	Purity (%)
Blue μ -LED	469.33	31.85	98.64
Green μ -LED	537.21	34.86	90.32
Yellow-emitting phosphor	569.81	83.70	63.12
Orange-emitting phosphor	599.70	66.30	91.28
Red-emitting phosphor	622.36	63.21	97.98
Far-red-emitting phosphor	646.89	78.29	59.41

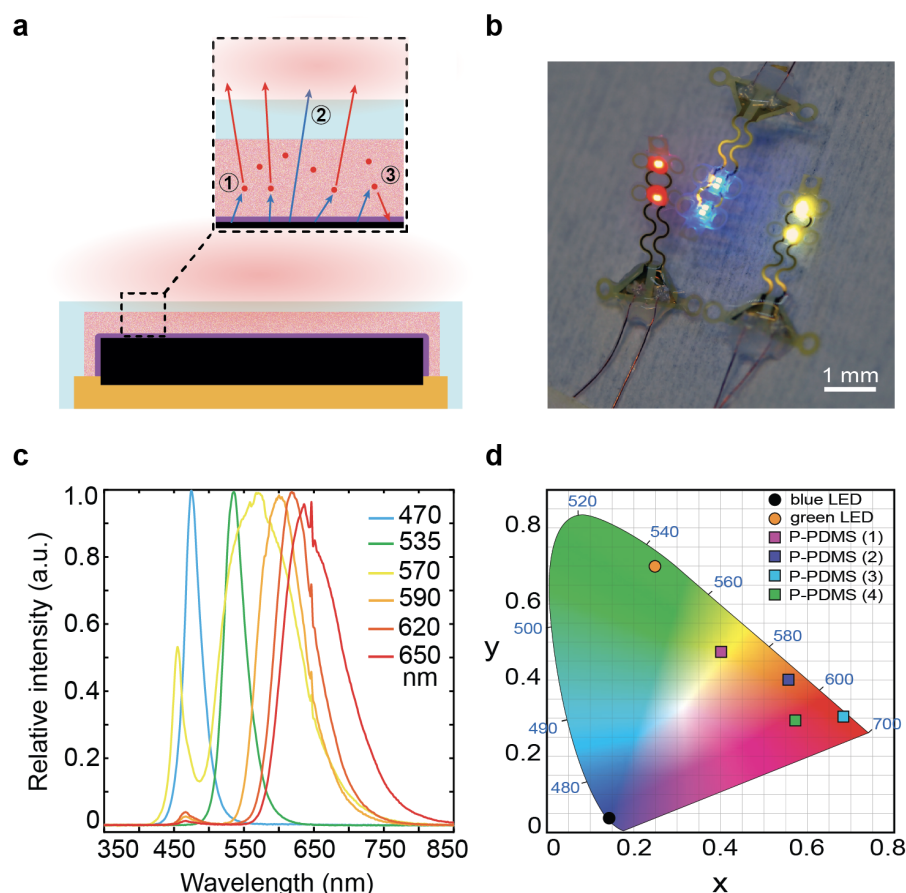


Figure 3.9 – Phosphor-based light conversion enables broad optogenetic experiments

a, Illustration of phosphor-based light conversion with a blue LED and red phosphor materials. Blue photons are converted to red photons (1), directly transmitted through the encapsulation (2) or scattered back to the LED surface (3). Adapted from [172]. **b**, Picture of μ -LED arrays with red and yellow phosphor-based light conversion. **c**, Emission spectra of μ -LED arrays ($i = 5$ mA) with phosphor-based light conversion of 470 nm light or with different μ -LED (535 nm). Phosphor emission peaks are specified. **d**, Color conversion represented on the CIE 1931 color space diagram. Circles represent the blue (473 nm) and green (535 nm) LEDs. Squares represent luminescence spectra from blue LEDs covered with phosphor-PDMS composites (50% wt). The phosphor emission peaks were 570 nm (1), 590 nm (2), 620 nm (3) and 650 nm (4).

3.2.4 μ -LED array bio-integration

The soft μ -LED array was designed for implantation on the mouse sciatic nerve. The surgical procedure is illustrated in Appendix A.2.2. In order to investigate the implant biocompatibility, we conducted histology and behavioural experiments at various time points. Histological cross-sections of the nerve at the implant site did not show signs of injury, demyelination or abnormal immune cell infiltration, 1 month after implantation, as shown in Figure 3.10 (immunohistological methods described in Appendix A.2.3).

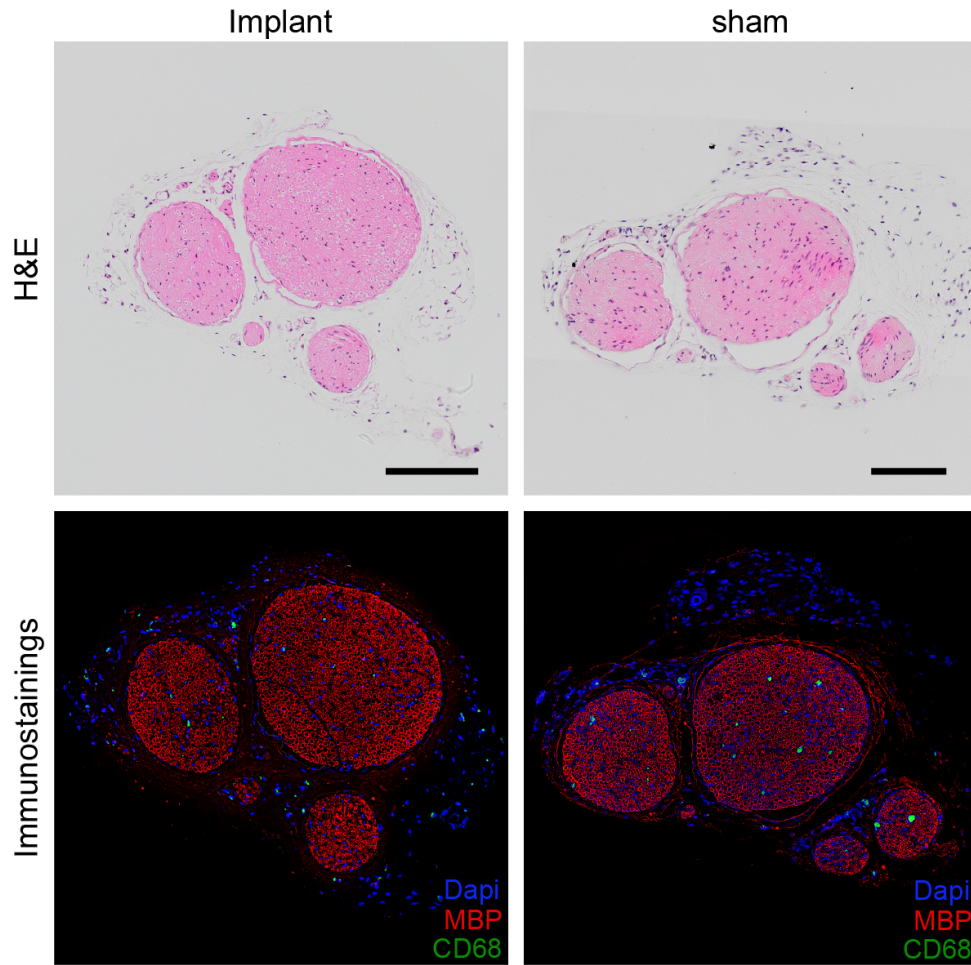


Figure 3.10 – Histology following μ -LED array implantation

Sciatic nerve cross-sections at the μ -LED implant site for an implanted mouse and a sham-operated mouse, 1 month after surgery. H&E (top row) stainings show intact nerve structure in both groups. Immunostainings (bottom row) do not reveal variations in myelination or immune cell activation. Scale bars, 200 μ m.

Coherent with the histological results, sensory and motor behavioural assessments did not reveal any change after implantation (Figure 3.11). Von Frey and Hargreaves tests did not show significant changes in the mechanical and thermal pain thresholds prior implantation (baseline) and as early as 3 days post-surgery (Figure 3.11.b,c). The sensorimotor coordination was evaluated with the accelerating rotarod test (Figure 3.11.d). Similar with the pain assays, the animals did not exhibit loss in coordination following the μ -LED implantation. Exploratory activity and voluntarily wheel running were tested 6 days post-implantation (Figure 3.11.e-f). There was no significant differences between the implant and sham groups. Behavioural experiment methods are described in Appendix A.2.4.

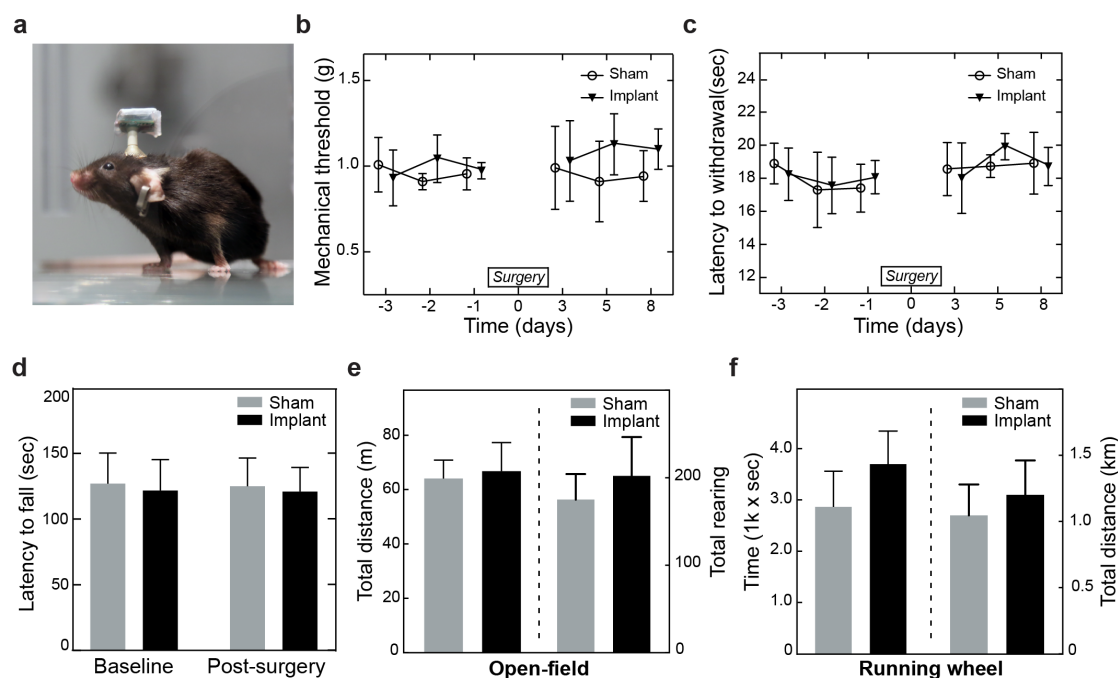


Figure 3.11 – Mouse behaviour following the μ -LED array implantation

a, Picture of an implanted mouse carrying the wireless head-stage. **b, c**, von Frey (**b**) and Hargreaves (**c**) tests did not reveal significant changes in pain thresholds following implantation compared to sham-operated mouse ($n = 6$ per group, mean \pm s.d.). The surgery took place on day 0. The latency to fall of mice prior to the μ -LED array implantation or a sham surgery and 7 days post-surgery ($n = 6$ per group, 3 trials per condition, mean \pm s.d.). **d**, The latency to fall of mice on the rotarod prior to the μ -LED array implantation or a sham surgery and 7 days post-surgery ($n = 6$ per group, 3 trials per condition, mean \pm s.d.). **e, f**, No significant changes in the mouse behaviour was observed with the open-field test (**e**) and the running-wheel test (**f**). ($n = 6$ per group, mean \pm s.d.).

3.3 Remote optogenetic stimulation of peripheral pain pathways

We have developed a soft μ -LED implant to deliver epineural optogenetic stimulations to the mouse sciatic nerve. The μ -LED implant, with the ultra-miniaturized wireless head-stage, enables untethered, freely-behaving optogenetic interrogation of the PNS. Through our collaboration with Woolf's group at Harvard Medical School, we demonstrated the wireless system functionality *in vivo* with the optogenetic activation of Chr2 expressed in TRPV1⁺ neurons (see Figure 3.13). The system allowed for single-pulse and repeated stimulation of these pain-specific primary afferent neurons, resulting in strong nocifensive behaviors and real-time place aversion. We investigated then the recruitment of immune cells via specific nociceptor stimulation.

3.3.1 Targeted expression of ChR2 in TRPV1⁺ neurons

Nociception of potentially damaging stimuli relies on specialized primary afferent neurons, known as nociceptors. The transient receptor potential channel vanilloid 1 (TRPV1) is a cation channel that responds to heat, capsaicin (the pungent component in chili peppers) and irritant chemicals. TRPV1 is an essential ion channel for heat transduction, pain sensitization and inflammatory pain [173, 174]. To deliver optogenetic stimulation to the TRPV1⁺ neurons, we used a transgenic cre-recombinase approach to specifically expressed ChR2 in TRPV1⁺ neurons. Engineering of *TRPV1::ChR2* mice is described in Appendix A.2.5. Histological analysis of the transgenic mouse DRG revealed ChR2-tdTomato was predominantly expressed in small diameter, unmyelinated neurons (Figure 3.12.a). ChR2-tdTomato expression overlays at $16 \pm 3\%$ with NF200⁺ (i.e. myelinated) neurons [13]. There was no expression of ChR2-tdTomato found in the littermate control mice. Expression of ChR2-tdTomato is carried along the nerve fibers (Figure 3.12.b) and validate an epineural light-delivery strategy.

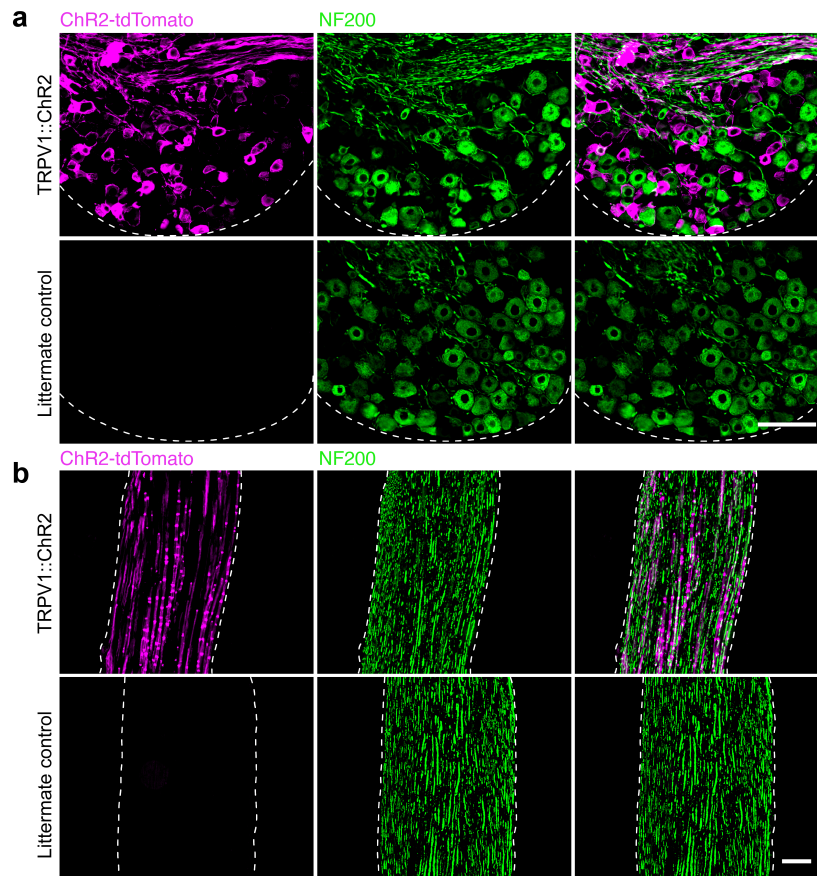


Figure 3.12 – Expression of ChR2 in *TRPV1::ChR2* mice

Expression of ChR2-tdTomato in *TRPV1::ChR2* mice was found in nociceptors located in the DRG (a) and in the sciatic nerve (b). The fluorescence is overlayed with NF200 immunostaining. The dashed lines circumscribe the DRG cross-sections or the sciatic nerve longitudinal sections. Scale bars, 100 μm .

3.3.2 Single-pulse optogenetic activation of nociceptors

To determine the wireless optoelectronic system utility in the study of peripheral pathways, we implanted the μ -LED array in *TRPV1::ChR2* and littermate control (Cre-negative) mice. One week after implantation, we tested whether the optogenetic stimulation of *TRPV1*⁺ neurons would produce nocifensive behaviors. We recorded the evoked responses in awake, freely behaving mice by combining single-pulse epineural stimulation with millisecond (500 Hz) sampling behavior (Figure 3.14).

In *TRPV1::ChR2* mice, a short (3 ms) wireless activation of the μ -LED array produced a paw elevation or hindlimb withdrawal in most trials (Figure 3.14.a). This response is a characteristic nocifensive behavior and has been previously reported with transdermal stimulation of nociceptors through the glabrous skin [13, 88, 89]. Probability of behavioural response to epineural stimulation was higher with longer pulses and reached 100% for pulses longer than 10 ms (Figure 3.14.b). The high-sampling rate allowed us to study the response dynamics (Figure 3.14.c-d).

The delay for the evoked responses was stable for pulses > 3 ms (mean 43.4 ± 3.2 ms) and was coherent with the optogenetic activation of A δ fibers [13]. On the other hand, very short (2 ms) stimulation pulses had a low probability for evoking a behavioural response. This result reflects ChR2 low photocurrents for very short pulse duration, preventing *TRPV1*⁺ neurons from action potential generation [175]. The delay for the 2 ms evoked responses was significantly longer and is more likely to be explained by the conduction velocity of slow, unmyelinated C fibers. The latter constitutes the majority (~ 84%) of the *TRPV1*⁺ neurons and are therefore more likely to be activated with near-subthreshold stimulation. The absence of response in the littermate control mice demonstrated the stimulation was optogenetic-specific and was not caused by an optical or electrical artefact.

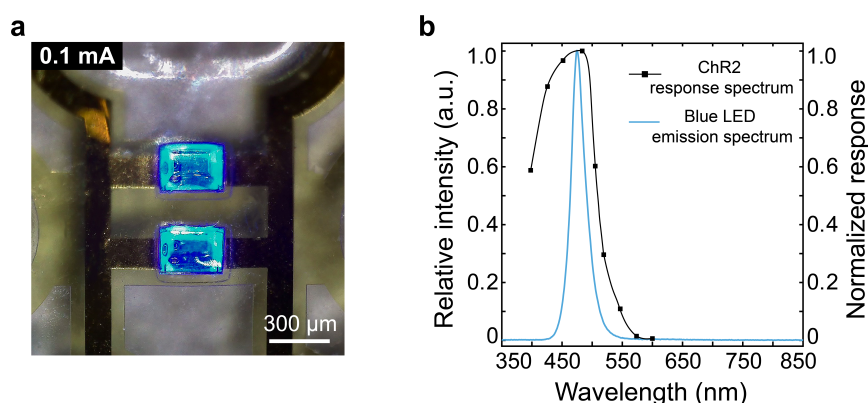


Figure 3.13 – Channelrhodopsin-specific μ -LED implant

a, Microscopic picture of 2 activated μ -LEDs. **b**, μ -LED emission spectrum fits into the ChR2 response spectrum enabling ChR2 activation. ChR2 response spectrum was adapted from [176].

3.3. Remote optogenetic stimulation of peripheral pain pathways

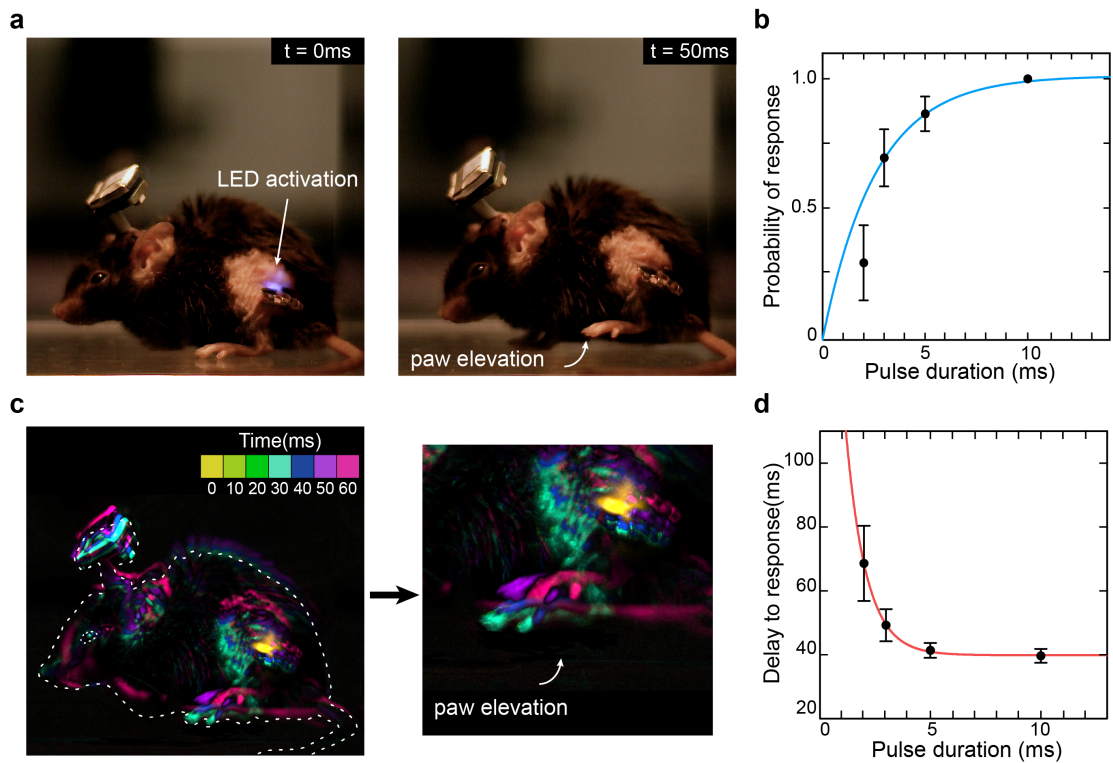


Figure 3.14 – Remote, single-pulse, epineural activation of TRPV1⁺ neurons results in fast protective behaviour

a, Behaviour elicited by a 3 ms light pulse to the *TRPV1::ChR2* mouse sciatic nerve monitored using a camera recording at 500 frames per second. μ -LED implant activation can be observed transcutaneously. The stimulation resulted in a paw elevation response. **b**, The probability of behavioural response depends on the pulse width (10 - 15 trials per condition, mean \pm s.e.m.). **c**, Motion detected by comparing the pixel difference between frames. Each color represents the position of the animal at a point in time. The first motion was detected 30 ms after stimulation. The panel on the right shows a closer view on the hindpaw. **d**, The delay to the single-pulse stimulation has a low dependency on the pulse width for pulses > 3 ms (mean \pm s.e.m.).

3.3.3 Conditioned place aversion

To demonstrate the reliability of the optoelectronic system, we tested the mice with a real-time place aversion task. Previous studies have demonstrated *in vivo* that specific activation of primary afferents with transdermal [88, 90] or epidural [101, 177] illumination induces place aversion in mice. To test this paradigm with epineural stimulation, mice were first allowed to explore freely an open-field. If the mouse entered the stimulation-paired area, it did not result in the μ -LED implant activation ("Stim Off"). During the 2nd acquisition, if the mouse entered the stimulation-paired area, it resulted in the remote activation of the μ -LED implant at 0.5 Hz ("Stim On"). Epineural optical stimulations in *TRPV1::ChR2* mice caused consistent increased nocifensive behaviors and real-time place aversion as measured by the time in stimulation-paired side - time in non-stimulation-paired side (Figure 3.15.b) and % of time in

Chapter 3. A wireless optoelectronic system for optogenetic control of the peripheral nervous system

stimulation-paired side (Figure 3.15.d). As expected, photostimulation in littermate control (Cre-negative) mice did not result in a significant change of behavior (Figure 3.15.c). The protocol for this conditioned place aversion test is described in Appendix A.2.7.

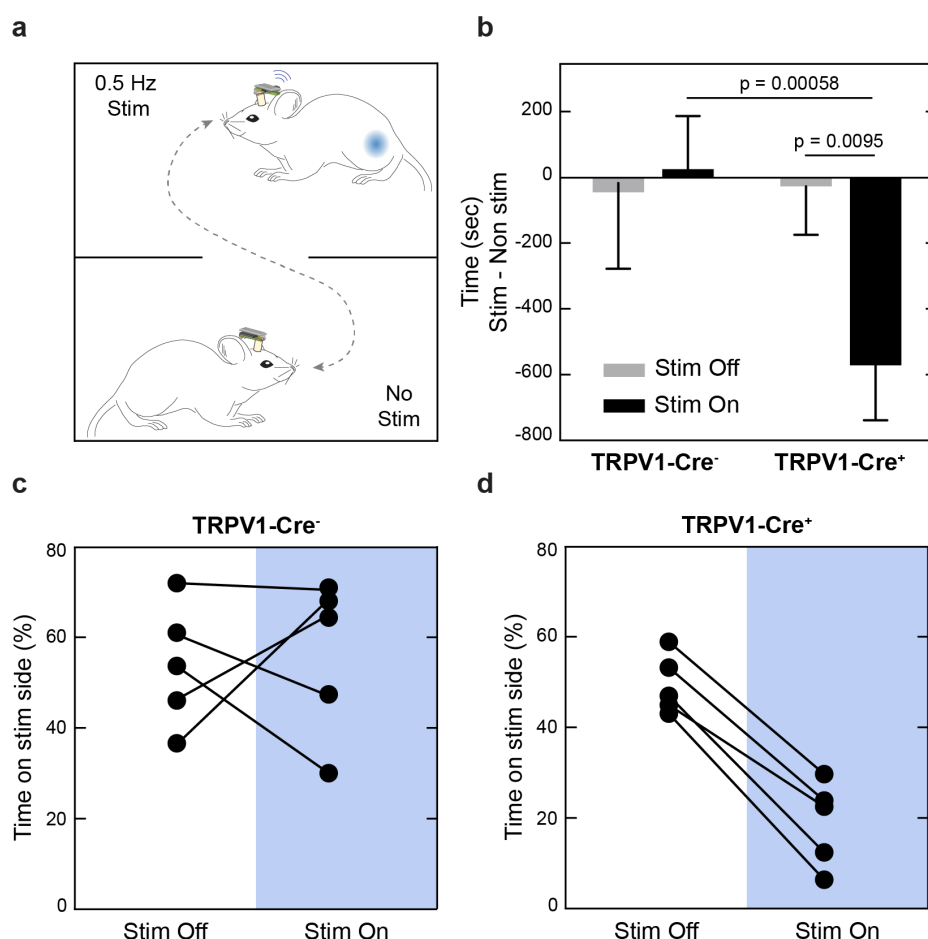


Figure 3.15 – Place aversion following remote, optogenetic stimulation of peripheral TRPV1⁺ neurons

a, Cartoon representing the experimental setup. The mice were allowed to explore freely the 2 chambers. The mice received a 0.5 Hz epineural photostimulation when entering the "0.5 Hz Stim" area. **b - d**, Baseline recordings ("Stim Off", no stimulation in both chambers) were compared with recordings where one chamber resulted on a 0.5 Hz stimulation ("Stim On"). Optogenetic stimulation in TRPV1-Cre mice expressing ChR2 decreases significantly the time spent in the stimulation area compared to mice not expressing ChR2 ($n = 5$, mean \pm s.d.; unpaired t-test), and compared with the absence of stimulation (**c, d**).

3.3.4 Study of the neuroimmune interaction

The nervous and immune systems are tightly integrated in order to protect the organism from danger, such as noxious stimuli or pathogen invasion. For example, when activated, nociceptors release peptides (e.g. substance P, CGRP) in their peripheral terminals to increase vasodilatation and capillary permeability. As a result, it promotes activation and recruitment of immune cells, and can lead to neurogenic inflammation [178]. On the other hand, upon pathogen invasion, immune cells can produce mediators (e.g. cytokine, chemokine) acting on sensory neurons and heightening nociceptor sensitivity. However, neuroimmune interactions may also contribute to hypersensitivity and chronic inflammatory pain [179], suggesting that treatments should target both systems [180].

We hypothesized that specific activation of nociceptors in a healthy animal can trigger a neurogenic inflammation. This hypothesis was relayed by visual observations of swollen hind-paws (neurogenic inflammation marker) after single-pulse stimulations in awake animals. To study this neuroimmune interaction, we implanted the soft μ -LED array in *TRPV1::ChR2* mice. Under anaesthesia, mice received epineural optical stimulations to the sciatic nerve. Later, the paw skin was removed and processed for lymphocyte infiltration by flow cytometry (methods described in Appendix A.2.8). The quantified immune cell populations following optical stimulation are presented in Figure 3.16. These results are showing a trend (i.e. non-significant) for increased immune cell activation in the ipsilateral paw skin following optogenetic stimulation in *TRPV1::ChR2* mice. This immune cell recruitment was in average higher in the ipsilateral side compare to its contralateral side in *TRPV1::ChR2* mice. As this induction of immune cells may reflect potential damages induced by the μ -LED array implantation or by the optical stimulation, we used the same stimulation protocol with littermate control mice (*TRPV1-Cre*(+/-)::*ChR2*(-/-)). Again, we did not observe a significant difference in the activated immune cells for both populations (ipsilateral vs contralateral). These results denoted the relative safety of the μ -LED array implantation and the stimulation protocol. Eventually, we can compare these results with the quantified immune cells in non-implanted (i.e. non-stimulated) mice (negative control). This group presented as well a variability among its immune cell population recruitment.

All together, as a proof-of-concept, these results suggested increased neuroimmune interactions with the optogenetic stimulation of *TRPV1*⁺ neurons. The optogenetic activation in this experiment was hindered by the anesthetic used during the stimulation, as groups reported on the sensitization of *TRPV1* channels with isoflurane [181, 182]. Furthermore, these results may also reflect a low reproducibility with the tissue preparation protocol (e.g. variance in the negative control group). Ongoing experiments are investigating this neuroimmune interaction.

Chapter 3. A wireless optoelectronic system for optogenetic control of the peripheral nervous system

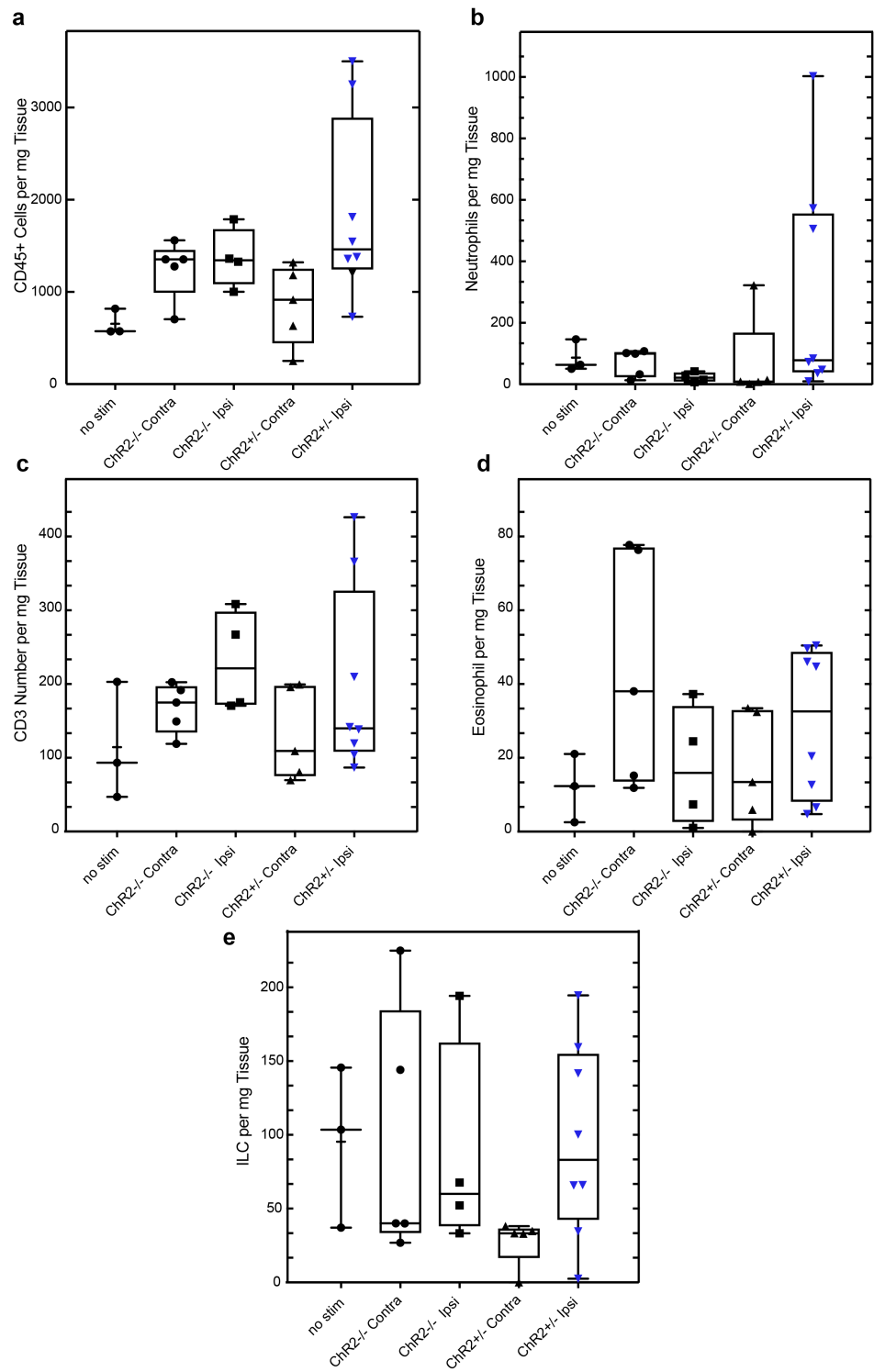


Figure 3.16 – Recruitment of activated immune cells driven by nociceptor activity

Box plot of immune cell populations (T cells (a - c), neutrophils (b), eosinophils (d) and innate lymphoid cells (e)) in sciatic nerve innervated paw skin assessed 6 hours following epineural optogenetic stimulation.

3.4 Discussion

We reported on an optoelectronic system that enables remote optogenetic stimulation of the PNS in freely-behaving mice. This system is powered by an ultra-miniaturized head-stage that provides controlled and consistent μ -LED activation *in vivo* without interfering with the normal animal behaviour. The soft implant encircles the sciatic nerve, positioning μ -LEDs at the surface of the neural tissue to allow effective optogenetic stimulation. The long-term implantation of the μ -LED array did not provoke a foreign body reaction as demonstrated by histology and behavioural experiments. Using this system, the specific activation of TRPV1⁺ neurons produced characteristic nocifensive behaviors and dramatic place aversion.

The system's wireless capability provided minimal interruption in the mouse natural behaviors, allowing for unaltered optical interrogation of the peripheral pathways. Tethered optogenetic systems can create stress and discomfort in the animals, hampering fine neural modulation readout [183–185]. These wired systems may also limit compatibility with traditional behavioral experimental setups such as mazes, rotarods or swim chambers. In comparison, the lightweight wireless system tolerates simultaneous and prolonged control over multiple mice in complex environments. Furthermore, the battery-powered approach and the current check functionality enable consistent optical stimulation, promoting highly reproducible experimentation. Further work may be dedicated to the implementation of electrophysiological recording capabilities in the wireless head-stage. This would be a first step towards the development of an optogenetic peripheral closed-loop system. For example, precise recording and detection of neural firing in the nociceptors could in real-time trigger optical stimulations for silencing these neurons. This concept may alleviate ectopic activation of nociceptors that is often occurring with neuropathic pain [16].

Long-term optical coupling with peripheral nerves is particularly challenging due to the anatomy of these soft biological tissues. We implemented optical interfacing with the nerve through miniaturization and reduced mechanical mismatch of the device to the tissue. The implant compliance allows its structure to seamlessly follow the normal nerve motion, while maintaining its optical stimulation precision. Although non-invasive transdermal illumination has proven useful for the modulation of sensory afferents [13, 88, 90], interfacing the whole nerve offers a larger range of opportunities. An epineural light-delivery strategy enables deep and accurate control over the end-organ innervated by the light-sensitive nerve fibers. Broader access to the nerve structures promotes fine optogenetic deciphering, especially if the optical modulation has to be paired to external stimuli (e.g. mechanical, thermal or chemical). Coupling downstream optogenetic modulation with various sensory inputs may be key for the inhibition of on-going pain [185, 186]. Furthermore, the μ -LED array can be tailored for interfacing with smaller nerves in the PNS. This epineural optical strategy would enable the neuromodulation of neural structures that can not be reached with transdermal illumination. For instance, the μ -LED array can be optimized for the delivery of optical stimulation in the vagus nerve.

Chapter 3. A wireless optoelectronic system for optogenetic control of the peripheral nervous system

We demonstrated color down-conversion of the μ -LED emitted light with the integration of a phosphor-loaded encapsulation. Tailoring the optoelectronic device wavelength allows to activate an array of opsins, thereby extending the range of potential applications. This includes neural stimulation with finer temporal control (e.g. ChrimsonR, ReaChR) or deeper light penetration (e.g. VChR1) [62, 187, 188] and neural inhibition (e.g. Jaws, Arch, NpHr) [61, 67]. Further optimization in the μ -LED array would allow for the simultaneous activation of spectrally-distinct opsins [127]. Implemented to a pain alleviation application, optical stimulations targeting spectrally-distinct neural subsets may enable to silence specific modality of pain (e.g. thermal, mechanical) or to localized spatially the effect of this neuromodulation.

Optogenetics is designed for temporally precise (millisecond-timescale) control of neuronal activity using light [57]. In our study, we combined high spatiotemporal stimulation resolution and same order of magnitude behavioural recording resolution. Epineural single-shot activation of TRPV1⁺ neurons resulted in fast protective behaviours, with kinematics similar to those observed with their transdermal activation [13]. These results suggest that the global-evoked response to optogenetic nociceptor stimulation does not differ with the locus of stimulation. Furthermore, the types of response (e.g. paw elevation, paw withdrawal) were similar to those observed with common experimental stimuli (e.g. von Frey, Hargreaves), implying that epineural optical stimulation in these neurons mimicked their naturalistic activation. Fine optogenetic modulation in the PNS using a wireless system enables accurate and realistic elucidation of the primary afferent subpopulations. For example, the cellular mechanisms underlying the development of neuropathic pain may be investigated through activation of genetically-selected sensory afferents [16]. Similar selective control of activity may also contribute to a better understanding of abnormal nociception coding that results in highly debilitating chronic pain [189, 190]. For instance, we could transcribe afferent neural activity recorded in a chronic pain model into a selective optogenetic stimulation of distinct afferent subsets. Parsing methodically the PNS in this fashion may enable to track down the specific role of each subset in the establishment of pain hypersensitivity. Finally, specific activation of sensory neurons *in vivo* provides a unique tool to study their efferent components. This was highlighted by the study of neuroimmune interactions. Our results infer the development of neurogenic inflammation via repeated nociceptor activation. Further work may investigate if prolonged activation induces a similar chronic immune response as the one observed in an inflammatory pain model. This would mean activity in nociceptors is sufficient to trigger complex maladaptive immune reactions, falsely protecting the organism from a virtual danger.

3.5 Conclusion

In this chapter, we presented a unique wireless optoelectronic system suitable for optical stimulation in awake, freely behaving animals. Parallel developments of a state-of-the-art ultra-miniaturized head-stage and of a soft μ -LED-based implant, were combined to allow untethered optogenetic interrogation of the PNS. We demonstrated *in vivo* consistent activation of genetically-targeted primary afferents, both with single-shot and pulsed stimulations.

Although we aimed for a long-term coupling with the sciatic nerve, only a few modifications would be necessary to interface with deeper nerve structures, such as the vagus nerve or the visceral nerves. Our approach is also versatile, as further optimization would allow probing of higher hierarchy in the nervous system, such as the spinal cord (presented in Chapter 5). Eventually, optogenetics can be applied to explore other peripheral processes, beyond sensory and pain processing. Finally, this wireless optoelectronic system support the unravelling of the PNS, offering new experimental perspectives with potential therapeutic outcomes.

3.6 Contribution

Data presented in this chapter are the result of a team effort :

- I developed the soft μ -LED array interface and performed its characterisation. I designed the experimental plan for its validation *in vivo*, including the single-pulse and the place aversion experiments. I performed the implant surgical implantation and directed the behavioural experiments.
- Philipp Schönle, Noé Brun and Pascale Meier developed the ultra-miniaturized wireless head-stage.
- Rachel Moon and Benjamin Doyle provided assistance during the surgery, ran the behavioural experiments and were responsible for the animal breeding.
- Liam Browne characterize the *TRPV1::Chr2* lineage.
- Katia Galan performed the nerve histology.

4 A transversal spinal electrode array for rehabilitation of locomotion after spinal cord injury

Abstract Although electrical stimulation is not cell-type specific, the spinal cord anatomy and organisation allow selective stimulation of sensory fibers. Spinal cord injury (SCI) often leads to severe locomotor deficits or even complete paralysis. Electrical stimulation of proprioceptive afferents has been shown to improve motor control after SCI in animal models and in human patients. Recent development of spatiotemporal neuromodulation strategies allows for more refined activation of muscle synergies naturally involved in locomotion. However, limited specificity and inter-subject anatomical variability hinder the clinical deployment of this technology. In this chapter, I report on a transversal spinal electrode array for enhanced spatial selectivity in the spinal cord stimulation. This soft neural implant was inserted in the rat epidural space, with its electrodes fitting on the most lateral aspects of the spinal cord. The mechanical match of this implant and the spinal tissue allowed for seamless integration and the delivery of tailored multipolar electrical stimulations to selectively recruit posterior spinal roots. I detail the development of such spinal implant and demonstrate its validation both *in vitro* and *in vivo*. Finally, I describe its implementation to a spatiotemporal neuromodulation protocol for restoring locomotion in a paralysed animal model. This unique stimulation paradigm may steer a new therapeutical approach to treat patients suffering from SCI.

Some of the information presented in this chapter appears in the following manuscript:

[191] GANDAR* Jérôme, ROWALD* Andreas, MICHOU* Frederic, WENGER Nikolaus, SHKORBATOVA Polina, BICHAT Arnaud, LACOUR Stéphanie P, CAPOGROSSO Marco, COURTINE Grégoire, Optimized multipolar stimulation protocol for the recovery of locomotion after spinal cord injury in humans based on comparative anatomy in rats, *in preparation*, 2018.

4.1 Epidural electrical stimulations to restore locomotion after SCI

Spinal cord injury (SCI) disrupts the communication within the central nervous system (CNS), which leads to a range of motor and sensory deficits, including complete paralysis. In the early 20th century, pioneer experiments in transected cats paved the way for modern neuromodulation strategies. Sherrington reported on the cat automated locomotion on a treadmill, due to the sensory information arising from the moving joints that was engaging a motor reflex in the spinal circuits [192]. However, the lack of such automated locomotion in patients (and in rodent animal models) with complete SCI suggested that additional activity in the dormant spinal circuits is necessary [193]. These observations led to the development of neuromodulation strategies to stimulate neural circuits below the level of injury. In particular, epidural electrical stimulation (EES) emerged as a promising approach to improve motor recovery [194, 195]. First, I describe the concept of EES and its recent applications in restoring locomotion after SCI. Then, I review the existing neurotechnologies to deliver EES in the spinal cord.

4.1.1 Specific recruitment of sensory proprioceptive neurons

Since decades, EES of the spinal cord has been used to alleviate chronic pain through the application of the gate control theory [26]. Since then, groups reported on improved motor skills with EES in patients suffering from Parkinson's disease [196], multiple sclerosis [197] and spinal cord injury [198]. In rodent models of SCI, the combination of EES with a pharmacologically-based neuromodulation and a robot-assist training demonstrated spectacular rehabilitation of locomotion [40] (Figure 4.1.b). However, the mechanisms of EES on the spinal circuits were still poorly understood. For example, midline electrical stimulation of the lumbar segments promotes flexion of the hindlimb whereas stimulation of the sacral level initiates extension movements [199]. The recent development of realistic finite element models demonstrated EES recruits large myelinated proprioceptive fibers, activating motoneurons through spinal circuits [44, 45]. The increased excitability of the spinal circuits with EES modulates the central pattern-generating networks, producing locomotion-specific movements [200]. Until recently, the electrode location and the stimulation patterns (i.e. frequency, amplitude, pulse width) were guided by empirical knowledge and remained fixed within the neuromodulation therapy.

Although continuous EES of the spinal cord resulted in limited motor recovery, it was hypothesized that a stimulation matching dynamically the various gait phases (e.g. left stance, right swing) would improve the therapeutical outcome [201]. In other terms, EES would have to mimic the motoneurons naturalistic activation through precise recruitment of proprioceptive fibers in space (i.e. flexion, extension, left, right) and in time (i.e. gait cycle). This paradigm steered the development of closed-loop neuromodulation protocols, integrating the spatiotemporal components of locomotion in the stimulation [202]. These spatially selective and temporally accurate neuromodulation therapies enhanced significantly the outcome of EES in rodent models of SCI. Finally, Bonizzato *et al.* and Capogrosso *et al.* reported on brain-

4.1. Epidural electrical stimulations to restore locomotion after SCI

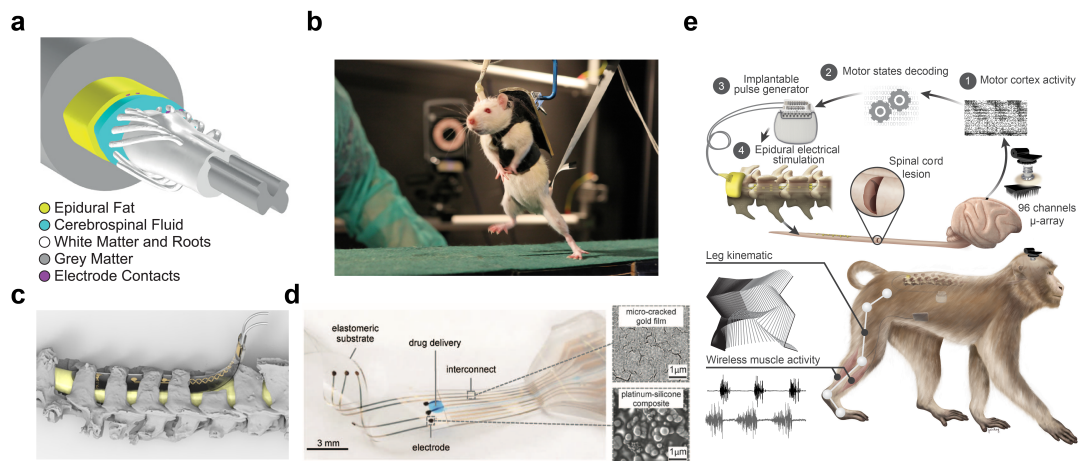


Figure 4.1 – Neurotechnologies for electrical stimulation of the spinal cord in animal models

a, Anatomically realistic computational model of the rat spinal cord representing the spinal segments L1 and S2. Finite element modelling predicts the recruitment of neural structures with electrical stimulation. Adapted from [206]. **b**, Restoration of voluntary locomotion in paralysed rat using an electrochemical neuroprosthesis and robotic-assisted training. Adapted from [40]. **c**, A 3D reconstruction of a softening electrode array inserted at the rat cervical spine. Adapted from [207]. **d**, A soft multimodal subdural implant with mechanical properties mimicking the dura mater. This implant comprises stretchable interconnects, high performance neural electrodes and a drug-delivery canal. Adapted from [75]. **e**, Design of a brain-spine interface to deliver tailored EES in a non-human primate model of SCI. Adapted from [204].

spine interfaces, respectively in rat and in non-human primate, that integrate the volitional aspect of locomotion in the neuromodulation therapy [203, 204]. In this brain-controlled neuromodulation concept, a microelectrode array implanted in the motor cortex detected the intention of locomotion and triggers specific (i.e. flexion, extension) EES of the spinal cord via a spinal implant in the lumbar segments (Figure 4.1.e).

4.1.2 Spinal implant neurotechnologies

The development of fine EES-based neuromodulation therapies is intrinsically coupled to the progress of neurotechnologies, and in particular of spinal cord stimulation systems. Although EES of the spinal cord has been introduced decades ago, mechanical failures prevail the implant long-term effectiveness [205]. Due to the repetitive flexion and extension of the spinal cord, implants may migrate from the initial insertion area, and in the worst case, break due to the imposed mechanical load. The spinal cord neural tissues are highly dynamic, extension and compression with natural postural movements can produce large local strains thereof. A study reported on spinal cord maximum strains $\sim 14\%$ at the cervical level with a flexion of the neck [79]. This range of motion can become problematic for commercially-available spinal implants, generally composed of thick platinum electrodes embedded in silicone rubber.

The delivery of electrical stimulation in rodent animal models of SCI steered the development

Chapter 4. A transversal spinal electrode array for rehabilitation of locomotion after spinal cord injury

of mechanically compliant spinal implants. These animal models exhibit similar ranges of motion of the spinal cord, albeit within smaller dimensions. Garcia-Sandoval *et al.* reported on a softening cervical implant made from shape memory polymers (Figure 4.1.c). This device remains mechanically-stiff at RT and softens following implantation to facilitate long-term integration [207]. Minev *et al.* pioneered implantable soft electronics, presenting a silicone-based multimodal electrode array, mimicking the elasticity of the dura mater (Figure 4.1.d). This neural interface, termed e-dura, was chronically implanted subdurally in the rat spinal cord and presented remarkable bio-integration properties. This implant enabled the fine delivery of an electrochemical spinal neuromodulation, restoring locomotion after SCI [75].

Recent spatiotemporal neuromodulation therapies require high-density electrode arrays to deliver spatially-accurate EES. Nandra *et al.* presented a microelectrode array for insertion in the lumbar segments of the rat spinal cord [208]. Standard thin-film photolithography processes allowed for the integration of 27 electrodes in a 10 μm -thick parylene strip. However, the array exhibited clear mechanical damages 6 weeks following implantation. The mechanical mismatch between the parylene-based array and the soft spinal tissues may have hindered prolonged functional interfacing [75]. Furthermore, increasing the electrode density involves smaller track dimensions and more fastidious connections. Giagka *et al.* reported on the first active (with embedded electronics) spinal electrode array [209]. Using application specific integrated circuits (ASICs) along the device, 12 electrodes were independently accessed via only 3 interconnects. Although this approach can be appealing for high-density electrode arrays, the lack of redundancy in the circuit would induce a complete breakdown if one track or one ASIC is lost. This group did not report on the *in vivo* application of the device.

4.2 A soft transversal epidural spinal implant, the belt array

Based on the detailed anatomy of the rat lumbosacral spine, we identified the precise dorsal root trajectories innervating the hindlimbs (Appendix A.3.1). Using multipolar stimulation, we envisioned to improve EES specificity by tailoring the electrical field to the exact root anatomy and functionality. Multi-contact stimulation allows to increase spatial selectivity by providing an anodic electrical fields to the conventional cathodic fields, preventing the activation of non-targeted structures [52]. This endeavour promoted the development of a transversal epidural implant - which we called belt array - to precisely recruit posterior spinal roots (Figure 4.2). The belt array conforms to the morphology of the spinal cord and distributes its neural electrodes over a single spinal segment. The soft neurotechnology of the belt array was previously described by my colleagues Minev *et al.* [75]. However, several challenges were raised by the transversal epidural application. First, narrower and longer interconnects ensued the raised electrode density. Second, a significantly thinner substrate was necessary to fit in the intended area of implantation. Third, multipolar stimulation requires high performance neural electrodes. The process of fabrication was consequently improved to ensure more reliability and reproducibility. I describe this optimized process and the implant performances *in vitro*. Finally, I describe the belt array bio-integration following chronic implantation.

4.2. A soft transversal epidural spinal implant, the belt array

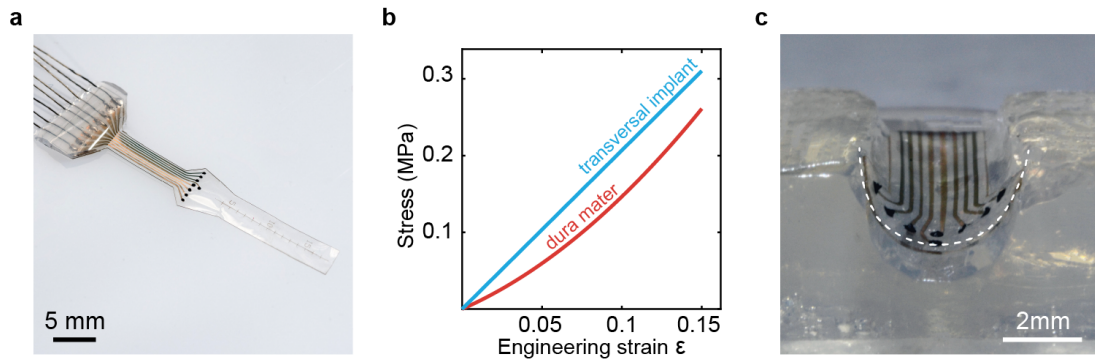


Figure 4.2 – A transversal spinal electrode array

a, Optical image of the belt array. This soft implant is composed of 8 Pt-PDMS electrodes and stretchable Cr/Au interconnects embedded in a polymeric substrate/superstrate. **b**, Stress-strain curves of the rat spinal dura mater and the transversal implant, measured in saline at 37 °C. **c**, Conformation of the soft electrode array to an agarose negative mold of the rat spinal cord.

4.2.1 Micro-cracked gold film topography

The dynamical nature of the spinal cord hinders mechanically-stiff implant interfacing. The development of electrode arrays that conform the spinal cord morphology and accommodate its motion requires stretchable interconnects. Thin films formed by gold physical vapor deposition on PDMS substrates display a micro-cracked morphology (Figure 4.3). This pattern allows the film to stretch by deflecting and twisting out of plane around these micro-cracks, reducing the strain in the film [83, 84, 210]. These intrinsically stretchable thin films are promising for biological applications, including *in vitro* [211, 212] and *in vivo* electrode arrays [75, 213].

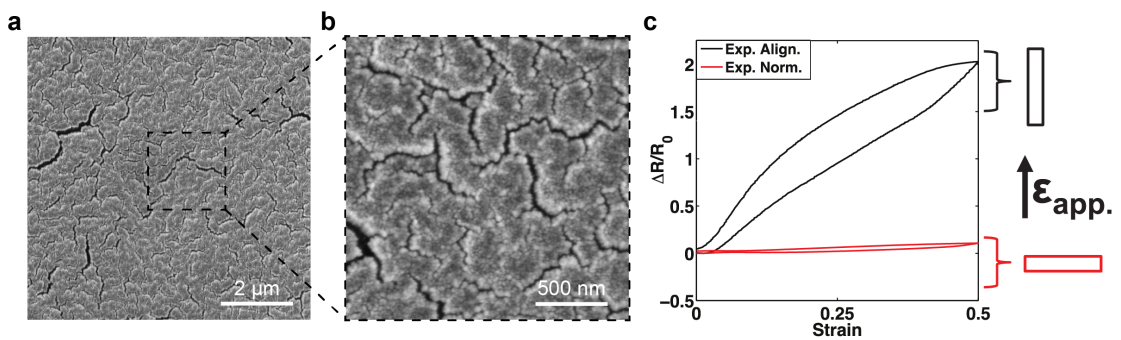


Figure 4.3 – Intrinsically stretchable micro-cracked gold thin film

a, b, SEM pictures of a 5/45 nm Cr/Au film thermally evaporated on a PDMS substrate. This thin film contains built-in tri-branched micro-cracks (0.5 to 2 μm long) that ensure electrical conductivity under elongation. **c**, Change in resistance of a strain gauge made of a $5 \times 0.5 \text{ mm}^2$ micro-cracked gold track on PDMS substrate when applying aligned and normal strain. Comparison between experimental measurements performed on 25 nm Au thin films on PDMS. Adapted from [214].

Chapter 4. A transversal spinal electrode array for rehabilitation of locomotion after spinal cord injury

Although this micro-cracked morphology is reproducible from batch to batch [215], we do not understand fully its formation. Further observation on a 60° tilted sample showed the film complex topography (see Appendix A.3.2). The film displays submicrometric wavy structures (appearing as white streaks) with randomly-distributed micro-cracks. The micro-cracked gold film topography has not yet been measured and this property may be essential to comprehend the film growth mechanisms and its behaviour under elongation, improving the film distinct features thereof (e.g. sheet resistance, reliability, maximum elongation).

The micro-cracked gold film topography was quantified via atomic force microscopy (Figure 4.4, methods described in Appendix A.3.3). The film exhibited an heterogeneous topography, with peaks surrounding systematically the micro-cracks. Furthermore, the height of the film around the cracks seemed correlated positively with the size of the cracks. We can also observe the cracks formed at the gold grain boundaries, as it has been previously described [83]. This topography was reproducible for metallization with the same deposition parameters. Next, we measured the topography of the film under 10% uni-axial strain (Figure 4.5). First, we can observe the cracks propagated and opened in the tensile direction to accommodate the

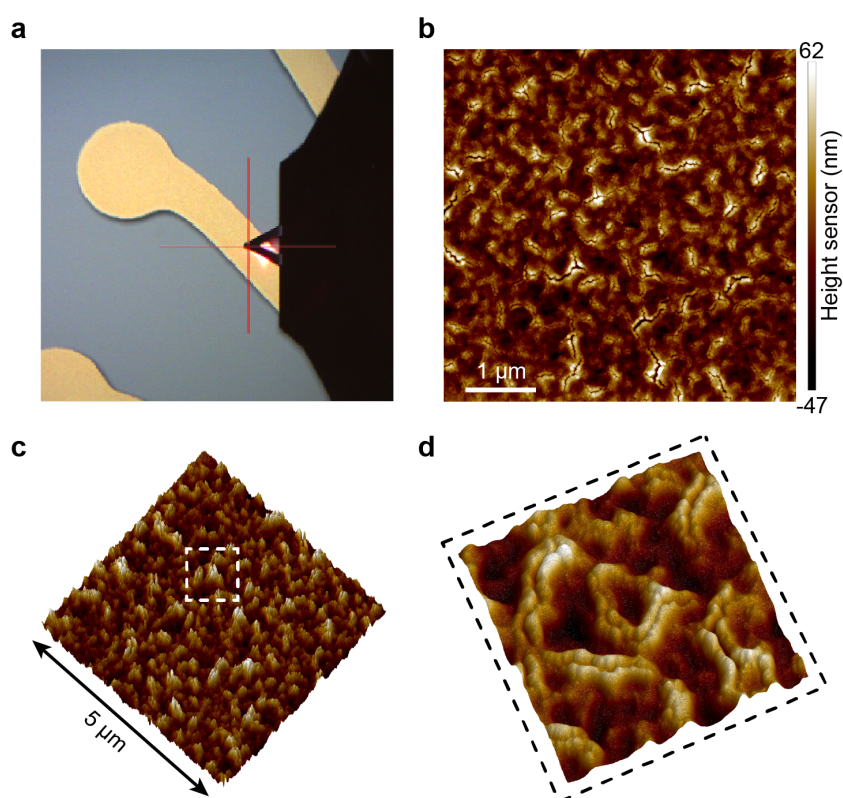


Figure 4.4 – Atomic force microscopy of the micro-cracked gold film

a, Optical image of the AFM cantilever probing the belt array interconnects. **b** Representative AFM image of the corresponding micro-cracked gold film surface. **c-d**, 3D reconstruction of the gold film surface topography exhibits its heterogeneity property.

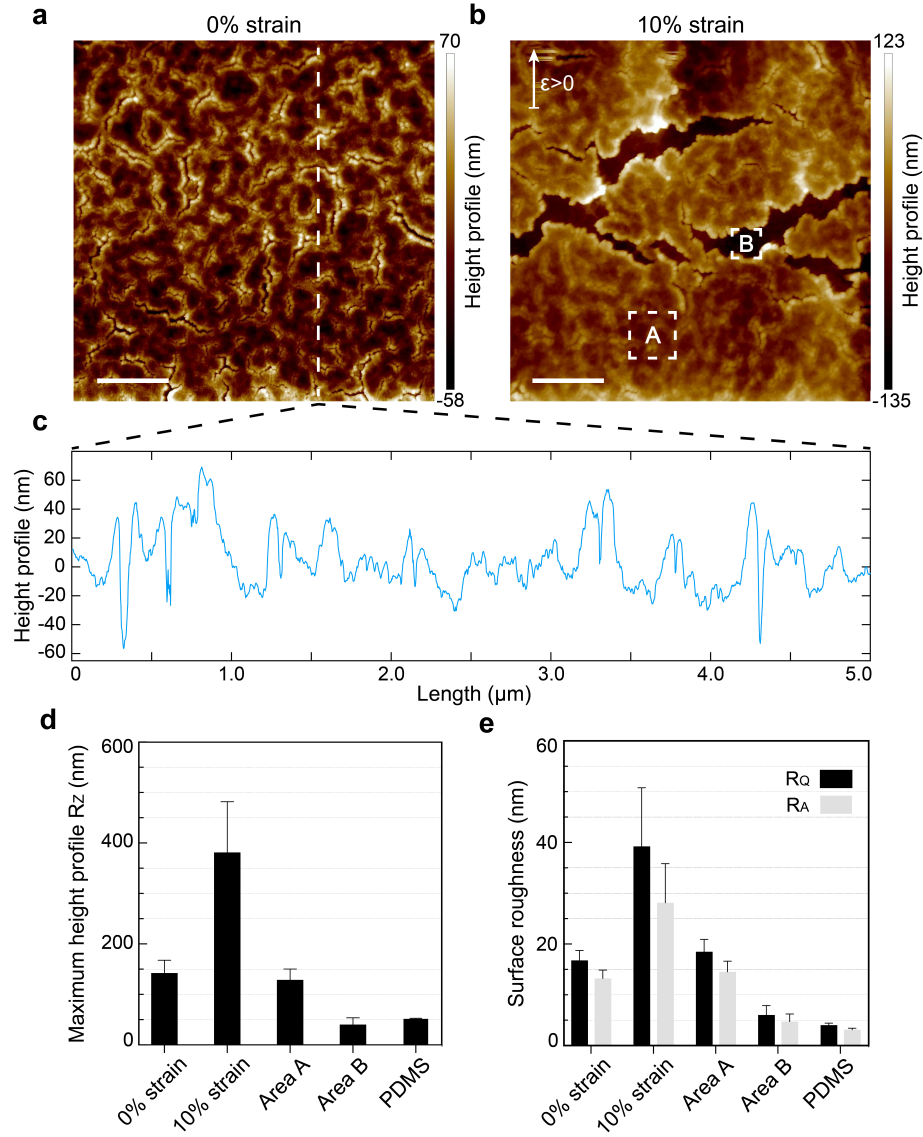


Figure 4.5 – Analysis of the micro-cracked gold film topography under uni-axial strain

a, b, Representative AFM images of the micro-cracked gold film at 0% (**a**) and 10% (**b**) strain. Area A is defined as an area with no-apparent changes in topography. Area B is defined as the topography measured inside the cracks. Scale bars, $1\mu\text{m}$. **c,** AFM height profile signal measured within one scanned line of the micro-cracked film surface at 0% strain. **d, e,** The maximum height of the profile R_z (**d**) and the roughness (roughness average R_A , root mean square roughness R_Q) of micro-cracked gold film surfaces ($n = 6$ per condition, 2 for PDMS, mean \pm s.d.).

elongation. The film maintained a percolating path to ensure electrical conductivity and as expected, it deflected around the cracks [210]. For further analysis of the film topography, we defined, subjectively, **A** an area without apparent changes in topography, and **B** an area within the opened cracks. We computed the maximum height of the profile (R_z) and the roughness (average R_A , root mean square R_Q) for various regions (Figure 4.5.c-e). We found

Chapter 4. A transversal spinal electrode array for rehabilitation of locomotion after spinal cord injury

the film roughness and R_z increased significantly with the applied strain (0 vs 10% strain). We measured similar roughness in the 0% strain case and in **A**, motivating the paradigm of strain being reduced in the film with the mechanical displacement of the cracks. Finally, the roughness measured inside the cracks is analogous to the one measured on PDMS surface (illustrated in Figure A.5). This indicated the surface probed in **B** was probably bare PDMS, and the cracks propagated through interfacial decohesion of the Cr/Au film with the substrate due to the tensile stress upon elongation [216].

These first AFM measurements showed the complex micro-crack gold film topography contributes to the film stretchability. This topography evolved dynamically to maintain an electrical path under strain. Although previous FEM demonstrated the film deflection out-of-plane mechanisms, these models did not take into account the film roughness [85, 210, 217]. More realistic modelling would allow to predict precisely the micro-cracked gold performances, batch to batch. Finally, these observations validated this metallization process to constitute the belt array stretchable interconnects.

4.2.2 Soft neurotechnology for transversal spinal array

The general fabrication process of the soft transversal spinal implant is depicted in Figure 4.6. First, a 60 μm thick substrate layer of PDMS (Sylgard 184, Dow Corning, mixed at 10:1, w:w, base:curing-agent) was spin-coated on a 3" silicon wafer coated with a water-soluble layer of poly(4-styrenesulfonic acid) (PSS, Sigma-Aldrich, spin-coated at 2000 rpm for 1 minute). Following PDMS curing (80°C overnight), a 23 μm thick PET stencil mask (Mylar, Dupont) was laminated on the PDMS substrate. The shadow mask was patterned to the interconnects layout using an excimer femtosecond laser (1030 nm, Amplitude Systèmes, MM200-USP, Optec). Then, a 5 nm thick film of chromium and a 45 nm thick film of gold were successively thermally evaporated (Auto 306, Edwards) to the PDMS substrate, shaping the implant interconnects. The latter were encapsulated with a 30 μm thick layer of silicone rubber (Elastosil M 4600, Wacker). This passivation layer was spin-coated over a 23 μm PET film (Mylar, Dupont) laminated on a 4" silicon wafer. Following the silicone rubber curing (80°C overnight), a second PET film was laminated over the silicone rubber using a dry film laminator (Photopro 33). The triple stack PET-rubber-PET was released from the wafer and then customized to the electrode negative layout using an excimer laser (Optec). Finally, the top PET film was carefully peeled off the stack and the silicone rubber superstrate was bonded to the PDMS substrate following oxygen plasma surface activation. The implant electrodes were coated with a platinum-silicone composite, as described in [218]. Briefly, 100 mg of platinum microparticles (Pt powder, Goodfellow) were mixed to 110 μL of a PDMS/cyclohexane solution (200 mg/500 μL , Dow Corning, Sigma-Aldrich). The mixture was thoroughly stirred and the cyclohexane evaporated until the mixture became a paste via percolation. Finally, the paste was printed to the electrode sites by spreading the paste over the second PET film. Right before printing, the paste was diluted with a drop of cyclohexane. The PET film was then peeled off the superstrate and the platinum-silicone composite cured

4.2. A soft transversal epidural spinal implant, the belt array

(60°C overnight). The substrate-superstrate stack was precisely cut to the implant shape using an excimer laser (Optec). The last step consisted in connecting the implant interconnects to stainless-steel wires (AS 632, Cooner Wire) with Ag paste (H27D, Epoxy Technology Inc.) printing to the connection pads. After sealing (734, Down Corning), the transversal array was released from the wafer after immersion in deionized water.

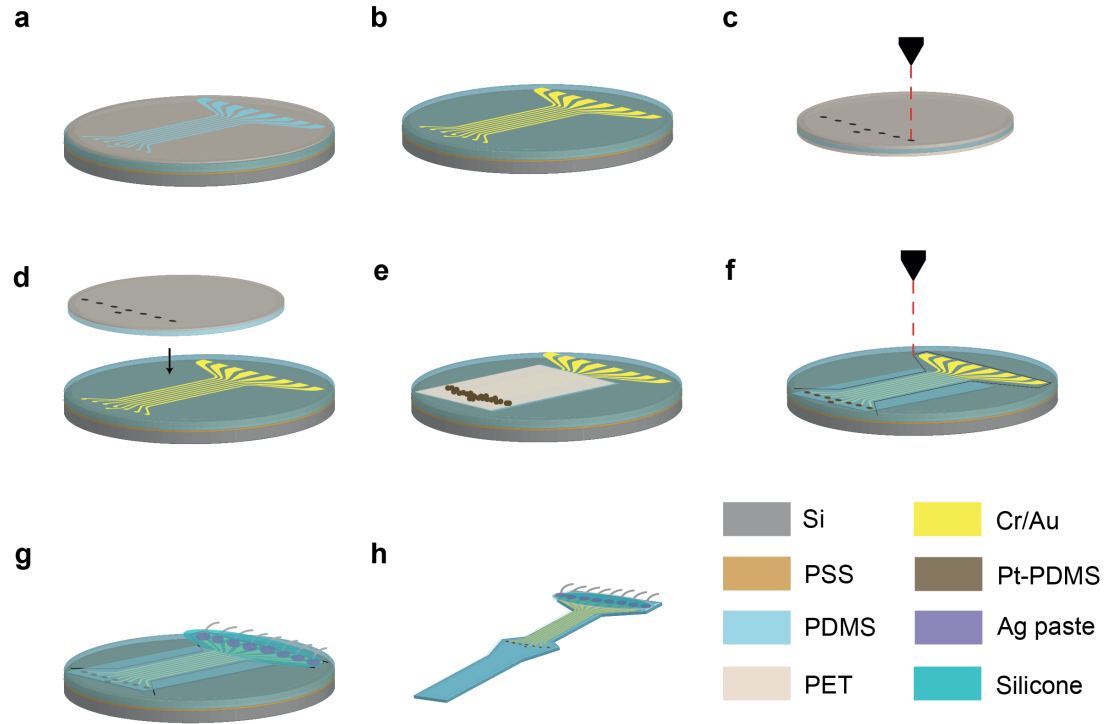


Figure 4.6 – Transversal spinal electrode array microfabrication

a, A PET stencil mask is laminated on a PDMS substrate. The latter was previously spin-coated and cured on a PSS-coated Si wafer. **b**, The interconnect thin film is thermally evaporated and the stencil mask peeled off. **c**, In parallel, a PDMS membrane laminated with a PET film on both sides is prepared for the implant encapsulation. Laser ablation of this stack formed the electrode sites. **d**, After a single PET film removal, the stack is aligned and O₂ plasma bonded to the metallized PDMS substrate. **e**, The 2nd PET film is used as a stencil mask for the Pt-PDMS mesocomposite screen printing at the electrode sites. **f**, After peeling-off the PET film, the implant shape is defined by laser ablation through the elastosil superstrate and PDMS substrate. **g**, Stainless-steel micro-wires are carefully placed and connected to the implant interconnects via silver paste dispensing. The connector is eventually encapsulated with a room temperature vulcanized (RTV) silicone. **h**, Finally, the implant is released from the wafer in deionized water.

The platinum-PDMS mesocomposite for electrode coating combines the electrochemical properties of platinum with the mechanical compliance of PDMS [75,218]. The composite was prepared with the loading of Pt particles (< 3 μm in size) in the elastomer matrix. The paste-like rheology of the composite allowed fine coating of the belt array electrodes (300 μm \varnothing ; Figure 4.7). At the macro-scale, the surface of the coated electrodes appeared to be hilly as the composite filled non-homogeneously the electrode site (Figure 4.7.b). Care was taken to avoid

Chapter 4. A transversal spinal electrode array for rehabilitation of locomotion after spinal cord injury

major bumps in the electrode coating as it would hamper the implant mechanical compliance with the spinal cord. Finally, the coating exhibited an important roughness at the micro-scale (Figure 4.7.c). The Pt particle distribution and the porous micro-structure conferred a large electrochemical effective surface area to the electrodes, fostering high performance interfacing with the neural tissues.

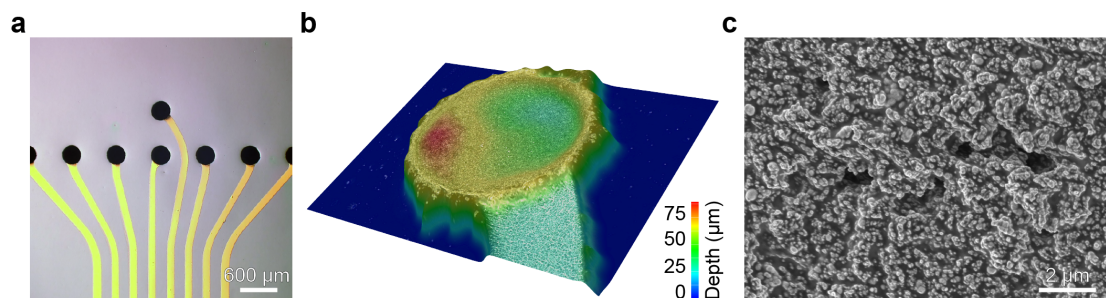


Figure 4.7 – Platinum-PDMS mesocomposite for electrode coating

a, Long-focal optical image of the transversal electrode array morphology. **b**, Representative 3D reconstruction of the electrode coating reveals the non-homogeneous macro-scale electrode coating topography. **c**, High magnification SEM of the electrode coating shows the composite porous micro-structure.

4.2.3 Belt array functionality

The belt array was characterized *in vitro* with electrochemical measurements performed under elongation (methods described in Appendix A.3.4). The electrodes displayed a low impedance magnitude (1.65 k Ω at 1 kHz) that was maintained under large deformation (13.78 k Ω at 40% strain; Figure 4.8.b). The phase spectrum showed a resistive behavior and shifted toward the left when strain was applied (-21.9° at 0% vs -2.0 at 40% strain, at 1 kHz). The change in the phase spectrum emphasized the increase in track resistivity (i.e. R series) with applied strain, while the interface capacitance remained the same. Cyclic voltammograms (CV) demonstrated the large cathodal charge storage capacity (cCSC) of the Pt-PDMS electrode coating (Figure 4.8.c). We observed a larger cCSC when strain was applied to the belt array. This behavior may be due to an increase in the electrode coating effective area, demonstrating the composite mechanical compliance. We measured cCSC of 54.7 mC/cm² at 0% strain and 149.8 mC/cm² at 40% strain (assuming the electrode surface area was conserved; geometric surface area GSA = 0.071 mm²).

Next, we investigated the electrode maximal charge injection limit by applying biphasic, charge-balanced current pulses with gradually increasing current densities (Figure 4.8.d). The electrode coating supported a charge injection limit of 117 μ C/cm², which is significantly higher compared to the 57 μ C/cm² previously reported [75]. This rise is partially explained by the effect of temperature (37°C vs RT) during the measurements [219], and may also reflect a larger effective surface area due to increased roughness or porosity of the composite. Although these parameters were not measured, SEM showed qualitatively that more Pt particles

4.2. A soft transversal epidural spinal implant, the belt array

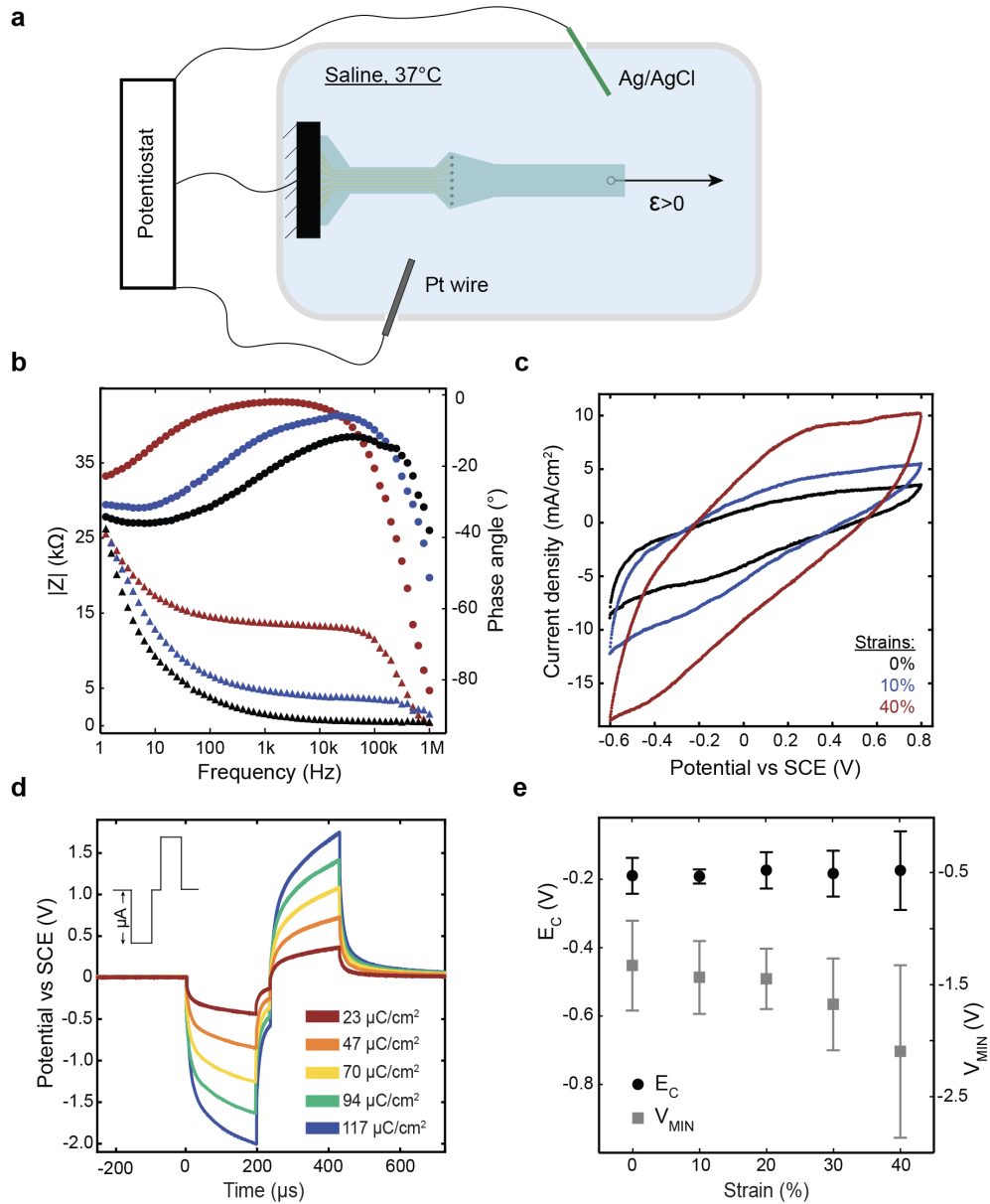


Figure 4.8 – Electrode properties *in vitro* and under tensile strain

a, Illustration of the system for conducting electrochemical characterization of the transversal electrode array under uni-axial strain. The electrode array is clamped to an extensometer equipment and immersed in a circulating bath of saline (pH 7.4, 37 °C). Ports allow for insertion of an Ag/AgCl SCE (reference electrode) and a platinum wire (counter electrode) inside the solution. **b**, Magnitude (\blacktriangle) and phase (\bullet) of electrode impedance recorded in this configuration. Spectra were collected at 0% (black), 10% (blue) and 40% (red) strains. **c**, Cyclic voltammograms (100 mV/s) recorded in saline during a uni-axial stretch cycle (GSA = 0.071 mm²). Larger cathodal charge storage capacity is measured at larger strains. **d**, Voltage transients at the electrode coating surface recorded for different current densities. Charge-balanced, biphasic current pulses were injected through electrodes. The duration of each pulse phase was fixed to 200 μ s with an interphase period of 40 μ s. **e**, The cathodal electrode potential (E_C) and the maximum negative voltage (V_{MIN}) at the electrode coating surface were measured for different uni-axial strains ($n = 8$ electrodes, mean \pm s.d.). The pulse current density was fixed to 47 μ C/cm², which corresponds to the typical maximum current pulse during *in vivo* experiments. Through the experiment, E_C remains within the water window (-0.6 V).

Chapter 4. A transversal spinal electrode array for rehabilitation of locomotion after spinal cord injury

were exposed in the belt electrode coating. Finally, we measured the effect of strain on the electrode polarization (Figure 4.8.e). We measured the cathodal electrode potential (E_C) and the maximum negative voltage (V_{MIN}) for a typical maximal current density used in EES of the rat spinal cord ($47 \mu\text{C}/\text{cm}^2$, corresponding to $200 \mu\text{A}$). While V_{MIN} significantly decreased at 40% strain due to the interconnect resistive component, E_C remained relatively stable ($-0.19 \pm 0.05 \text{ V}$), demonstrating the electrode ability to deliver fine and consistent EES *in vivo*.

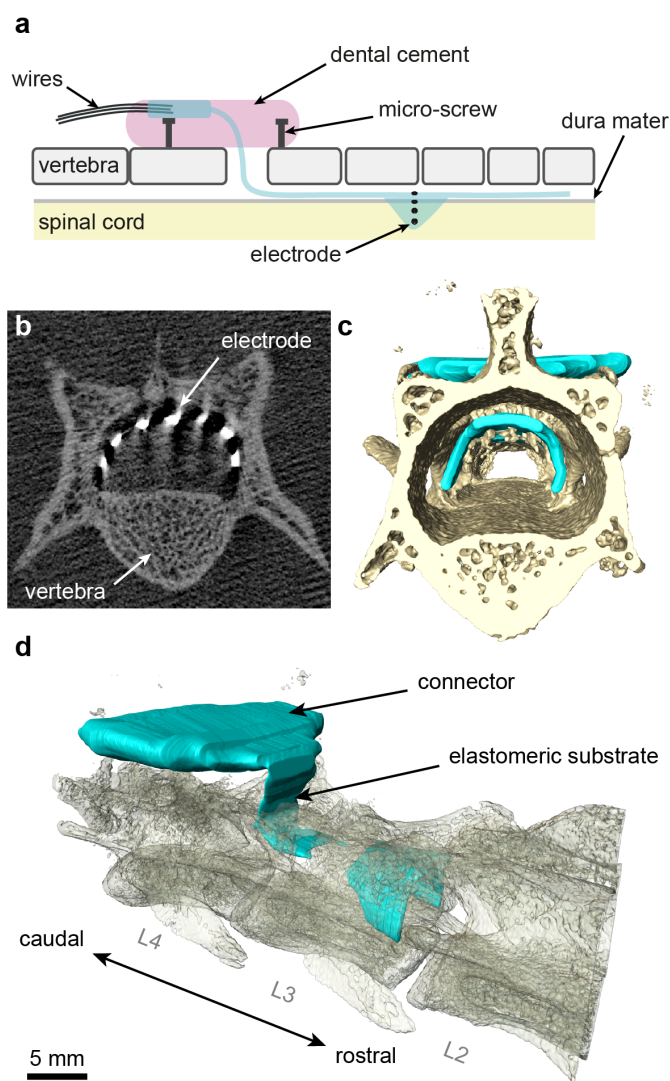


Figure 4.9 – Insertion of the spinal transversal array

a, Surgical procedure for the insertion of the transversal electrode array in the rat spinal epidural space. The side view schematic details the vertebral orthosis that secures the implant connector, ensuring long-term electrode functionality *in vivo*. The neural electrodes are placed transversally to the same spinal segment. **b**, A CT scan shows the wide electrode distribution over the L2 spinal segment. **c**, **d**, The 3D reconstructed CT scans show the bone tissues (light yellow) and the implanted electrode array material (blue), in coronal view (**c**) and in lateral view (**d**).

4.2.4 Belt array biocompatibility

The belt array positions its electrodes circumferentially to the lumbar segments of the rat spinal cord. This unusual electrode distribution was designed to promote higher spacial selectivity with EES. In order to wrap the spinal cord and to place electrodes to its most lateral aspects, the belt array employs a thin elastomeric substrate and superstrate (total thickness < 100 μm). This structure confers a remarkable softness to this implant, matching the tensile modulus of the dura mater, the protective membrane of the spinal cord (Figure 4.2.b). We implanted the belt array in the rat epidural space of the spinal cord (surgical procedure described in Appendix A.3.5) and confirmed the implant disposition *in vivo* via microcomputed tomography (methods detailed in Appendix A.3.6). The results are presented in Figure 4.9. We can observe the transversal electrode distribution over the whole lumbar spinal cord segment (Figure 4.9.b). The implant complied to this narrow space and did not compress the spinal tissue. This imaging data emphasized on the advantage of soft neurotechnology and silicone substrate to conform with the spinal cord.

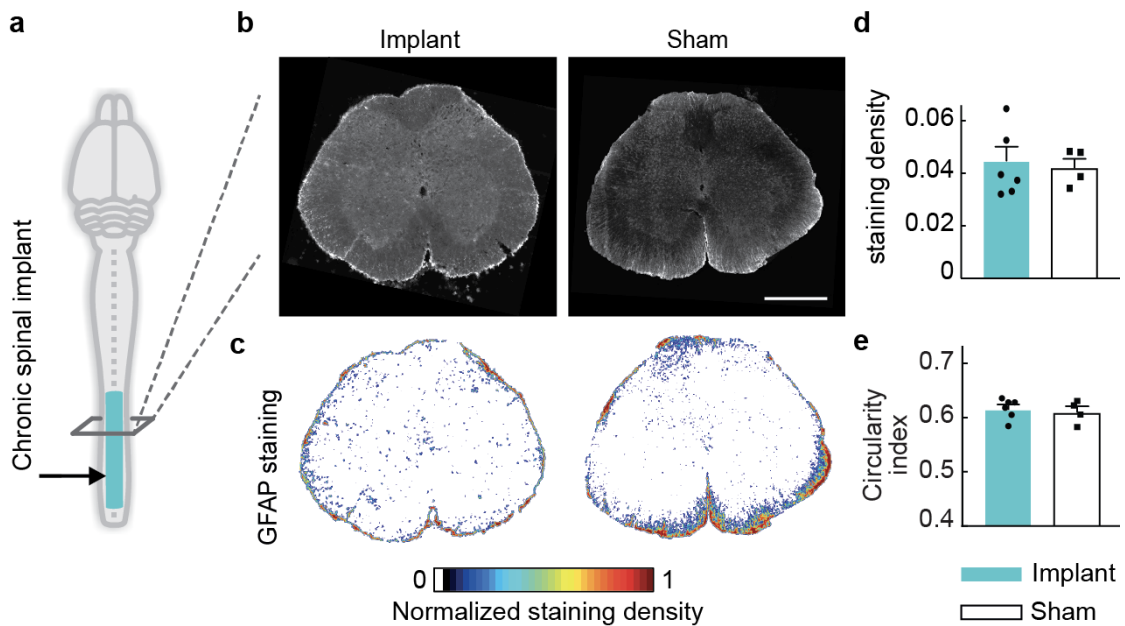


Figure 4.10 – Histology of the spinal cord following long-term belt implantation

a, Schematic of the rat CNS illustrating the belt array placement over the spinal cord. **b**, Representative scans of S1 spinal segment stained for GFAP are shown for the implanted and sham-operated groups. Scale bar, 1 mm. **c**, Digitalization and color-filtering by means of density was performed on each slide with constant threshold parameters. **d**, **e**, Bar plots reporting values of computed GFAP density and circularity index for each group ($n = 6$ for implant, $n = 4$ for sham; mean + s.m.). No statistical significance were found (unpaired t-tests, $p = 0.715$, $p = 0.917$ respectively).

Chapter 4. A transversal spinal electrode array for rehabilitation of locomotion after spinal cord injury

Next, we investigated the belt array biocompatibility following long-term implantation (Figure 4.10). We carefully explanted the rat spinal cord 10 weeks after the belt insertion and performed immunohistochemistry (methods described in Appendix A.3.7) to reveal astrocytes activity, a marker of foreign-body reaction [220]. A density analysis for positive cells to the staining against GFAP was performed on the spinal tissue located below the transversal implant and did not show a significantly different foreign body response (Figure 4.10.d) nor mechanical compression (Figure 4.10.e) compared with sham-operated animals. These results demonstrate the long-term biocompatibility of the belt array.

4.3 Selective, multipolar stimulation of the spinal cord

We have developed a transversal spinal implant to deliver fine EES to the most lateral aspects of the spinal cord. This soft and thin implant complied to the intricate epidural space and distributed its neural electrodes at the spinal tissue vicinity. We have previously characterized the implant functionality *in vitro* and will investigate now its application for the recruitment of proprioceptive fibers *in vivo*. Together with our colleagues from Courtine's group, we demonstrate the benefits of multipolar EES for unravelling the posterior spinal roots. This stimulation pattern was motivated by a realistic computational model of the rat spinal cord anatomy, which is not addressed in this section. Finally, we combine this stimulation paradigm with a spatiotemporal neuromodulation strategy for restoring locomotion after severe SCI.

4.3.1 Spatially-selective electrode distribution

The belt array folded around the spinal tissue with its electrode accessing the most lateral parts of the spinal cord. This unique electrode disposition allowed EES of an array of posterior spinal roots (see Figure A.3), therefore promoting spatially-selective recruitment of proprioceptive fibers. To confirm this hypothesis, we conducted acute electrophysiological recordings in an intact (no SCI) anesthetized rat (methods described in A.3.8). The belt was inserted in the epidural space below L2 vertebra, and its electrodes were aiming toward S1 spinal segment.

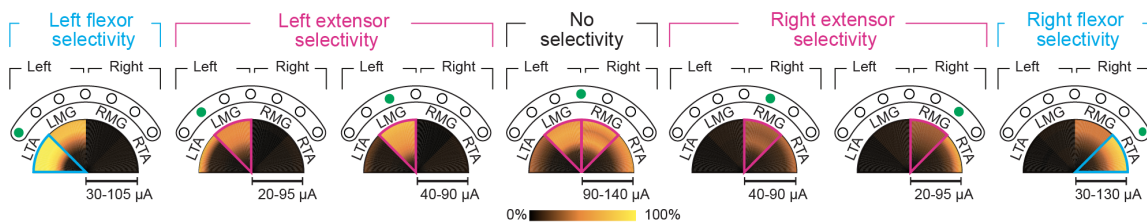


Figure 4.11 – Transversal, monopolar stimulation of the spinal cord

Electrophysiological recording *in vivo* of motor-evoked recruitments following belt array electrode monopolar stimulation. For each active site (green dot), a semi-circular plot sums the EMG activity for various stimulation amplitudes. TA, *tibialis anterior*; MG, *gastrocnemius medialis*.

4.3. Selective, multipolar stimulation of the spinal cord

Bipolar electrodes were implanted in the *tibialis anterior* (TA; ankle flexor) and in the *medialis gastrocnemius* (MG; ankle extensor) to record EMG responses evoked by current pulse stimulation (Figure 4.11). Monopolar EES (200 μ s pulse width) were applied on each active site individually around the spinal cord. The muscular recruitment was determined with the quantification of the monosynaptic peak for each EMG and circular plots transcribed this muscle activity in function of the current amplitude. Stimulation through the most lateral electrodes generated flexion movements whereas central electrode stimulations produced hindlimb extension. Except for the midline electrode, this monopolar EES was also selective left to right. These results demonstrate a degree of spacial selectivity with stimulations spread over a single spinal segment and validate the EES transversal approach.

4.3.2 Acute multipolar stimulation of the spinal cord

We tested whether multipolar stimulation of the spinal cord would enhance muscle recruitment selectivity. The belt array electrode distribution allowed to precisely tailor the stimulation electrical field to the spinal cord anatomy. Under anaesthesia, we repeated the previous electrophysiological recording experiment using multipolar stimulations. The multipolar stimulation patterns were developed *in silico* based on realistic modelling of the voltage potential spreading with EES. We added the recording of the *iliopsoas* (IL; hip flexor) muscles to increase EMG coverage. We compared the selectivity of monopolar and multipolar stimulations (Figure 4.12). In the extensor case, multipolar stimulations increased the specific recruitment of the MG. The addition of an anodic electrical field with the adjacent electrode prevents the recruitment of non-targeted dorsal roots and enables significantly more selective MG recruitment with higher stimulation amplitudes ($n = 6$ rats, $p < 0.05$, Figure 4.12.b, specificity index defined as targeted muscle EMG/sum of EMGs recorded). In the flexor case, monopolar stimulation was already selective for the recruitment of IL and TA flexor muscles. Although multipolar stimulations allowed to recruit specifically the IL, no statistical significance were found in the IL selectivity index compared with monopolar stimulation ($n = 6$ rats, n.s. $p > 0.05$, Figure 4.12.d).

Moreover, the fine positioning of an epidural electrode array is delicate and may deteriorate with long-term implantation due to the spinal tissue dynamic nature. Electrode misalignment reduces the stimulation selectivity and hinders the outcome of EES-based neuromodulation therapy. Multipolar stimulation allows the orientation of the electrical field to compensate for the implant misalignment. In the case of a right-shifted implant (Figure 4.12.e), monopolar stimulation in the midline electrode did not evoke a bilateral movement (left MG is recruited first). With multipolar stimulations, the cathodic electric field was pushed back toward the midline and both extensors were recruited at the same stimulation amplitude. The amplitude difference between the first muscle activated and the second was normalized and compared with the multipolar condition ($n = 4$) (Figure 4.12.f).

Chapter 4. A transversal spinal electrode array for rehabilitation of locomotion after spinal cord injury

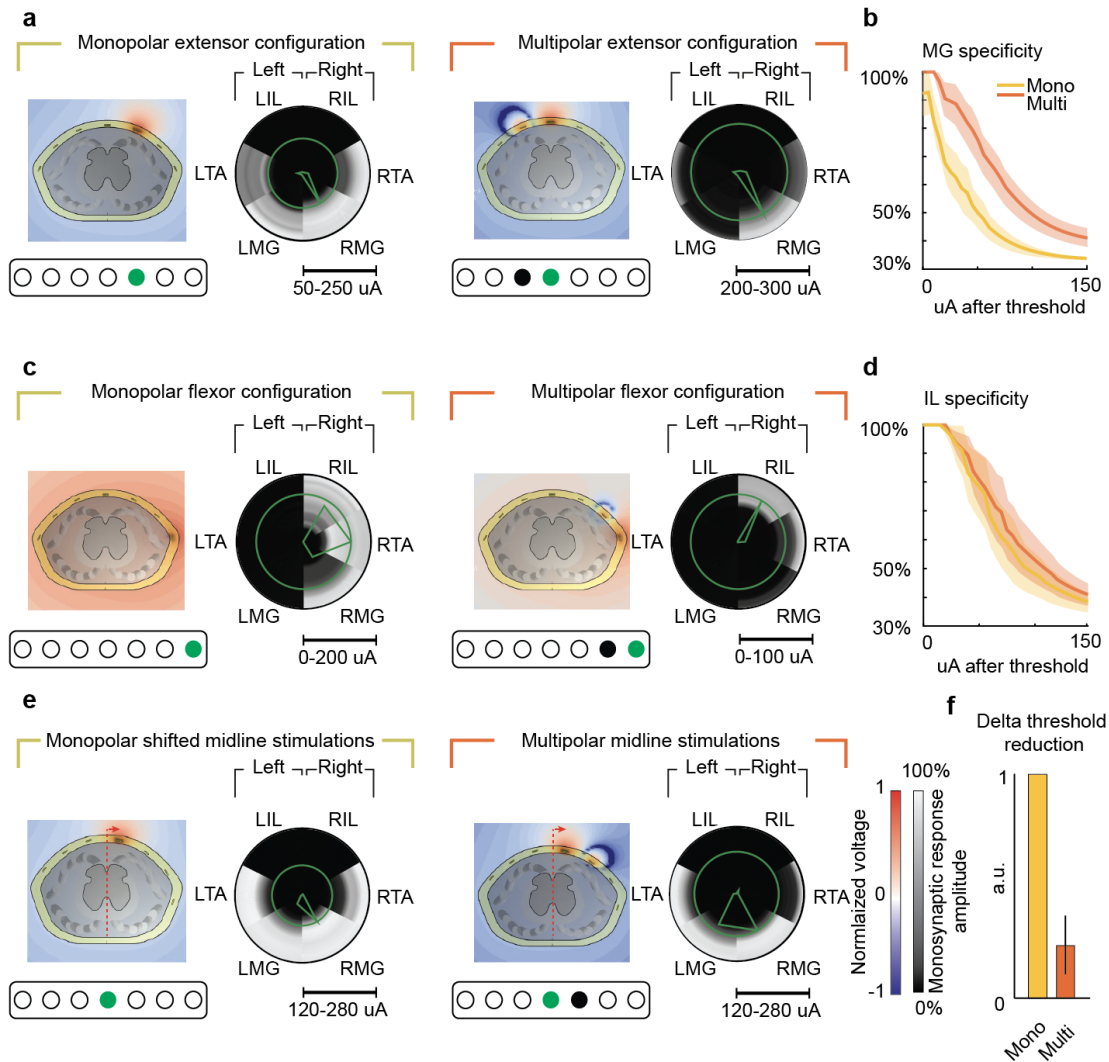


Figure 4.12 – Monopolar versus multipolar stimulation of the spinal cord

a, c, e, Muscle recruitments elicited by monopolar and multipolar stimulation of the spinal cord, in yellow and orange respectively. For each stimulation strategy, a green polygon describes the muscle selectivity index evoked at the optimal stimulation amplitude (green circle). Schematic cross-sections of the spinal cord illustrate the stimulation electrical field. **b, d,** Graphs report muscle selectivity indexes (mean \pm s.m., $n = 6$ rats) after activation threshold, for extension and flexion respectively. **e,** In the case of implant misalignment (red arrow), monopolar stimulation through the midline electrode favours one side. Multipolar stimulation allows to equalized the muscle recruitment. **f,** Histogram plot represents the normalized differential threshold mean ($n = 4$ rats) between mono- and multi-polar stimulation. For a perfectly aligned implant, the differential threshold is 0.

4.3.3 Multipolar stimulation combined with spatiotemporal neuromodulation

We investigated the performances of multipolar stimulations for restoring locomotion after SCI. The belt multipolar stimulations were integrated to a spatiotemporal protocol. First, the rats ($n = 6$) received a spinal contusion (a clinically relevant SCI) at the T8-T9 spinal segment using a mechanical impactor (methods described in Appendix A.3.9). Following SCI, the animals were implanted with the belt array, and its neural electrodes were placed over the S1 spinal segment. The rats were trained for 6 weeks with a continuous midline neuromodulation and were tested with multipolar stimulations 7 weeks after SCI (Figure 4.13). The methods describing the rehabilitation strategy, the recording of kinematics and the close-loop neuromodulation platform are presented in Appendix A.3.10.

First, we characterized the hindlimb movements after SCI using multipolar stimulation patterns. In this configuration, the animals were attached to a jacket maintained in the air with the robotic body weight support system and their feet were not touching the floor (Figure 4.13.a). Using reflective markers placed on the hindlimb joints, we measured the vertical displacement of the foot induced by multipolar stimulations of the spinal cord, both in the extensor and in the flexor case (Figure 4.13.b). The stimulations produced clear, unilateral and antagonist movements, with their amplitudes increasing with the stimulation intensity. This step validated the transversal multipolar approach for restoring functional stepping after SCI.

Finally, we tested the transversal multipolar approach in a spatiotemporal neuromodulation protocol after SCI. In this configuration, the multipolar stimulation patterns alternated in real-time to promote extension and flexion movements according to the gait cycle (see Figure A.7). The rats were harnessed using the robotic body weight support and their feet were in contact with a treadmill belt (Figure 4.13.c). The animal locomotion was tested with 3 experimental conditions and the resulting typical stepping sequences are presented in Figure 4.13.d. In the first recording condition, there was no electrical neuromodulation applied to the rat spinal cord. The foot trajectory remained approximately flat on the treadmill belt while small synchronous bursts of EMG activity were recorded in the TA and MG. These results emphasize the animals did not recover from the SCI and could not engage locomotion spontaneously. For the second condition, continuous midline EES of the spinal cord were applied and resulted in improved stepping compared with the previous case. The kinematic stick diagram and the ground reaction force demonstrate the animal standing posture. Alternating bursts of EMG activity were recorded and show the dynamical component of the restored locomotion. During the third experimental condition, transversal multipolar EES of the spinal cord were applied in phase with the animal gait cycle (spatiotemporal approach). This last condition enhanced the stepping quality, as the kinematics and the foot trajectory exhibited clear and reproducible stance and swing phases. This neuromodulation approach induced longer bursts of EMG activity in the MG during the stance phase compared with continuous neuromodulation.

Chapter 4. A transversal spinal electrode array for rehabilitation of locomotion after spinal cord injury

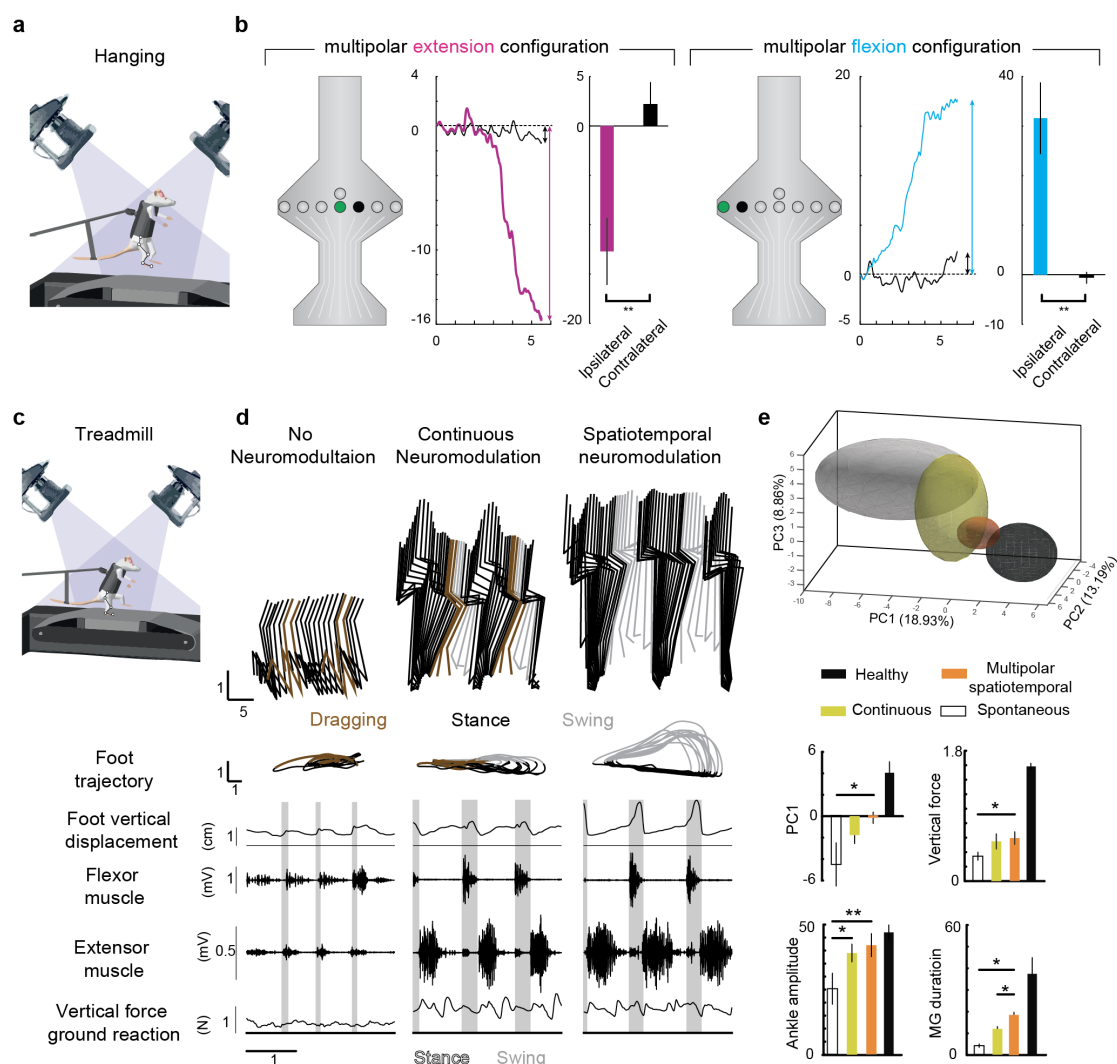


Figure 4.13 – Multipolar neuromodulation for locomotion rehabilitation after spinal cord injury

a, Rats were hanging in a body weight support harness and received a train of multipolar stimulations with increasing current amplitude. **b**, These stimulations targeted the hindlimb extension (purple) or its flexion (blue). The resulting foot trajectories are shown for the ipsilateral (color) and the contralateral (black) sides to the stimulation. Histogram plots report the foot vertical displacement ($n = 6$ rats, mean \pm s.e.m., $**p < 0.01$). **c**, **d**, Locomotion was recorded on a treadmill without electrical neuromodulation, with continuous midline neuromodulation and during spatiotemporal transversal neuromodulation. For each experimental condition (same animal), a stick diagram decomposition of the right limb movement is shown, in addition with the foot trajectory, vertical foot displacement, flexor and extensor EMG and vertical ground reaction force during a continuous sequence. **d**, The gait cycles recorded under the different neuromodulation conditions are computed for 12 consecutive steps and represented in the principal component space. Histogram plots report PC1, the vertical ground reaction force, the ankle angle amplitude and the extensor muscle activity duration ($n = 6$, mean \pm s.e.m.; $*p < 0.05$; $**p < 0.01$).

Using a principal component analysis (PCA) on 118 computed parameters during the animal locomotion, we visualized the recorded gait sequences in the new space created by the three first PCs. These PCs showed the highest amount of variance and reflected a progression of locomotion from a paralyzed animal toward a healthy rat (Figure 4.13.e). Further analysis of the PC1 allowed to extract several parameters highly correlated with the locomotion progression, such as the vertical force, the ankle amplitude or the EMG duration in MG. This analysis demonstrate that spatiotemporal neuromodulation at S1 spinal cord segment using multipolar stimulations significantly improved key features of the locomotor system.

4.4 Discussion

We developed a transversal spinal implant to deliver multipolar stimulations to the spinal cord for enhanced muscle recruitment selectivity. This unique electrode distribution was motivated by computational modelling of EES voltage potentials integrated in a realistic 3D anatomical volume of the rat spinal cord. We implemented this stimulation paradigm into a closed-loop spatiotemporal neuromodulation protocol [202] to restore locomotion after severe SCI and demonstrated improved stepping quality compared to a continuous neuromodulation strategy.

The belt array relies on a soft neurotechnology previously exploited in the context of a subdural spinal implant [75]. It comprises stretchable interconnects and high performance neural electrodes embedded in a soft silicone, matching the static and dynamic mechanical properties of the dura mater. This configuration allows the belt array to comply with the complex morphology of the spinal cord. Moreover, this soft conformable interface exhibited remarkable long-term bio-integration and functionality. However, more-demanding applications of this soft neurotechnology approach would require fundamental changes to ensure versatility and reliability. For example, further increase in the track density is not compatible with soft lithography and the micro-cracked gold film. The rupture strain in these interconnects is size-dependent [85] and does hardly tolerate narrower structures ($< 100 \mu\text{m}$). However, patterned (e.g. Y-shaped motifs) thin films can display a reversible elasticity [221]. The fabrication process relies on photolithography and allows smaller feature sizes, compatible with high-density electrode arrays. However, this approach requires thin plastic foils and may increase slightly the implant flexural stiffness. In addition, the belt electrode coating promoted functional interfacing over long-term implantation. Yet, the manual deposition process of this composite material lacks reproducibility for a large electrode number. Conductive hydrogel is a promising approach for neural electrode coating [222, 223], as it enables high electrochemical performances within a mechanically-soft matrix. Electrodeposition of a conductive hydrogel on the active sites allows to control precisely the electrode coating formation. Future studies will have to investigate conductive hydrogel stability over long-term implantation.

Furthermore, silicone-based neural implants use predominantly PDMS Sylgard 184 to embed their electronics [75, 101, 224]. Although this elastomer is used extensively in microengineering,

Chapter 4. A transversal spinal electrode array for rehabilitation of locomotion after spinal cord injury

other silicone materials have appealing properties [225,226]. We have introduced a passivation layer made of Elastosil M4600 in the belt array. The mechanical properties of the Sylgard 184 and the Elastosil M4600 are compared in Appendix A.3.11. Softer and more resilient elastomers may widen the neural interface application spectrum, while fostering enhanced bio-integration with the biological tissue due to the reduced mechanical mismatch. These materials can also be compatible with the micro-cracked gold film process as we obtained a similar cracked morphology with a Cr/Au vapor deposition on an elastosil substrate (Figure 4.14). The resulting film displayed unprecedented stretchable properties for this metallization and was integrated to the fabrication of a softer, yet more robust, belt array. Finally, PDMS has good biocompatibility properties but its high water permeability hinders the longevity of implantable electronics. More chronic experiments will require thicker encapsulation [227], the introduction of a dedicated barrier layer (e.g. PIB, cf. 3.2.3) or doping PDMS with a low water absorption polymer, such as parylene C [228]. The need for stretchable, chronic neural interfaces steered the development of parylene-caulked PDMS as a promising surface composite, cumulating the PDMS soft properties with enhanced water permeability [229].

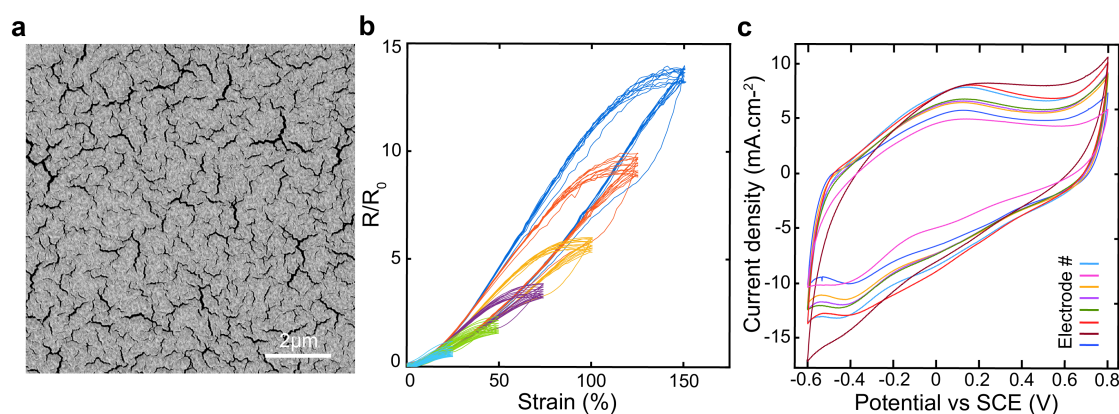


Figure 4.14 – Softer neurotechnology for future spinal implants

a, SEM picture of the surface of a thermally evaporated 5/45 nm Cr/Au film on an elastosil substrate. The film morphology displays similar intrinsic stretchability properties compared to films evaporated on Sylgard 184. **b**, Relative changes in electrical resistance of tracks (200 μm in width) of micro-cracked gold film on elastosil for various uni-axial strain cycles. The film maintains electrical conductivity under very large strains. **c**, Cyclic voltammograms (100 mV/s) of a transversal spinal electrode array made with an elastosil substrate and superstrate.

We investigated the recruitment of muscle activity with the delivery of transversal EES at a single spinal level. Computational models have previously shown that EES primarily activate large afferent fibers in the dorsal roots, inducing spatially-specific evoked motor responses [44, 230]. The transversal approach demonstrated a selective recruitment of afferents fibers involved in flexion or extension using monopolar stimulation. The flexor motoneurons are located up to 4 spinal segments rostral to the electrode location (S1). Previous spinal implants had a longitudinal shape and reached similar spatial-selectivity by delivering EES closer to the dorsal root spinal cord entries [202, 204]. However, the circumspinal electrode position and the array

resolution gave for the first time the opportunity to deliver multipolar stimulations to the spinal cord. Multipolar stimulations demonstrated improved muscle recruitment compared to monopolar stimulations, particularly in the extensor case. The multipolar strategy allowed tailoring the EES functionality to unravel the dorsal roots located at the electrode vicinity. This approach may be promising for applications requiring fiber-specific, spatially-controlled, modulation of sensory neurons, such as chronic pain alleviation. Furthermore, inspired by the emerging dorsal root ganglion stimulator systems, we could foresee their potential application in muscle recruitment after SCI. This strategy would employ multiple electrode arrays surfacing the DRGs innervating locomotion-associated muscles. Coupled with a multipolar stimulation paradigm, this strategy would grant further spatial selectivity. Eventually, the DRGs offer a more static and safer site of implantation.

We integrated this stimulation paradigm into a closed-loop spatiotemporal protocol to restore locomotion after SCI via the activation of muscle synergies [202]. The gain in stimulation specificity may allow to refine muscle synergy recruitment to mimic their natural activation during locomotion [231]. Furthermore, a system coupling a transversal approach to a closed-loop control strategy may promote further flexibility. The spinal cord detailed anatomy and the precise location of the electrode array vary substantially from one patient to the other. The aforementioned system may offer more robustness to this inter-subject variability, facilitating a large-scale implementation of these innovative therapies. Finally, current spinal cord stimulation systems may allow to translate to some extent the concept of multipolar stimulations in human suffering from SCI [42, 232]. Further translation of selective multipolar neuromodulation therapies will steer the development of softer, more compliant, transversal spinal implants.

4.5 Conclusion

In this chapter, we presented a transversal epidural spinal implant tailored to the anatomy of the rat posterior roots. The soft neurotechnology underlying the implant fabrication allows to conform to the complex morphology of the spinal cord and to distribute its neural electrodes over a single spinal segment. This electrode array maintains functionality under elongation naturally occurring in the spinal tissues and demonstrate seamless bio-integration following long-term implantation. The electrode configuration allowed to maximize stimulation specificity for recruiting functionally-distinct dorsal root fibers. A realistic computational model of the spinal cord optimized multipolar stimulation patterns, that were hereafter tested *in vivo*. We demonstrated this multipolar stimulation paradigm resulted in improved selectivity compared to a previous monopolar approach. We finally integrated this implant to a spatiotemporal neuromodulation protocol to restore locomotion in rats after SCI and showed the benefits in stepping quality compared to a continuous neuromodulation strategy. Transversal interfacing with the spinal cord is a promising approach to deliver fine electrical stimulations tailored to the patient specific anatomy.

4.6 Contribution

Data presented in this chapter are the result of a team effort :

- I developed the transversal spinal electrode array and characterised its electrochemical performances *in vitro*. I ran the study on the micro-cracked gold film topography. I occasionally assisted with the surgical procedures and the behavioural experiments. Finally, I analysed the biocompatibility data.
- Jerome Gandar developed the multipolar EES concept and led the study for its validation *in vivo*. Jerome performed the CT scans and the electrophysiological recordings (acute and chronic). Finally, Jerome analysed the *in vivo* data.
- Andreas Rowald developed the FEM for predicting the recruitment of sensory fibers with transversal EES. Andreas ran simulations to find the suitable stimulation patterns.
- Nikolaus Wenger assisted in the development of the spatiotemporal multipolar neuro-modulation protocol.
- Polina Shkorbatova and Arnaud Bichat performed all the surgical procedures, including transversal implant insertion.

5 A soft optoelectronic implant for optogenetics in deep spinal structures

Abstract As we have seen in the previous chapter, selective stimulation of proprioceptive afferents can engage spinal circuits capable of restoring locomotion after spinal cord injury. Although the anatomical organisation of the spinal cord allows for the electrical modulation of its most dorsal components, deep structures within the spine cannot be reached using this modality. Moreover, its lack of cell-type selectivity hinders fine mechanistic parsing of the spinal circuits involved with motor, somatosensory and autonomic functions. The degree of precision of optogenetics allows for further elucidation of the mechanisms and underlying circuitry of the spinal cord. In this final chapter, I present a soft optoelectronic implant able to interface optically deep structures within the spinal cord. This thin μ -LED array was inserted in the epidural space of the mouse spinal cord without causing significant tissue damages, as I demonstrate with histological and behavioural analyses. This μ -LED array was implemented to the wireless stimulator presented in Chapter 3, thereby promoting untethered experimental conditions for the fine interrogation of spinal circuits. As a proof-of-concept, I report on the orderly recruitment of motor units with optical epidural stimulations in non-anaesthetized *Thy1::ChR2* mice. The distribution of μ -LEDs in the rostro-caudal axis allows for further spatial selectivity. Computational modelling of the light propagation in the spinal tissues shows this implant can interface efficiently with deeper neural structures. Finally, this optoelectronic implant supports the use of optogenetics to unravel the spinal circuitry in awake, freely-behaving rodents.

5.1 Background and state of the art

As with the peripheral nervous system (Chapter 2), the use of optogenetics in the spinal cord has been relatively modest compared to optogenetic control in the brain [87]. The dynamic nature of these neural tissues, exhibiting tensile strains in the 10 - 20% range, prevents the use of penetrating implants in awake experimental conditions. The spinal cord complex morphology, its size and the neural tissue opacity are additional challenges limiting the development of optical spinal interfaces. Yet, the spinal cord contains numerous potential targets for fine optogenetic modulation, including somatosensory afferents, descending pathways (e.g. corticospinal tract) and interneurons. I review here the different strategies presented in the literature to deliver optical stimulations in the spinal tissues.

5.1.1 Fiber-based interfaces with the spinal cord

The extensive use of optic fibers in optogenetics has been translated to interface with the spinal cord. Although light delivery with penetrating fibers in the brain has been established, their relative stiffness and the motion of the spinal tissues require an epidural light delivery approach. Among the first demonstrations in freely-behaving mice, Caggiano *et al.* reported on the implantation of an optic fiber cannula perpendicular to the spinal cord [112]. The surgical procedure involved a laminectomy of 1-2 vertebrae, the preparation of a silicone-based optical window above the dura mater and the cementation of the cannula to the surrounding structures. This spinal implant enabled optogenetic stimulation of inhibitory GABAergic interneurons, resulting in the inhibition of ipsilateral hindlimb movements in awake mice. Despite its relative invasiveness, this fiber-based approach was used to investigate the role of somatostatin (SOM) interneurons in itch-related behaviors [233] and spinal astrocytes in pain hypersensitivity [234]. The recent development of multifunctional optic fibers, integrating recording electrodes to the fiber construct, was used in a similar fashion to probe spinal tissues (Figure 5.1.a). These thin hybrid fibers were inserted 300 μm deep into the spinal cord to record electrophysiological activity with simultaneous optogenetic stimulation of Thy1 neurons [113]. The lack of histological quantification does not allow assessing the fiber bio-integration. Finally, Bonin *et al.* presented an optic fiber implanted transversally in the mouse epidural space [235]. This epidural optic fiber (\varnothing 250 μm) was inserted from C1 to L1 vertebral segments and its diffusion tip allowed for the orientation of light to the dorsal aspects of the spinal cord. This implant carried the optogenetic modulation of pain-associated neurons in the dorsal horn and demonstrated an analgesic effect with the silencing of GABAergic interneurons.

Interfacing the spinal cord with optic fibers suffers from several pitfalls. First, the motion of the spinal tissues versus the fixed fiber can hamper stimulation consistency. Then, this cumbersome approach does not support the implantation of multiple fibers to probe spatially distinct areas. Eventually, the tethered experimental conditions associated with optic fibers impede the animal normal behavior, thus hindering fine neuromodulation study.

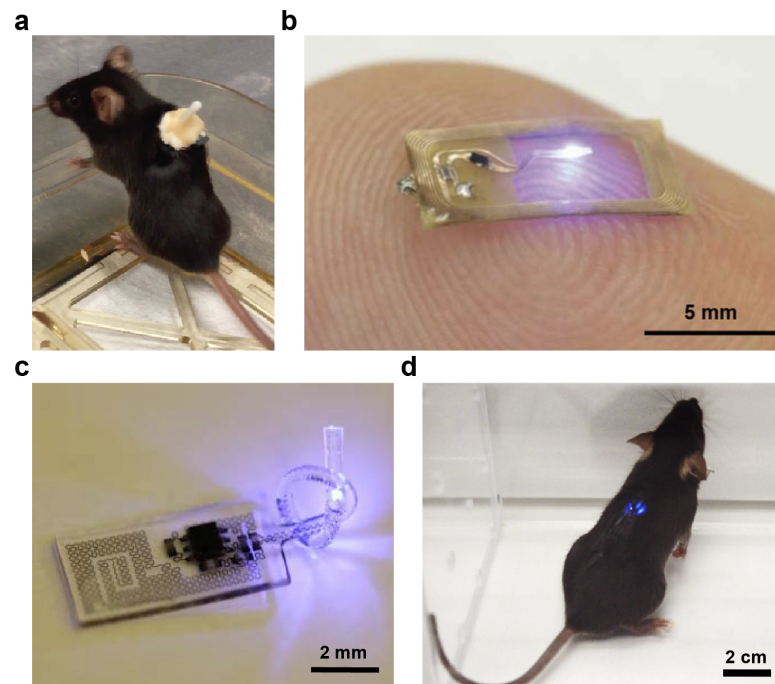


Figure 5.1 – Neural interfaces for optogenetics in the spinal cord

a, Multifunctional fibers cemented to the intervertebral space. These fibers allow electrophysiological recording of neural activity with simultaneous optogenetic stimulation. Adapted from [113]. **b**, Fully-implantable optoelectronic system on a finger tip. When implanted, a μ -LED is placed above the spinal column to allow optogenetic stimulation in the superficial layers of the dorsal horn. Adapted from [177]. **c-d**, Soft, stretchable, fully-implantable optoelectronic system for optogenetics in the spinal cord. The optical interface relies on a μ -LED placed in the epidural space. Adapted from [101].

5.1.2 Optoelectronics interfacing with the spinal cord

LED-based neural interfaces represent an alternative approach to optic fibers in optogenetics. Their miniaturization and the integration of wireless capability make them particularly suitable for delivering light in the spinal cord. A first strategy for their implantation shares similarity with the fiber-based spinal interfaces, and relies on the fixation of a μ -LED to the dorsal column after laminectomy. Montgomery *et al.* presented a wireless optoelectronic implant capable of carrying optogenetic stimulation in the dorsal horn of the spinal cord (Figure 2.1.c, [99]). This implant comprised a power receiving coil, a small electrical circuit board and a μ -LED. Packaging of these components in a minimally-invasive construct (ca. 10 mm³) allowed for its implantation in a hole drilled into a lumbar vertebra. A similar approach for the implantation of a wireless optoelectronic system was reported by Samineni *et al.* (Figure 5.1.b). This device was wirelessly-powered by RF scavenging, hence the integration of a Cu coil implanted subcutaneously. The substrate flexibility allowed for the positioning of a μ -LED in the intervertebral space for optogenetic modulation of superficial spinal tissues. Finally, a second approach for delivering light in these tissues consisted in interfacing mechanically

the spinal cord with a surface optoelectronic implant. The limited dimensions of the epidural space and the motion of the spinal tissues necessitated the development of thin and soft optoelectronic solutions. Park *et al.* presented a fully-implantable, wireless, spinal LED implant and demonstrated optogenetic stimulation of nociceptor-specific sensory neurons (SNS-Cre) in the dorsal horn of the spinal cord (Figure 5.1.c-d). This implant functionality relied on a stretchable electrical circuit, encapsulated in a soft elastomeric matrix, and the integration of 1 or 2 μ -LED(s) on a distal extension. Following laminectomy, this extension was inserted in the epidural space, placing the μ -LED in the vicinity of spinal tissues. This optoelectronic system constituted a remarkable proof-of-concept for the interfacing of the spinal cord with a LED-mounted surface implant. Unfortunately, the authors gave only limited informations on the device dimensions, its long-term performances or bio-integration.

These optoelectronic systems provide attractive solutions to deliver optical stimulations in the spinal cord of freely-behaving mice. Their wireless operation eliminates the stress applied by tethered optic fiber approaches. Conversely, optic fibers enables optogenetic modulation in deeper neural structures as their associated external light sources (e.g. laser) generally provide superior optical power compared with μ -LEDs. Furthermore, wireless powering limits significantly the output irradiance of these implants in behavioral experimental conditions (cf. Chapter 3). The optical properties of neural tissues reduce substantially light propagation, particularly in the blue spectrum [66]. Consequently, these wireless systems targeted activation of ChR2-expressing neurons in the most superficial laminae of the dorsal horn. Eventually, these LED-based implants missed demonstrating the optogenetic neuromodulation of spatially distinct areas.

5.2 A soft spinal optoelectronic implant

Optogenetic control in the spinal cord offers an exciting approach to selectively modulate neural activity within these highly heterogeneous neural tissues. Based on the development of optoelectronic implants for the PNS (Chapter 3) and the experience gained from interfacing the spinal cord with compliant electrode arrays (Chapter 4), we proposed here a soft spinal μ -LED array for delivering optical stimulations in the mouse spinal cord. This thin ($< 100 \mu\text{m}$) implant fits in the epidural space and stretches to accommodate the spinal cord motion. I describe here its fabrication process and functional performances. Optical and thermal characterisations were then implemented to a computational model to evaluate the stimulation efficiency and safety for *in vivo* applications. Finally, I report on the implant bio-integration following chronic implantation using behavioural and histological analyses.

5.2.1 Spinal μ -LED array microfabrication

The spinal implant fabrication process, analogous to the one developed for the PNS application, is illustrated in Figure 5.2. Briefly, a $2 \mu\text{m}$ -thick layer of polyimide (PI2610, HD Microsystems GmbH) was spin-coated on a 4-inch silicon wafer and cured (2 hours at 300°C

5.2. A soft spinal optoelectronic implant

in a N₂ oven for hard bake). Next, a Ti/Au (20/300 nm) metallization layer was sputtered (AC450, Alliance Concept) on the PI substrate after O₂ surface activation. The conductive film was patterned by photolithography and etching (wet, RIE). The array interconnects were then encapsulated via spin-coating of a PI layer (1.6 μm -thick). The PI substrate and superstrate were patterned with a 2nd photolithography and RIE to the meander geometry and defined the connection pads for μ -LED integration. A 23 μm -thick layer of PDMS (Sylgard 184, Dow Corning) was spin-coated after O₂ surface activation of a sputtered SiO₂ adhesion layer (20 nm-thick). This coating layer was patterned to the final implant shape by photolithography and RIE using an hybrid Al and PR etch mask. Optical and electrical inspections attributed this fabrication process with a 90-100% yield across the wafer.

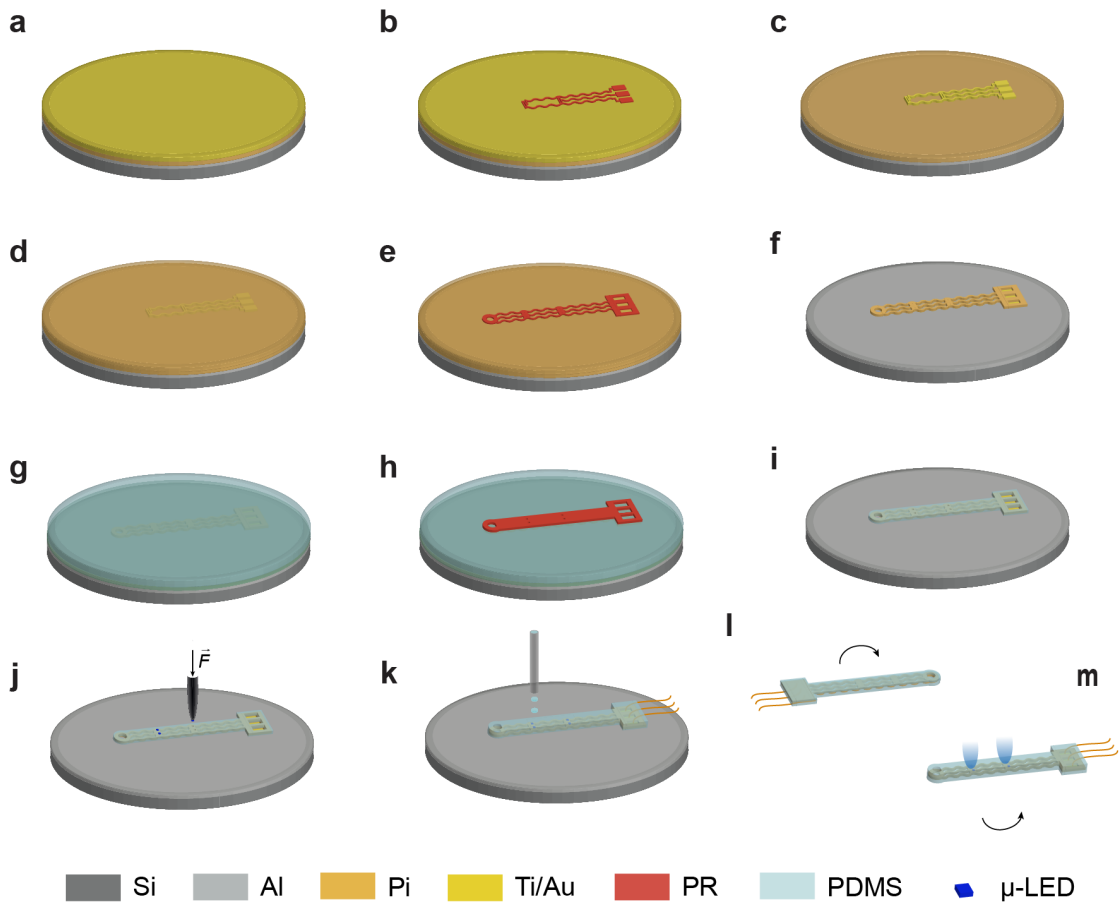


Figure 5.2 – Spinal μ -LED array microfabrication

a - c, Ti/Au photolithography and etching (wet + RIE) expose the implant interconnects. **d - f**, Encapsulation via spin-coating of a PI superstrate, followed by the patterning and RIE of the PI stack. **g**, PDMS is spin-coated after O₂ plasma activation of a SiO₂ adhesion layer. **h, i**, PDMS is patterned to the implant shape through photolithography and RIE. **j**, Integration of the μ -LEDs with a pick-and-place equipment. **k**, Wiring and encapsulation of the μ -LEDs with fine dispensing of PDMS. **l - m**, Release of the μ -LED array and PDMS coating of its backside.

Following these microfabrication steps, the μ -LED bare dies are integrated to the electrical circuit using a flip-chip approach. In order to fit in the mouse epidural space, smaller and thinner ($220 \times 270 \times 50 \mu\text{m}^3$) μ -LEDs (TR2227, Cree Inc.) were used. These dies were precisely deposited on the integration sites with a pick-and-place equipment. Following the reflow of the solder paste (SMDLTLFP10T5, Chipquik), the dies were first covered with a drop of a 14% by weight ratio solution of PIB (Oppanol, BASF) in cyclohexane (Sigma-Aldrich), and then with a drop of PDMS after O_2 plasma surface activation. Finally, the μ -LED array was released from the wafer after anodic dissolution of an Al layer, and the backside of the array was coated with PDMS. The differences in the dimensions of the spinal and peripheral optoelectronic implants are highlighted in Table A.2.

5.2.2 Spinal μ -LED array functionality

The spinal optoelectronic implant is presented in Figure 5.3. This array integrated 4 μ -LEDs, distributed over 2 independent channels for distinct light delivery in the rostro-caudal axis when implanted. A common anode configuration was used for these 2 channels, as it reduced the number of interconnects and fitted the ultra-miniaturized wireless system specifications. Each channel was composed of 2 μ -LEDs connected in a parallel fashion and spaced according to the spinal cord anatomy to allow homogeneous light delivery in both dorsal horns. The interconnects were patterned to a meander geometry and allowed the elongation of the array structure, designed to accommodate the surgical insertion and the motion of the spinal cord. Furthermore, the substrate flexibility facilitated the surgical insertion of the LED-mounted distal extension in the epidural space while the connector can be cemented over the dorsal column. The PDMS coating (Figure 5.3.b) softened the mechanical interfacing of the implant with the spinal cord and contributed to both its compliance (e.g. spinal cord morphology) and resilience (e.g. surgical insertion). Due to the narrow dimensions of the mouse epidural space, thorough preparation optimised the array thickness to a bare minimum. The maximum thickness of the implant was observed at the μ -LED, and was measured $< 80 \mu\text{m}$, including these successive layers: PDMS back encapsulation, PI stack, solder paste, μ -LED, PIB, PDMS front encapsulation. The minimal thickness of the implant was measured $> 40 \mu\text{m}$ at its most distal extension.

Next, we measured the optoelectronic performances of the spinal μ -LED array while sweeping gradually the current applied to one LED channel (i.e. 2 μ -LEDs in parallel; Figure 5.3.c). The total optical power at 460 nm was superior to 15 mW for $i = 25 \text{ mA}$. Translated to the μ -LED surface area ($A = 0.0594 \text{ mm}^2$), these measurements denote a high irradiance capability (12 mW optical power corresponds to an irradiance of 100 mW/mm^2), enabling efficient optogenetic stimulation in deep spinal structures. The increase in voltage allowed the miniaturized wireless system to provide a maximum current generally in the 25-30 mA range. This variability can arise from inconsistency in the μ -LED integration, the electrical wire connection, or simply due to the charge of the system battery.

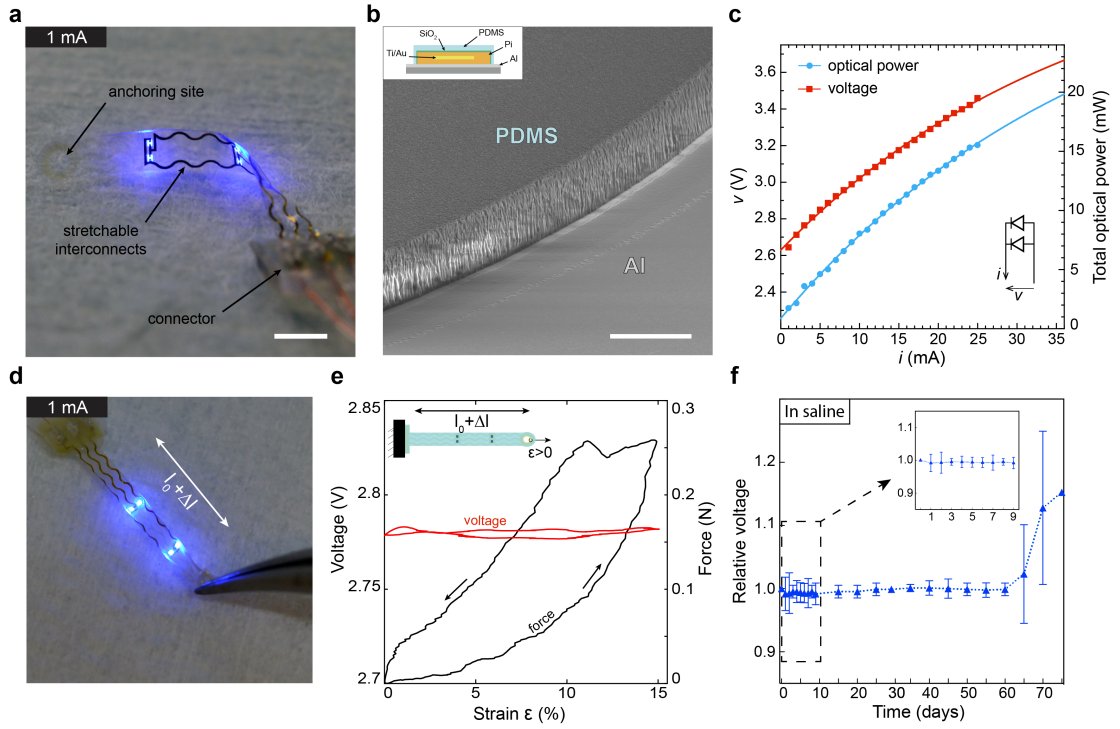


Figure 5.3 – μ -LED array for epidural optogenetic modulation in the spinal cord

a, Picture of the spinal optoelectronic implant. The device is composed of 4 μ -LEDs distributed over 2 distinct channels and integrated to a stretchable circuit. The anchoring site allows the implant to be pulled in the epidural space. Scale bar, 2 mm. **b**, SEM image of the PDMS coating patterned by photolithography (tilted view, 65°). Top left inset shows a schematic cross-section of an interconnect. Scale bar, 40 μ m. **c**, Array optoelectronic characterisation, I-V-P. The voltage across the 2 μ -LEDs and the total optical power were measured for incrementing current. **d**, **e**, The interconnect geometry allows for the elongation of the μ -LED array. The voltage and the force applied during an uniaxial stretch cycle to 15% strain were measured. The voltage remains stable during this tensile test. **f**, Accelerated ageing of the μ -LED array in saline solution at 67°C ($n = 3$ per group, mean \pm s.d.). There was no array functioning on day 75.

The stretchability of the μ -LED array dwelled in the interconnects designed with a serpentine geometry. These interconnects deflect out-of-plane with applied strains, resulting in the elongation of the structure. However, due to restricted dimensions and the integration of μ -LEDs, these interconnect geometry allowed only for a limited elongation ($< 20\%$ strain). The comparison in track geometry with the PNS implant is presented in Table A.2. We measured the voltage for a continuous $i = 5$ mA while applying an uniaxial stretch cycle to 15% strain (strain rate of $1\% \cdot s^{-1}$). The change in voltage remained minimal during the test (Figure 5.3.e). Although this range of elongation corresponds to the strains observed in the human spinal cord [79], further optimisation of the track geometry (e.g. width, opening angle) would allow for more stretchability, thereby promoting more robustness.

We evaluated the array encapsulation for long-term experiments with an accelerated ageing test. The devices were immersed in a saline solution and placed in an oven at 67°C. We measured the voltage for an applied $i = 5$ mA and reported the results (Figure 5.3.f). The devices started behaving erratically on day 65, and on the course of day 70-75, there was no device functioning. Optical inspections revealed an infiltration in the interconnects. Further accelerated ageing experiments would allow to extrapolate device functionality at 37°C. Compared with the PNS implant, this deterioration could be explained by the reduction in encapsulation thickness, principally in the PI layers.

The use of opsins with absorption spectra shifted from the blue to the red is particularly attractive for optogenetic interrogation of deep spinal circuits. In our current experiments, we modulate the activity of neurons expressing ChrimsonR (i.e. activating opsin) and Jaws (i.e. silencing opsin). Due to their early stage, these experiments will not be presented in this chapter. ChrimsonR and Jaws have respectively their spectral peaks at 590 and 635 nm [61, 62]. Due to the lack of red μ -LEDs with dimensions suitable a spinal application, we chose a phosphor-based light conversion approach (Figure 5.4). This phosphor-based technique was previously described in 3.2.3. Briefly, a phosphor-PDMS matrix at 50% weight ratio is applied at the surface of blue μ -LEDs. To fit the absorption spectra of ChrimsonR and Jaws, we used phosphors with emission peaks at 590 and 620 nm. The addition of this coating layer usually increased the thickness by 20-30 μ m. We measured the resultant emission spectra using a spectrometer (CCS200/M, Thorlabs) and represented the normalized spectral flux in Figure 5.4.b. The down-conversion of blue light produced emission peaks at 598 and 620 nm. These peaks were significantly larger compared with the narrow emission peak

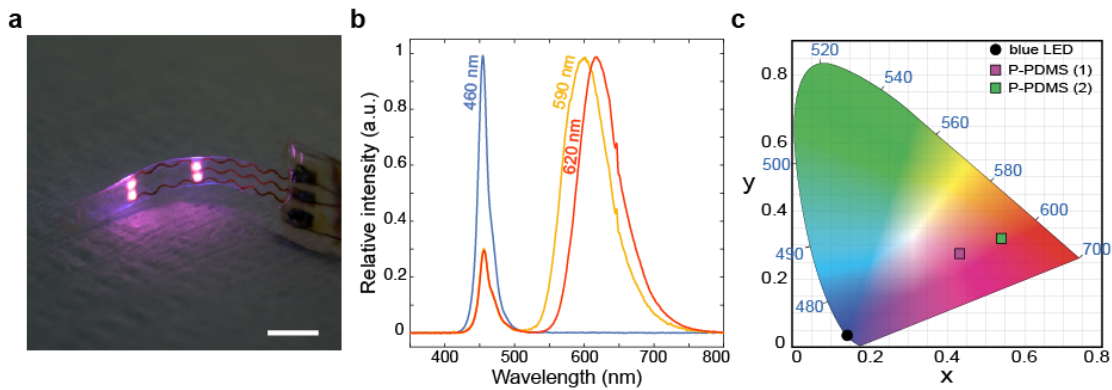


Figure 5.4 – Phosphor-based light conversion in the spinal μ -LED array

a, Picture of a spinal μ -LED array with a red (i.e. 620 nm) phosphor-based light conversion. The phosphor-PDMS matrix was applied specifically to the μ -LED surface. Scale bar, 2 mm. **b**, Emission spectra of spinal μ -LED arrays with phosphor-based light conversion of 460 nm light. Phosphor emission peaks are specified. Note the leakage of blue light for both light conversions. **c**, Color conversion represented in the CIE 1931 color space diagram. The dark circle represents the blue μ -LED, and squares the same μ -LED covered with a phosphor-PDMS matrix. The phosphor emission peaks were 590 nm (1) and 620 nm (2).

of the blue μ -LED (FWHM ~ 66 nm vs. 15 nm). Furthermore, the conversion of light was not total for both phosphors, as we measured small emission peaks around 460 nm. The transmission of blue photons through the phosphor-PDMS encapsulation resulted probably from its reduced thickness compared with the PNS application [172]. This incomplete color conversion was observable in the CIE diagram as the light emitted through the phosphor-PDMS matrix displayed a low purity (Figure 5.4.c). Although this phosphor technique is perfectible, the large absorption spectra and the high light sensitivities of ChrimsonR and Jaws make this approach workable.

5.2.3 Optical and thermal modelling

We designed the spinal μ -LED array for optogenetic interrogation in deep spinal structures. The μ -LED parallel distribution was based on the anatomy of the lumbosacral segments and allowed for homogeneous light delivery in the dorsal horns of the spinal cord. Yet, the propagation of light is limited by the tissue opacity. To predict the effective depth of optical stimulation, we developed a finite element model (FEM) of the μ -LED array activation at the surface of the spinal cord. Considering the spacing between the 2 LED channels (ca. 5 mm), we assumed their respective light beams do not overlap and modelled a single LED channel (i.e. 2 μ -LEDs in parallel). Furthermore, we modelled the spinal tissues as a non-homogeneous medium with constant absorption (μ_a) and reduced scattering (μ'_s) coefficients extracted from the literature at 480 and 660 nm. The methods relative to the development of the FEM are detailed in Appendix A.4.2. From these simulations, we first extracted the light transmission exponential decay in the spinal tissues (Figure 5.5.b). We found an attenuation of $\sim 95\%$ at depths of 300 μm , 500 μm for 480 nm and 660 nm lights respectively. As expected with the propagation of light in neural tissues, this attenuation was reduced for red light [67]. These results corroborated light transmittance measurements reported in [177] for an attenuation of $\sim 95\%$ at 500 μm for 470 nm light. Then, based on these FEM simulations, we represented the μ -LED array activation in the mouse lumbosacral spinal segments depending on the light irradiance and wavelength (Figure 5.5.c,d). Given the light sensitivity of ChR2 and its activation for 473 nm light at ~ 1 mW/mm² [236], we used this value to plot the extent of light propagation. Optical stimulations at 480 nm and 50 mW/mm² were restrained to the dorsal horns of the spinal cord and higher irradiances (e.g. 150 mW/mm²) scarcely reached the spinal cord central canal. For comparison, we represented the correspondent boundary for 660 nm light and found that an irradiance of 100 mW/mm² would be transmitted to the ventral horns of the spinal cord. However, these results at 660 nm cannot be translated directly to the spinal μ -LED array as our experiments involved optical stimulations at 590 and 620 nm. Moreover, we did not reported the irradiance of light following a phosphor-based conversion. The addition of a phosphor layer and the partial conversion is likely reducing irradiance. Conversely, red-shifted opsins have generally higher sensitivity to light compared with ChR2. For instance, a low irradiance of 0.015 mW/mm² at 617 nm was reported sufficient for the activation of Chrimson [62]. Finally, this light propagation model did not take into account the array conformability when surfacing the spinal cord.

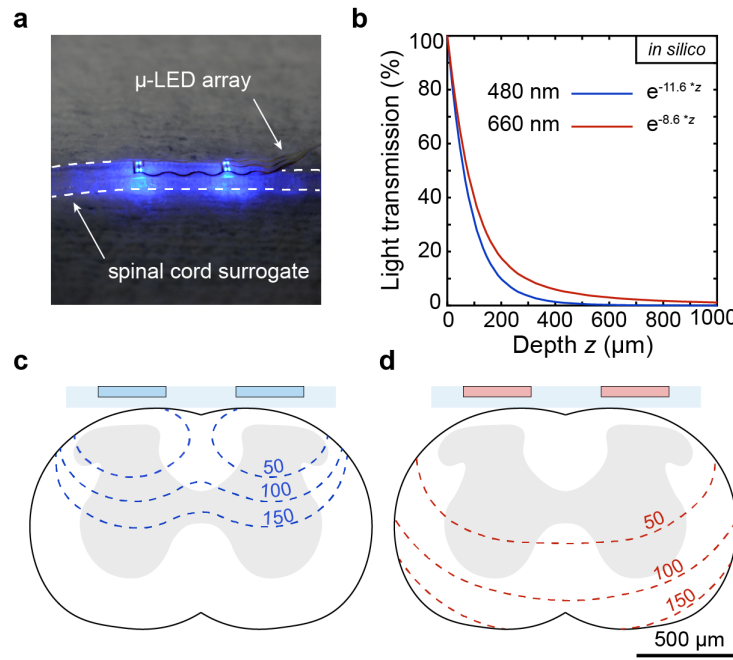


Figure 5.5 – Light propagation in spinal tissues

a, Picture of the μ -LED array placed on an agarose gel surrogate of mouse spinal cord. The μ -LED activations are colocalized to 2 areas. Note the internal light reflection due to the surrogate transparency. **b**, Computational modelling of light transmission in spinal tissues depending on the incident light wavelength. Red (660 nm) light propagates deeper compared with blue (480 nm) light. **c**, **d**, Representation of the μ -LED array light propagation in a mouse lumbar spinal level. The dashed curves represent the 1 mW/mm^2 boundary for different initial irradiances (50, 100, 150 mW/mm^2). Blue light (**c**) is further attenuated compared with red light (**d**). Light blue represents the PDMS encapsulation.

High irradiance optical stimulations are further propagating in the neural tissues. On the other hand, such activation of the μ -LEDs would generate significantly more heat and could harm the surrounding biological tissues [171]. We measured the changes of temperature at the surface of the spinal μ -LED array using an infrared camera (A325sc, FLIR) for incrementing duty cycles (DC) and irradiances, and following a 1 minute μ -LED activation (Figure 5.6.a). We found that activation at 50% DC and 150 mW/mm^2 generated an increment of 14°C at the surface of the device. We modelled the heat generation and its dissipation in the array encapsulation (Figure 5.6.b, methods described in Appendix A.4.3). These simulations correctly corroborated the temperature changes for an irradiance of 50 mW/mm^2 but failed at 100 and 150 mW/mm^2 . Nevertheless, we represented the correspondent propagation of an increment of 0.5°C in the spinal tissues for a fixed DC at 20% (Figure 5.6.c). This boundary reached the superficial layers of the dorsal horns of the spinal cord for an irradiance of 150 mW/mm^2 . On-going work is dedicated to the improvement of this model and measurements of the temperature at the μ -LED surface is being investigated. In order to safely stimulate deep spinal structures (e.g. GABAergic interneurons would require 10-50% DC [112]), we will model the rise of temperature with respect to the μ -LED activation duration [237].

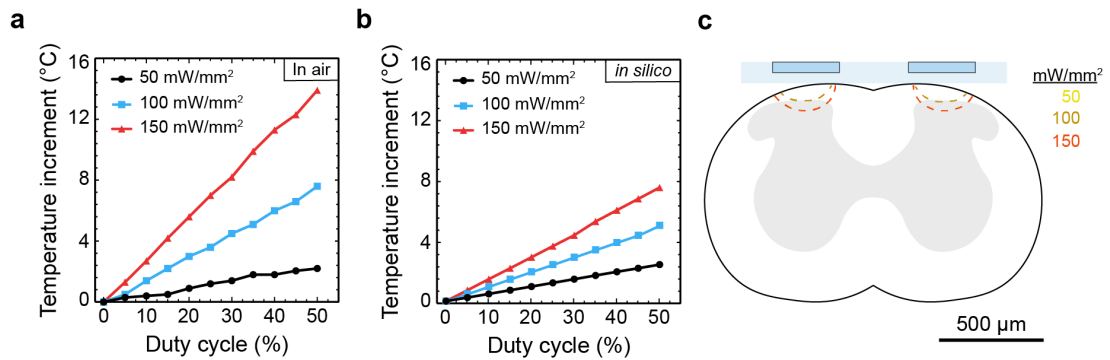


Figure 5.6 – Heat generation with μ -LED activation

a, Changes in temperature at the surface of an operating array depending on the optical irradiance and the μ -LED duty cycle. These measurements were conducted in air with an infrared camera. **b**, Computational modelling of the temperature at the surface of an operating array depending on the optical irradiance and the μ -LED duty cycle. The model behaves correctly for an irradiance of 50 mW/mm² but fails at 100 and 150 mW/mm². **c**, Representation of the temperatures changes in spinal tissues depending on the irradiance. The duty cycle was fixed at 20%. The dashed-curves represent the 0.5°C temperature increase boundary. At 50 mW/mm², this boundary was contained in the PDMS.

5.2.4 Bio-integration of the spinal μ -LED array

The spinal μ -LED array was designed to mechanically interface with the spinal cord to deliver optical stimulations in several spatial areas. We emphasized previously its minimal thickness, built-in stretchability and elastomeric coating, tailored to the mouse epidural space. The implantation procedures consisted in sliding carefully the μ -LED strip over the dura mater with a thin thread attached to its extremity (Figure 5.7.a-c). The implantation procedure is described in Appendix A.4.4. This technique required 2 partial laminectomies at T12-T13 and L2-L3, making this implantation arguably less-invasive compared with fiber-based spinal interfaces. We fixed the connector with a spinal orthosis attached to the spinal column to avoid implant migration. We observed the μ -LED array position *in vivo* after 2 weeks of implantation via microcomputed tomography (Figure 5.7.d,e; methods described in Appendix A.4.5). Through the CT scan resolution, the μ -LED array conformed to the spinal cord dorsal morphology without causing compression and maintained its original position. These results confirmed the surgical procedure for weeks of implantation.

Next, we assessed the device bio-integration with histological analyses following long-term (i.e. 6 weeks) implantation (Figure 5.8). Immunohistochemistry targeting the expression of markers for astrocyte reaction (i.e. GFAP) and neuro-inflammatory responses (i.e. Iba1) demonstrated the implantation did not trigger a significant immune response compared with healthy mice (Figure 5.8.b-e). Methods relative to this histological process are described in Appendix A.4.6. Furthermore, we measured the circularity of cross-sections at the lumbosacral spinal level and did not observe a significant change compared with the healthy mouse group (Figure 5.8.f). These results demonstrated the μ -LED array did not compress mechanically the spinal cord

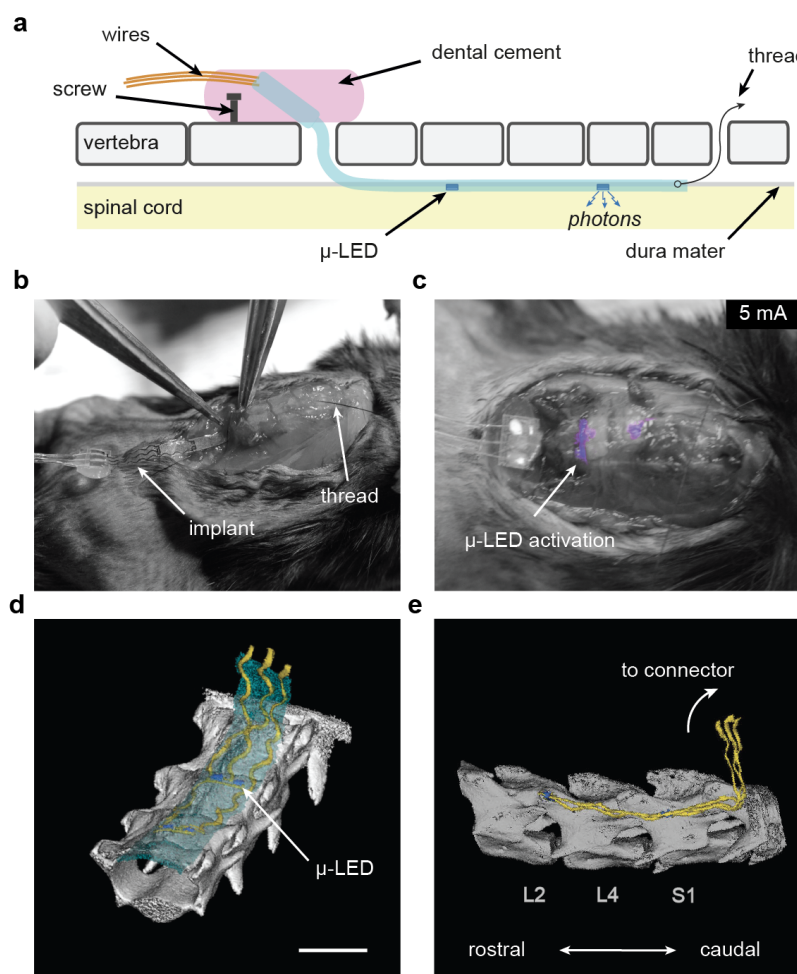


Figure 5.7 – Implantation of the spinal μ -LED array in the mouse epidural space

a, Illustration of the surgical procedure for the spinal μ -LED array implantation. A thread allows the implant to be pulled in the epidural space, placing the μ -LEDs above the dura mater. A vertebral orthosis secured the connector for long-term functionality of the implant. **b, c**, Pictures of the surgical procedure. Following insertion, the μ -LEDs are tested and their activation is visible through the vertebrae (**c**). **d - e**, 3D reconstructions of the spinal implant and the spinal column after CT scan (grey, vertebrae; yellow, interconnects; dark blue, μ -LEDs; light blue, PDMS coating). Scale bar, 2 mm.

over the time of implantation. Altogether, these results emphasized on the implant adequate bio-integration to deliver fine optogenetic stimulations to intact spinal tissues.

Finally, we assessed the spinal μ -LED array bio-integration with behavioral analyses (Figure 5.9). Mice were implanted with the spinal device and penetrating bipolar EMG electrodes in the *gastrocnemius medialis* and *tibialis anterior* hindlimb muscles. Although the implantation of EMG electrodes may affect the mouse locomotion, this configuration was relevant for future optogenetic experiments. Methods relative to the kinematics recording are analogous to the one presented in Chapter 4 (Appendix A.3.10). First, we compared the kinematics of a mouse

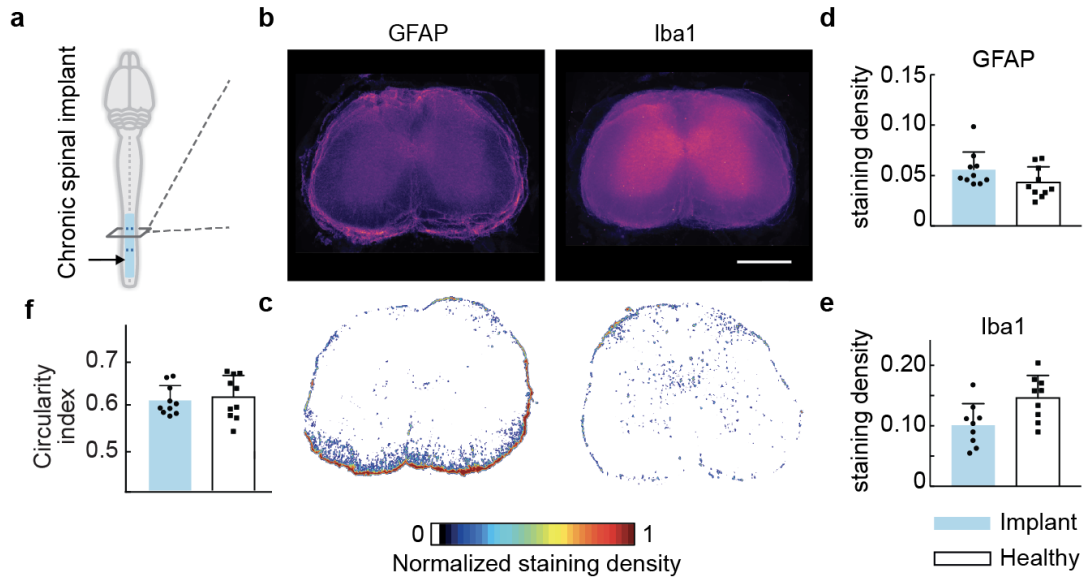


Figure 5.8 – Histology of the spinal cord following long-term belt implantation

a, Schematic of the mouse CNS illustrating the μ -LED array placement over the spinal cord. **b**, Stacked images of the lumbosacral spinal segment stained for GFAP and Iba1 to reveal neuro-inflammatory responses following 6 weeks of implantation. Scale bar, 500 μ m. **c**, Representative quantification of staining density following digitalization with constant threshold parameters. **d - f**, Bar plots reporting values of computed GFAP density (**d**), Iba1 density (**e**) and circularity index (**f**) for each group ($n = 10$ for implant and healthy; mean + s.m.). No statistical significances were found (paired t-tests, $p > 0.1$).

walking on a treadmill before the implantation and 3 days post-surgery (Figure 5.9.a). At this early time point, the mouse locomotion was not visually hampered. Then, we ran the same comparison with an horizontal ladder task to assess finer locomotor skills (Figure 5.9.b). At this early stage, the mouse was able to walk across the ladder, yet the kinematics revealed the mouse locomotion may be impaired. We quantified the number of missed steps on the ladder task and plotted its progression at relevant time points (Figure 5.9.c). Mice exhibited a slight ($< 10\%$) deficit at 5 days and 2 weeks post-implantation. Future experiments may investigate if this impairment was caused by the EMG electrodes or the spinal array. We also investigated the mouse sensorimotor coordination with a rotarod test 5 days post-surgery (Figure 5.9.d) and did not observe a significant loss of coordination during this task. In general, these behavioural results corroborated the histological analyses and demonstrated fine bio-integration of the spinal μ -LED array. The swift recovery of the mice following its implantation enabled optogenetic interrogation of locomotor-related spinal circuits.

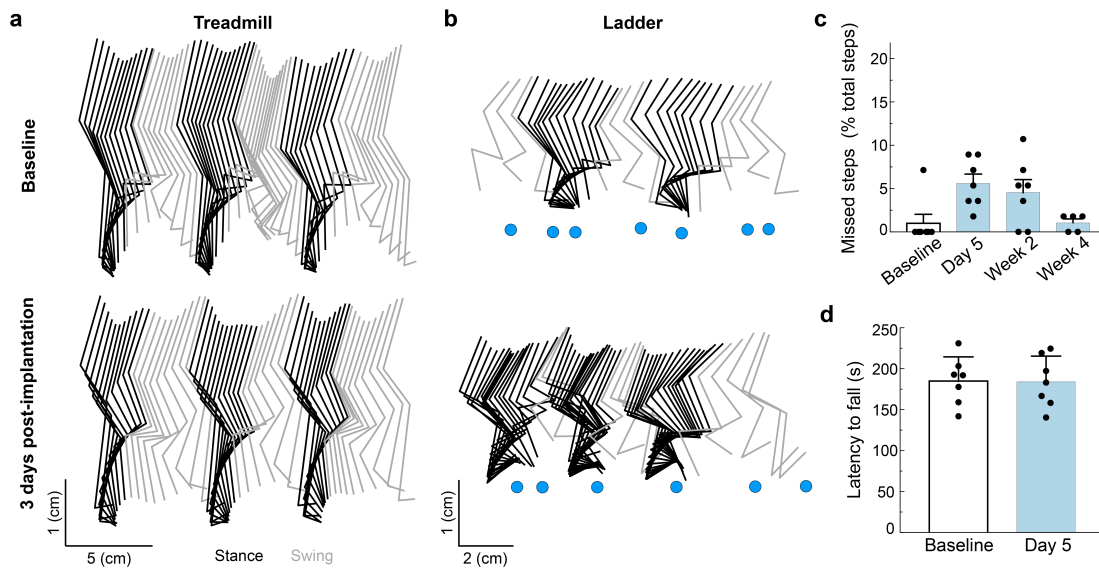


Figure 5.9 – Behaviour analyses following implantation of the spinal μ -LED array and hindlimb EMG electrodes

a, b, Representative stick diagrams of the mouse left hindlimb kinematics on a treadmill (**a**; belt speed: 17 cm/s) and a ladder (**b**), before or 3 days post-implantation. **c**, Quantification of the number of missed steps during the ladder test ($n = 7$, mean + s.m.). **d**, The latency to fall of mice on an accelerating rotarod prior to the implantation and 5 days post-implantation ($n = 7$, mean + s.m.). No statistical significance was found (paired t-test, $p > 0.5$).

5.3 Epidural optogenetic stimulation in the spinal cord

We have developed a spinal μ -LED array to conduct optogenetic experimentations in awake, freely-behaving mice. Previously, we characterised the spinal μ -LED array *in vitro* and *in silico* with high optical capabilities, allowing optogenetic interrogation of deep spinal structures. Moreover, we demonstrated the μ -LED array seamless bio-integration over long-term implantation, motivating the delivery of selective optical stimulations in intact neural tissues. Together with our colleagues from Courtine's group, we demonstrate the functionality of this implant *in vivo*. We implemented the spinal array to the ultra-miniaturized wireless head-stage presented in Chapter 3 (cf. 3.1.3) to drive the μ -LED activation. As a proof-of-concept, we report the recruitment of motor units with epidural optogenetic stimulation in *Thy1::ChR2* mice.

The light-activated ion channel ChR2 was expressed under the Thy1 promoter in a broad class of excitatory neurons in the spinal cord (Figure 5.10). As presented in Chapter 2, Thy1 is expressed both in sensory afferents and motor efferents. Groups have also reported its expression across locomotion-associated interneurons in the spinal cord [238, 239]. Furthermore, optogenetic stimulation of Thy1⁺ neurons in the lumbosacral spinal cord has been shown to evoke motor outputs in anesthetized mice [94, 240]. These motor outputs are likely induced by the optical stimulation of Thy1⁺ interneurons in lamina VII (i.e. large area in the grey matter

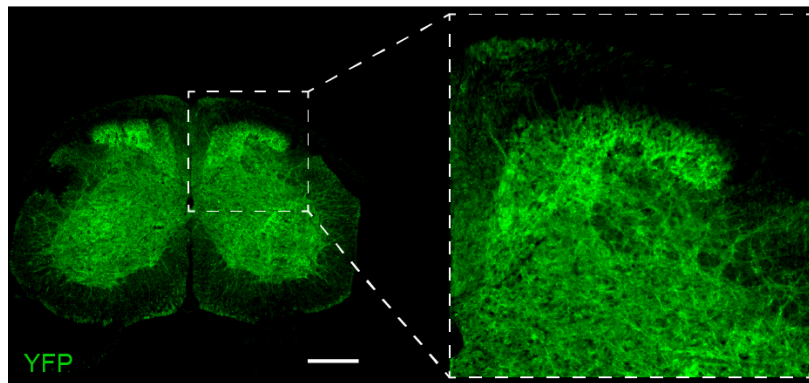


Figure 5.10 – Expression of ChR2 in the spinal cord of *Thy1::ChR2* mice

Histological picture of the spinal cord cross-section highlighting the broad expression of ChR2-eYFP in *Thy1::ChR2* mice. Scale bar, 250 μm .

surrounding the central canal) that are monosynaptically connected to motoneurons. Hence, these evoked motor outputs in the mouse hindlimbs displayed complex force fields depending on the optical stimulation locus. The recruitment of motor units through epidural optical stimulation of Thy1^+ neurons in awake animals has not yet been reported.

We implanted *Thy1::ChR2* mice with the spinal μ -LED array and bipolar EMG electrodes in the *iliopsoas* (IL, hip flexion) and *tibialis anterior* (TA, ankle flexor) muscles. Following the recovery of the mice from the surgical procedure (> 3 days), we tested whether optogenetic stimulation of Thy1^+ neurons in non-anaesthetized conditions would produce EMG activity in the mouse hindlimbs. Methods describing EMG data acquisition are presented in Appendix A.4.7. During the experiment, mice were restrained in a vertical position with their hindlimbs hanging and received single pulse optical epidural stimulations. Each stimulation through the wireless system triggered the EMG acquisition system. In a parallel experiment, we appended the recording of hindlimb kinematics. The results from these experiments are presented in Figure 5.11.

Epidural optical stimulation through the μ -LED array produced motor outputs in the mouse hindlimbs as demonstrated with the kinematic and EMG recordings (Figure 5.11.a,b). The μ -LED spatial distribution allowed for 3 independent stimulation configurations (i.e. stimulation at L2, S1 or both). Movements induced by the optical stimulation were differentiated by the stimulation configuration. Stimulation at L2 evoked a strong flexion in the hip joint whereas stimulation at S1 produced flexion in both the hip and the ankle. These characteristic movements transcribed distinct EMG activities. Stimulation at L2 resulted in a higher activity in the IL compared with the TA hereof. Optical stimulation at S1 or both L2 & S1 produced important activity in both the IL and the TA. We quantified the recruitment of motor units for incrementing stimulation amplitudes (Figure 5.11.c). As suggested, stimulation at S1 or both L2 & S1 recruited significantly more the TA compared with stimulation at L2 only. The IL did not exhibit a significant selectivity for any of the configurations. Stimulation at L2 tended

scarcely to be more selective for IL. Finally, we quantified the changes in joint angle induced by epidural optical stimulations (Figure 5.11.d). The hip joint displayed significantly bigger flexion for stimulations at S1 compared with L2. We hypothesized that due to the spinal cord anatomy, the rostral configuration targeted activation in lamina VII interneurons that are connected with IL-innervating motoneurons. Conversely, the caudal configuration recruited TA-innervating motoneurons and the IL posterior dorsal root fibers. Future experiments will investigate this hypothesis via the study of the delay for EMG activity and using markers for neuronal activity (e.g. c-Fos). In addition, we did not observe any motor outputs with epidural optical stimulations carried in wild type mice, confirming these results were not caused by stimulation artefacts. These results demonstrated the spinal μ -LED array functionality *in vivo* and the benefits of distributing spatially optical stimulations over the spinal cord.

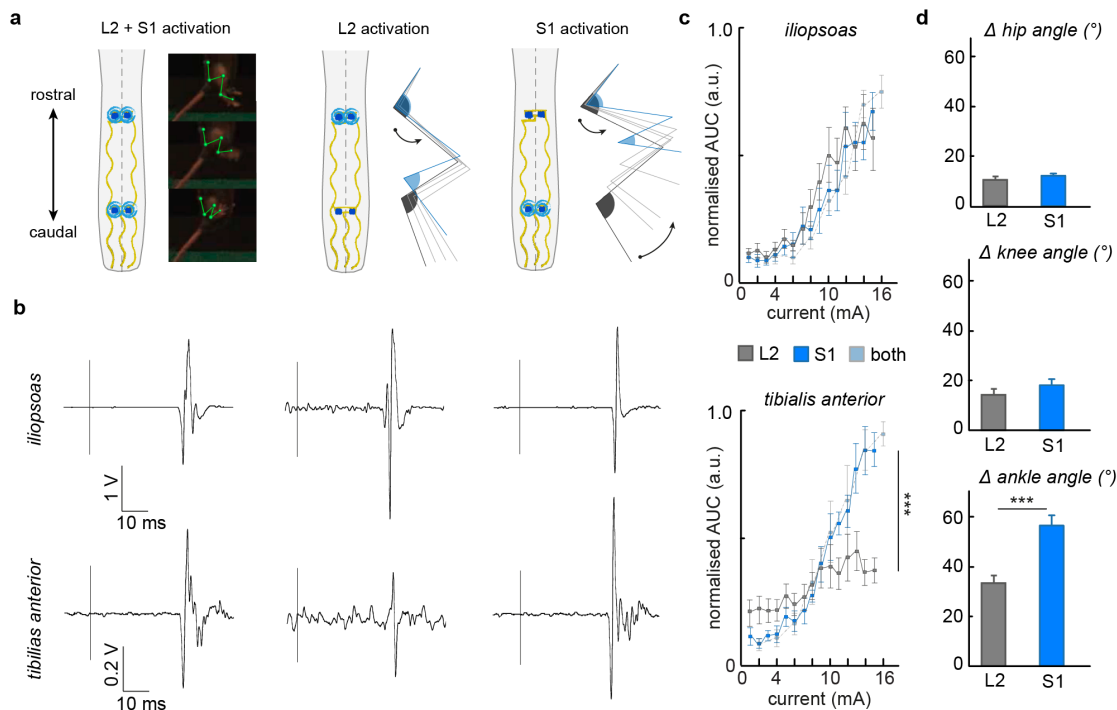


Figure 5.11 – Orderly recruitment of motor units with epidural optical stimulations in *Thy1::ChR2* mice

a, Illustration of the distribution of μ -LEDs at the spinal cord surface. The array allows for 3 independent stimulation configurations (i.e. L2, S1 or both). Stick diagrams of the characteristic hindlimb movements following single pulse epidural stimulation. Black sticks, initial position. Blue sticks, final position. **b**, Representative EMG traces in the *iliopsoas* and *tibialis anterior* muscles elicited via a single pulse epidural optical stimulation (pulse width 5 ms, current amplitude 12 mA) and depending on the stimulation configuration. The wireless system introduced a latency of ~ 20 ms. **c**, EMG quantification for each muscle depending on the stimulation current and the array configuration ($n = 5$ mice, 3-5 pulse per condition per mouse, mean \pm s.m.; AUC, area under the curve). Stimulation at S1 was more specific for the recruitment of the *tibialis anterior*. **d**, Quantification of the hindlimb kinematics following single pulse stimulation at L2 or S1. Stimulation at S1 induced significantly more flexion of the ankle (5 ms pulse width, current amplitude 10 mA; mean \pm s.m.; ANOVA, *** $p < 0.001$).

5.3. Epidural optogenetic stimulation in the spinal cord

Futhermore, we investigated the stimulation specificity and selectivity by delivering different epidural stimulation modalities in a *Thy1::ChR2* mouse (Figure 5.12). In order to compared the stimulus-evoked motor outputs, these stimulations were carried in the same animal. The mouse was administered general anaesthesia (mixture of 80 mg ml⁻¹ ketamine, 10 mg ml⁻¹ xylazine, diluted in saline) using intraperitoneal injections (8.5 ml kg⁻¹). Then, we recorded at the IL and TA EMG activity while delivering epidural optical stimulations at various wavelengths. Distinct μ -LED arrays were used for each wavelengths. Optical stimulations at 460 nm exhibited a coherent selectivity for the TA when stimulations were carried in S1. Moreover, stimulations at L2 recruited selectively more the IL compared with stimulations at S1. Ketamine/xylazine anaesthesia is associated with strong analgesic effects, silencing neuronal activity in the somatosensory system [241, 242]. We hypothesized that these optical stimulations did not effectively recruit *Thy1*⁺ neurons in the afferent fibers, but most likely did in the lamina VII interneurons and deeper motoneurons. This hypothesis was correlated to the high stimulation amplitudes used during this experiment (e.g. 30 mA corresponds to ~150 mW/mm²). The absence of EMG activity for optical stimulations at 535 and 650 nm validated the wavelength-specific activation of ChR2. Interestingly, high amplitude stimulations at 590 nm produced limited EMG activity. These results reflected the partial conversion of light with the phosphor-based approach at 590 nm (cf. Figure 5.4). Finally, we compared optical and electrical stimulations by delivering EES at L2 and S1. Electrical stimulations did not exhibit any selectivity for IL or TA based on the stimulation locus. In anesthetized conditions, EES produced a "all-or-none" recruitment of motor units. Altogether, these results emphasized the cell-type selectivity of optogenetics and the validation of the μ -LED array to deliver spatially-distributed, effective optical stimulations in the spinal cord.

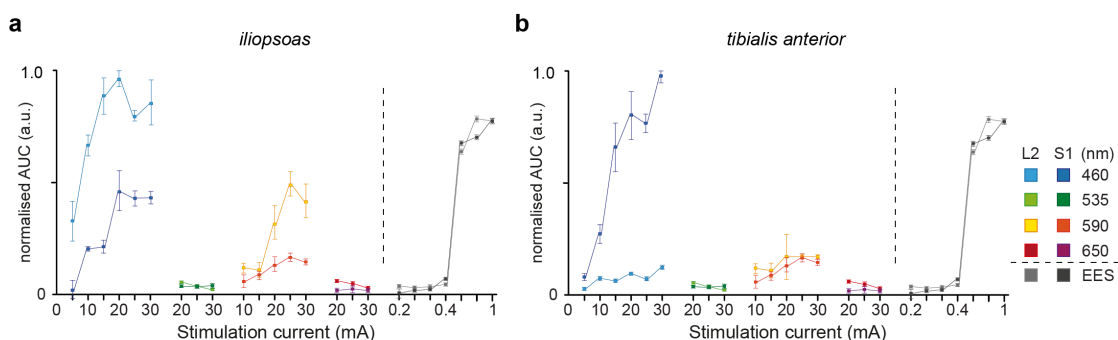


Figure 5.12 – Wavelength and modality specific recruitment of motor units

Recruitment of motor units in the *iliopsoas* (a) and *tibialis anterior* (b) muscles depending on the stimulation optical wavelength and the stimulation modality (optical vs. electrical) in an anesthetized *Thy1::ChR2* mouse (pulse width 5 ms, $n = 3-5$ pulses per condition, mean \pm s.m.). The different wavelengths were obtained using distinct μ -LEDs (460 and 535 nm) or with the phosphor light conversion approach (590, 650 nm). EES were carried with the insertion of wire electrodes in the epidural space. Light and dark colors represents stimulation at L2 and S1 respectively.

5.4 Discussion

We developed a soft and thin μ -LED array for optogenetic modulation of spinal neural circuits. Compared with fiber-based optical interfaces, the surgical implantation did not require a large lumbosacral laminectomy, preserving the integrity of the dorsal column [112]. Furthermore, the delivery of optical stimulations through an optic fiber or a LED-mounted device fixed to the vertebrae suffers from inconsistency in the precise stimulation locus. The dorsal column and the spinal cord motions, even though closely correlated, can vary in a rostro-caudal translation-like movement [243]. Our μ -LED array surfaced directly the spinal cord and maintained its initial position after weeks of implantation. In addition, current optical and optoelectronic implants interface optically the spinal cord in a single area. Bilateral stimulation requires the placement of a light source/fiber on the dorsal midline [101, 177], which is not ideal for optogenetic modulation in the lateral aspects of the grey matter. This statement is exacerbated in the case of limited irradiance capability. Although unilateral stimulation enables the delivery of light more homogeneously in the grey matter (e.g. in the dorsal horn) [99, 112], this approach reduces *de facto* the scope of the optical stimulation. Conversely, our strategy enables bilateral, homogeneous light delivery, promoting deeper optogenetic interrogation of spinal circuits. Moreover, our spinal implant distributes μ -LEDs along the rostro-caudal axis, allowing to probe spatially distinct areas. We demonstrated the benefits of this approach via functionally-selective stimulation of broadly-expressed Thy1^+ neurons.

The spinal μ -LED array exhibited remarkable bio-integration properties. These results reflected efforts undertaken towards minimizing its footprint and the mechanical mismatch between the implant and the spinal cord. The combination of thin (i.e. with a low bending stiffness) interconnects patterned to a meander geometry and a soft elastomeric coating promoted conformability and compliance with the static and dynamic nature of the spinal cord. However, the dimensions of the mouse spinal cord and the pitch of the μ -LEDs hindered the interconnect geometry, hence reducing the implant compliance to elongation. Further optimisation of the track geometry (e.g. width, opening angle) would grant a few extra per cent of strain. Accommodating significantly larger deformations would require fundamental changes. Engineering elasticity in the metal film through the patterning of Y-shaped motifs is an appealing strategy as it allows stretchability in a track with a linear geometry [221]. However, the increase in track resistivity would hamper powering with a battery system. Biphasic (solid-liquid) metal thin films using gallium are highly stretchable and display a low sheet resistance [244]. Moreover, this metallisation process is compatible with elastomeric substrates, which would enable the fabrication of softer implants. However, these films are prone to corrosion which would significantly limit long-term functionality when implanted [245].

We implemented the spinal μ -LED array to the ultra-miniaturized wireless head-stage to promote untethered experimental conditions. This characteristic is crucial for the study of fine locomotion modulation requiring naturalistic behavior. However, in our current experimental set-up, the recording of EMG activity involves the tethering of the animal to the

acquisition system. The development of bi-directional (i.e. stimulation and recording) wireless systems would enable minimal disruption of the animal behavior. Furthermore, integrating the recording of electrophysiological and/or external (e.g. kinematics) signals would allow in the future to tailor the optical stimulations in the temporal and spatial domains. This may steer the development of innovative spatiotemporal neuromodulation protocols [202]. Finally, the long-term functionality of the spinal μ -LED array suffers from the deterioration of the subcutaneously implanted wires. Further optimisation of the wireless system would enable its implantation and its integration to the spinal μ -LED array. For instance, near-infrared power transmission allows to charge a battery through the skin [246].

Finally, from a neurobiological point of view, optogenetic modulation in the spinal cord offers a vast range of applications. First and foremost, the spinal cord anatomy allows to probe easily somatosensory neural circuits. Epidural optical stimulations target both afferent fibers and superficial dorsal horn interneurons. The selective stimulation of sensory-related neuronal populations would allow to dissect the mechanisms involved in peripheral and central sensitizations [247]. An approach combining neuromodulation of these subpopulations with concomitant activation of nociceptors (via thermal or mechanical noxious stimuli) would investigate the spinal circuits involved in the gate control [3]. For example, alleviation of neuropathic hyperalgesia was reported with the pharmacogenetic activation of glycinergic neurons (i.e. GlyT2⁺) in the dorsal horn [248]. An optogenetic approach would enable further spatial (i.e. localized light delivery) and temporal control of these neurons. The μ -LED array emission spectrum can be tailored to suit hyperpolarizing opsins for selective silencing of neural activity. Optogenetic inhibition of projection neurons that express the neurokinin-1 (NK1) receptor may prevent the transmission of nociception to the brain [249]. Furthermore, the spinal μ -LED array enables optogenetic interrogation of deep neural structures, allowing the deciphering of the locomotion circuitry. The fine parsing of these circuits may be essential to comprehend the mechanisms involved in the restoration of locomotion after SCI. Epidural optogenetic stimulation may also target proprioceptive fibers (e.g. PV⁺ neurons) and emulates the recruitment of motor units of EES [44]. Upon success, it would not be far-fetched to imagine recruiting specific motor units innervated by neurons expressing spectrally distinct opsins via a single spinal implant [127].

5.5 Conclusion

In this chapter, I presented a soft optoelectronic implant capable of delivering optical stimulations in the spinal cord. This device integrated an array of μ -LEDs to a stretchable and compliant circuit coated with a thin silicone layer. The μ -LED disposition and the implant opto-electrical properties enabled optogenetic modulation in deep neural structures. Computational modelling of light propagation in spinal tissues corroborated this argument. Following long-term implantation in the mouse epidural space, the spinal μ -LED array demonstrated a seamless bio-integration. We validated its functionality *in vivo* by orderly recruitment of motor units with epidural optical stimulation in *Thy1::ChR2* mice. The unique distribution of

μ -LEDs allowed to selectively target activation in functionally distinct muscle groups. Finally, we proposed this optoelectronic implant as a tool to unravel the spinal circuitry in untethered, freely-behaving conditions.

5.6 Contribution

Data presented in this chapter are the result of a team effort :

- I developed the spinal μ -LED array and characterised its functionality *in vitro*. I assisted during the surgical procedures and the behavioural recordings. I analysed the data relative to the implant bio-integration.
- Claudia Kathe designed the experiments for validation *in vivo*. Claudia performed the surgical procedures and the tissue preparation for histology. Claudia also analysed the EMG and kinematic data.
- Noaf Alwahab made the computational models for light propagation and heat dissipation.
- Philipp Schönle, Noé Brun and Pascale Meier developed the ultra-miniaturized wireless head-stage used for stimulation.
- Laurent Vinet performed the CT scans.

6 Discussion and perspectives

6.1 Selective neuromodulation

In this thesis, I introduced a variety of neural interfaces seeking to improve the selectivity of neuromodulation, primarily in the somatosensory system. These interfaces achieved this goal by either utilizing the optogenetic technology or via the spatial distribution of neural electrodes at the surface of a targeted structure. For the first approach, I developed two peripheral neural implants capable of carrying epineural optical stimulations in the mouse PNS. Delivering selective neuromodulation downstream the afferent signals is of primary interest for the study or suppression of pain. Furthermore, interfacing peripheral nerves with a passive, optic fiber-based implant presents several advantages, including a relative simplicity and a high optical efficacy. Yet, the mechanical stiffness of silica fibers hampers the interfacing of thinner and more delicate peripheral nerves. Nevertheless, the development of implantable, highly flexible and stretchable optical waveguides offers an opportunity to expand this concept. Groups have reported on such light-guiding conducts using polyethylene glycol-based hydrogels [250] or monocrystalline silicon filaments [251]. Coupling efficiently these waveguides to a implantable light source remains a non-addressed challenge. Progress in photonics towards the miniaturization of InGaN laser diodes may steer the development of relevant optical coupling solutions [252].

LED-mounted interfaces represent an alternative to the optic fiber approach. The implantation of multiple, micrometric light sources at the vicinity of the neural tissues enables further spatial selectivity, and potentially over larger areas. Yet, the development of higher resolution, biologically transparent and long-term μ -LED implants remains an intense field of research. The technologies underlying these advancements will necessarily promote conformal integration and dynamical compliance. I discuss possible neurotechnology routes in the next section. Progress in optoelectronics will foster more selective optogenetic interrogation of the nervous system. This may include the emergence of smaller (so called "cellular-scale") μ -LEDs with improved optical capabilities, enabling to finely localised multiple optical stimulations [147]. Optoelectronics may also expand the μ -LED wavelength repertoire with solutions matching

recently engineered opsins. This would support future experiments for simultaneous selective modulation of multiple neural subsets expressing spectrally-distinct opsins. Finer conversion of light, using quantum dot downconverters for example [253], may address this challenge. Finally, the advent of organic light emitting diodes (OLEDs) in consumer electronics will steer the development of truly soft and compliant optoelectronic devices. This technology has already been proven capable of effective optical stimulation in *drosophila* [254]. Its translation to implantable devices suffers from several pitfalls, such as a poor optical performances and stability. In optogenetics, this technology may be first applied to transdermal stimulation applications. These light-emitting devices could take the form of a skin patch and deliver selective, non-invasive neuromodulation therapies.

Although electrical stimulation is not granted with optogenetic exquisite resolutions, the distribution of small neural electrodes at the surface of a targeted structure can achieve a certain level of spatial and structural selectivity. Many factors may influence the selectivity of electrical stimulation, including the dimensions and materials of the electrode, the implant conformability and interface resolution with the neural tissue, the stimulation parameters (e.g. mode, pulse waveform, current amplitude, frequency, pulse width) and the tissue intrinsic properties for its electrical stimulation (e.g. chronaxy, morphology). Unlike optogenetics, this quest for electrical stimulation selectivity can be rapidly translated into clinical applications. The emergence of bioelectronics, defined as a new class of medicines based on electrical neuromodulation of the PNS [131], represents an opportunity for the validation of selective therapies. The miniaturization of electrodes with a parallel improvement of their electrochemical properties (e.g. impedance, charge injection capacity) is sought for fine tailoring of neural activity. Conducting polymers, such as PEDOT:PSS, may answer this challenge. However, this electrode coating material suffers from a low stability and a tendency to delaminate after prolonged implantation. Groups have recently reported highly stretchable variations of PEDOT:PSS that may solve these issues [255, 256]. Then, the use of soft technologies for interfacing neural structures will improve conformability, granting a better contact of the electrodes with the tissues. This strategy enables to refine the stimulation electrical field, thus improving its selectivity. Finally, improving the electrode density has potential for accessing specific functional targets. The benefits of this strategy may be amplified by the application of multipolar stimulation protocols. However, this increase in the interface resolution is technically nontrivial. Although the development of multiplexed electrocorticographic (ECoG) arrays offers some answers to this problem, their lack of conformability hinders selectivity [257]. An alternative solution may be the integration of ASIC chips into soft neural implants. Yet, the soft to hard integration remains challenging.

6.2 Towards softer and more robust neurotechnologies

The soft neural implants presented in this thesis interfaced mechanically with the nervous system without triggering any harsh form of foreign body reaction. Compared with more traditional implantable electronics, these implants matched more closely the mechanical

properties of the underlying biological tissues. Furthermore, engineering soft properties into neural interfaces is sought for improving conformability, thus allowing to access more intricate areas. Moreover, the peripheral nerves and the spinal cord are highly dynamic tissues, exhibiting tensile strains of tens of per cent. Soft neural implants are designed to emulate this range of motion. Recent progress in material science and microengineering offer new perspectives for the development of softer, more conformable and long-term implants.

One major component in the fabrication of soft neural interfaces is the substrate and superstrate material. PDMS, in particular Sylgard 184, is a common silicone in the field. Yet, its mechanical properties may not suit emerging implantable electronic applications. Ideally, these elastomers should exhibit a high compliance (e.g. maximum elongation) with a concomitant resilience (e.g. tear strength). In this thesis, I explored the use of softer silicone elastomers to interface the sciatic nerve and the spinal cord. Platinum-cured silicones such as Ecoflex (cf. Chapter 2) and Elastosil (cf. Chapter 4) are promising for future applications. The latter has the advantage of being compatible with interfacial bonding (e.g. plasma O_2) and reactive ion etching techniques. The processes presented in this thesis can be easily adjusted to this silicone, which from a mechanical point of view, would be only beneficial. Nonetheless, handling and surgical insertion may be hindered by the implant softness. Engineering transient stiff mechanical properties in the substrate material, using shape-memory polymers for instance [207], may address this challenge. Furthermore, techniques developed in the field of soft-robotics may enable consistent mechanical coupling and decoupling with neural structures. It would not be far-fetched to conceive a soft peripheral cuff implant that conform temporarily to a peripheral nerve to deliver neuromodulation therapies and then loosen when stimulation is not needed. Pneumatic actuators made of PDMS microtubes enable reversible tentacle motion suitable for interfacing peripheral nerves [258]. Eventually, following a neuromodulation therapy, neural implants that are no longer needed may dissolve harmlessly in the body. Bioresorbable electronics is an active field of research that may be translated to the clinic in a distant future [259]. For example, ECoG electrode arrays are used today to localized focal seizures and their implantation does generally not exceed one month. Bioresorbable materials, such as silicon nanomembranes through the process of hydrolysis, could form the array substrate and encapsulation. Following implantation, these components would degrade in a controlled fashion, enabling electrophysiological recording over a defined period of time. Recently, the integration of resorbable dielectric layers, such as poly (lactic-co-glycolic acid) (PLGA), enabled the development of bioresorbable peripheral nerve stimulation systems [260]. When fully optimized, this technological route may foster the pinnacle of bioelectronics.

Of course these improvements towards softer interfacing would only be meaningful if accompanied with relevant metallization techniques. In this thesis, I introduced two strategies for engineering stretchability in the implant interconnects. Intrinsically stretchable micro-cracked gold films are compatible with soft lithography processes. These thin metal films are directly evaporated on an elastomeric substrate, promoting a remarkable softness and a relative simplicity of fabrication. This approach has proven successful for delivering electrical and pharmacological neuromodulations in the rat spinal cord [75]. Unfortunately, the transla-

tion of this technology to optoelectronic applications suffers from a high sheet resistance and a phenomenon of hysteresis. Emerging technologies offer an alternative for the fabrication of highly conductive electrical circuits on elastomers. For instance, direct ink writing is an appealing technique for the fabrication of highly stretchable circuits [261]. Hybrid 3D printing allows for the successive formation of the elastomeric substrate, the stretchable circuit, and the integration of active components such as LEDs. Due to its level of automation, this technique is highly reproducible. However, it is not yet compatible with the small feature sizes required for the fabrication of implantable optoelectronics. Biphasic gold-gallium thin films on silicone can be processed by photolithography to the desired dimensions [244]. Yet, the stability of these films when implanted hinders their long-term functionality and would require significant hermeticity improvements. For the peripheral and spinal μ -LED implants presented in this thesis, I utilized thick gold wavy interconnects that deflect out of plane under elongation. This approach was compatible with the powering of LEDs and did exhibit minimal influence of strain on the electrical performances. This popular strategy in stretchable electronics has constantly been improved. Optimisation in the serpentine geometry, with a fractal approach for example, enables further elongation. These circuits can also be precisely designed to mimic the stress-strain behaviors of biological tissues [262]. One major drawback when implementing this concept to the μ -LED implants was the relative important footprint of the interconnects. Engineering elasticity in metal thin films via the patterning of tri-branch motifs is an appealing alternative [221]. The resulting stretchable interconnects remain linear and can sustain multiaxial strains.

Finally, improving the longevity of these thin devices is generally a necessity for their translation to the clinic. Physically, ensuring a barrier against moisture and ions with a stretchable material is counter-intuitive. The gaps formed in between the polymeric chains allow the diffusion of small molecules, ions and water. In this thesis I introduced the use of polyisobutylene (PIB) in the μ -LED encapsulation. This material, commonly used for the sealing of solar panels, has remarkable water-vapor permeability properties. However, this polymer is mechanically tacky and should be covered with silicone to prevent interfacial decohesion. Therefore, we should investigate the permeability of a silicone-PIB-silicone stack. Furthermore, groups have reported on flexible encapsulation materials capable of preventing the degradation of implanted devices over several years [263, 264]. Fine integration of these materials in an intricate mesh network may promote conformability and long-term functionality.

6.3 The advent of optogenetics and novel modalities for parsing the nervous system

The concept of optogenetics has been introduced more than 10 years ago and has been constantly booming through the years. In fact, the total number of scientific publications on this topic has reached nearly 4'000 (source: Web of Science). Delivering cell-type specific, millisecond-scale neuromodulations has revolutionized neuroscience. Intensive efforts promoted the extension of the optogenetic toolbox. A large variety of opsins has been introduced,

displaying considerable improvements in terms of photocurrent, kinetics and sensitivity. For instance, a new class of light-sensitive proteins, SwiChR, enables both activation and inhibition of neural activity with spectrally-distinct optical stimulations [126]. This tool may foster more thorough parsing of the nervous system. Furthermore, the development of light-sensitive proteins with absorption spectra shifted from the blue allows to probe deeper neural structures. An innovative alternative strategy is to inject upconversion nanoparticles at the vicinity of the targeted neural populations [265]. These nanoparticles absorb in the near-infrared spectrum and emit locally wavelength-specific visible light. This approach has proven successful for delivering deep brain stimulations with transcranial near-infrared illumination. This concept may be implemented for optogenetic control in the PNS and the spinal cord, and would allow to probe those tissues non-invasively.

The advent of optogenetics has triggered the development of complementary, genetically-associated neuromodulation techniques. The concept of chemogenetics is analogous to optogenetics and relies on the expression of drug receptors in genetically-selected neural populations. Commonly, Designer Receptors Exclusively Activated by Designer Drugs (DREADD) are engineered proteins that can activate or silence neuronal firing [266]. Briefly, this technique involves the mutation of acetyl choline receptors so that they are activated by clozapine-N-oxide (CNO). Subsequent delivery of CNO through systemic injection or food ingestion activates DREADD. Compared with an optogenetic approach, chemogenetics promotes a similar spatial control but lacks its fine temporal resolution. Yet, this technique is relevant for long term neuromodulation. DREADD stimulation of $vGluT2^+$ interneurons in the spinal cord was reported to alleviate breathing-associated motor deficits following cervical SCI [267]. Soft neural implants may enable precise and chronic delivery of CNO in the nervous system.

A newcomer in the modality-specific genetic techniques is sonogenetics. Although transcranial pulsed ultrasound has been reported to mechanically stimulate neural firing [268], its underlying mechanisms are not yet fully understood. The volume of neural tissues activated by pulsed ultrasound can be localized in $\sim 3 \text{ mm}^3$ of tissues, yet this technique does not target specifically one type of cell. Sonogenetics relies on the genetically-selective expression of mechanotransduction channels, such as TRP-4 [269]. Thus, low-pressure ultrasounds target activation in the TRP-4⁺ neurons, causing behavioural outputs in *C. elegans*. One main advantage of this technique is the permeability of biological tissues to ultrasound waves. Pending on the establishment of sonogenetics as a true alternative to optical stimulation, future neural interfaces may explore the integration of this modality.

6.4 Translation to the clinic

Selective neuromodulation therapies offer tremendous perspectives for the treatment of dysfunctional nervous systems. However, the translation of microengineered research tools into real clinical applications present numerous pitfalls. Based on the aforementioned properties, a major concern is the long-term functionality of these neural implants. From a mechanical

point of view, these stretchable devices shall remain compliant and resilient after prolonged implantation. Silicone rubber has been reported to become brittle after 25 years of implantation [270]. This phenomenon would likely be exacerbated with thinner substrates. From a material point of view, ensuring hermeticity with flexible or stretchable materials is challenging. The implementation of novel encapsulation techniques should minimally interfere with the implant soft properties. From a biological point of view, these materials must be biocompatible according to human application standards. Polyimide is not a USP class VI polymer, and therefore not allowed for long-term implantation. Parylene C could be a suitable alternative. Finally, from an electrical point of view, the implant stimulation performances must remain stable and safe over time. Due to the harsh environment, metals at the electrode site may corrode and caused harmful stimulation by-products [166]. This would affect the implant integrity and ultimately hinder its functionality.

Despite the luring potential of optogenetics for the treatment of neurological disorders, this technology is not yet approved for human application. One major barrier is the transfection of the opsin gene in human cells. Although optogenetic researches in rodents and non-human primates did not report a severe immune reaction following viral delivery of the opsin gene [271], no one can safely predict what would be this immune response in humans. The expression of a foreign body might have dramatic consequences. The emergence of gene therapies and human-compatible viral vectors may slowly steer the translation of optogenetics. In fact, a clinical trial is currently investigating the use of optogenetics for the treatment of retinitis pigmentosa (clinicaltrials.gov # NCT02556736). The eyes are considered immune privilege and do not trigger harsh reactions upon antigen injections. Ideally, the opsin delivery should not involve any genetic materials and its expression should remain transient. We could imagine it would be feasible in a distant future rendering specific receptors light-sensitive by temporarily binding of a molecule (e.g. retinal).

Finally, we should consider the ethical issues raised by the rapid expansion of neuroprosthetics. Today, selective neuromodulations are designed for the replacement or restoration of damaged functions. However, the potential misuse of the technologies developed in this context would be detrimental to society. Enabling selective writing into the nervous system may be considered as opening a Pandora's box. Future technologies could lead to augmented or supplemented capabilities, exacerbating inequality among individuals. On the other hand, these technologies would be salutary for the people suffering from a dysfunctional nervous system. Considering the pace to which the field is progressing, it becomes pressing to debate this matter. Settling the boundaries of selective neuromodulation application will certainly be a dilemma of the century.

A Appendix

A.1 Optical cuff for optogenetics in the peripheral nervous system

A.1.1 Optocuff implantation

All animal procedures were approved by the institutional animal care and safety guidelines and with IACUC approval at Boston Children's Hospital. Healthy adult (3–6 month old) male and female Thy1::ChR2 mice of average mass 27.5 g were implanted with the optical cuff. Mice were anesthetized under isoflurane (1–3%) and the body temperature was maintained with a heated surgical table (37 °C). The left hindlimb and head of the mouse were shaved and the skin disinfected using successive applications of betadine and isopropyl alcohol. Under sterile conditions, a skin incision exposed the skull, where 2 precision screws were drilled. The sciatic nerve was exposed at the mid-thigh level after a parallel 1 cm long skin incision and blunt muscles separation. The optical cuff and optic fiber were threaded subcutaneously, the ferrule end laying down the mouse skull and the cuff proximal to the sciatic nerve. A loop was formed on the optic fiber so the cuff has a 90° incidence angle on the sciatic nerve and to relieve the strain along the fiber after implantation. The cuff was then applied to wrap the sciatic nerve and a loose suture secured the optic fiber to surrounding muscles. The separated muscles were sewed back together with absorbable sutures. The ferrule was anchored to the skull with a small amount of dental cement, and the incisions at the head and hindlimb closed with sutures (6-0, Ethicon). Full surgical procedure took 45 minutes. Control mice used in behavioural experiments underwent similar surgical procedure with the skull and sciatic nerve being exposed. Only a ferrule fixed on a 1 cm long optic fiber was mounted on the skull so blinded experimenters could not distinguish experimental groups. Mice were allowed to recover in single housed cage and subcutaneously injected with post-operative meloxicam analgesic for 3 days.

A.1.2 Thy1::ChR2 mouse breeding

All mice were purchased from Jackson Laboratories and Thy1-Cre mice were backcrossed to C57BL/6 for at least five generations. Targeted expression of ChR2-tdTomato was achieved by breeding heterozygous Rosa-CAG-LSLhChR2(H134R)-tdTomato-WPRE (Ai27D) mice with Thy1-Cre mice. Resultant Thy1-Cre::ChR2 mice were heterozygous for both transgenes and were housed with control littermates. Mice were given ad libitum access to food and water and were housed in at 22 ± 1 °C, 50% relative humidity, and a 12 h light:12 h dark cycle. Male and female mice were pooled by genotype to limit the number of animals used.

A.1.3 Mechanical sensitivity assessment

Mice were habituated, single housed in a small transparent chamber ($7.5 \times 7.5 \times 15$ cm³) elevated on a wire grid. Mechanical sensitivity was measured by applying an increasing perpendicular force to the lateral plantar surface of the left hindpaw using graded series of six von Frey filaments (with bending force of 0.04, 0.07, 0.16, 0.4, 0.6, 1 g) and counting the number of withdrawal responses across ten applications. The pain mechanical threshold was defined as the minimal force triggering at least five withdrawals.

A.1.4 Thermal sensitivity assessment

Each mouse was habituated on a warmed (29 °C) glass platform of a Hargreave's apparatus (IITC Life Science). Thermal sensitivity was determined by applying a radiant heat source to the plantar hindpaw while measuring the duration before hindpaw withdrawal. The latency for the onset of nocifensive behavior was timed. This latency was determined three times per animal, per session, with a 5 minutes interval to prevent thermal sensitization.

A.1.5 Dynamic weight bearing

Mice inflammatory pain was assessed using a dynamic weight bearing test (Bioseb). Each mouse was placed 5 minutes in a Plexiglas chamber ($11 \times 19.7 \times 11$ cm³) with a pressure transducers array on the floor. A camera recorded each movement while the mouse was exploring the chamber. Using a software matching pressure data and the video recordings, we discriminated and measured the weight (in grams) applied by the limbs. Finally, we extracted the duration of the cuff implanted hindpaw on the floor over the contralateral one.

A.1.6 Motor sciatic nerve assessment

Motor recovery in mice was assessed using a DigiGait apparatus (Mouse Specifics). Mice were recorded walking on the treadmill videography system at 20 cm.s⁻¹. Measures of toe spread (TS) and the print length (PL, distance of the 3rd toe tip to the most posterior paw part) were

A.1. Optical cuff for optogenetics in the peripheral nervous system

used to calculate the sciatic nerve functional index (SFI) using the following formula [272]:

$$SFI = 118.9 \left(\frac{TS_{left} - TS_{right}}{TS_{right}} \right) 51.2 \left(\frac{PL_{left} - PL_{right}}{PL_{right}} \right) 7.5 \quad (A.1)$$

A.1.7 DRG neuron culture and electrophysiology

Dorsal root ganglia neurons were isolated from adult (3–6 month old) mice and maintained at 37 °C in 5% carbon dioxide. Electrophysiological recordings were made at 20–22 °C up to 24 h after DRG neuron dissociation, using the whole-cell configuration of the patch-clamp technique. Recording pipettes had tip resistances of 4–8 MΩ when filled with (in mM): 135 K-gluconate, 10 KCl, 1 MgCl₂, 5 EGTA, and 10 HEPES, pH 7.3. The extracellular solution contained (in mM): 145 NaCl, 5 KCl, 2 CaCl₂, 1 MgCl₂, 10 HEPES, and 10 glucose, pH 7.4. All solutions were maintained at 300–315 mOsm.l⁻¹. Membrane potential was recorded in current clamp mode with an Axopatch 200A amplifier and Digidata 1400A A/D interface using pClamp 10.2 software (Molecular Devices). The data were low-pass filtered at 5 kHz (4-pole Bessel filter) and sampled at 10 kHz. Input resistance was typically >500 MΩ, and cells with resistances <200 MΩ were discarded. Care was taken to maintain membrane access resistance as low as possible (usually 3–7 MΩ and always less than 10 MΩ). Detailed methods can be found in Browne *et al.* (2017) [13].

A.1.8 Histology and immunohistochemistry

Mice were anesthetized with pentobarbital (100 mg.kg⁻¹ intraperitoneal) and fixed by transcardial perfusion with 4% paraformaldehyde dissolved in phosphate buffered saline (PBS). DRGs (L3-L5) and sciatic nerves were dissected, postfixed, washed, cryoprotected with sucrose in PBS (30% w/v) for 2-3 d, and frozen (O.C.T., Tissue-Tek). Cryosections of DRG (10 μm thick) and sciatic nerves (10 μm longitudinal sections, 10 μm cross-sections) were blocked with 1% bovine albumin serum (BSA) and 0.1% triton X-100 in PBS for one hour. Sections were incubated with NF200 (1:2000), CGRP (1:500) primary antibody in fresh blocking solution overnight at 4°C and washed three times (10 min each) in saline. They were then incubated with secondary IgG antibody (1:500, Life Technologies) for one hour at room temperature, washed three times (10 min each) in PBS, and mounted in Vectashield (H-1200). Fluorescein-conjugated GSL I was used at 1:1000. Finally, sciatic nerve cross-sections were incubated with DAPI (1:1000, 15min, Sigma) and washed in PBS. DRG and sciatic nerve sections were imaged using a Nikon Eclipse 80i microscope using a Nikon 10x objective and Nikon DS-Qi1MC camera. In DRGs and sciatic nerves, fluorescence corresponding to tdTomato was absent in tissues from littermate mice that did not express ChR2-tdTomato or that did not express the Cre recombinase.

A.1.9 EMG electrode implantation and data acquisition

All surgical procedures were performed in accordance with Swiss federal legislation and under the guidelines established at EPFL and approved by local Swiss Veterinary Offices. The mice were administered general anaesthesia (mixture of 80 mg ml⁻¹ ketamine, 10 mg ml⁻¹ xylazine, diluted in saline) using intraperitoneal injections (8.5 ml kg⁻¹). Bipolar intramuscular electrodes (AS632, Cooner Wire) were inserted unilaterally in the • (TA, ankle flexor) muscles to record electromyographic activity. Recording electrodes were created prior to implantation by removing a small part (200 µm notch) of PTFE insulation. All the wires were connected to a percutaneous amphenol connector (Omnetics Connector Corporation). EMG recordings were synchronized with the laser stimulation onset using a custom-developed Tucker-Davis Technology (TDT) code. Signals were amplified (x 1000) and pre-filtered (Bandpass: 100 Hz - 1 kHz) with an AM systems amplifier.

A.1.10 Optogenetic control *in vivo* and high-speed behavioural imaging

The optical cuff was coupled to the laser with a multimode FC/PC optic fiber cable (105 µm core diameter, 2 m length, Thorlabs) using a ceramic mating sleeve (ADAL1, Thorlabs) on the ferrule. It was critical avoiding any physical stress on the mouse during the operation. Mice were housed in a small (7.5 × 7.5 × 15 cm³) chambers and acclimatized for at least 30 minutes. A counter-balance lever arm (Harvard Apparatus) relieved the mouse from the laser optic fiber cable weight. A computer-controlled pulse generator (OPTG-4, Doric) was used to supply TTL signals to the laser driver. Simultaneous epineural optogenetic stimulation (average 40 mW laser output) and high-speed recordings were performed. Behaviour was sampled at 1000 frames per second using an acA2040-180kmNIR cameralink CMOS camera (Basler) with a 8 mm lens and set at 500 pixels × 350 pixels. Acquisition was carried out in LabVIEW on a computer with excess buffer capacity to ensure all frames were successfully retained. Littermate control mice without Cre recombinase and implanted with the optical cuff did not react to blue light pulse (20 ms, 60 mW). Cuff implanted Thy1::ChR2 mice did not respond to an equivalent off-spectra pulse of light (594 nm, LaserGlow).

A.1.11 Stretchable optic fiber fabrication

First, a 100 µm thick SU8 (Gersteltec GM 1070) layer was spin-coated on 6-inch silicon wafer. The wafer dimensions allowed for long (> 10 cm) fibers to be processed. After curing and standard UV photolithography (Karl Suss MJB4 mask aligner, λ= 365nm), SU8 was patterned to thin (100 µm in width) stripes that will be used to mold the optic fiber core. The resulting wafer was functionalized with a 1H,1H,2H,2H- perfluorooctyltriethoxysilane (Sigma-Aldrich) release monolayer under vacuum. Then, a 150 µm thick layer of PDMS (Sylgard 184, Dow Corning) was spin-coated on the wafer. After curing (2 hours, 80 °C), the PDMS layer was carefully released from the SU8 mold. The resulting silicone membrane was plasma O₂ bonded to a 50 µm thick PDMS layer processed on a 2nd 6-inch wafer. The empty thin stripes formed via

A.1. Optical cuff for optogenetics in the peripheral nervous system

SU8 patterning were filed with a low viscosity optical gel (LS1-3252, Nusil) using capillarity. After curing of the optical gel (12 hours, 80 °C), the PDMS-gel-PDMS stack was cut with a razor blade and released from the wafer. The gel core was finally coupled to a commercial optic fiber (1 cm in length, FG105UCA, Thorlabs) terminated with a 1.25 mm ceramic ferrule (CFLC128, Thorlabs).

A.2 A wireless optoelectronic system for optogenetic control of the peripheral nervous system

A.2.1 Meander-track geometry

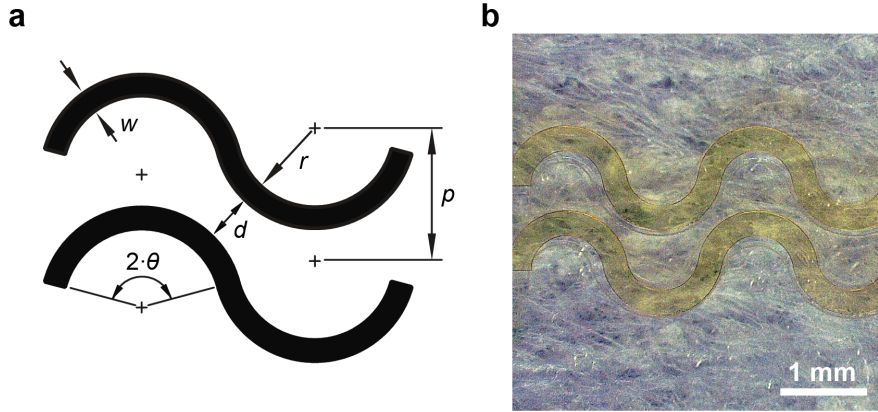


Figure A.1 – Stretchable interconnects using a serpentine design

a, Illustration of 2 adjacent meander-tracks and the parameters describing their geometry. w is the width of the tracks, d the minimum distance between two adjacent tracks of the pitch p , r the radius, and θ the opening angle which defines the curvature. Adapted from [81]. **b**, Picture of the wavy PNS implant interconnects. The interconnect parameters are: $w = 250 \mu\text{m}$, $r = 750 \mu\text{m}$ and $\theta = 75^\circ$.

A.2.2 μ -LED implant surgery

All experiments were carried out at Boston Children's Hospital and Harvard Medical School and were conducted according to institutional animal care and safety guidelines and with Institutional Animal Care and Use Committee (IACUC) approval. Healthy adult (3–6 month old) male and female mice of average mass 23.5 g were implanted with the μ -LED array. The surgical procedure shares similarities with the optocuff implantation protocol. Mice were anesthetized under isoflurane (1.5%) and the body temperature was maintained with a heated surgical table. The left hindlimb and head of the mouse were shaved and the skin disinfected using 3 successive applications of betadine and isopropyl alcohol. Under sterile conditions, a skin incision exposed the skull, where 3 precision screws were drilled. The left sciatic nerve was exposed at the mid-thigh level after a parallel 1 cm long skin incision and blunt muscles separation. The connector and the electrical wires were threaded subcutaneously from the mid-thigh to the skull, with the μ -LED array laying proximal to the sciatic nerve. To adjust the wire length to the mouse dimensions and to not impede locomotion, a loop was formed on the wires. Then, the μ -LED array was delicately pull with a thread attached to its extremity to pass the most far-off μ -LED panel below the nerve. Under a microscope, 2 parallel suture threads (vicryl 6-0, Ethicon) passing through the array anchoring sites were tighten around the nerve. As a result, the most far-off μ -LED panel bent and the μ -LEDs faced the nerve. A drop of surgical silicone (Kwik-sil, World Precision Instruments) secured the μ -LED position.

A.2. A wireless optoelectronic system for optogenetic control of the peripheral nervous system

Next, the implant connector was sutured to the surrounding muscles below the skin incision. The separated muscles were sewed back together. The head-connector was anchored to the skull with a small amount of dental cement. The hindlimb incision was closed with surgical clips. Full surgical procedure took 45 minutes. Sham-operated mice used in behavioural experiments underwent similar surgical procedure with the skull and sciatic nerve being exposed. Only a bare connector was mounted on the skull so blinded experimenters could not distinguish experimental groups. Mice were allowed to recover in single housed cage and were injected subcutaneously with post-operative meloxicam analgesic for 3 days. The surgical procedure is illustrated in Figure A.2.

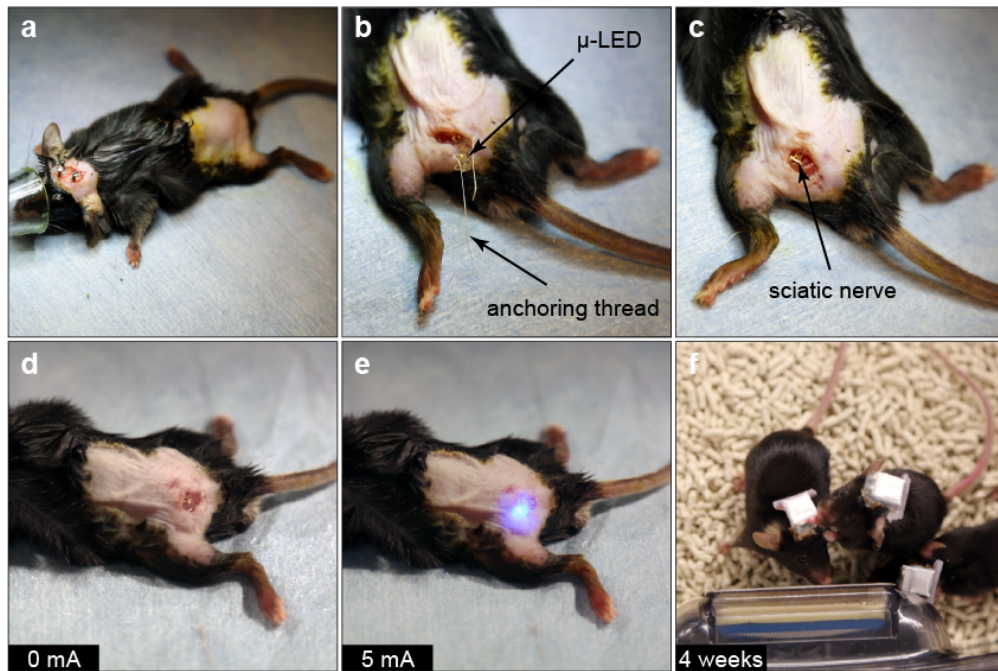


Figure A.2 – μ -LED array implantation procedure on the mouse sciatic nerve

a, Mouse is anaesthetized under 1.5% isoflurane induction. Following craniotomy, three surgical micro-screws are fixed on the mouse skull. **b, c**, The implant wires are first threaded subcutaneously and the implant is placed transversally to the sciatic nerve. Carefully, the most far-off LED panel is slid below the sciatic nerve and bent to have the 4 μ -LEDs facing the nerve. Anchoring threads are tighten around the nerve, resulting in the μ -LED alignment. **d, e**, Implant is tested intraoperatively and the skin incision is then closed with surgical clips. **f**, Picture of 3 mice, 4 weeks following the surgical procedure. The wireless head-stage does not impede the mouse behaviour.

A.2.3 Histology and immunochemistry

Mice were anesthetized with pentobarbital (100 mg·kg⁻¹ intraperitoneal) and fixed by transcardial perfusion with 4% paraformaldehyde dissolved in phosphate buffered saline (PBS). Sciatic nerves and DRGs (L3-L5) were dissected, postfixed, washed, cryoprotected with sucrose in PBS (30% w/v) for 2-3 d and either embedded in paraffin blocks (4 μ m-thick cross-sections)

or frozen (10 μm -thick nerve longitudinal sections and DRG sections). Hematoxylin and Eosin (H&E) staining of nerve cross-sections was performed with an automated equipment (ST5020, Leica) and imaged with a virtual slide scanner and 20x objective (VS120, Olympus). For immunostaining, sections were incubated with chicken anti-NF200 (1:2000, Millipore), mouse anti-CD68 (1:200, Abcam) and rabbit anti-Myelin Basic Protein (MBP; 1:100, Abcam). Fluorescence secondary antibodies were conjugated to Alexa 488 (green, 1:500, Thermofisher) and Alexa 555 (red, 1:500, Thermofisher). A nuclear stain was also performed with 4',6'-diamidino-2-phenylindole dihydrochloride (DAPI; 2 ng/ml, Molecular Probes). Sections were coverslipped using ProLong Gold anti-fade reagent (Invitrogen). Nerve cross-sections were examined and photographed using deconvolution fluorescence microscopy and scanning confocal laser microscopy (LSM 880, Zeiss). Tiled scans of individual whole sections were prepared using a 20x objective and the post-processing was conducted with Zen software (Zeiss). Nerve longitudinal sections and DRG sections were imaged using a Nikon Eclipse 80i microscope with a Nikon 20x objective and 10x objective respectively. In DRGs and sciatic nerve longitudinal sections, fluorescence corresponding to tdTomato was absent in tissues from littermate mice that did not express Chr2-tdTomato or that did not express the Cre recombinase. In sciatic nerve cross-sections, tdTomato fluorescence was not found in any experimental groups.

A.2.4 Behavioural experiments

Sensorimotor coordination

To investigate sensorimotor coordination following the μ -LED array implantation, mice were first trained on the accelerating rotarod (Omnitech Electronics). For training, mice were placed on a rotarod moving at 4 rpm for 10 min. If a mouse fell, it was placed back on the rotarod. Training took place on three consecutive days. For behavioural testing, the mice ran on the accelerating rotarod at 4 rpm + 0.1 rpm.s⁻¹. The time to fall was automatically recorded. The test was repeated 3 times with 10 min intervals.

Physical performance and endurance assessment

Wheel running is a voluntary activity that enable to assess the mouse physical performance and endurance [273]. The running wheel test may also point out on-going pain if fewer activity is being recorded [274]. Mice were single-housed in a cage containing a stainless-steel running wheel (23 cm in diameter) with a ball-bearing axle (BIO-ACTIVW-M, Bioseb). The wheel could be turned in either direction. The wheels were connected to a computer that automatically recorded the distance travelled by each animal. No experimenters were present in the room during the recording sessions. As mice run more during the active dark light cycle, the running wheel activity was monitored from 10 pm to 8 am.

A.2. A wireless optoelectronic system for optogenetic control of the peripheral nervous system

Exploratory activity monitoring

The mouse exploratory activity was assessed with the open-field test. The open-field (LE802SC, Bioseb) contained a 45 x 45 cm² floor and 40 cm high walls. Horizontal exploratory activity was recorded by infrared detectors with 2.5 cm interval distance in the horizontal plane at a height of 1 cm. Vertical activity (e.g. rearing) was recorded by a second row of sensors at a height of 5 cm. The mice were placed in the middle of the field and monitored for 10 minutes. No experimenters were present in the room during the recording sessions.

A.2.5 ChR2 expression in TRPV1⁺ neurons

Specific expression of ChR2 in the TRPV1 primary afferents has been previously described in [13]. ChR2-tdTomato was expressed in nociceptive afferents by breeding heterozygous Rosa-CAG-LSL-hChR2(H134R)-tdTomato-WPRE (Ai27D) mice [65] with mice with Cre recombinase inserted downstream of the *Trpv1* gene [275]. Resultant mice were heterozygous for both transgenes (i.e. TRPV1-Cre(+/-)::ChR2(+/-)) and were housed with control littermates. Mice were given ad libitum access to food and water and were housed in 22°C ± 1°C, 50% relative humidity, and a 12 hr light:12 hr dark cycle.

A.2.6 Single pulse optogenetic stimulation *in vivo*

Mice with the wireless head-stage connected were housed in small transparent chambers (7.5 × 7.5 × 15 cm³) and acclimatized for at least 30 minutes. Simultaneous single-pulse epineural optogenetic stimulation and high-speed recordings were performed. The wireless system was controlled via an Android tablet (Galaxy Tab A, Samsung) where stimulations parameters (i.e. pulse duration, current) were set. Behaviour was sampled at 500 frames per second using a high-speed camera (SC1, edgetronic) with a 28 mm lens (Nikon) and set at 896 pixels × 896 pixels. Optogenetic stimulations were carried when the mice were in a calm and awake idle state and not grooming or exploring. The stimulation amplitude was set to the threshold for activation + 30 % (usually $i = 12$ mA). The mice were stimulated with an interval > 5 minutes in between 2 recordings. Following acquisition, mouse behaviour was analysed manually frame per frame (QuickTime Player). Littermate controls (without Cre recombinase) did not react to any optical stimulation.

A.2.7 Conditioned place aversion

Real-time place aversion was tested in an open-field (ENV-515S, Med Associates Inc.) with a plexiglass separation that divides the field in 2 areas (43 x 21 cm² each). An opening in the divider center allows for a mouse to cross the separation and to walk in between the 2 areas. For the baseline recording ("Stim Off"), a mouse, connected to the wireless system, was placed in the "No Stim" area and was allowed to explore the whole field freely. Real-time place aversion was tested during a 2nd recording ("Stim On"). Upon entry of the mouse in the

stimulation-paired area, an experimenter initiated the wireless epineural photostimulation (10 ms, 0.5 Hz). The stimulation was turned off as soon as the mouse exited the stimulation-paired area. Each recordings were 15 minutes long. Following recording, the time spent in each area was computed with the Activity Monitor 7 software (Med Associates Inc.).

A.2.8 Flow cytometry

One week after μ -LED array implantation, mice received prolonged optical stimulations to the left sciatic nerve. The stimulation parameters were 15 mA, 10 ms, 2 Hz for 20 minutes. Mice were anesthetized with 2.0% isoflurane during the stimulation duration. Six hours following stimulation, paw skin was removed and processed for lymphocyte infiltration. Briefly, skin was cut into small fragments in 2 ml of a 0.25 mg/ml solution of Liberase TL (Roche) in DMEM (Dulbecco's Modified Eagle's medium, ThermoFisher) and incubated for 1 hour at 37°C on a shaker. Following incubation, solution was filtered through a 100 μ m strainer and centrifuged at 1700 RPM for 5 minutes. Cell suspension was resuspended in 150 μ l buffer containing 3% FBS and stained for the following lineage defining cell surface markers: CD45, CD3, Thy1.2, CD11b, Gr-1, and Siglec-F (all antibodies from Thermo Fisher, eBioscience). Samples were analyzed by flow cytometry on a LSR Fortessa (BD biosciences).

A.3 A transversal spinal electrode array

A.3.1 Dorsal root trajectories

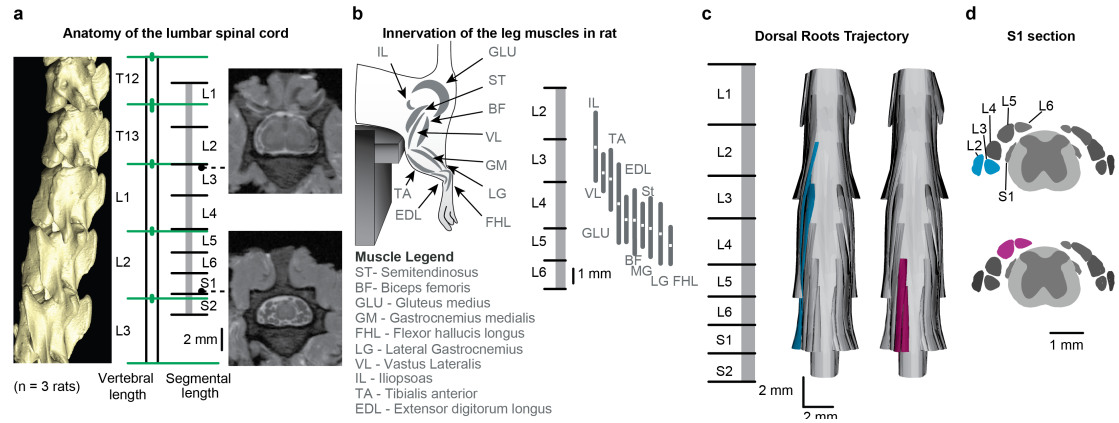


Figure A.3 – Rat spinal cord anatomy

a, Spatial organization of spinal segments in the Lewis Rat in relation to vertebrae. 3D reconstructions of the rat spinal cord show the exact vertebrae organisation and dimensions (left). These reconstructions were extracted from CT scans. MRI scanners captured the spinal cord and the roots trajectories (right). **b**, Location of the motoneuron pools for the principal leg muscles in relation to the segments of the lumbar spinal cord. **c**, 3D dorsal root trajectories in relation to the lumbar spinal segments. **d**, Cross-section of the S1 spinal cord level highlighting the dorsal roots involved in flexion (blue) and extension (purple).

A.3.2 Scanning electron microscopy and micro-cracked gold morphology

Morphologies of the micro-cracked gold film and the Pt-PDMS composite were processed via scanning-electron microscopy (SU5000, Hitachi). The samples were imaged under high-vacuum and using the secondary electron detector. The landing voltage varied from 3.0 to 5.0 kV depending on the sample conductivity.

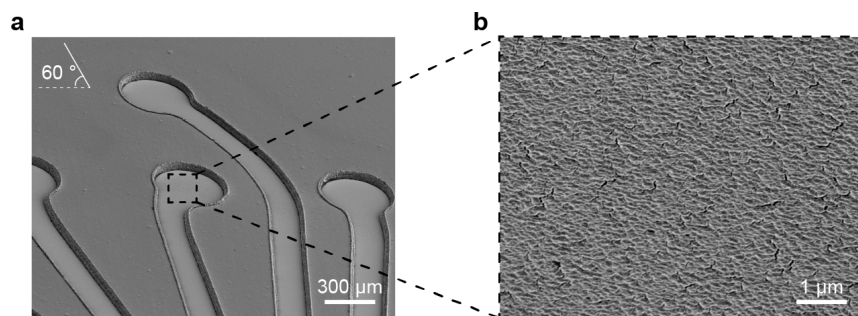


Figure A.4 – Morphology of the micro-cracked gold thin film

a, SEM pictures of the micro-cracked gold film tilted at 60° through the belt array stencil mask. **b**, Higher magnification of the tilted film reveals the film complex topography.

A.3.3 Surface topography measurement and analysis

Microcracked-gold topographic images were obtained using atomic force microscopy (Dimension Icon, Bruker). The sample surface was probed with a SiN cantilever (tip radius: 2 nm; Scanasyst-air, Bruker) and the AFM was set to the Peak Force Tapping mode (PFT). The Peak Force setpoint was 1 nN and the cantilever spring constant was calibrated from the thermal noise prior to the measurements. After successful approach of the AFM tip to the sample surface, the scan area was set to $5 \times 5 \mu\text{m}^2$ (2048 lines with a scan rate of 0.5 Hz). The image analysis was processed with the AFM native software (Nanoscope, Bruker). To compensate the drift of the tip over the long measurement (~ 1 hour), images were post-processed with a 2nd order plane fitting. The sample roughness was quantified using the following equations [276]:

$$R_Z = | \max Z(x) | \text{ with } 0 \leq x \leq L \quad (\text{A.2})$$

$$R_A = \frac{1}{L} \int_0^L | Z(x) | dx \quad (\text{A.3})$$

$$R_Q = \sqrt{\frac{1}{L} \int_0^L | Z^2(x) | dx} \quad (\text{A.4})$$

Regarding the topographic measurements of the micro-cracked gold film under strain, the sample was first released from the carrier wafer by dissolution of the PSS layer in deionized water. Then, one extremity of the sample was fixed back to the wafer using RTV silicone. Above a deionized water pellicle, the sample was manually stretched to 10% strain. Drying of the water pellicle allowed the sample to lay flat on the wafer.

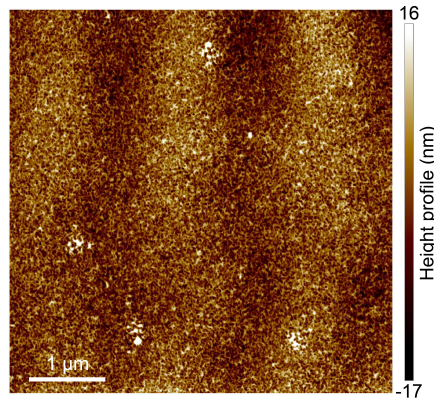


Figure A.5 – Topography of PDMS

A.3.4 Electrochemical characterization of belt electrodes under elongation

In order to characterize the electrode electrochemical performances under stretch, the belt arrays were clamped in a tensile testing platform (Model 42, MTS Criterion) equipped with an environmental circulating bath (Bionix EnviroBath, MTS Criterion). The electrochemical measurements (i.e. impedance spectroscopy, cyclic voltammetry) were conducted in the circulating bath filled with warm PBS (37°C) using a three-electrode setup and a potentiostat (Reference 600, Gamry Instruments). The counter and the reference electrodes (a 5 cm long platinum rod and an Ag/Cl standard calomel electrode (SCE) respectively) were inserted horizontally in the fluid chamber and remained close to the belt array electrodes. For the impedance measurements, the excitation voltage amplitude was set to 10 mV. The CV were recorded with a potential scan rate of 100 mV/s applied within the potential range [-0.6, 0.8] V. These measurements were conducted to each electrode individually and at tensile strains of 0%, 10% and 40%.

Voltage transient measurements were performed to determine the charge injection capacity of the belt electrodes and the influence of stretching on the electrode performances. In the circulating bath filled with warm PBS, biphasic current pulses (cathodic first, 200 μ s per phase, interphase 40 μ s) were passed between the belt electrode and the platinum rod counter electrode. These pulses were generated with an isolated stimulator (Model 3800, A-M Systems) and the electrode polarization was measured with an oscilloscope (DPO 2024, Tektronix). The pulse amplitude was gradually increased until the electrode polarization exited the water window. For the experiment involving voltage transients under uni-axial strain, the pulse amplitude was fixed to 200 μ A.

A.3.5 Surgical procedures

All experiments were approved by Local Swiss Veterinary Offices and conducted under the guidelines established at EPFL in accordance with the Swiss federal legislation. General condition of surgical procedures have been detailed in previous works ([40,75,201]). Presented *in vivo* experiments involved female Lewis rats with initial weight of 180–220 g (LEW-ORlj, Janvier Labs). Each surgical procedures were performed under general anaesthesia with isoflurane in oxygen-enriched air (1–2%). Rats recovered from anaesthesia in an incubator after surgery.

Implantation of intramuscular EMG electrodes

To record at the electromyographic activity, hindlimb muscles were implanted with bipolar electrodes, the combinations depending on experiments: *iliopsoas* (IL), *gastrocnemius medialis* (MG) and *tibialis anterior* (TA). Recording electrodes were fabricated from stainless steel wires (AS631, Cooner Wire) where a small part (0.5-mm notch) of the PTFE insulation was removed. A common ground was created with the same type of wire by removing about 1 cm

of Teflon from the distal extremity and was placed subcutaneously. All electrode wires were connected to a transcutaneous amphenol connector (Omnetics), later cemented to the rat skull.

Transversal spinal array insertion

The surgical procedure for spinal implantation into the rat epidural space was previously detailed in [202]. Briefly, two partial laminectomies at vertebrae levels L3–L4 and L1–L2 gave access to the rat epidural space. A surgical suture (Ethicon) is used to pull the transversal implant below vertebrae and above the dura mater. The electrode position over the spinal cord is finely tuned with intra-operative electrophysiological testings. To avoid any displacement of the implant, the connector was secured with dental cement on top of the L3–L4 vertebra.

A.3.6 Microcomputed tomography

Images of the transversal spinal implants *in vivo* were produced via microcomputed tomography, or CT scan. The scanner (Skyscan 1076, Bruker) rotated around the animal body and combined multiple angles of view to extract a 3D image. Scanner settings were adjusted to avoid artefacts induced by metallic parts of the vertebral orthosis (0.5–1 mm aluminum filter, voltage 70–100 kV, current 100–140 μ A, exposure time 120–160 ms, rotation step 0.5°). The reconstruction in 3D occurred in NRecon software using GPURecon Server (Bruker). Inhalation of isoflurane to keep the animals anaesthetized during the scanning procedure reduced the motion artefacts. Amira software (FEI Visualization Sciences Group) was used to segment each component (vertebrae, implant, connector) and for the final rendering.

A.3.7 Histology of the spinal cord

To assess the implant bio-integration, histology was performed after 10 weeks of implantation on $n = 6$ rats. The animals were perfused with 4% PFA and their spinal cords were explanted. The spine was first kept in 4% PFA, then in sucrose and finally conserved in PBS. The spinal cords were frozen and cut into 40 μ m-thick slices using a cryostat (Leica Instruments). We used immunohistological staining against glial fibrillary acidic protein (GFAP) to reveal astrocytic reactivity. Slices were incubated overnight in anti-GFAP antibody solution (1:1000, Dako Z0334, USA) and visualized with a secondary antibody (Alexa fluor® 488 or 555, Thermofisher). Sections were imaged with a virtual slide scanner and 10x objective (VS120, Olympus). Immunostaining density was measured offline using an image analysis custom Matlab script with 3 representative images of sacral segment per rat. The circularity index was defined as $4\pi * \text{area} / \text{perimeter}^2$.

A.3.8 Acute EES of the spinal cord

Motor-evoked potential recruitments were performed on anesthetized animals (urethane 1 g/kg, intraperitoneal injection, Sigma- Aldrich). Large laminectomy was performed, exposing the lumbar-sacral segments and dorsal roots. Epidural electrodes delivered asymmetric pulses (200 μ s pulse width) at 0.5 Hz while motor-evoked potentials were recorded simultaneously. EES intensity was gradually increased from 0 up to 300 μ A. EMG signals were amplified, filtered (1–5000 Hz bandpass), and recorded for offline analysis. The peak to peak amplitude of the monosynaptic response was calculated and normalized for each muscle, and represented in black and yellow polar maps of motoneuron activation. Threshold of activation was defined as 10% of the total activation. When curve failed to reach a plateau, we extrapolated missing values using Matlab fitting function for sigmoidal non-linear curves.

A.3.9 Spinal cord injury model

Under aseptic conditions and general anaesthesia, the spinal cord segment T8-T9 was revealed after partial laminectomy at T9 vertebra segment. A force-controlled spinal cord impactor (IH-0400 Impactor, Precision Systems and Instrumentation LLC) applied a 230 kdyn (1 dyn = 10 μ N) to create severe contusion injury. The extent of the spinal lesion was evaluated using coronal tissue sections stained with antibodies against GFAP (Dako Z0334) and is represented in Figure A.6.

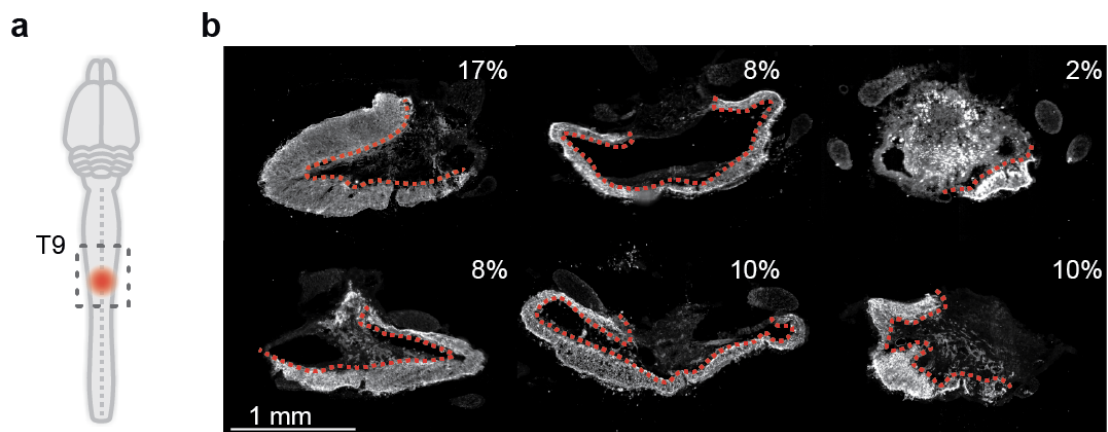


Figure A.6 – Spinal cord injury model

a, After partial laminectomy, rats received a spinal cord contusion to the T9 spinal segment. Spinal cord contusion is a clinically relevant model of injury. **b**, Quantification of the spinal lesions using coronal tissue sections stained with antibodies against GFAP. The red dashed line shows the lesion boundary. The ratio of intact tissue versus a control non-injured spinal cord is specified for each animal.

A.3.10 Rehabilitation after spinal cord injury

Each rats followed a training protocol starting 7 days after the injury. The neurorehabilitation program was conducted on a treadmill using a robotic body weight support system (Robomedica) that was adjusted to provide optimal assistance during bipedal stepping. To enable locomotion, a serotonergic replacement therapy combining the 5HT_{2A} agonist quipazine and the 5HT_{1A-7} agonist 8-OHDPAT was administered systemically 5 minutes before training [40]. The rehabilitation training was performed daily with electrical neuromodulation for 30 minutes.

Kinematics and muscle activity recording during neuromodulation

Methods for multimodal recordings during neuromodulation was previously described in [201]. An high-speed motion capture system (Vicon Motion Systems) tracked reflective markers with 12 infrared cameras (200 Hz). These markers were affixed to the rat hindlimb joints, including the iliac crest, greater trochanter (hip), lateral condyle (knee), lateral malleolus (ankle) and distal end of the fifth metatarsal (limb endpoint) of both legs. Their final 3D position was reconstructed offline using a native software (Nexus, Vicon). The system allows for the recording of EMG signals (2 kHz) after amplification and filtering (10–2000 Hz bandpass), and the monitoring of ground reaction forces in the vertical, anteroposterior and mediolateral directions using a force plate (2 kHz, HE6X6, AMTI) located below the treadmill belt. The system was synchronized with two cameras recording video (100 Hz, Basler Vision Technologies) oriented at 90 degrees and 270 degrees with respect to the direction of locomotion.

Closed-loop, real-time neuromodulation platform

The closed-loop spatiotemporal neuromodulation platform has been previously described in [202]. Briefly, the motion capture system generated raw 3D positions of the reflective markers and send them into a real-time algorithm via Ethernet using DataStream SDK software. A control platform implemented in a C++ environment (Visual Studio 2012, Microsoft). A processing unit (RZ5D, Tucker-Davis Technologies) connected to an MS16 Stimulus Isolator (Tucker-Davis Technologies) delivered the appropriate stimulation patterns. Inside a custom algorithm designed for online performance, we filtered signals, interpolated missing markers through triangulation and relabeled them to the actual position. According to each leg, the angular trajectory of the foot around a virtual center of rotation in the sagittal plane was continuously calculated. Based on angular values, the control algorithm triggered appropriate electrode combination stimulation. The platform process flow is illustrated in Figure A.7.

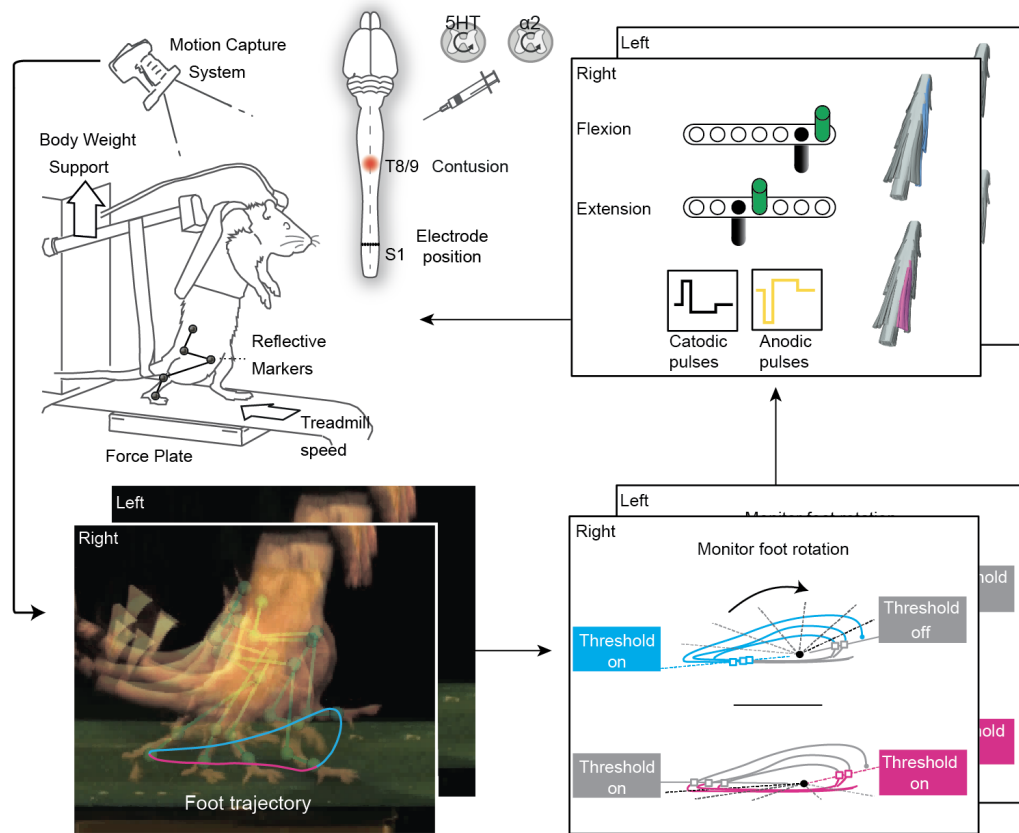


Figure A.7 – Real-time control platform

Following SCI, rats were placed on a treadmill in bipedal position supported by a robotic system to compensate the weight bearing. A 3D motion tracking system measures left and right foot positions. An angle is computed between the current foot position and a virtual center of gait cycle. This angle triggers On and Off states for each electrode when a defined threshold is crossed. The multipolar stimulation pattern respects the genetic algorithm prediction. Stimulation amplitude is tuned by user for fine adjustment. The asymmetric shape allow voltage balanced pulses and a dominant polarity.

Behavioural experiments

Paralysed rats were recorded bipedally on treadmill while a robotic body weight support system provided optimal assistive force against gravity. A serotonergic drug was injected systemically before each recording session. Five minutes after injection, EES were applied through the relevant electrode combination and an external ground electrode located subcutaneously. In the multipolar approach, the stimulation amplitude ratio was determined by a predictive algorithm. The exact intensity of electrical stimulation was then manually tuned (biphasic asymmetric rectangular pulses, 60 Hz, 50–300 μ A, 1/5 ratio, 200 μ s duration) to obtained the best kinematics. We compared the spatiotemporal and continuous neuromodulation performances in the same animals. The assistive body weight support was adapted for each

Appendix A. Appendix

animal and maintained constant across stimulation conditions. Furthermore, the stimulation intensity was adapted for each condition, as the high stimulation amplitudes of spatiotemporal neuromodulation would impede the continuous neuromodulation outcome. For performance analysis, we recorded 10 to 20 successive steps during continuous neuromodulation and during spatially multipolar stimulation. All the experimental conditions within and between recording sessions were randomized for the analysis.

A.3.11 Belt array substrate and superstrate material properties

Table A.1 – Mechanical properties of the belt silicone elastomers

Elastomers	Elongation at break (%)	Tear strength (N/mm)	Young's modulus (MPa)
Sylgard 184	100	3.4	3.9
Elastosil M4600	787	33.8	1.7

A.4 A soft optoelectronic implant for optogenetics in deep spinal structures

A.4.1 Comparison between the peripheral and spinal optoelectronic implants

Table A.2 – Optoelectronic implant dimensions

Parameters	Peripheral implant	Spinal implant
Pi thickness (μm)	7	3.6
Track width (μm)	150	120
Opening angle θ ($^\circ$)	75	45
PDMS substrate thickness (μm)	35	23
μ -LED thickness (μm)	140	50
# channels (# μ -LEDs/channel)	1 (4)	2 (2)
min, max thickness (μm)	100, 200	40, 100

A.4.2 Model of the light propagation in the spinal cord

A computational model was built using Comsol Multiphysics software to simulate and approximate the μ -LED array optical stimulation propagation in the spinal tissues. A single μ -LED channel was modelled with respect to the 3D dimensions of the μ -LEDs and encapsulation layers (i.e. PIB and PDMS). The PDMS encapsulation was modelled affixed to a large vertical cylindrical medium representing the spinal tissues. The propagation of light was computed using the Helmholtz equation for diffusion across a non-homogeneous medium:

$$\nabla(-c\nabla u) + \mu_a u = f \quad (\text{A.5})$$

$$c = \frac{1}{3}(\mu_a + \mu'_s) \quad (\text{A.6})$$

With μ_a , μ'_s the medium absorption and reduced scattering coefficients respectively, f the source term and u a dependent variable. The μ_a and μ'_s coefficients of the spinal tissues were extracted from the literature (cf. Table A.3). We did not find the coefficients for blue light diffusion in the spinal cord and assumed these were within the same order of magnitude as the coefficients of the brain white matter. The boundary conditions were set to confine the light source to the modelled μ -LEDs. The extent of light propagation through the tissues was estimated while varying the μ -LED output irradiance between 50-150 mW/mm².

Table A.3 – Absorption and scattering coefficients depending on the light wavelength

Wavelength (nm)	μ_a (mm ⁻¹)	μ_s (mm ⁻¹)	g	Reference
480	0.35	43	0.89	[277]
660	0.0216	15.47	0.9	[278]

A.4.3 Thermal model

In order to simulate the magnitude of heat generated by the μ -LEDs and its diffusion in the spinal tissues, a bio-heat transfer equation in solids, at steady-state, was implemented to the Comsol model:

$$\rho C \frac{dT}{dt} - \nabla \cdot (k \frac{dT}{dt}) = Q \quad (A.7)$$

With ρ the material density, C the specific heat capacity, k the heat conductivity, Q a heat source ($= \frac{power}{volume}$) and T a dependent variable. The parameters used for each material are displayed in Table A.4. As our μ -LEDs are fabricated on a SiC substrate, we modelled the μ -LEDs as a volume of SiC with corresponding thermal properties. The neural tissues thermal properties were extracted from the literature [171]. The changes in temperature was computed with respect to the power driving the μ -LEDs as well as their activation duty cycle. The boundary conditions were the room temperature during the infrared measurements (i.e. 28°C) for the model validation in air and 37°C for the heat propagation in tissues. A sweep of parameters was configured where the power per μ -LED varied from 3-9 mW (corresponding to 50-150 mW/mm²) and the duty cycle from 0-50%.

Table A.4 – Parameters of the heat transfer equation

Material	ρ (Kg/m ³)	C (J/(Kg.K))	k (W/(m.K))
SiC	3211	690	370
PIB	920	2000	0.19
PDMS	970	1460	0.16
Tissues	1075	3700	0.51

A.4.4 Spinal μ -LED array implantation

All surgical procedures were performed in accordance with Swiss federal legislation and under the guidelines established at EPFL and approved by local Swiss Veterinary Offices. Presented *in vivo* experiments involved C57BL/6 mice (male and female). Surgical procedures were performed under general anaesthesia with isoflurane in oxygen-enriched air (1–2%). The insertion of the spinal μ -LED array is analogous to the rat transversal array implantation. Briefly, two partial laminectomies at vertebrae levels T12-T13 and L2-L3 gave access to the mouse epidural space. A surgical suture (6-0, Ethicon) is used to pull the transversal implant

A.4. A soft optoelectronic implant for optogenetics in deep spinal structures

below vertebrae and above the dura mater. Following insertion, the activation of μ -LEDs was controlled. To avoid displacement of the implant, the spinal connector was secured with dental cement to the L3–L4 vertebra. Finally, the head connector (Omnetics) was cemented to the skull of the mouse. Following the surgery, mice were placed in an incubator to facilitate their recovery.

A.4.5 Microcomputed tomography

3D reconstructions of the spinal μ -LED array *in vivo* were produced via microcomputed tomography 2 weeks after implantation. The scanner (Quantum GX, Perkin Elmer) rotated around the mouse body and combined multiple angles of view to extract a 3D image. To reduce artefacts, we used a titanium μ -screw in the vertebral orthosis. The segmentation and reconstruction in 3D were made offline on the Analyze 12.0 software.

A.4.6 Histology and immunochemistry

We assessed the implant bio-integration after 6 weeks of implantation using histological analyses. The protocol is analogous to the one presented for the transversal electrode array. Mice were perfused with 4% PFA and their spinal cords were explanted. The spine was first kept in 4% PFA, then in sucrose and finally conserved in PBS. The spinal cords were frozen and cut into 40 μ m-thick slices using a cryostat (Leica Instruments). We used immunohistological stainings against glial fibrillary acidic protein (GFAP) to reveal astrocyte reactivity and against the ionized calcium binding adapter molecule 1 (Iba1) for inflammatory responses. Slices were incubated overnight in anti-GFAP antibody solution (1:1000, Dako Z0334) or in anti-Iba1 antibody (1:1000, Wako). Then, slices were incubated with a secondary antibody (1:1000, Alexa fluor® 594, Thermofisher). Sections were imaged with a virtual slide scanner and 20x objective (VS120, Olympus). Immunostaining density was measured offline using an image analysis custom Matlab script. The circularity index was defined as $4\pi \cdot \text{area} / \text{perimeter}^2$.

A.4.7 EMG electrode implantation and data acquisition

To record electromyographic activity, bipolar intramuscular electrodes (AS632, stainless-steel, Cooner Wire) were inserted bilaterally in the *tibialis anterior* (TA, ankle flexor) and the *iliopsoas* (IL, hip flexion) muscles. Recording electrodes were prepared prior to implantation by removing a small part (200 μ m notch) of PTFE insulation. A common ground was created with the same type of wire by removing about 1 cm of PTFE insulation from the distal extremity and was placed subcutaneously. All the wires were connected to a percutaneous amphenol connector (Omnetics) cemented on the animal skull. EMG recordings were synchronized with the wireless system stimulation onset using a custom-built trigger on the acquisition system (PowerLab 4/35, ADInstruments). Signals were amplified (x 1000) and pre-filtered (Band-pass: 100 Hz - 1 kHz) with an AM systems amplifier.

Bibliography

- [1] C. J. Woolf and Q. Ma, “Nociceptors—noxious stimulus detectors,” *Neuron*, vol. 55, no. 3, pp. 353–364, 2007.
- [2] S. C. Koch, D. Acton, and M. Goulding, “Spinal circuits for touch, pain, and itch,” *Annual review of physiology*, vol. 80, pp. 189–217, 2018.
- [3] J. Braz, C. Solorzano, X. Wang, and A. I. Basbaum, “Transmitting pain and itch messages: a contemporary view of the spinal cord circuits that generate gate control,” *Neuron*, vol. 82, no. 3, pp. 522–536, 2014.
- [4] D. Purves, G. J. Augustine, D. Fitzpatrick, W. Hall, A. LaMantia, J. McNamara, and L. White, “Neuroscience, 2008,” *De Boeck, Sinauer, Sunderland, Mass*, 2014.
- [5] T. Akay, W. G. Tourtellotte, S. Arber, and T. M. Jessell, “Degradation of mouse locomotor pattern in the absence of proprioceptive sensory feedback,” *Proceedings of the National Academy of Sciences*, vol. 111, no. 47, pp. 16877–16882, 2014.
- [6] A. I. Basbaum, D. M. Bautista, G. Scherrer, and D. Julius, “Cellular and molecular mechanisms of pain,” *Cell*, vol. 139, no. 2, pp. 267–284, 2009.
- [7] F. Lallemand and P. Ernfors, “Molecular interactions underlying the specification of sensory neurons,” *Trends in neurosciences*, vol. 35, no. 6, pp. 373–381, 2012.
- [8] C.-L. Li, K.-C. Li, D. Wu, Y. Chen, H. Luo, J.-R. Zhao, S.-S. Wang, M.-M. Sun, Y.-J. Lu, Y.-Q. Zhong, *et al.*, “Somatosensory neuron types identified by high-coverage single-cell rna-sequencing and functional heterogeneity,” *Cell research*, vol. 26, no. 1, p. 83, 2016.
- [9] I. M. Chiu, L. B. Barrett, E. K. Williams, D. E. Storchlic, S. Lee, A. D. Weyer, S. Lou, G. S. Bryman, D. P. Roberson, N. Ghasemlou, *et al.*, “Transcriptional profiling at whole population and single cell levels reveals somatosensory neuron molecular diversity,” *Elife*, vol. 3, p. e04660, 2014.
- [10] C. Peirs and R. P. Seal, “Neural circuits for pain: recent advances and current views,” *Science*, vol. 354, no. 6312, pp. 578–584, 2016.
- [11] A. E. Dubin and A. Patapoutian, “Nociceptors: the sensors of the pain pathway,” *The Journal of clinical investigation*, vol. 120, no. 11, pp. 3760–3772, 2010.

Bibliography

- [12] D. Julius and A. I. Basbaum, "Molecular mechanisms of nociception," *Nature*, vol. 413, no. 6852, p. 203, 2001.
- [13] L. E. Browne, A. Latremoliere, B. P. Lehnert, A. Grantham, C. Ward, C. Alexandre, M. Costigan, F. Michoud, D. P. Roberson, D. D. Ginty, *et al.*, "Time-resolved fast mammalian behavior reveals the complexity of protective pain responses," *Cell reports*, vol. 20, no. 1, pp. 89–98, 2017.
- [14] S. K. Mishra, S. M. Tisel, P. Orestes, S. K. Bhangoo, and M. A. Hoon, "Trpv1-lineage neurons are required for thermal sensation," *The EMBO journal*, vol. 30, no. 3, pp. 582–593, 2011.
- [15] I. Vandewauw, K. De Clercq, M. Mulier, K. Held, S. Pinto, N. Van Ranst, A. Segal, T. Voet, R. Vennekens, K. Zimmermann, *et al.*, "A trp channel trio mediates acute noxious heat sensing," *Nature*, vol. 555, no. 7698, p. 662, 2018.
- [16] M. Costigan, J. Scholz, and C. J. Woolf, "Neuropathic pain: a maladaptive response of the nervous system to damage," *Annual review of neuroscience*, vol. 32, pp. 1–32, 2009.
- [17] S. Tamburin, S. Paolucci, N. Smania, and G. Sandrini, "The burden of chronic pain and the role of neurorehabilitation: consensus matters where evidence is lacking," *Journal of pain research*, vol. 10, p. 101, 2017.
- [18] C. B. Johannes, T. K. Le, X. Zhou, J. A. Johnston, and R. H. Dworkin, "The prevalence of chronic pain in united states adults: results of an internet-based survey," *The Journal of Pain*, vol. 11, no. 11, pp. 1230–1239, 2010.
- [19] R. Andrew, S. Derry, R. S. Taylor, S. Straube, and C. J. Phillips, "The costs and consequences of adequately managed chronic non-cancer pain and chronic neuropathic pain," *Pain Practice*, vol. 14, no. 1, pp. 79–94, 2014.
- [20] O. Van Hecke, S. K. Austin, R. A. Khan, B. Smith, and N. Torrance, "Neuropathic pain in the general population: a systematic review of epidemiological studies," *PAIN®*, vol. 155, no. 4, pp. 654–662, 2014.
- [21] D. J. Gaskin and P. Richard, "The economic costs of pain in the united states," *The Journal of Pain*, vol. 13, no. 8, pp. 715–724, 2012.
- [22] J. N. Doctor, A. Nguyen, R. Lev, J. Lucas, T. Knight, H. Zhao, and M. Menchine, "Opioid prescribing decreases after learning of a patient's fatal overdose," *Science*, vol. 361, no. 6402, pp. 588–590, 2018.
- [23] N. D. Volkow and A. T. McLellan, "Opioid abuse in chronic pain—misconceptions and mitigation strategies," *New England Journal of Medicine*, vol. 374, no. 13, pp. 1253–1263, 2016.

-
- [24] P. Seth, L. Scholl, R. A. Rudd, and S. Bacon, "Overdose deaths involving opioids, cocaine, and psychostimulants—united states, 2015–2016," *American Journal of Transplantation*, vol. 18, no. 6, pp. 1556–1568, 2018.
- [25] T. Gomes, M. Tadrous, M. M. Mamdani, J. M. Paterson, and D. N. Juurlink, "The burden of opioid-related mortality in the united states," *JAMA Network Open*, vol. 1, no. 2, pp. e180217–e180217, 2018.
- [26] R. Melzack, P. D. Wall, *et al.*, "Pain mechanisms: a new theory," *Science*, vol. 150, no. 3699, pp. 971–979, 1965.
- [27] T. R. Deer, E. Grigsby, R. L. Weiner, B. Wilcosky, and J. M. Kramer, "A prospective study of dorsal root ganglion stimulation for the relief of chronic pain," *Neuromodulation: Technology at the Neural Interface*, vol. 16, no. 1, pp. 67–72, 2013.
- [28] B. A. Meyerson and B. Linderöth, "Mode of action of spinal cord stimulation in neuropathic pain," *Journal of pain and symptom management*, vol. 31, no. 4, pp. S6–S12, 2006.
- [29] B. Duan, L. Cheng, S. Bourane, O. Britz, C. Padilla, L. Garcia-Campmany, M. Krashes, W. Knowlton, T. Velasquez, X. Ren, *et al.*, "Identification of spinal circuits transmitting and gating mechanical pain," *Cell*, vol. 159, no. 6, pp. 1417–1432, 2014.
- [30] S. G. Boccard, E. A. Pereira, and T. Z. Aziz, "Deep brain stimulation for chronic pain," *Journal of Clinical Neuroscience*, vol. 22, no. 10, pp. 1537–1543, 2015.
- [31] T. Deer, I. Chapple, A. Classen, K. Javery, V. Stoker, L. Tonder, and K. Burchiel, "Intrathecal drug delivery for treatment of chronic low back pain: report from the national outcomes registry for low back pain," *Pain Medicine*, vol. 5, no. 1, pp. 6–13, 2004.
- [32] L. Colloca, T. Ludman, D. Bouhassira, R. Baron, A. H. Dickenson, D. Yarnitsky, R. Freeman, A. Truini, N. Attal, N. B. Finnerup, *et al.*, "Neuropathic pain," *Nature Reviews Disease Primers*, vol. 3, p. 17002, 2017.
- [33] E. M. Hagen, "How to prevent early mortality due to spinal cord injuries? new evidence & update," *The Indian journal of medical research*, vol. 140, no. 1, p. 5, 2014.
- [34] B. H. Dobkin and L. A. Havton, "Basic advances and new avenues in therapy of spinal cord injury," *Annu. Rev. Med.*, vol. 55, pp. 255–282, 2004.
- [35] E. M. Medica, S. Paolucci, A. Martinuzzi, G. Scivoletto, N. Smania, C. Solaro, *et al.*, "Assessing and treating pain associated with stroke, multiple sclerosis, cerebral palsy, spinal cord injury and spasticity. evidence and recommendations from the italian consensus conference on pain in neurorehabilitation," *Eur J Phys Rehabil Med*, vol. 52, no. 6, pp. 827–40, 2016.
- [36] M. Berkowitz, D. Kruse, P. O'Leary, and C. Harvey, *Spinal cord injury: an analysis of medical and social costs*. Demos Medical Publishing, 1998.

Bibliography

- [37] A. Ackery, C. Tator, and A. Krassioukov, "A global perspective on spinal cord injury epidemiology," *Journal of neurotrauma*, vol. 21, no. 10, pp. 1355–1370, 2004.
- [38] L. A. Simpson, J. J. Eng, J. T. Hsieh, Wolfe, and D. L. the Spinal Cord Injury Rehabilitation Evidence (SCIRE) Research Team, "The health and life priorities of individuals with spinal cord injury: a systematic review," *Journal of neurotrauma*, vol. 29, no. 8, pp. 1548–1555, 2012.
- [39] J. C. Baldi, R. Jackson, R. Moraille, and W. J. Mysiw, "Muscle atrophy is prevented in patients with acute spinal cord injury using functional electrical stimulation," *Spinal cord*, vol. 36, no. 7, p. 463, 1998.
- [40] R. van den Brand, J. Heutschi, Q. Barraud, J. DiGiovanna, K. Bartholdi, M. Huerlimann, L. Friedli, I. Vollenweider, E. M. Moraud, S. Duis, *et al.*, "Restoring voluntary control of locomotion after paralyzing spinal cord injury," *science*, vol. 336, no. 6085, pp. 1182–1185, 2012.
- [41] V. R. Edgerton and S. Harkema, "Epidural stimulation of the spinal cord in spinal cord injury: current status and future challenges," *Expert review of neurotherapeutics*, vol. 11, no. 10, pp. 1351–1353, 2011.
- [42] M. L. Gill, P. J. Grahm, J. S. Calvert, M. B. Linde, I. A. Lavrov, J. A. Strommen, L. A. Beck, D. G. Sayenko, M. G. Van Straaten, D. I. Drubach, *et al.*, "Neuromodulation of lumbosacral spinal networks enables independent stepping after complete paraplegia.," *Nature medicine*, 2018.
- [43] C. H. Tator, K. Minassian, and V. K. Mushahwar, "Spinal cord stimulation: therapeutic benefits and movement generation after spinal cord injury," in *Handbook of clinical neurology*, vol. 109, pp. 283–296, Elsevier, 2012.
- [44] M. Capogrosso, N. Wenger, S. Raspopovic, P. Musienko, J. Beauparlant, L. B. Luciani, G. Courtine, and S. Micera, "A computational model for epidural electrical stimulation of spinal sensorimotor circuits," *Journal of Neuroscience*, vol. 33, no. 49, pp. 19326–19340, 2013.
- [45] E. M. Moraud, M. Capogrosso, E. Formento, N. Wenger, J. DiGiovanna, G. Courtine, and S. Micera, "Mechanisms underlying the neuromodulation of spinal circuits for correcting gait and balance deficits after spinal cord injury," *Neuron*, vol. 89, no. 4, pp. 814–828, 2016.
- [46] S. Luan, I. Williams, K. Nikolic, and T. G. Constandinou, "Neuromodulation: present and emerging methods," *Frontiers in neuroengineering*, vol. 7, p. 27, 2014.
- [47] V. A. Sironi, "Origin and evolution of deep brain stimulation," *Frontiers in integrative neuroscience*, vol. 5, p. 42, 2011.

-
- [48] C. C. McIntyre and W. M. Grill, "Extracellular stimulation of central neurons: influence of stimulus waveform and frequency on neuronal output," *Journal of neurophysiology*, vol. 88, no. 4, pp. 1592–1604, 2002.
- [49] K. W. Horch and G. S. Dhillon, *Neuroprosthetics: theory and practice*. World Scientific, 2004.
- [50] N. P. Aryan, H. Kaim, and A. Rothermel, *Stimulation and recording electrodes for neural prostheses*, vol. 1. Springer, 2015.
- [51] W. E. Finn and P. G. LoPresti, *Handbook of neuroprosthetic methods*. CRC Press, 2002.
- [52] J. P. Slopsema, E. Peña, R. Patriat, L. J. Lehto, O. Gröhn, S. Mangia, N. Harel, S. Michaeli, and M. D. Johnson, "Clinical deep brain stimulation strategies for orientation-selective pathway activation," *Journal of neural engineering*, vol. 15, no. 5, p. 056029, 2018.
- [53] M. Dali, O. Rossel, D. Andreu, L. Laporte, A. Hernández, J. Laforet, E. Marijon, A. Hagège, M. Clerc, C. Henry, *et al.*, "Model based optimal multipolar stimulation without a priori knowledge of nerve structure: application to vagus nerve stimulation," *Journal of neural engineering*, vol. 15, no. 4, p. 046018, 2018.
- [54] S. Raspopovic, M. Capogrosso, J. Badia, X. Navarro, and S. Micera, "Experimental validation of a hybrid computational model for selective stimulation using transverse intrafascicular multichannel electrodes," *IEEE Transactions on Neural Systems and Rehabilitation Engineering*, vol. 20, no. 3, pp. 395–404, 2012.
- [55] F. Crick, "The impact of molecular biology on neuroscience," *Philosophical Transactions of the Royal Society of London B: Biological Sciences*, vol. 354, no. 1392, pp. 2021–2025, 1999.
- [56] K. Deisseroth, "Optogenetics," *Nature methods*, vol. 8, no. 1, p. 26, 2011.
- [57] E. S. Boyden, F. Zhang, E. Bamberg, G. Nagel, and K. Deisseroth, "Millisecond-timescale, genetically targeted optical control of neural activity," *Nature neuroscience*, vol. 8, no. 9, p. 1263, 2005.
- [58] A. R. Adamantidis, F. Zhang, A. M. Aravanis, K. Deisseroth, and L. De Lecea, "Neural substrates of awakening probed with optogenetic control of hypocretin neurons," *Nature*, vol. 450, no. 7168, p. 420, 2007.
- [59] L. Fenno, O. Yizhar, and K. Deisseroth, "The development and application of optogenetics," *Annual review of neuroscience*, vol. 34, 2011.
- [60] F. Zhang, J. Vierock, O. Yizhar, L. E. Fenno, S. Tsunoda, A. Kianianmomeni, M. Prigge, A. Berndt, J. Cushman, J. Polle, *et al.*, "The microbial opsin family of optogenetic tools," *Cell*, vol. 147, no. 7, pp. 1446–1457, 2011.

Bibliography

- [61] A. S. Chuong, M. L. Miri, V. Busskamp, G. A. Matthews, L. C. Acker, A. T. Sørensen, A. Young, N. C. Klapoetke, M. A. Henninger, S. B. Kodandaramaiah, *et al.*, “Noninvasive optical inhibition with a red-shifted microbial rhodopsin,” *Nature neuroscience*, vol. 17, no. 8, p. 1123, 2014.
- [62] N. C. Klapoetke, Y. Murata, S. S. Kim, S. R. Pulver, A. Birdsey-Benson, Y. K. Cho, T. K. Morimoto, A. S. Chuong, E. J. Carpenter, Z. Tian, *et al.*, “Independent optical excitation of distinct neural populations,” *Nature methods*, vol. 11, no. 3, p. 338, 2014.
- [63] J. G. Bernstein and E. S. Boyden, “Optogenetic tools for analyzing the neural circuits of behavior,” *Trends in cognitive sciences*, vol. 15, no. 12, pp. 592–600, 2011.
- [64] A. Stroh, *Optogenetics: A Roadmap*. Springer, 2018.
- [65] L. Madisen, T. Mao, H. Koch, J.-m. Zhuo, A. Berenyi, S. Fujisawa, Y.-W. A. Hsu, A. J. Garcia III, X. Gu, S. Zanella, *et al.*, “A toolbox of cre-dependent optogenetic transgenic mice for light-induced activation and silencing,” *Nature neuroscience*, vol. 15, no. 5, p. 793, 2012.
- [66] O. Yizhar, L. E. Fenno, T. J. Davidson, M. Mogri, and K. Deisseroth, “Optogenetics in neural systems,” *Neuron*, vol. 71, no. 1, pp. 9–34, 2011.
- [67] J. S. Wiegert, M. Mahn, M. Prigge, Y. Printz, and O. Yizhar, “Silencing neurons: tools, applications, and experimental constraints,” *Neuron*, vol. 95, no. 3, pp. 504–529, 2017.
- [68] M. R. Warden, J. A. Cardin, and K. Deisseroth, “Optical neural interfaces,” *Annual review of biomedical engineering*, vol. 16, pp. 103–129, 2014.
- [69] X. Navarro, T. B. Krueger, N. Lago, S. Micera, T. Stieglitz, and P. Dario, “A critical review of interfaces with the peripheral nervous system for the control of neuroprostheses and hybrid bionic systems,” *Journal of the Peripheral Nervous System*, vol. 10, no. 3, pp. 229–258, 2005.
- [70] S. P. Lacour, G. Courtine, and J. Guck, “Materials and technologies for soft implantable neuroprostheses,” *Nature Reviews Materials*, vol. 1, no. 10, p. 16063, 2016.
- [71] S. Cheng, E. C. Clarke, and L. E. Bilston, “Rheological properties of the tissues of the central nervous system: a review,” *Medical engineering & physics*, vol. 30, no. 10, pp. 1318–1337, 2008.
- [72] R. Feiner and T. Dvir, “Tissue–electronics interfaces: from implantable devices to engineered tissues,” *Nature Reviews Materials*, vol. 3, p. 17076, 2017.
- [73] A. Branner and R. A. Normann, “A multielectrode array for intrafascicular recording and stimulation in sciatic nerve of cats,” *Brain research bulletin*, vol. 51, no. 4, pp. 293–306, 2000.

- [74] B. Rubehn, C. Bosman, R. Oostenveld, P. Fries, and T. Stieglitz, "A mems-based flexible multichannel ecog-electrode array," *Journal of neural engineering*, vol. 6, no. 3, p. 036003, 2009.
- [75] I. R. Mineev, P. Musienko, A. Hirsch, Q. Barraud, N. Wenger, E. M. Moraud, J. Gandar, M. Capogrosso, T. Milekovic, L. Asboth, *et al.*, "Electronic dura mater for long-term multimodal neural interfaces," *Science*, vol. 347, no. 6218, pp. 159–163, 2015.
- [76] H. C. Elliott, "Cross-sectional diameters and areas of the human spinal cord," *The Anatomical Record*, vol. 93, no. 3, pp. 287–293, 1945.
- [77] M. Rigaud, G. Gemes, M.-E. Barabas, D. I. Chernoff, S. E. Abram, C. L. Stucky, and Q. H. Hogan, "Species and strain differences in rodent sciatic nerve anatomy: implications for studies of neuropathic pain," *Pain*, vol. 136, no. 1-2, pp. 188–201, 2008.
- [78] J.-W. Jeong, G. Shin, S. I. Park, K. J. Yu, L. Xu, and J. A. Rogers, "Soft materials in neuro-engineering for hard problems in neuroscience," *Neuron*, vol. 86, no. 1, pp. 175–186, 2015.
- [79] Q. Yuan, L. Dougherty, and S. S. Margulies, "In vivo human cervical spinal cord deformation and displacement in flexion," *Spine*, vol. 23, no. 15, pp. 1677–1683, 1998.
- [80] K. S. Topp and B. S. Boyd, "Structure and biomechanics of peripheral nerves: nerve responses to physical stresses and implications for physical therapist practice," *Physical therapy*, vol. 86, no. 1, pp. 92–109, 2006.
- [81] M. Schuettler, D. Pfau, J. S. Ordonez, C. Henle, P. Woias, and T. Stieglitz, "Stretchable tracks for laser-machined neural electrode arrays," in *Engineering in Medicine and Biology Society, 2009. EMBC 2009. Annual International Conference of the IEEE*, pp. 1612–1615, IEEE, 2009.
- [82] J. A. Fan, W.-H. Yeo, Y. Su, Y. Hattori, W. Lee, S.-Y. Jung, Y. Zhang, Z. Liu, H. Cheng, L. Falgout, *et al.*, "Fractal design concepts for stretchable electronics," *Nature communications*, vol. 5, p. 3266, 2014.
- [83] S. P. Lacour, Z. Huang, Z. Suo, and S. Wagner, "Deformable interconnects for conformal integrated circuits," *MRS Online Proceedings Library Archive*, vol. 736, 2002.
- [84] S. P. Lacour, S. Wagner, and Z. Suo, "Stretchable conductors: Thin gold films on silicone elastomer," *MRS Online Proceedings Library Archive*, vol. 795, 2003.
- [85] O. Graudejus, Z. Jia, T. Li, and S. Wagner, "Size-dependent rupture strain of elastically stretchable metal conductors," *Scripta materialia*, vol. 66, no. 11, pp. 919–922, 2012.
- [86] F. Michoud, L. Sottas, L. E. Browne, L. Asboth, A. Latremoliere, M. Sakuma, G. Courtine, C. J. Woolf, and S. P. Lacour, "Optical cuff for optogenetic control of the peripheral nervous system," *Journal of neural engineering*, vol. 15, no. 1, p. 015002, 2018.

- [87] K. L. Montgomery, S. M. Iyer, A. J. Christensen, K. Deisseroth, and S. L. Delp, "Beyond the brain: Optogenetic control in the spinal cord and peripheral nervous system," *Science translational medicine*, vol. 8, no. 337, pp. 337rv5–337rv5, 2016.
- [88] I. Daou, A. H. Tuttle, G. Longo, J. S. Wieskopf, R. P. Bonin, A. R. Ase, J. N. Wood, Y. De Koninck, A. Ribeiro-da Silva, J. S. Mogil, *et al.*, "Remote optogenetic activation and sensitization of pain pathways in freely moving mice," *Journal of Neuroscience*, vol. 33, no. 47, pp. 18631–18640, 2013.
- [89] A. Arcourt, L. Gorham, R. Dhandapani, V. Prato, F. J. Taberner, H. Wende, V. Gangadharan, C. Birchmeier, P. A. Heppenstall, and S. G. Lechner, "Touch receptor-derived sensory information alleviates acute pain signaling and fine-tunes nociceptive reflex coordination," *Neuron*, vol. 93, no. 1, pp. 179–193, 2017.
- [90] S. M. Iyer, K. L. Montgomery, C. Towne, S. Y. Lee, C. Ramakrishnan, K. Deisseroth, and S. L. Delp, "Virally mediated optogenetic excitation and inhibition of pain in freely moving nontransgenic mice," *Nature biotechnology*, vol. 32, no. 3, p. 274, 2014.
- [91] I. Daou, H. Beaudry, A. R. Ase, J. S. Wieskopf, A. Ribeiro-da Silva, J. S. Mogil, and P. Séguéla, "Optogenetic silencing of nav1. 8-positive afferents alleviates inflammatory and neuropathic pain," *eNeuro*, pp. ENEURO–0140, 2016.
- [92] B. E. Maimon, A. N. Zorzos, R. Bendell, A. Harding, M. Fahmi, S. Srinivasan, P. Calvaresi, and H. M. Herr, "Transdermal optogenetic peripheral nerve stimulation," *Journal of neural engineering*, vol. 14, no. 3, p. 034002, 2017.
- [93] F. Wu, E. Stark, M. Im, I.-J. Cho, E.-S. Yoon, G. Buzsáki, K. D. Wise, and E. Yoon, "An implantable neural probe with monolithically integrated dielectric waveguide and recording electrodes for optogenetics applications," *Journal of neural engineering*, vol. 10, no. 5, p. 056012, 2013.
- [94] C. Lu, U. P. Froriep, R. A. Koppes, A. Canales, V. Caggiano, J. Selvidge, E. Bizzi, and P. Anikeeva, "Polymer fiber probes enable optical control of spinal cord and muscle function in vivo," *Advanced Functional Materials*, vol. 24, no. 42, pp. 6594–6600, 2014.
- [95] M. T. Alt, E. Fiedler, L. Rudmann, J. S. Ordonez, P. Ruther, and T. Stieglitz, "Let there be light—optoprobes for neural implants," *Proceedings of the IEEE*, vol. 105, no. 1, pp. 101–138, 2017.
- [96] E. Iseri and D. Kuzum, "Implantable optoelectronic probes for in vivo optogenetics," *Journal of neural engineering*, vol. 14, no. 3, p. 031001, 2017.
- [97] L. E. Browne and C. J. Woolf, "Casting light on pain," *Nature biotechnology*, vol. 32, no. 3, p. 240, 2014.
- [98] C. Towne, K. L. Montgomery, S. M. Iyer, K. Deisseroth, and S. L. Delp, "Optogenetic control of targeted peripheral axons in freely moving animals," *PloS one*, vol. 8, no. 8, p. e72691, 2013.

- [99] K. L. Montgomery, A. J. Yeh, J. S. Ho, V. Tsao, S. M. Iyer, L. Grosenick, E. A. Ferenczi, Y. Tanabe, K. Deisseroth, S. L. Delp, *et al.*, “Wirelessly powered, fully internal optogenetics for brain, spinal and peripheral circuits in mice,” *Nature methods*, vol. 12, no. 10, p. 969, 2015.
- [100] M. E. Llewellyn, K. R. Thompson, K. Deisseroth, and S. L. Delp, “Orderly recruitment of motor units under optical control in vivo,” *Nature medicine*, vol. 16, no. 10, p. 1161, 2010.
- [101] S. I. Park, D. S. Brenner, G. Shin, C. D. Morgan, B. A. Copits, H. U. Chung, M. Y. Pullen, K. N. Noh, S. Davidson, S. J. Oh, *et al.*, “Soft, stretchable, fully implantable miniaturized optoelectronic systems for wireless optogenetics,” *Nature biotechnology*, vol. 33, no. 12, p. 1280, 2015.
- [102] B. R. Arenkiel, J. Peca, I. G. Davison, C. Feliciano, K. Deisseroth, G. J. Augustine, M. D. Ehlers, and G. Feng, “In vivo light-induced activation of neural circuitry in transgenic mice expressing channelrhodopsin-2,” *Neuron*, vol. 54, no. 2, pp. 205–218, 2007.
- [103] K. M. Tye and K. Deisseroth, “Optogenetic investigation of neural circuits underlying brain disease in animal models,” *Nature Reviews Neuroscience*, vol. 13, no. 4, p. 251, 2012.
- [104] D. R. Sparta, A. M. Stamatakis, J. L. Phillips, N. Hovelsø, R. Van Zessen, and G. D. Stuber, “Construction of implantable optical fibers for long-term optogenetic manipulation of neural circuits,” *Nature protocols*, vol. 7, no. 1, p. 12, 2012.
- [105] A. Canales, X. Jia, U. P. Froriep, R. A. Koppes, C. M. Tringides, J. Selvidge, C. Lu, C. Hou, L. Wei, Y. Fink, *et al.*, “Multifunctional fibers for simultaneous optical, electrical and chemical interrogation of neural circuits in vivo,” *Nature biotechnology*, vol. 33, no. 3, p. 277, 2015.
- [106] J. Wang, F. Wagner, D. A. Borton, J. Zhang, I. Ozden, R. D. Burwell, A. V. Nurmikko, R. van Wagenen, I. Diester, and K. Deisseroth, “Integrated device for combined optical neuromodulation and electrical recording for chronic in vivo applications,” *Journal of neural engineering*, vol. 9, no. 1, p. 016001, 2011.
- [107] M. Schwaerzle, P. Elmlinger, O. Paul, and P. Ruther, “Miniaturized 3 × 3 optical fiber array for optogenetics with integrated 460 nm light sources and flexible electrical interconnection,” in *Micro Electro Mechanical Systems (MEMS), 2015 28th IEEE International Conference on*, pp. 162–165, IEEE, 2015.
- [108] P. Anikeeva, A. S. Andalman, I. Witten, M. Warden, I. Goshen, L. Grosenick, L. A. Gunaydin, L. M. Frank, and K. Deisseroth, “Optetrode: a multichannel readout for optogenetic control in freely moving mice,” *Nature neuroscience*, vol. 15, no. 1, p. 163, 2012.

Bibliography

- [109] J. Voigts, J. H. Siegle, D. L. Pritchett, and C. I. Moore, "The flexdrive: an ultra-light implant for optical control and highly parallel chronic recording of neuronal ensembles in freely moving mice," *Frontiers in systems neuroscience*, vol. 7, p. 8, 2013.
- [110] A. Kiliyas, A. Canales, U. P. Froriep, S. Park, U. Egert, and P. Anikeeva, "Optogenetic entrainment of neural oscillations with hybrid fiber probes," *Journal of Neural Engineering*, 2018.
- [111] B. Rubehn, S. B. Wolff, P. Tovote, A. Lüthi, and T. Stieglitz, "A polymer-based neural microimplant for optogenetic applications: design and first in vivo study," *Lab on a Chip*, vol. 13, no. 4, pp. 579–588, 2013.
- [112] V. Caggiano, M. Sur, and E. Bizzi, "Rostro-caudal inhibition of hindlimb movements in the spinal cord of mice," *PloS one*, vol. 9, no. 6, p. e100865, 2014.
- [113] C. Lu, S. Park, T. J. Richner, A. Derry, I. Brown, C. Hou, S. Rao, J. Kang, C. T. Moritz, Y. Fink, *et al.*, "Flexible and stretchable nanowire-coated fibers for optoelectronic probing of spinal cord circuits," *Science advances*, vol. 3, no. 3, p. e1600955, 2017.
- [114] S. I. Al-Juboori, A. Dondzillo, E. A. Stubblefield, G. Felsen, T. C. Lei, and A. Klug, "Light scattering properties vary across different regions of the adult mouse brain," *PloS one*, vol. 8, no. 7, p. e67626, 2013.
- [115] I. Trujillo-Pisanty, C. Sanio, N. Chaudhri, and P. Shizgal, "Robust optical fiber patch-cords for in vivo optogenetic experiments in rats," *MethodsX*, vol. 2, pp. 263–271, 2015.
- [116] T. Miyashita, Y. R. Shao, J. Chung, O. Pourzia, and D. Feldman, "Long-term channelrhodopsin-2 (chr2) expression can induce abnormal axonal morphology and targeting in cerebral cortex," *Frontiers in neural circuits*, vol. 7, p. 8, 2013.
- [117] K. D. Campsall, C. J. Mazerolle, Y. De Repentingy, R. Kothary, and V. A. Wallace, "Characterization of transgene expression and cre recombinase activity in a panel of thy-1 promoter-cre transgenic mice," *Developmental dynamics: an official publication of the American Association of Anatomists*, vol. 224, no. 2, pp. 135–143, 2002.
- [118] H. Steffens, P. Dibaj, and E. Schomburg, "In vivo measurement of conduction velocities in afferent and efferent nerve fibre groups in mice," *Physiological research*, vol. 61, pp. 203–214, 2012.
- [119] C. K. Harnett, H. Zhao, and R. F. Shepherd, "Stretchable optical fibers: Threads for strain-sensitive textiles," *Advanced Materials Technologies*, vol. 2, no. 9, p. 1700087, 2017.
- [120] J. Guo, X. Liu, N. Jiang, A. K. Yetisen, H. Yuk, C. Yang, A. Khademhosseini, X. Zhao, and S.-H. Yun, "Highly stretchable, strain sensing hydrogel optical fibers," *Advanced Materials*, vol. 28, no. 46, pp. 10244–10249, 2016.
- [121] J. Guo, M. Niu, and C. Yang, "Highly flexible and stretchable optical strain sensing for human motion detection," *Optica*, vol. 4, no. 10, pp. 1285–1288, 2017.

-
- [122] C. Klein, H. C. Evrard, K. A. Shapcott, S. Haverkamp, N. K. Logothetis, and M. C. Schmid, "Cell-targeted optogenetics and electrical microstimulation reveal the primate konio-cellular projection to supra-granular visual cortex," *Neuron*, vol. 90, no. 1, pp. 143–151, 2016.
- [123] C. Pawela, E. DeYoe, and R. Pashaie, "Intracranial injection of an optogenetics viral vector followed by optical cannula implantation for neural stimulation in rat brain cortex," in *Optogenetics*, pp. 227–241, Springer, 2016.
- [124] L. F. Hernández, I. Castela, I. Ruiz-DeDiego, J. A. Obeso, and R. Moratalla, "Striatal activation by optogenetics induces dyskinesias in the 6-hydroxydopamine rat model of parkinson disease," *Movement Disorders*, vol. 32, no. 4, pp. 530–537, 2017.
- [125] S. Senova, C. Poupon, J. Dauguet, H. Stewart, G. Dugué, C. Jan, K. Hosomi, G. Ralph, L. Barnes, X. Drouot, *et al.*, "Optogenetic tractography for anatomo-functional characterization of cortico-subcortical neural circuits in non-human primates," *Scientific reports*, vol. 8, no. 1, p. 3362, 2018.
- [126] A. Berndt, S. Y. Lee, C. Ramakrishnan, and K. Deisseroth, "Structure-guided transformation of channelrhodopsin into a light-activated chloride channel," *Science*, vol. 344, no. 6182, pp. 420–424, 2014.
- [127] B. E. Maimon, K. Sparks, S. Srinivasan, A. N. Zorzos, and H. M. Herr, "Spectrally distinct channelrhodopsins for two-colour optogenetic peripheral nerve stimulation," *Nature Biomedical Engineering*, vol. 2, no. 7, p. 485, 2018.
- [128] H. Liske, X. Qian, P. Anikeeva, K. Deisseroth, and S. Delp, "Optical control of neuronal excitation and inhibition using a single opsin protein, chr2," *Scientific reports*, vol. 3, p. 3110, 2013.
- [129] J. B. Bryson, C. B. Machado, M. Crossley, D. Stevenson, V. Bros-Facer, J. Burrone, L. Green-smith, and I. Lieberam, "Optical control of muscle function by transplantation of stem cell-derived motor neurons in mice," *Science*, vol. 344, no. 6179, pp. 94–97, 2014.
- [130] T. Kim, M. Folcher, M. D.-E. Baba, and M. Fussenegger, "A synthetic erectile optogenetic stimulator enabling blue-light-inducible penile erection," *Angewandte Chemie International Edition*, vol. 54, no. 20, pp. 5933–5938, 2015.
- [131] K. Birmingham, V. Gradinaru, P. Anikeeva, W. M. Grill, V. Píkov, B. McLaughlin, P. Pasricha, D. Weber, K. Ludwig, and K. Famm, "Bioelectronic medicines: a research roadmap," *Nature Reviews Drug Discovery*, vol. 13, no. 6, p. 399, 2014.
- [132] V. K. Samineni, A. D. Mickle, J. Yoon, J. G. Grajales-Reyes, M. Y. Pullen, K. E. Crawford, K. N. Noh, G. B. Gereau, S. K. Vogt, H. H. Lai, *et al.*, "Optogenetic silencing of nociceptive primary afferents reduces evoked and ongoing bladder pain," *Scientific Reports*, vol. 7, no. 1, p. 15865, 2017.

- [133] P. Schönle, F. Michoud, N. Brun, A. Guex, S. P. Lacour, Q. Wang, and Q. Huang, "A wireless system with stimulation and recording capabilities for interfacing peripheral nerves in rodents," in *Engineering in Medicine and Biology Society (EMBC), 2016 IEEE 38th Annual International Conference of the*, pp. 4439–4442, IEEE, 2016.
- [134] K. Birmingham, V. Gradinaru, P. Anikeeva, W. M. Grill, V. Píkov, B. McLaughlin, P. Pasricha, D. Weber, K. Ludwig, and K. Famm, "A wireless optoelectronic system for optogenetic control of the peripheral nervous system," *Nature Reviews Drug Discovery*, vol. 13, no. 6, p. 399, 2014.
- [135] S. Park, Y. Guo, X. Jia, H. K. Choe, B. Grena, J. Kang, J. Park, C. Lu, A. Canales, R. Chen, *et al.*, "One-step optogenetics with multifunctional flexible polymer fibers," *Nature neuroscience*, vol. 20, no. 4, p. 612, 2017.
- [136] P. Anikeeva, "Optogenetics unleashed," *Nature biotechnology*, vol. 34, no. 1, p. 43, 2016.
- [137] S. Rudaz and R. Fletcher, "Advances in ingan technology for light-emitting diodes and semiconductor lasers," in *High-Temperature Electronic Materials, Devices and Sensors Conference, 1998*, pp. 123–131, IEEE, 1998.
- [138] M.-H. Chang, D. Das, P. Varde, and M. Pecht, "Light emitting diodes reliability review," *Microelectronics Reliability*, vol. 52, no. 5, pp. 762–782, 2012.
- [139] B. Fan and W. Li, "Miniaturized optogenetic neural implants: a review," *Lab on a Chip*, vol. 15, no. 19, pp. 3838–3855, 2015.
- [140] K. Kampasi, E. Stark, J. Seymour, K. Na, H. G. Winful, G. Buzsáki, K. D. Wise, and E. Yoon, "Fiberless multicolor neural optoelectrode for in vivo circuit analysis," *Scientific reports*, vol. 6, p. 30961, 2016.
- [141] N. McAlinden, D. Massoubre, E. Richardson, E. Gu, S. Sakata, M. D. Dawson, and K. Mathieson, "Thermal and optical characterization of micro-led probes for in vivo optogenetic neural stimulation," *Optics letters*, vol. 38, no. 6, pp. 992–994, 2013.
- [142] T.-i. Kim, J. G. McCall, Y. H. Jung, X. Huang, E. R. Siuda, Y. Li, J. Song, Y. M. Song, H. A. Pao, R.-H. Kim, *et al.*, "Injectable, cellular-scale optoelectronics with applications for wireless optogenetics," *Science*, vol. 340, no. 6129, pp. 211–216, 2013.
- [143] S. Ayub, F. Barz, O. Paul, and P. Ruther, "Heterogeneous 3d optrode with variable spatial resolution for optogenetic stimulation and electrophysiological recording," in *Engineering in Medicine and Biology Society (EMBC), 2016 IEEE 38th Annual International Conference of the*, pp. 1762–1765, IEEE, 2016.
- [144] S. Ayub, L. J. Gentet, R. Fiáth, M. Schwaerzle, M. Borel, F. David, P. Barthó, I. Ulbert, O. Paul, and P. Ruther, "Hybrid intracerebral probe with integrated bare led chips for optogenetic studies," *Biomedical microdevices*, vol. 19, no. 3, p. 49, 2017.

-
- [145] J.-W. Jeong, J. G. McCall, G. Shin, Y. Zhang, R. Al-Hasani, M. Kim, S. Li, J. Y. Sim, K.-I. Jang, Y. Shi, *et al.*, “Wireless optofluidic systems for programmable in vivo pharmacology and optogenetics,” *Cell*, vol. 162, no. 3, pp. 662–674, 2015.
- [146] F. Wu, E. Stark, P.-C. Ku, K. D. Wise, G. Buzsáki, and E. Yoon, “Monolithically integrated μ leds on silicon neural probes for high-resolution optogenetic studies in behaving animals,” *Neuron*, vol. 88, no. 6, pp. 1136–1148, 2015.
- [147] A. E. Mendrela, K. Kim, D. English, S. McKenzie, J. P. Seymour, G. Buzsáki, and E. Yoon, “A high-resolution opto-electrophysiology system with a miniature integrated headstage,” *IEEE transactions on biomedical circuits and systems*, no. 99, 2018.
- [148] T. D. Kozai, A. S. Jaquins-Gerstl, A. L. Vazquez, A. C. Michael, and X. T. Cui, “Brain tissue responses to neural implants impact signal sensitivity and intervention strategies,” *ACS chemical neuroscience*, vol. 6, no. 1, pp. 48–67, 2015.
- [149] K. Y. Kwon, B. Sirowatka, A. Weber, and W. Li, “Opto- μ ecog array: A hybrid neural interface with transparent μ ecog electrode array and integrated leds for optogenetics,” *IEEE transactions on biomedical circuits and systems*, vol. 7, no. 5, pp. 593–600, 2013.
- [150] M. A. Rossi, V. Go, T. Murphy, Q. Fu, J. Morizio, and H. H. Yin, “A wirelessly controlled implantable led system for deep brain optogenetic stimulation,” *Frontiers in integrative neuroscience*, vol. 9, p. 8, 2015.
- [151] G. Gagnon-Turcotte, Y. LeChasseur, C. Bories, Y. Messaddeq, Y. De Koninck, and B. Gosselin, “A wireless headstage for combined optogenetics and multichannel electrophysiological recording,” *IEEE transactions on biomedical circuits and systems*, vol. 11, no. 1, pp. 1–14, 2017.
- [152] L. Lu, P. Gutruf, L. Xia, D. L. Bhatti, X. Wang, A. Vazquez-Guardado, X. Ning, X. Shen, T. Sang, R. Ma, *et al.*, “Wireless optoelectronic photometers for monitoring neuronal dynamics in the deep brain,” *Proceedings of the National Academy of Sciences*, vol. 115, no. 7, pp. E1374–E1383, 2018.
- [153] M. Hashimoto, A. Hata, T. Miyata, and H. Hirase, “Programmable wireless light-emitting diode stimulator for chronic stimulation of optogenetic molecules in freely moving mice,” *Neurophotronics*, vol. 1, no. 1, p. 011002, 2014.
- [154] C. T. Wentz, J. G. Bernstein, P. Monahan, A. Guerra, A. Rodriguez, and E. S. Boyden, “A wirelessly powered and controlled device for optical neural control of freely-behaving animals,” *Journal of neural engineering*, vol. 8, no. 4, p. 046021, 2011.
- [155] S. T. Lee, P. A. Williams, C. E. Braine, D.-T. Lin, S. W. John, and P. P. Irazoqui, “A miniature, fiber-coupled, wireless, deep-brain optogenetic stimulator,” *IEEE Transactions on Neural Systems and Rehabilitation Engineering*, vol. 23, no. 4, pp. 655–664, 2015.

Bibliography

- [156] G. Shin, A. M. Gomez, R. Al-Hasani, Y. R. Jeong, J. Kim, Z. Xie, A. Banks, S. M. Lee, S. Y. Han, C. J. Yoo, *et al.*, “Flexible near-field wireless optoelectronics as subdermal implants for broad applications in optogenetics,” *Neuron*, vol. 93, no. 3, pp. 509–521, 2017.
- [157] P. Schönle, S. Fateh, T. Burger, and Q. Huang, “A power-efficient multi-channel ppg asic with 112db receiver dr for pulse oximetry and nirs,” in *Custom Integrated Circuits Conference (CICC), 2017 IEEE*, pp. 1–4, IEEE, 2017.
- [158] B. Razavi, *Principles of data conversion system design*, vol. 126. IEEE press New York, 1995.
- [159] M. Ying, A. P. Bonifas, N. Lu, Y. Su, R. Li, H. Cheng, A. Ameen, Y. Huang, and J. A. Rogers, “Silicon nanomembranes for fingertip electronics,” *Nanotechnology*, vol. 23, no. 34, p. 344004, 2012.
- [160] T. Pan, M. Pharr, Y. Ma, R. Ning, Z. Yan, R. Xu, X. Feng, Y. Huang, and J. A. Rogers, “Experimental and theoretical studies of serpentine interconnects on ultrathin elastomers for stretchable electronics,” *Advanced Functional Materials*, vol. 27, no. 37, p. 1702589, 2017.
- [161] J. Garra, T. Long, J. Currie, T. Schneider, R. White, and M. Paranjape, “Dry etching of polydimethylsiloxane for microfluidic systems,” *Journal of Vacuum Science & Technology A: Vacuum, Surfaces, and Films*, vol. 20, no. 3, pp. 975–982, 2002.
- [162] M. D. Kempe, D. L. Nobles, L. Postak, and J. A. Calderon, “Moisture ingress prediction in polyisobutylene-based edge seal with molecular sieve desiccant,” *Progress in Photovoltaics: Research and Applications*, vol. 26, no. 2, pp. 93–101, 2018.
- [163] A. Mercanzini, K. Cheung, D. L. Buhl, M. Boers, A. Maillard, P. Colin, J.-C. Bensadoun, A. Bertsch, and P. Renaud, “Demonstration of cortical recording using novel flexible polymer neural probes,” *Sensors and Actuators A: Physical*, vol. 143, no. 1, pp. 90–96, 2008.
- [164] B. Ketola, K. R. McIntosh, A. Norris, M. K. Tomalia, *et al.*, “Silicones for photovoltaic encapsulation,” in *23rd European Photovoltaic Solar Energy Conference*, pp. 1–5, 2008.
- [165] M. Gonzalez, F. Axisa, M. V. Bulcke, D. Brosteaux, B. Vandeveld, and J. Vanfleteren, “Design of metal interconnects for stretchable electronic circuits,” *Microelectronics Reliability*, vol. 48, no. 6, pp. 825–832, 2008.
- [166] C. Hassler, T. Boretius, and T. Stieglitz, “Polymers for neural implants,” *Journal of Polymer Science Part B: Polymer Physics*, vol. 49, no. 1, pp. 18–33, 2011.
- [167] I. Benedek and M. M. Feldstein, *Technology of pressure-sensitive adhesives and products*. CRC Press, 2008.

-
- [168] K. Kunal, M. Paluch, C. Roland, J. Puskas, Y. Chen, and A. Sokolov, "Polyisobutylene: A most unusual polymer," *Journal of Polymer Science Part B: Polymer Physics*, vol. 46, no. 13, pp. 1390–1399, 2008.
- [169] P. E. Keller and R. T. Kouzes, "Water vapor permeation in plastics," tech. rep., Pacific Northwest National Lab.(PNNL), Richland, WA (United States), 2017.
- [170] S. Allen, M. Fujii, V. Stannett, H. Hopfenberg, and J. Williams, "The barrier properties of polyacrylonitrile," *Journal of Membrane Science*, vol. 2, pp. 153–163, 1977.
- [171] M. M. Elwassif, Q. Kong, M. Vazquez, and M. Bikson, "Bio-heat transfer model of deep brain stimulation-induced temperature changes," *Journal of neural engineering*, vol. 3, no. 4, p. 306, 2006.
- [172] D. Dinakaran, C. Gossler, C. Mounir, O. Paul, U. T. Schwarz, and P. Ruther, "Phosphor-based light conversion for miniaturized optical tools," *Applied optics*, vol. 56, no. 13, pp. 3654–3659, 2017.
- [173] Y. Qi, N. Mair, K. K. Kummer, M. G. Leitner, M. Camprubí-Robles, M. Langeslag, and M. Kress, "Identification of chloride channels clcn3 and clcn5 mediating the excitatory cl⁻ currents activated by sphingosine-1-phosphate in sensory neurons," *Frontiers in molecular neuroscience*, vol. 11, p. 33, 2018.
- [174] J. Huang, X. Zhang, and P. A. McNaughton, "Inflammatory pain: the cellular basis of heat hyperalgesia," *Current neuropharmacology*, vol. 4, no. 3, pp. 197–206, 2006.
- [175] K. Nikolic, N. Grossman, M. S. Grubb, J. Burrone, C. Toumazou, and P. Degenaar, "Photocycles of channelrhodopsin-2," *Photochemistry and photobiology*, vol. 85, no. 1, pp. 400–411, 2009.
- [176] G. Nagel, T. Szellas, W. Huhn, S. Kateriya, N. Adeishvili, P. Berthold, D. Ollig, P. Hegemann, and E. Bamberg, "Channelrhodopsin-2, a directly light-gated cation-selective membrane channel," *Proceedings of the National Academy of Sciences*, vol. 100, no. 24, pp. 13940–13945, 2003.
- [177] V. K. Samineni, J. Yoon, K. E. Crawford, Y. R. Jeong, K. C. McKenzie, G. Shin, Z. Xie, S. S. Sundaram, Y. Li, M. Y. Yang, *et al.*, "Fully implantable, battery-free wireless optoelectronic devices for spinal optogenetics," *Pain*, vol. 158, no. 11, pp. 2108–2116, 2017.
- [178] I. M. Chiu, C. A. Von Hehn, and C. J. Woolf, "Neurogenic inflammation and the peripheral nervous system in host defense and immunopathology," *Nature neuroscience*, vol. 15, no. 8, p. 1063, 2012.
- [179] N. Ghasemlou, I. M. Chiu, J.-P. Julien, and C. J. Woolf, "Cd11b⁺ ly6g⁻ myeloid cells mediate mechanical inflammatory pain hypersensitivity," *Proceedings of the National Academy of Sciences*, vol. 112, no. 49, pp. E6808–E6817, 2015.

Bibliography

- [180] S. Talbot, S. L. Foster, and C. J. Woolf, "Neuroimmunity: physiology and pathology," *Annual review of immunology*, vol. 34, pp. 421–447, 2016.
- [181] P. Cornett, J. Matta, and G. Ahern, "General anesthetics sensitize the capsaicin receptor trpv1," *Molecular pharmacology*, 2008.
- [182] A. Leffler, M. J. Fischer, D. Rehner, S. Kienel, K. Kistner, S. K. Sauer, N. R. Gavva, P. W. Reeh, and C. Nau, "The vanilloid receptor trpv1 is activated and sensitized by local anesthetics in rodent sensory neurons," *The Journal of clinical investigation*, vol. 118, no. 2, pp. 763–776, 2008.
- [183] R. Pinnell, J. Dempster, and J. Pratt, "Miniature wireless recording and stimulation system for rodent behavioural testing," *Journal of neural engineering*, vol. 12, no. 6, p. 066015, 2015.
- [184] J. G. McCall, T.-i. Kim, G. Shin, X. Huang, Y. H. Jung, R. Al-Hasani, F. G. Omenetto, M. R. Bruchas, and J. A. Rogers, "Fabrication and application of flexible, multimodal light-emitting devices for wireless optogenetics," *Nature protocols*, vol. 8, no. 12, p. 2413, 2013.
- [185] B. A. Copits, M. Y. Pullen, and R. W. Gereau IV, "Spotlight on pain: optogenetic approaches for interrogating somatosensory circuits," *Pain*, vol. 157, no. 11, p. 2424, 2016.
- [186] S. M. Iyer, S. Vesuna, C. Ramakrishnan, K. Huynh, S. Young, A. Berndt, S. Y. Lee, C. J. Gorini, K. Deisseroth, and S. L. Delp, "Optogenetic and chemogenetic strategies for sustained inhibition of pain," *Scientific reports*, vol. 6, p. 30570, 2016.
- [187] J. Y. Lin, P. M. Knutsen, A. Muller, D. Kleinfeld, and R. Y. Tsien, "Reachr: a red-shifted variant of channelrhodopsin enables deep transcranial optogenetic excitation," *Nature neuroscience*, vol. 16, no. 10, p. 1499, 2013.
- [188] O. Yizhar, L. E. Fenno, M. Prigge, F. Schneider, T. J. Davidson, D. J. O'shea, V. S. Sohal, I. Goshen, J. Finkelstein, J. T. Paz, *et al.*, "Neocortical excitation/inhibition balance in information processing and social dysfunction," *Nature*, vol. 477, no. 7363, p. 171, 2011.
- [189] S. A. Prescott, Q. Ma, and Y. De Koninck, "Normal and abnormal coding of somatosensory stimuli causing pain," *Nature neuroscience*, vol. 17, no. 2, p. 183, 2014.
- [190] T. Kumazawa, ". the polymodal receptor: bio-warning and defense system," in *Progress in brain research*, vol. 113, pp. 3–18, Elsevier, 1996.
- [191] K. Birmingham, V. Gradinaru, P. Anikeeva, W. M. Grill, V. Piskov, B. McLaughlin, P. Pasricha, D. Weber, K. Ludwig, and K. Famm, "Optimized multipolar stimulation protocol for the recovery of locomotion after spinal cord injury in humans based on comparative anatomy in rats," *Nature Reviews Drug Discovery*, vol. 13, no. 6, p. 399, 2014.
- [192] C. S. Sherrington, "Flexion-reflex of the limb, crossed extension-reflex, and reflex stepping and standing," *The Journal of physiology*, vol. 40, no. 1-2, pp. 28–121, 1910.

-
- [193] D. Borton, S. Micera, J. d. R. Millán, and G. Courtine, “Personalized neuroprosthetics,” *Science translational medicine*, vol. 5, no. 210, pp. 210rv2–210rv2, 2013.
 - [194] M. R. Carhart, J. He, R. Herman, S. D’luzansky, and W. T. Willis, “Epidural spinal-cord stimulation facilitates recovery of functional walking following incomplete spinal-cord injury,” *IEEE Transactions on neural systems and rehabilitation engineering*, vol. 12, no. 1, pp. 32–42, 2004.
 - [195] V. R. Edgerton, G. Courtine, Y. P. Gerasimenko, I. Lavrov, R. M. Ichiyama, A. J. Fong, L. L. Cai, C. K. Otsoshi, N. J. Tillakaratne, J. W. Burdick, *et al.*, “Training locomotor networks,” *Brain research reviews*, vol. 57, no. 1, pp. 241–254, 2008.
 - [196] G. Fénelon, C. Goujon, J.-M. Gurruchaga, P. Cesaro, B. Jarraya, S. Palfi, and J.-P. Lefaucheur, “Spinal cord stimulation for chronic pain improved motor function in a patient with parkinson’s disease,” *Parkinsonism & related disorders*, vol. 18, no. 2, pp. 213–214, 2012.
 - [197] L. Illis, E. Sedgwick, A. Oygar, and M. S. Awadalla, “Dorsal-column stimulation in the rehabilitation of patients with multiple sclerosis,” *The Lancet*, vol. 307, no. 7974, pp. 1383–1386, 1976.
 - [198] S. Harkema, Y. Gerasimenko, J. Hodes, J. Burdick, C. Angeli, Y. Chen, C. Ferreira, A. Willhite, E. Rejc, R. G. Grossman, *et al.*, “Effect of epidural stimulation of the lumbosacral spinal cord on voluntary movement, standing, and assisted stepping after motor complete paraplegia: a case study,” *The Lancet*, vol. 377, no. 9781, pp. 1938–1947, 2011.
 - [199] P. Musienko, J. Heutschi, L. Friedli, R. Van Den Brand, and G. Courtine, “Multi-system neurorehabilitative strategies to restore motor functions following severe spinal cord injury,” *Experimental neurology*, vol. 235, no. 1, pp. 100–109, 2012.
 - [200] S. M. Danner, U. S. Hofstoetter, B. Freundl, H. Binder, W. Mayr, F. Rattay, and K. Minasian, “Human spinal locomotor control is based on flexibly organized burst generators,” *Brain*, vol. 138, no. 3, pp. 577–588, 2015.
 - [201] N. Wenger, E. M. Moraud, S. Raspopovic, M. Bonizzato, J. DiGiovanna, P. Musienko, M. Morari, S. Micera, and G. Courtine, “Closed-loop neuromodulation of spinal sensorimotor circuits controls refined locomotion after complete spinal cord injury,” *Science translational medicine*, vol. 6, no. 255, pp. 255ra133–255ra133, 2014.
 - [202] N. Wenger, E. M. Moraud, J. Gandar, P. Musienko, M. Capogrosso, L. Baud, C. G. Le Goff, Q. Barraud, N. Pavlova, N. Dominici, *et al.*, “Spatiotemporal neuromodulation therapies engaging muscle synergies improve motor control after spinal cord injury,” *Nature medicine*, vol. 22, no. 2, p. 138, 2016.
 - [203] M. Bonizzato, G. Pidpruzhnykova, J. DiGiovanna, P. Shkorbatova, N. Pavlova, S. Micera, and G. Courtine, “Brain-controlled modulation of spinal circuits improves recovery from spinal cord injury,” *Nature communications*, vol. 9, no. 1, p. 3015, 2018.

Bibliography

- [204] M. Capogrosso, T. Milekovic, D. Borton, F. Wagner, E. M. Moraud, J.-B. Mignardot, N. Buse, J. Gandar, Q. Barraud, D. Xing, *et al.*, “A brain–spine interface alleviating gait deficits after spinal cord injury in primates,” *Nature*, vol. 539, no. 7628, p. 284, 2016.
- [205] J. M. Henderson, C. Schade, J. Sasaki, D. L. Caraway, and J. C. Oakley, “Prevention of mechanical failures in implanted spinal cord stimulation systems,” *Neuromodulation: Technology at the Neural Interface*, vol. 9, no. 3, pp. 183–191, 2006.
- [206] M. Capogrosso, J. Gandar, N. Greiner, E. M. Moraud, N. Wenger, P. Shkorbatova, P. Musienko, I. Minev, S. Lacour, and G. Courtine, “Advantages of soft subdural implants for the delivery of electrochemical neuromodulation therapies to the spinal cord,” *Journal of neural engineering*, vol. 15, no. 2, p. 026024, 2018.
- [207] A. Garcia-Sandoval, A. Pal, A. M. Mishra, S. Sherman, A. R. Parikh, A. Joshi-Imre, D. Arreaga-Salas, G. Gutierrez-Heredia, A. C. Duran-Martinez, J. Nathan, *et al.*, “Chronic softening spinal cord stimulation arrays,” *Journal of neural engineering*, vol. 15, no. 4, p. 045002, 2018.
- [208] M. S. Nandra, I. A. Lavrov, V. R. Edgerton, and Y.-C. Tai, “A parylene-based microelectrode array implant for spinal cord stimulation in rats,” in *Micro Electro Mechanical Systems (MEMS), 2011 IEEE 24th International Conference on*, pp. 1007–1010, IEEE, 2011.
- [209] V. Giagka, A. Demosthenous, and N. Donaldson, “Flexible active electrode arrays with asics that fit inside the rat’s spinal canal,” *Biomedical microdevices*, vol. 17, no. 6, p. 106, 2015.
- [210] S. P. Lacour, D. Chan, S. Wagner, T. Li, and Z. Suo, “Mechanisms of reversible stretchability of thin metal films on elastomeric substrates,” *Applied Physics Letters*, vol. 88, no. 20, p. 204103, 2006.
- [211] Z. Yu, C. Tsay, S. P. Lacour, S. Wagner, and B. Morrison, “Stretchable microelectrode arrays a tool for discovering mechanisms of functional deficits underlying traumatic brain injury and interfacing neurons with neuroprosthetics,” in *Engineering in Medicine and Biology Society, 2006. EMBS’06. 28th Annual International Conference of the IEEE*, pp. 6732–6735, IEEE, 2006.
- [212] A. Buccarello, M. Azzarito, F. Michoud, S. P. Lacour, and J. P. Kucera, “Uniaxial strain of cultured mouse and rat cardiomyocyte strands slows conduction more when its axis is parallel to impulse propagation than when it is perpendicular,” *Acta physiologica*, vol. 223, no. 1, p. e13026, 2018.
- [213] I. R. Minev, D. J. Chew, E. Delivopoulos, J. W. Fawcett, and S. P. Lacour, “High sensitivity recording of afferent nerve activity using ultra-compliant microchannel electrodes: an acute in vivo validation,” *Journal of neural engineering*, vol. 9, no. 2, p. 026005, 2012.
- [214] H. O. Michaud, J. Teixidor, and S. P. Lacour, “Soft metal constructs for large strain sensor membrane,” *Smart Materials and Structures*, vol. 24, no. 3, p. 035020, 2015.

-
- [215] O. Graudejus, P. Gorn, and S. Wagner, "Controlling the morphology of gold films on poly (dimethylsiloxane)," *ACS applied materials & interfaces*, vol. 2, no. 7, pp. 1927–1933, 2010.
- [216] M. George, C. Coupeau, J. Colin, and J. Grilhé, "Atomic force microscopy observations of successive damaging mechanisms of thin films on substrates under tensile stress," *Thin solid films*, vol. 429, no. 1-2, pp. 267–272, 2003.
- [217] O. Graudejus, T. Li, J. Cheng, N. Keiper, R. Ponce Wong, A. Pak, and J. Abbas, "The effects of bending on the resistance of elastically stretchable metal conductors, and a comparison with stretching," *Applied Physics Letters*, vol. 110, no. 22, p. 221906, 2017.
- [218] I. R. Mineev, N. Wenger, G. Courtine, and S. P. Lacour, "Research update: platinum-elastomer mesocomposite as neural electrode coating," *APL Materials*, vol. 3, no. 1, p. 014701, 2015.
- [219] S. F. Cogan, "Neural stimulation and recording electrodes," *Annu. Rev. Biomed. Eng.*, vol. 10, pp. 275–309, 2008.
- [220] P. Moshayedi, G. Ng, J. C. Kwok, G. S. Yeo, C. E. Bryant, J. W. Fawcett, K. Franze, and J. Guck, "The relationship between glial cell mechanosensitivity and foreign body reactions in the central nervous system," *Biomaterials*, vol. 35, no. 13, pp. 3919–3925, 2014.
- [221] N. Vachicouras, C. M. Tringides, P. B. Campiche, and S. P. Lacour, "Engineering reversible elasticity in ductile and brittle thin films supported by a plastic foil," *Extreme Mechanics Letters*, vol. 15, pp. 63–69, 2017.
- [222] N. A. Staples, J. A. Goding, A. D. Gilmour, K. Y. Aristovich, P. Byrnes-Preston, D. S. Holder, J. W. Morley, N. H. Lovell, D. J. Chew, and R. A. Green, "Conductive hydrogel electrodes for delivery of long-term high frequency pulses," *Frontiers in neuroscience*, vol. 11, p. 748, 2018.
- [223] L. Ferlauto, A. N. D'Angelo, P. Vagni, A. Leccardi, M. J. Idelfonsa, F. M. Mor, E. A. Cuttaz, M. Heuschkel, L. Stoppini, and D. Ghezzi, "Development and characterization of pedot: Pss/alginate soft microelectrodes for application in neuroprosthetics," *Frontiers in Neuroscience*, vol. 12, p. 648, 2018.
- [224] K. M. Musick, J. Rigosa, S. Narasimhan, S. Wurth, M. Capogrosso, D. J. Chew, J. W. Fawcett, S. Micera, and S. P. Lacour, "Chronic multichannel neural recordings from soft regenerative microchannel electrodes during gait," *Scientific reports*, vol. 5, p. 14363, 2015.
- [225] I. Johnston, D. McCluskey, C. Tan, and M. Tracey, "Mechanical characterization of bulk sylgard 184 for microfluidics and microengineering," *Journal of Micromechanics and Microengineering*, vol. 24, no. 3, p. 035017, 2014.

Bibliography

- [226] S. Park, K. Mondal, R. M. Treadway III, V. Kumar, S. Ma, J. D. Holbery, and M. D. Dickey, "Silicones for stretchable and durable soft devices: Beyond sylgard-184," *ACS applied materials & interfaces*, vol. 10, no. 13, pp. 11261–11268, 2018.
- [227] G. Firpo, E. Angeli, L. Repetto, and U. Valbusa, "Permeability thickness dependence of polydimethylsiloxane (pdms) membranes," *Journal of Membrane Science*, vol. 481, pp. 1–8, 2015.
- [228] Y. Lei, Y. Liu, W. Wang, W. Wu, and Z. Li, "Studies on parylene c-caulked pdms (pcpdms) for low permeability required microfluidics applications," *Lab on a Chip*, vol. 11, no. 7, pp. 1385–1388, 2011.
- [229] J. Jeong, N. Chou, and S. Kim, "Long-term characterization of neural electrodes based on parylene-caulked polydimethylsiloxane substrate," *Biomedical microdevices*, vol. 18, no. 3, p. 42, 2016.
- [230] J. Ladenbauer, K. Minassian, U. S. Hofstoetter, M. R. Dimitrijevic, and F. Rattay, "Stimulation of the human lumbar spinal cord with implanted and surface electrodes: a computer simulation study," *IEEE Transactions on Neural Systems and Rehabilitation Engineering*, vol. 18, no. 6, pp. 637–645, 2010.
- [231] N. Dominici, Y. P. Ivanenko, G. Cappellini, A. d'Avella, V. Mondì, M. Cicchese, A. Fabiano, T. Silei, A. Di Paolo, C. Giannini, *et al.*, "Locomotor primitives in newborn babies and their development," *Science*, vol. 334, no. 6058, pp. 997–999, 2011.
- [232] C. A. Angeli, M. Boakye, R. A. Morton, J. Vogt, K. Benton, Y. Chen, C. K. Ferreira, and S. J. Harkema, "Recovery of over-ground walking after chronic motor complete spinal cord injury," *New England Journal of Medicine*, 2018.
- [233] A. J. Christensen, S. M. Iyer, A. François, S. Vyas, C. Ramakrishnan, S. Vesuna, K. Deisseroth, G. Scherrer, and S. L. Delp, "In vivo interrogation of spinal mechanosensory circuits," *Cell reports*, vol. 17, no. 6, pp. 1699–1710, 2016.
- [234] Y. Nam, J.-H. Kim, J.-H. Kim, M. K. Jha, J. Y. Jung, M.-G. Lee, I.-S. Choi, I.-S. Jang, D. G. Lim, S.-H. Hwang, *et al.*, "Reversible induction of pain hypersensitivity following optogenetic stimulation of spinal astrocytes," *Cell reports*, vol. 17, no. 11, pp. 3049–3061, 2016.
- [235] R. P. Bonin, F. Wang, M. Desrochers-Couture, A. Gąsecka, M.-E. Boulanger, D. C. Côté, and Y. De Koninck, "Epidural optogenetics for controlled analgesia," *Molecular pain*, vol. 12, p. 1744806916629051, 2016.
- [236] J. Y. Lin, "A user's guide to channelrhodopsin variants: features, limitations and future developments," *Experimental physiology*, vol. 96, no. 1, pp. 19–25, 2011.
- [237] G. Arias-Gil, F. W. Ohl, K. Takagaki, and M. T. Lippert, "Measurement, modeling, and prediction of temperature rise due to optogenetic brain stimulation," *Neurophotonics*, vol. 3, no. 4, p. 045007, 2016.

- [238] A. Al-Mosawie, J. Wilson, and R. Brownstone, "Heterogeneity of v2-derived interneurons in the adult mouse spinal cord," *European Journal of Neuroscience*, vol. 26, no. 11, pp. 3003–3015, 2007.
- [239] J. Zhang, G. M. Lanuza, O. Britz, Z. Wang, V. C. Siembab, Y. Zhang, T. Velasquez, F. J. Alvarez, E. Frank, and M. Goulding, "V1 and v2b interneurons secure the alternating flexor-extensor motor activity mice require for limbed locomotion," *Neuron*, vol. 82, no. 1, pp. 138–150, 2014.
- [240] V. Caggiano, V. C. Cheung, and E. Bizzi, "An optogenetic demonstration of motor modularity in the mammalian spinal cord," *Scientific reports*, vol. 6, p. 35185, 2016.
- [241] Y. Zhang, H. Lin, and W.-B. Yi, "Evaluation of the effects of ketamine on spinal anesthesia with levobupivacaine or ropivacaine," *Experimental and therapeutic medicine*, vol. 12, no. 4, pp. 2290–2296, 2016.
- [242] S. Zandieh, R. Hopf, H. Redl, and M. Schlag, "The effect of ketamine/xylazine anesthesia on sensory and motor evoked potentials in the rat," *Spinal Cord*, vol. 41, no. 1, p. 16, 2003.
- [243] J. Reid, "Effects of flexion-extension movements of the head and spine upon the spinal cord and nerve roots," *Journal of neurology, neurosurgery, and psychiatry*, vol. 23, no. 3, p. 214, 1960.
- [244] A. Hirsch, H. O. Michaud, A. P. Gerratt, S. De Mulatier, and S. P. Lacour, "Intrinsically stretchable biphasic (solid–liquid) thin metal films," *Advanced Materials*, vol. 28, no. 22, pp. 4507–4512, 2016.
- [245] D. J. Ellerbrock and D. D. Macdonald, "Passivity breakdown on solid versus liquid gallium," *Journal of The Electrochemical Society*, vol. 141, no. 10, pp. 2645–2649, 1994.
- [246] K. Goto, T. Nakagawa, O. Nakamura, and S. Kawata, "An implantable power supply with an optically rechargeable lithium battery," *IEEE Transactions on Biomedical Engineering*, vol. 48, no. 7, pp. 830–833, 2001.
- [247] C. A. von Hehn, R. Baron, and C. J. Woolf, "Deconstructing the neuropathic pain phenotype to reveal neural mechanisms," *Neuron*, vol. 73, no. 4, pp. 638–652, 2012.
- [248] E. Foster, H. Wildner, L. Tudeau, S. Haueter, W. T. Ralvenius, M. Jegen, H. Johannssen, L. Hösli, K. Haenraets, A. Ghanem, *et al.*, "Targeted ablation, silencing, and activation establish glycinergic dorsal horn neurons as key components of a spinal gate for pain and itch," *Neuron*, vol. 85, no. 6, pp. 1289–1304, 2015.
- [249] R. Suzuki, S. Morcuende, M. Webber, S. P. Hunt, and A. H. Dickenson, "Superficial nk1-expressing neurons control spinal excitability through activation of descending pathways," *Nature neuroscience*, vol. 5, no. 12, p. 1319, 2002.

Bibliography

- [250] M. Choi, J. W. Choi, S. Kim, S. Nizamoglu, S. K. Hahn, and S. H. Yun, "Light-guiding hydrogels for cell-based sensing and optogenetic synthesis in vivo," *Nature photonics*, vol. 7, no. 12, p. 987, 2013.
- [251] W. Bai, H. Yang, Y. Ma, H. Chen, J. Shin, Y. Liu, Q. Yang, I. Kandela, Z. Liu, S.-K. Kang, *et al.*, "Flexible transient optical waveguides and surface-wave biosensors constructed from monocrystalline silicon," *Advanced Materials*, vol. 30, no. 32, p. 1801584, 2018.
- [252] M. Malinverni, C. Tardy, M. Rossetti, A. Castiglia, M. Duelk, C. Vélez, D. Martin, and N. Grandjean, "Ingan laser diode with metal-free laser ridge using n+-gan contact layers," *Applied Physics Express*, vol. 9, no. 6, p. 061004, 2016.
- [253] C. Choi, A. R. Colón-Berríos, L. S. Hamachi, J. S. Owen, T. H. Schwartz, H. Ma, and I. Kymissis, "Localizing seizure activity in the brain using implantable micro-leds with quantum dot downconversion," *Advanced Materials Technologies*, p. 1700366, 2018.
- [254] A. Morton, C. Murawski, S. R. Pulver, and M. C. Gather, "High-brightness organic light-emitting diodes for optogenetic control of drosophila locomotor behaviour," *Scientific reports*, vol. 6, p. 31117, 2016.
- [255] Y. Wang, C. Zhu, R. Pfattner, H. Yan, L. Jin, S. Chen, F. Molina-Lopez, F. Lissel, J. Liu, N. I. Rabiah, *et al.*, "A highly stretchable, transparent, and conductive polymer," *Science advances*, vol. 3, no. 3, p. e1602076, 2017.
- [256] J. H. Lee, Y. R. Jeong, G. Lee, S. W. Jin, Y. H. Lee, S. Y. Hong, H. Park, J. W. Kim, S.-S. Lee, and J. S. Ha, "Highly conductive, stretchable, and transparent pedot: Pss electrodes fabricated with triblock copolymer additives and acid treatment," *ACS applied materials & interfaces*, vol. 10, no. 33, pp. 28027–28035, 2018.
- [257] J. Viventi, D.-H. Kim, L. Vigeland, E. S. Frechette, J. A. Blanco, Y.-S. Kim, A. E. Avrin, V. R. Tiruvadi, S.-W. Hwang, A. C. Vanleer, *et al.*, "Flexible, foldable, actively multiplexed, high-density electrode array for mapping brain activity in vivo," *Nature neuroscience*, vol. 14, no. 12, p. 1599, 2011.
- [258] J. Paek, I. Cho, and J. Kim, "Microrobotic tentacles with spiral bending capability based on shape-engineered elastomeric microtubes," *Scientific reports*, vol. 5, p. 10768, 2015.
- [259] S.-K. Kang, J. Koo, Y. K. Lee, and J. A. Rogers, "Advanced materials and devices for bioresorbable electronics," *Accounts of chemical research*, vol. 51, no. 5, pp. 988–998, 2018.
- [260] J. Koo, M. R. MacEwan, S.-K. Kang, S. M. Won, M. Stephen, P. Gamble, Z. Xie, Y. Yan, Y.-Y. Chen, J. Shin, *et al.*, "Wireless bioresorbable electronic system enables sustained nonpharmacological neuroregenerative therapy," *Nature medicine*, p. 1, 2018.
- [261] A. D. Valentine, T. A. Busbee, J. W. Boley, J. R. Raney, A. Chortos, A. Kotikian, J. D. Berrigan, M. F. Durstock, and J. A. Lewis, "Hybrid 3d printing of soft electronics," *Advanced Materials*, vol. 29, no. 40, p. 1703817, 2017.

- [262] Y. Ma, X. Feng, J. A. Rogers, Y. Huang, and Y. Zhang, "Design and application of 'j-shaped' stress-strain behavior in stretchable electronics: a review," *Lab on a Chip*, vol. 17, no. 10, pp. 1689–1704, 2017.
- [263] E. Song, R. Li, X. Jin, H. Du, Y. Huang, J. Zhang, Y. Xia, H. Fang, Y. K. Lee, K. J. Yu, *et al.*, "Ultrathin trilayer assemblies as long-lived barriers against water and ion penetration in flexible bioelectronic systems," *ACS nano*, 2018.
- [264] V. Woods, M. Trumpis, B. Bent, K. Palopoli-Trojani, C.-H. Chiang, C. Wang, C. Yu, M. Insanally, R. C. Froemke, and J. Viventi, "Long-term recording reliability of liquid crystal polymer μ ecog arrays," *Journal of neural engineering*, 2018.
- [265] S. Chen, A. Z. Weitemier, X. Zeng, L. He, X. Wang, Y. Tao, A. J. Huang, Y. Hashimoto-dani, M. Kano, H. Iwasaki, *et al.*, "Near-infrared deep brain stimulation via upconversion nanoparticle-mediated optogenetics," *Science*, vol. 359, no. 6376, pp. 679–684, 2018.
- [266] B. N. Armbruster, X. Li, M. H. Pausch, S. Herlitze, and B. L. Roth, "Evolving the lock to fit the key to create a family of g protein-coupled receptors potently activated by an inert ligand," *Proceedings of the National Academy of Sciences*, vol. 104, no. 12, pp. 5163–5168, 2007.
- [267] K. Satkunendrarajah, S. K. Karadimas, A. M. Laliberte, G. Montandon, and M. G. Fehlings, "Cervical excitatory neurons sustain breathing after spinal cord injury," *Nature*, p. 1, 2018.
- [268] Y. Tufail, A. Matyushov, N. Baldwin, M. L. Tauchmann, J. Georges, A. Yoshihiro, S. I. H. Tillery, and W. J. Tyler, "Transcranial pulsed ultrasound stimulates intact brain circuits," *Neuron*, vol. 66, no. 5, pp. 681–694, 2010.
- [269] S. Ibsen, A. Tong, C. Schutt, S. Esener, and S. H. Chalasani, "Sonogenetics is a non-invasive approach to activating neurons in *Caenorhabditis elegans*," *Nature communications*, vol. 6, p. 8264, 2015.
- [270] G. Brindley, "The first 500 sacral anterior root stimulators: implant failures and their repair," *Spinal Cord*, vol. 33, no. 1, p. 5, 1995.
- [271] A. Galvan, M. J. Caiola, and D. L. Albaugh, "Advances in optogenetic and chemogenetic methods to study brain circuits in non-human primates," *Journal of Neural Transmission*, vol. 125, no. 3, pp. 547–563, 2018.
- [272] A. F. Baptista, J. R. de Souza Gomes, J. T. Oliveira, S. M. G. Santos, M. A. Vannier-Santos, and A. M. B. Martinez, "A new approach to assess function after sciatic nerve lesion in the mouse—adaptation of the sciatic static index," *Journal of neuroscience methods*, vol. 161, no. 2, pp. 259–264, 2007.
- [273] J. Goh and W. Ladiges, "Voluntary wheel running in mice," *Current protocols in mouse biology*, vol. 5, no. 4, pp. 283–290, 2015.

Bibliography

- [274] E. J. Cobos, N. Ghasemlou, D. Araldi, D. Segal, K. Duong, and C. J. Woolf, "Inflammation-induced decrease in voluntary wheel running in mice: a nonreflexive test for evaluating inflammatory pain and analgesia," *PAIN®*, vol. 153, no. 4, pp. 876–884, 2012.
- [275] D. J. Cavanaugh, A. T. Chesler, A. C. Jackson, Y. M. Sigal, H. Yamanaka, R. Grant, D. O'Donnell, R. A. Nicoll, N. M. Shah, D. Julius, *et al.*, "Trpv1 reporter mice reveal highly restricted brain distribution and functional expression in arteriolar smooth muscle cells," *Journal of Neuroscience*, vol. 31, no. 13, pp. 5067–5077, 2011.
- [276] R. De Oliveira, D. Albuquerque, T. Cruz, F. Yamaji, and F. Leite, "Atomic force microscopy—imaging, measuring and manipulating surfaces at the atomic scale, measurement of the nanoscale roughness by atomic force microscopy: Basic principles and applications," *InTech*, 2012.
- [277] J. D. Johansson, "Spectroscopic method for determination of the absorption coefficient in brain tissue," *Journal of biomedical optics*, vol. 15, no. 5, p. 057005, 2010.
- [278] A. Shuaib and A. K. Bourisly, "Photobiomodulation optimization for spinal cord injury rat phantom model," *Translational neuroscience*, vol. 9, no. 1, pp. 67–71, 2018.

Glossary

AFM	atomic force microscope
Arch	archaerhodopsin
ASIC	application-specific integrated circuit
BLE	<i>Bluetooth</i> low energy
cCSC	cathodal charge storage capacity
CGRP	calcitonin gene-related peptide
ChR2	channelrhodopsin-2
CIE	International Commission on Illumination
CNS	central nervous system
CT	computed tomography
CV	cyclic voltammogram
DAC	digital-to-analogue converter
DBS	deep brain stimulation
DC	duty cycle
DRG	dorsal root ganglion
EES	epidural electrical stimulation
EMG	electromyography
FDA	Food and Drug Administration
FSM	finite state machine
FWHM	full widths at half maximum
GFAP	glial fibrillary acidic protein
GPIO	general purpose input/output
GSA	geometric surface area
H&E	hematoxylin and eosin
IC	integrated circuit
IL	iliopsoas
ILC	innate lymphoid cell

Glossary

IUAC	Institutional Animal Care and Use Committee
LED	light emitting diode
MBP	myelin basic protein
MG	medial gastrocnemius
MRI	magnetic resonance imaging
NA	numerical aperture
NpHr	<i>Natronomonas pharaonis</i> halorhodopsin
OLED	organic light emitting diodes
PBS	phosphate-buffered saline
PCA	principal component analysis
PCB	printed circuit board
PDMS	polydimethylsiloxane
PET	polyethylene terephthalate
PI	polyimide
PIB	polyisobuthylen
PNS	peripheral nervous system
PR	positive resist
PPG	photoplethysmograph
PSS	polystyrene-4-sulfonate
PTFE	polytetrafluoroethylene
ReaChR	red-activatable channelrhodopsin
RF	radio frequency
RIE	reactive ion etching
RMS	root mean square
RT	room temperature
RTV	room temperature vulcanization rubber
SCE	standard calomel electrode
SCI	spinal cord injury
SEM	scanning electron microscope
SFI	sciatic nerve functional index
SoC	system-on-chip
TA	tibialis anterior
TMA-O	transimpedance medical amplifier for oximetry
TRPV1	transient receptor potential channel vanilloid
USB	universal serial bus
VChR1	<i>Volvox</i> channelrhodopsin-1

Frédéric MICHOU, M.Sc. Bioengineering

+41 (0) 78 864 20 64

frederic.michoud@epfl.ch

[in /fredericmichoud/](https://www.linkedin.com/in/fredericmichoud/)

Geneva, Switzerland



EDUCATION

- 2014-2018 **PhD Candidate in Biotechnologies and Bioengineering**, Laboratory for Soft Bioelectronic Interfaces, Swiss Federal Institute of Technology, EPFL
- 2014 **Master in Bioengineering, Minor in Neuroprosthetics**, EPFL
- 2012 **Bachelor in Engineering of Life Sciences and Biology**, EPFL
- 2008 **Baccalauréat Scientifique** with honors, France

Languages

French: Native

English: Fluent

Spanish: Intermediary level

Computer skills

C++, MATLAB, Neuron, SolidWorks, AutoCAD, LaTeX, ImageJ, Office suite (Word, Excel, PowerPoint) & Adobe Creative suite (Illustrator, Photoshop)

Technical skills

Thin films, soft lithography, photolithography, packaging, SEM, AFM, electrochemistry, optoelectronics, fiber optics

Surgical skills, optogenetics, electrical stimulation, EMG, kinematics, immunochemistry, histology

Awards and Prizes

Winner of the CTI Entrepreneurship Business Concept Competition (2017)

Best Poster Award at the IEEE Life Sciences Grand Challenges Conference Singapore (2013)

Associative experiences

Summer School in Neurophysiology (NNBE) organiser, 2016 & 2017

Charity mission for the association «+ de vie»

Professional and Academic Experiences

- 2014 **Clifford Woolf lab, Harvard Medical School (6 months)**
Recording of neural activity *in vitro* using multi-electrode arrays (MEAs) and optogenetic modulation - Electrophysiology, data analysis
Development of mechanically soft optical cuffs for optogenetic stimulation in the mouse peripheral nervous system - Microfabrication, behavioural experiments, project management
- 2013 **SINAPSE (Singapore Institute for Neurotechnology), National University of Singapore (3 months)**
Restoration of hand functions after proximal nerve injury using neuroprosthetics
Cuff & LIFE neural electrode recording of the ulnar and median nerves - Signal processing, data classification, neural networks
- 2012 **NEUWalk Project, Grégoire Courtine lab, EPFL (1 year)**
Restoration of locomotion in rodent animal model of spinal cord injury with epidural electrical stimulation
Assessment of the biocompatibility of mechanically-soft spinal implants - Histology, confocal imaging, image analysis
- 2012 **Essential MED, in collaboration with SANARIA and the Swiss TPH, Tanzania (3 months)**
Creation a delivery network for a PfSPZ vaccine to prevent malaria in Africa – clinical trials, business model
- 2012 **BIOSENSORS, EPFL Innovation Park (6 months)**
Evaluation of a drug eluting technology minimizing infections for orthopaedic implants and hernia repair

Publications

Optical cuff for optogenetic control of the peripheral nervous system, *Journal of Neural Engineering* (2018)

Time-resolved fast mammalian behaviour reveals the complexity of protective pain responses, *Cell Reports* (2017)

A wireless system with stimulation and recording capabilities for interfacing peripheral nerves in rodents, *IEEE EMBC* (2016)

Correlation between muscular and nerve signals responsible for hand grasping in non-human primates, *IEEE EMBC* (2014)

